# NUCLEAR INSTRUMENTS & METHODS

A JOURNAL ON ACCELERATORS, INSTRUMENTATION
AND TECHNIQUES IN NUCLEAR PHYSICS

EDITOR: K. SIEGBAHN - UPPSALA

VOLUME 8

JULY 1960 — SEPTEMBER 1960

NORTH-HOLLAND PUBLISHING COMPANY — AMSTERDAM

PRINTED IN THE NETHERLANDS
DRUKKERIJ MEIJER N.V. WORMERVEER AND AMSTERDAM

64-06909

# NUCLEAR INSTRUMENTS AND METHODS

Per.
QC
786
N883
v.8-9

EDITORIAL BOARD:

J. B. ADAMS (CERN)
F. A. ALSINA (Buenos Aires)
E. AMALDI (Rome)
H. L. ANDERSON (Chicago)
K. T. BAINBRIDGE (Cambridge, Mass.)
P. R. BELL (Oak Ridge)
R. E. BELL (Montreal)
A. BERTHELOT (Saclay)
H. BRINKMAN (Groningen)
E. H. COOKE–YARBOROUGH (Harwell)
S. DE BENEDETTI (Pittsburgh)
M. DE HEMPTINNE (Louvain)
A. DE-SHALIT (Rehovoth)
M DEUTSCH (Cambridge, Mass.)
S. DU TOIT (Pretoria)
B. S. DŽELEPOV (Leningrad)
W. GENTNER (Heidelberg)
P. C. GUGELOT (Amsterdam)
H. HALBAN (Paris)
O. HAXEL (Heidelberg)
P. HUBER (Basel)
S. KIKUCHI (Tokyo)
J. KOCH (Copenhagen)
M. S. KOZODAEV (Moscow)
S. LIVINGSTON (Cambridge, Mass.)
E. M. MCMILLAN (Berkeley)
M. G. MEŠČERJAKOV (Moscow)
P. B. MOON (Birmingham)
M. L. OLIPHANT (Canberra)
W. PAUL (Bonn)
A. S. RAO (Bombay)
G. SALVINI (Rome)
P. SAVIĆ (Belgrade)
P. SCHERRER (Zürich)
CH. SCHMELZER (CERN)
R. TANGEN (Oslo)
D. TAYLOR (Northampton)
V. I. VEKSLER (Moscow)
G. VON DARDEL (CERN)
O. WERNHOLM (Stockholm)
R. R. WILSON (Cornell)
S. D. WINTER (Saclay)

JULY 1960 VOLUME 8 (1960) No. 1

GREGG M. SINCLAIR LIBRARY
UNIVERSITY OF HAWAII
8-7-63

# NUCLEAR INSTRUMENTS & METHODS

A JOURNAL ON ACCELERATORS, INSTRUMENTATION AND TECHNIQUES IN NUCLEAR PHYSICS

EDITOR: K. SIEGBAHN - UPPSALA

CONTENTS

J. VAN BLADEL, Fields excited by beam currents in circular accelerators . . . . . 1
A. F. DUNAITZEV, YU. D. PROKOSHKIN AND TANG SYAO-WEI, $\pi^-$star detector . . . . . 11
C. D. MOAK, Space-charge effects in cylindrical beams with uniform acceleration. . . . . 19
P. H. STOKER, On the construction and long-term performance of medium pressure $BF_3$ proportional counters used for cosmic-ray recording . . . . . 23
C. M. BRAAMS and P. B. SMITH, The Utrecht 850kV cascade generator. I. Beam deflection and energy control . . . . . 27
P. J. M. SMULDERS and P. B. SMITH, The Utrecht 850kV cascade generator. II. The beam integrator and galvanometer. . . . . 40
D. BRINI, A. GANDOLFI and G. L. TABELLINI, Transistorized apparatus for accumulation and binary-decimal conversion . . . . . 46
H. ENGELHARDT, I. HAUSER and U. KRECKER, Apparatus and laboratory for processing nuclear emulsion stacks . . . . . 55

*(continued on p. 3 of cover)*

NORTH-HOLLAND PUBLISHING COMPANY - AMSTERDAM

# NUCLEAR INSTRUMENTS AND METHODS

*A journal on accelerators, instrumentation and techniques in nuclear physics*

EDITOR: K. SIEGBAHN, UPPSALA



EDITORIAL BOARD:

J. B. ADAMS (CERN)
F. A. ALSINA (Buenos Aires)
E. AMALDI (Rome)
H. L. ANDERSON (Chicago)
K. T. BAINBRIDGE (Cambridge, Mass.)
P. R. BELL (Oak Ridge)
R. E. BELL (Montreal)
A. BERTHELOT (Saclay)
H. BRINKMAN (Groningen)
E. H. COOKE-VARBOROUGH (Harwell)
S. DE BENEDETTI (Pittsburgh)
M. DE HEMPTINNE (Louvain)
A. DE-SHALIT (Rehovoth)
M. DEUTSCH (Cambridge, Mass.)
S. DU TOIT (Pretoria)
B. S. DŽELEPOV (Leningrad)
W. GENTNER (Heidelberg)
P. C. GUGELOT (Amsterdam)
H. HALBAN (Paris)
O. HAXEL (Heidelberg)
P. HUBER (Basel)
S. KIKUCHI (Tokyo)
J. KOCH (Copenhagen)
M. S. KOZODAEV (Moscow)
S. LIVINGSTON (Cambridge, Mass.)
E. M. MCMILLAN (Berkeley)
M. G. MEŠČERJAKOW (Moscow)
P. B. MOON (Birmingham)
M. L. OLIPHANT (Canberra)
W. PAUL (Bonn)
A. S. RAO (Bombay)
G. SALVANI (Rome)
P. SAVIĆ (Belgrade)
P. SCHERRER (Zürich)
CH. SCHMELZER (CERN)
R. TANGEN (Oslo)
D. TAYLOR (Northampton)
V. I. VEKSLER (Moscow)
G. VON DARDEL (CERN)
O. WERNHOLM (Stockholm)
R. R. WILSON (Cornell)
S. D. WINTER (Saclay)


INSTRUCTIONS FOR CONTRIBUTORS

Contributions may be sent to the Editor, Professor K. Siegbahn, Institute of Physics, University of Uppsala, Sweden, either directly or through the intermediation of one of the members of the Editorial Board. Contributions may be written in English, French or German but should always, except for very short papers, be supplied with a brief abstract in English. Figures should be in inked original drawings or glossy prints and they should be sufficiently large. Contributors should make sure that important details in drawings and photographs will show up clearly in the diminished copy used by the publisher.

Books for review should be sent to Professor Siegbahn.

Objective and descriptive material on endeavours and product developments from the industry for the section "Spotlight on Industry" should be sent directly to the publishers, North-Holland Publishing Company, P.O. Box 103, Amsterdam.


Nuclear Instruments and Methods is published monthly. The subscription price of a volume of 360 pages is $ 17.00 (130 s), postage free.

Subscriptions should be sent to the publishers, North-Holland Publishing Company. P.O. Box 103, Amsterdam or to any subscription-agent.



No part of this issue may be reproduced in any form, by print, photoprint, microfilm or any other means without written permission from the publisher.

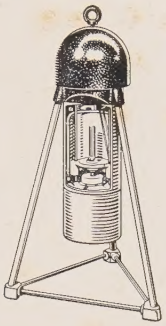

From time immemorial man has laboured on the provision of his drinking water, a fact strikingly demonstrated by the still existing aquaducts built by the Romans 2000 years ago.
To-day the degree of care demanded by the need for good quality water is steadily growing. Increasing use of radioactive isotopes and the putting into operation of nuclear reactors necessitate regular checking of the radioactive content of water, not only for human consumption but for the promotion of animal and plant life as well.

Radiation levels encountered in daily practice are low: tolerance level of contamination, as accepted by the I.C.R.P.*), has been defined to $10^{-7}$ $\mu$C per cm$^3$ of water. A further reduction of this standard might be expected in the future.

Measurement of these low activities calls for cumbersome and complicated equipment - if use is still made of conventional apparatus. However, Philips low-level beta counting assembly, type PW 4127, represents a remarkable solution.

# water - source of life

With a background count rate of only 1 c.p.m., the measurement of low intensity samples is reduced to short duration testing on a routine basis, yet with a definite accuracy:
Beta contamination of $15 \times 10^{-9}$ $\mu$C/cm$^3$ of drinking water is determined in one hour with a probable error of 12% (or in 30 minutes with a probable error of 17%) when measuring the sediment of 300 cm$^3$. This is less than 1/7th of the I.C.R.P. tolerance level.

*) I.C.R.P. = International Commission on Radiological Protection.

**PHILIPS**
**nuclear equipment**

N.V. PHILIPS' GLOEILAMPENFABRIEKEN
EINDHOVEN-HOLLAND

Particle accelerators ● Reactor control instrumentation ● Health protection and monitoring equipment ● Radiation measuring and detection equipment ● Geiger counter tubes ● Photomultipliers ● Radio-active isotopes ● Vacuum measuring equipment ● Air and gas liquefiers.

# EH ELECTROMETER AMPLIFIER

## *for DC and AC measurements in the ultra-low current region*

**MODEL 201C F.O.B. OAKLAND, CALIF. $650**

Excellent DC stability, fast transient response and high sensitivity make the 201C an outstanding instrument for research and engineering use. A nearly 9-decade range of $10^{-6}$ to $3x10^{-15}$ ampere gives it exceptional flexibility for numerous applications.

## SPECIFICATIONS

**16 CURRENT RANGES**
$3x10^{-14}$ to $10^{-6}$ ampere full scale

**ACCURACY**
2% (Pen Recorder Outputs); 3% of full scale (Panel Meter)

**DC STABILITY (after 45 min. warm up)**

**Short Term Stability** Better than 1%, 0.3%, or 0.1% of full scale depending on range position

**Line Voltage Effect** Less than 0.1%, 0.03%, or 0.01% of full scale per volt change in line voltage, depending on range position

**RESPONSE**

| Range | Time Constant |
|---|---|
| $10^{-6}$ (ampere full scale) | 40 microseconds |
| $3x10^{-7}$ to $3x10^{-8}$ | 50 microseconds |
| $10^{-8}$ to $10^{-9}$ | 250 microseconds |
| $3x10^{-10}$ to $3x10^{-11}$ | 5 milliseconds |
| $10^{-11}$ to $10^{-12}$ | 300 milliseconds |
| $3x10^{-13}$ to $3x10^{-14}$ | 5 seconds |

**GRID CURRENT**
Less than $3x10^{-15}$ ampere

**OUTPUTS**

1. BNC connector on front panel for oscilloscope or recorder: 3.0, 1.0, 0.3 volts available corresponding to full scale. Output impedance 10 ohms. Hum below 5 mv rms. Maximum output, ± 5 volts.
2. BNC connector on rear for recorder: 1000 ohms output impedance; 100 mv full scale
3. BNC connector on rear for recorder: 200 ohms output impedance; 10 mv full scale

*Write or wire E-H for additional information*

**E-H RESEARCH LABORATORIES, INC.**
163 ADELINE STREET • TEMPLEBAR 4-3030 • OAKLAND 20, CALIFORNIA

# 256 THE TMC 256-CHANNEL PULSE ANALYSIS SYSTEM

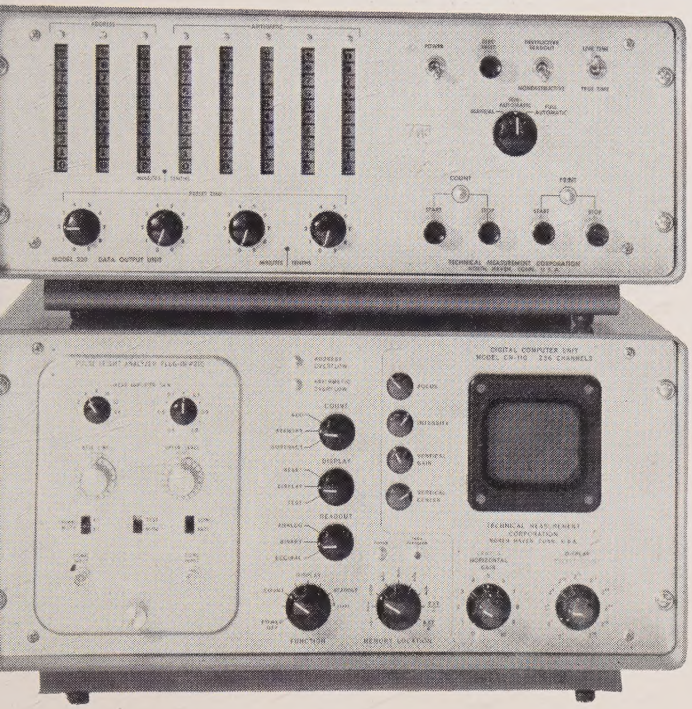

#220 DATA HANDLING UNIT usable as an active timer, event counter and readout device ... effective or actual counting times may be selected from 0.1 to 999.9 minutes in 0.1 min. steps ... manual, semi- or fully automatic operation, destructive and non-destructive readout.

PULSE HEIGHT ANALYSIS — #210 plug-in ... built-in linear amplifier, pulse generator ... 10-74 μs. dead time ... ±0.5% linearity

The Model CN-110 digital computer assembly ... only 8¾" high ... weighs 30 lbs. with plug-in ... operates on 25 watts

TIME-OF-FLIGHT MEASUREMENT #211 plug-in ... built-in delay of 0,1,2,3 times address cycle ... choice of 9 channel lengths from 0.25 to 64 μs. ... automatic channel advance

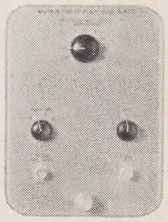

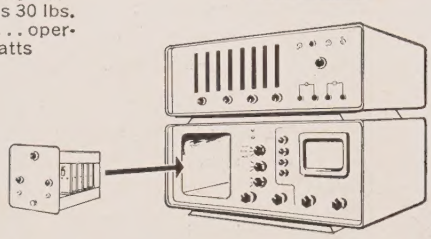

# ONE BENCH-TOP INSTRUMENT...

## Becomes a different pulse analyzer every time you change the logic

PULSED NEUTRON MEASUREMENT — #212 plug-in ... analysis channel lengths from 10 to 2560 μs. ... 10 μs. storage time ... (a high speed arithmetic scaler is supplied with the CN-110 at no extra charge when the 212 unit is purchased with it)

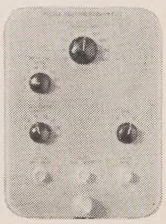

With just one CN-110 in your laboratory you have 256 channels of the pulse analysis you need — whether it's pulse height, time-of-flight, pulsed neutron or a special program. When you plug in the logic network, the instrument becomes a ready-to-use analysis system for that program. And you can change them in the time it takes to loosen a thumbscrew. Total weight is only 30 lbs., all circuits are transistorized — making this today's most versatile, compact pulse analyzer for research, field work or regular laboratory use. *They are now in production and deliveries are being made.*

**THE BASIC UNIT IS A COMPLETE DIGITAL COMPUTER** with all the circuitry for a 256-channel magnetic core memory and has the advantages of completely enclosed, plug-in memory ... choice of memory sub-groups ... pushbutton data transfer ... instantly selected analog, binary or digital readout.

**FOR DATA HANDLING,** a readout instrument has been designed specifically for use with the CN-110. The compact #220 data handling unit can be used as a live-timer during data gathering and as a readout system afterward. The #220 can be used with various types of paper tape printing and punching instruments.

Other readout devices that you can use with the CN-110 include strip chart and X-Y recorders, magnetic computer tape, punched paper cards.

Write for the new 6-page bulletin which contains complete details of the CN-110 and all accessories.

**TECHNICAL MEASUREMENT CORPORATION** TMC 441 WASHINGTON AVE., NORTH HAVEN, CONN.

Elcor inc.
1225 W. BROAD ST.,
FALLS CHURCH, VA.

## FEATURES

- Wide current range: 1 x $10^{-3}$ to 3 x $10^{-9}$ amp. in 12 switch settings.
- High accuracy: 1% of full scale.
- Internal calibrating current source to check proper operation.
- Front panel switch allows instrument to be used with current of either polarity.
- Pre-setting feature provides means of safeguarding against over-exposure.
- Developed especially for use with Van de Graaff and other high-voltage accelerators.
- Permits many experiments with particle accelerators that would otherwise be difficult or impossible.
- Register readout gives digital accuracy on charge measurement.

# MODEL A 309
# CURRENT INDICATOR AND INTEGRATOR

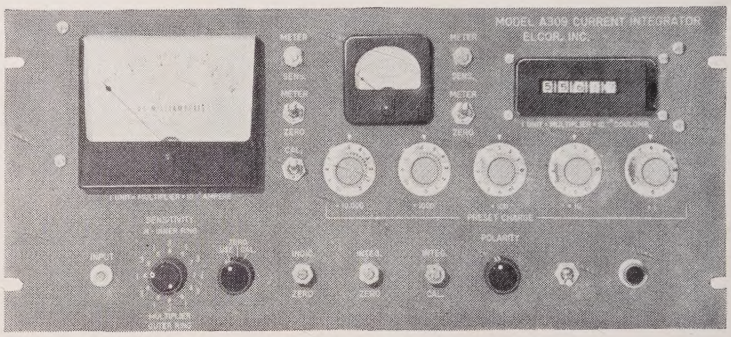


MODEL A 309 A

## The versatility and accuracy of two instruments in one!

1. Measures currents from 1 milliampere to 3 milli-microamperes.
2. Integrates input current and registers accumulated charge.

GENERAL DESCRIPTION—The Model A309 Current Indicator and Integrator is a sensitive current indicator that also measures the total charge collected in a given length of time. Developed especially for use with high-voltage particle accelerators such as the Van de Graaff generator, the instrument is also ideally suited for other applications requiring the measurement of accumulated charge or the integration of a variable current.

The full-scale sensitivity of the instrument can be varied from 1 milliampere to 3 milli-microamperes in twelve ranges. For convenience in checking the performance and accuracy of the instrument, an internal calibrating current source is provided for each range. The accumulated charge is indicated on a 5-decimal digit register. Any number up to 99,999 can be preset into the instrument, and upon reaching the corresponding charge a relay closes to actuate a warning device or control auxiliary equipment. In applications where X-rays are being generated, this feature affords protection against accidental over-exposure.

Input current of either polarity can be measured and integrated, and a front panel switch enables the instrument to be immediately changed from one polarity to the other. Advanced circuit techniques have been employed to achieve low input impedance, negligible drift, and a high overall accuracy and reliability.

Two models are available with the same specifications except for the method of presetting. In the Model A309A the presetting means consists of five front-panel switches. Presetting in the Model A309B is accomplished by manual adjustment of five presetting wheels that are accessible through the hinged cover of the register used in this model.

## SPECIFICATIONS

1. Input current for full-scale meter deflection: 1 x $10^{-3}$ to 3 x $10^{-9}$ ampere in twelve switch settings.
2. Polarity of input current: positive or negative, controlled by front-panel switch.
3. Current indicating means: 4½" meter.
4. Charge indicating means: 5-decimal-digit register and 2½" meter
5. Maximum charge indicating capacity: 99,999 units.
   Note: Each unit is equal to one coulomb multiplied by the numerical value of the full-scale current.
6. Maximum integrating time: 28 hours.
7. Integrating rate for full-scale current: 1 unit per second.
8. Method of presetting:
   Model A309A: five front-panel switches.
   Model A309B: five presetting wheels in register.
9. Accuracy (Indicating and integrating accuracy, based on full-scale current): 1%.
10. Maximum drift: .01% per hour.
11. Maximum input voltage for full-scale current: 2 millivolts.
12. Minimum signal-source impedance for 1% accuracy: 1 ohm divided by numerical value of full-scale current.
13. Calibration: Internal reference current provided for each current range.
14. Power Input: 110–125 volts, 50-60 cps.
15. Dimensions: 19" wide x 8¾" high x 13¼" deep.
16. Mounting: standard 19" relay rack.
17. Weight: approximately 25 lbs.
18. Price: Model A309A: $1674.00.
    Model A309B: $1524.00.

ELCOR,—INC. • 1225 W. BROAD STREET • FALLS CHURCH, VA.
Telephone JEfferson 2-7718
A subsidiary of Fairfax Manufacturing Co., Inc.
Bulletin No. 24-1258

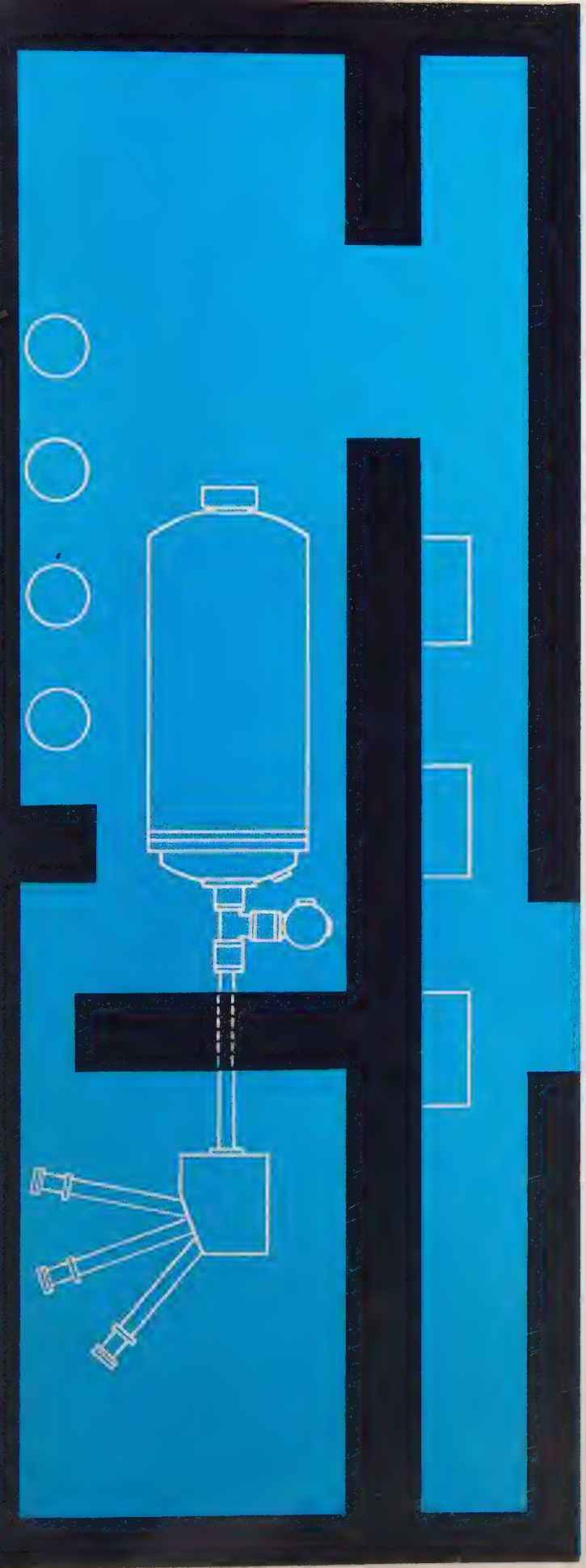

## FLOOR PLAN FOR MODERN RESEARCH

Dynamitron positive ion accelerators . . featuring wide voltage range, constant potential and the high current Dynamag ion source.

Dynamitron electron accelerators . . . featuring high power (up to 30 KW), and industrial reliability.

For detailed information, WRITE Dept. NIM.

**RADIATION DYNAMICS, INC.**

*Westbury Industrial Park*
*Westbury, Long Island, N. Y.*

Sales Agency:
C. ITOH & Co., Ltd.
2-4 Honcho
Nihon Bashi
Chuo-Ku
Tokyo, Japan

©N

Eldorado

DECIMAL SCALERS
FOR THE NUCLEAR PHYSICIST

100% SOLID STATE

...and Fast

Eldorado solid state all-electronic scalers count random events at a maximum rate of over one million counts per second. Resolving time is less than 1.0 microsecond. Especially well-suited for accelerator counting room service, these compact instruments weigh just 13 pounds and use ⅓ fewer transistors than comparable models. They can be used wherever the advantages of complete transistorization are important.

Eldorado offers three standard models in the SC-750 series, each with built-in regulated power supply. Two models provide full electronic storage of $10^7$ and $10^8$ counts. The third has 3 decades of electronic storage and a 4-digit mechanical register. Special versions can be furnished with other counting combinations and provisions for readout to a printer or tape punch.

**KEY SPECIFICATIONS**

| | |
|---|---|
| SCALER | |
| Resolution | Better than 1.0 microsecond |
| Max. Counting Rate | Greater than 1 megacycle |
| AMPLIFIER (optional) | |
| Minimum Input Signal | 10 millivolts |
| Overload Recovery | 100 X, 7 microsecond |
| DISCRIMINATOR TYPE | Integral |
| RANGE | 1 to 11 volts |
| SIZE | 19 x 3¼ x 10½ inches |

*Eldorado can furnish scalers and counters to fit your specific application. For more details, please address Dept.* 79

Eldorado Electronics
2821 Tenth Street
Berkeley 10, California

NOW!

an instrument designed to measure continuously . . . radioactive atmosphere and surface contamination!

THE TRITIUM MONITOR
MODEL TSM-91

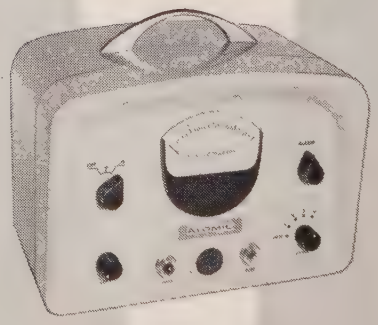

IDEALLY SUITED FOR THE MONITORING OF TRITIUM, ALPHA & OTHER LOW ENERGY BETA EMITTING RADIOISOTOPES

- Connections for external recorder
- Automatic signal alarm
- Includes "sniffer" hose attachment
- Portable . . . weighs only 12 pounds

For additional information write for bulletin TSM-91 N

ATOMIC accessories inc.
811 WEST MERRICK ROAD
VALLEY STREAM, NEW YORK

*One of a series of discussions on topics of particular interest to those employing radioisotopes and tracer techniques.*

# Let's Talk About SCALERS...

by Homer S. Myers, Vice President
Tracerlab, Inc.

Scalers have come a long way since Tracerlab designed and produced the first all-electronic automatic scaler back in 1946. Today several hundred types, made by more than 50 different companies, are available. So, if you are planning to buy a new one, this eight point check list will help you in making your decision. Consider:

1. The detectors it will accept.
2. Availability of preset count and preset time.
3. Resolving time.
4. Power Supply Range and Stability.
5. Ability to operate automatic systems.
6. Adaptability to future needs.
7. Reputation and experience of manufacturer.
8. Cost.

When we set out to design our new Tracermatic series of scalers, we "threw away the book", so to speak. Instead of going down the path of conventional design, where new instruments evolve by modification of existing types, we started afresh with the needs mentioned above as the principal design criteria. The result was the development of the Tracermatic family of scalers. They are, in actual fact, the only new scalers on the market today. Designed to be compatible with every standard radiation detector, the Tracermatic scalers have the one microsecond resolving time so desirable for proportional or scintillation counting. In addition, *both* resolving time and input sensitivity can be adjusted so as to permit you to choose the optimum values for all other types of detectors. The high voltage power supplies provide a high order of stability. Output voltage varies less than 0.003% for a 1% change in input voltage. The counting circuits employ cold cathode decades for long, trouble-free life and lower operating temperature. Data displays are simple, unique and non-ambiguous *and, furthermore, no mechanical registers are used.*

Electronically speaking, Tracermatic Scalers are designed to do all that any scaler should do — plus a little bit more. But, it is in functional versatility that the Tracermatic Scaler stands alone. You have never used or owned a scaler with which you can do *so much so easily*. Every Tracermatic Scaler has preset count. Most offer *both* preset count and preset time. All will operate automatic sample changers and data printout devices. In addition, Tracermatic Scalers can be adapted to work with standard commercial card or tape punch machines.

And here's an important extra— Tracermatic construction... an advanced concept under which all electronic components are mounted on two side chassis leaving open a central column for natural convection cooling. If your scaler ever requires maintenance, two lift-away side panels are quickly removed to expose *every* electronic component to view and to easy access with the instrument in a normal upright position.

Oh yes, and speaking of extras, don't forget those hidden extras you get every time you purchase a Tracerlab product. The first is your assurance that components and workmanship are of uniformly high quality. Another is your knowledge that your instrument is a member of a whole family of nuclear laboratory products serviced by a large staff of nuclear application engineers and a world-wide network of authorized service representatives.

There is a Tracermatic Scaler specifically designed for your needs (and your pocketbook). Write today for full details. Complete description of all Tracermatic Scalers available on request. *Ask for bulletins.*

Tracerlab KELEKET

Tracerlab *first in radiation measurement*

**TRACERLAB, INC.,** 1610 Trapelo Rd., Waltham 59, Massachusetts • 2030 Wright Ave., Richmond, California

## ALL-ROUND, LOW PRICED MONITOR

Typically developed as a laboratory equipment the monitor 111-A1 combines quality and high performance with low cost.

- Completely transistorized
- Designed as portable type
- Very low count rate: 0 to 5 c.p.s. full scale
- Highest count rate: 0 to 5000 c.p.s. full scale
- Equalizing accumulators
- Automatically recharged from A.C. mains
- Priced $ 410 F.O.B. Antwerp

For further information on this and other applications in the field of "Electronics for Nucleonics" ask :

AN ITT ASSOCIATE

**Bell Telephone Mfg Co**

"NUCLEAR ENERGY DIVISION"
33, Berkenrodelei
HOBOKEN-Antwerp
Belgium

---

NORTH-HOLLAND BOOKS

# *Paul Ehrenfest*

## COLLECTED SCIENTIFIC PAPERS

**XII + 632 pages**

**Guilders 45,00 (90s.)**

This volume makes widely scattered publications readily available. All Dutch articles appear here in English; the German publications are in the original language.

**Sole Agency for U.S.A.:**

**Interscience Publishers Inc. — New York**

**NORTH-HOLLAND PUBLISHING COMPANY - AMSTERDAM**

---

**FOR SCINTILLATION & PROPORTIONAL COUNTING**

***Non-overloading Linear Amplifiers***

**MODELS 108 and 108 p**

- GAIN–40,000, continuously variable
- RISE TIME–0.2 microsecond
- ACCEPTS + AND — PULSES

***Tremendous Dynamic Range***

**EXCEEDS 1,000,000 (0.1 mV to 100 V)**

Excellent linearity for small pulses in the presence of tremendous overloads that paralyze other amplifiers.
Model 108 P includes precision trigger type Pulse-Height Selector.

**Model 413 Mercury relay precision sliding Pulser**

**The one pulser that fills every need of the Nuclear Physics Laboratory**
0 to 100 Volts

10 full scale ranges from 1 mV to 100 volts
Fast rise and exponential decay of 1, 3, 10. 30, and 100 microsec simulate pulses from scintillation, proportional and Geiger counters.
Incorporates both manual control and precision motor drive.
The ideal instrument for precise calibration and test of pulse-height analyzers and other nuclear instrumentation.

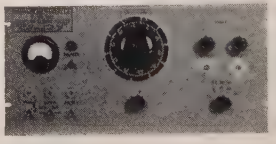

Window widths are determined AUTOMATICALLY, 10 × more ACCURATELY, 40 × FASTER than with conventional pulsers.

Model 108 Amplifier . . . . . $ 545.00
Model 108 P Amplifier (includes pulse-height selector) $ 595.00
Model 413 Precision Sliding Pulser . . . . . $ 630.00
Prices f.o.b. Silver Spring. Md.

**RADIATION INSTRUMENT CO.**

**P.O. BOX 733 SILVERSPRING, MARYLAND, U.S.A.**

N-371

AVAILABLE FROM **HAMNER**... A COMPLETE LINE OF

# NUCLEAR AMPLIFIERS

To fill any counting or budgetary requirement, Hamner now offers a complete line of three basic nuclear amplifiers, each available with a choice of discriminators on the same basic chassis. These three circuit types are:

- The ORNL double delay line A-8 circuit, for unexcelled overload protection and minimum base line shift, at high counting rates. (Ask about Hamner's exclusive fast coincidence pick-off circuit, optional on the same chassis).
- The N-302, Chase-Higinbotham design, for outstanding linearity, low noise and non-overload properties.
- The Hamner N-371, double RC circuit for low cost, routine counting or analysis applications.

Each amplifier is available with either integral discriminator or single channel pulse height analyzer on the same chassis. All units offer research quality specifications which will be demonstrated on request.

Hamner also markets a wide variety of other advanced type nuclear counting equipments which are tailored to operate with these amplifiers in forming various counting systems.

A-8

N-302

**WORLD-WIDE DISTRIBUTION AND ENGINEERING SERVICES**

EXPORT DEPARTMENT: 202 East 44th Street N.Y.C
CABLE: Henleysale, RCA Teletype 210 N.C.Y.

Hamner

## HAMNER ELECTRONICS CO., INC.

Department H.7, P.O. Box 531, Princeton, New Jersey, PEnnington 7-1320

# "PLANNAIR" GAS CIRCULATION BLOWERS FOR NUCLEAR PROJECTS

The AGR 19 Fuel Element Cluster $CO_2$ circulator, here illustrated, provides for reliable and efficient cooling of nuclear reactors. The blower, with its 11,500 r.p.m. motor (200V 400 c/s supply), is sealed within a long pressure vessel at the opposite end to which the nuclear reaction occurs. $CO_2$ circulates through the tube at 285 p.s.i. A and 95°C. The blower output is 6300 lb./hour at 7.5 p.s.i. pressure differential. A secondary radial impeller gives a cooling gas circuit via a demineralised water heat exchanger coil which keeps the motor operating at below 75°C.

This is but one of several gas circulating blowers which Plannair have designed for various nuclear projects. These include a Leaky Cartridge Test Rig Air-Blower, a Sodium Loop-Nitrogen Circulator, a Helium Circulator, Air Circulators and a Nitrogen Circulator for R.3 Adam, $CO_2$ circulator for Fuel Element Cluster Irradiation Test Rig, Burst Fuel Element Test Rig Air-Blower.

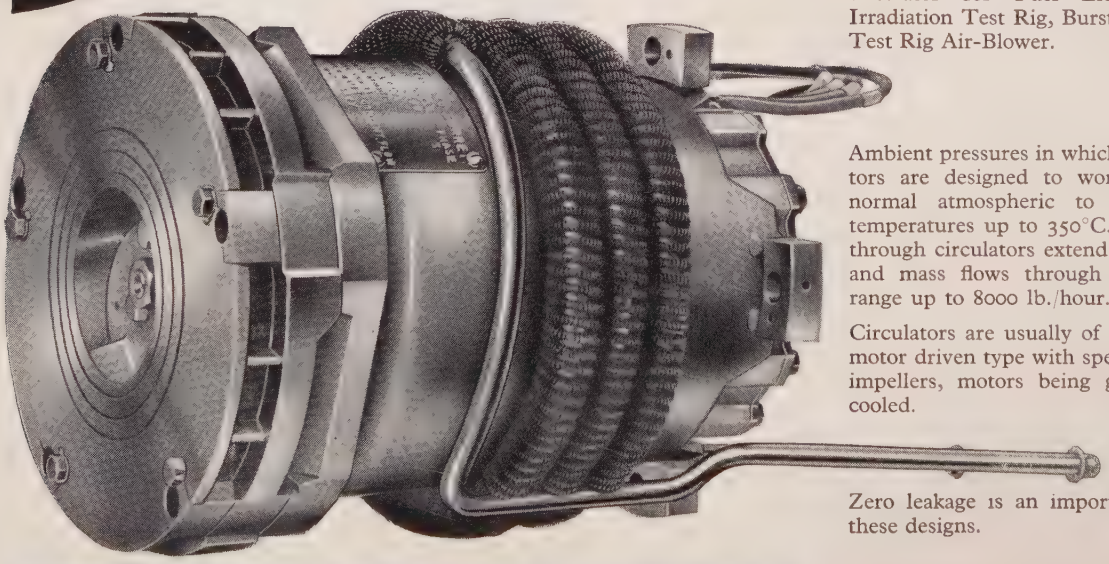

Ambient pressures in which these circulators are designed to work range from normal atmospheric to 300 p.s.i. at temperatures up to 350°C. Pressure rises through circulators extend up to 30 p.s.i. and mass flows through units cover a range up to 8000 lb./hour.

Circulators are usually of the high speed motor driven type with specially designed impellers, motors being gas and liquid cooled.

Zero leakage is an important feature of these designs.

*Further details available on request.*

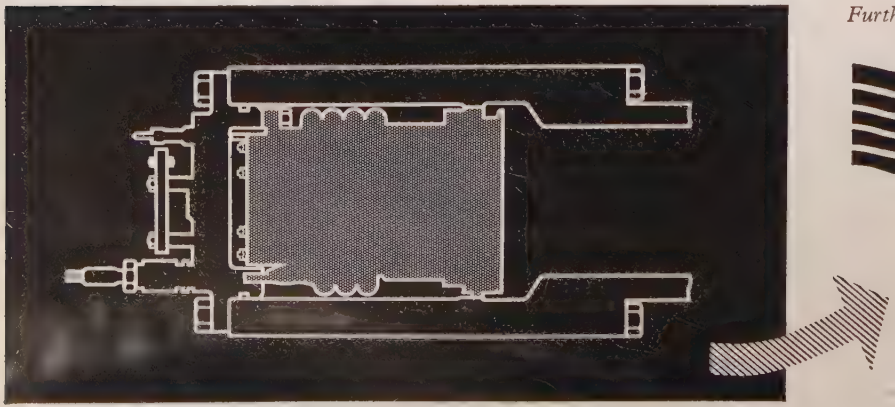

PLANNAIR

PLANNAIR LIMITED

Winfield House • Epsom Road

Leatherhead • Surrey

Tel: Leatherhead 4091/3, 2231

PLA39a

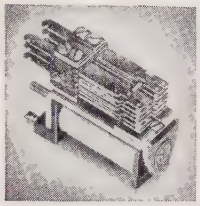

# customer evidence...

8

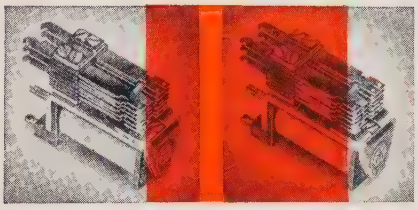

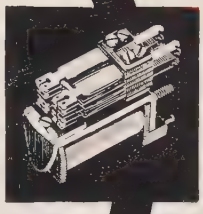

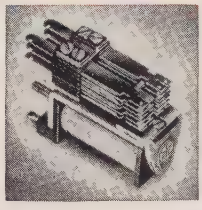

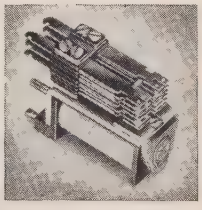

# operations

Modestly we claim that under suitable conditions this new miniature will give service in excess of 10 million operations but 100 millions leaves us breathless and not a little proud. Capable of handling springset arrangements of up to 12 springs normal duty loading and switching at speeds of better than 10 m.s. when required, the G.P.S.T. is a natural for computers and similar applications.

**See us on Stand D.153 at the I.E.A. Exhibition, Grand Hall, Olympia, London, from May 23rd — May 28th.**

ETELCO

For more details please write to the
TECHNICAL SERVICES DEPT.
**ELECTROMECHANICAL DIVISION**
BEESTON · NOTTINGHAM

T E L ENGLAND

ETELCO LIMITED · HEAD OFFICE · 22 LINCOLN'S INN FIELDS LONDON W.C.2

ER8a

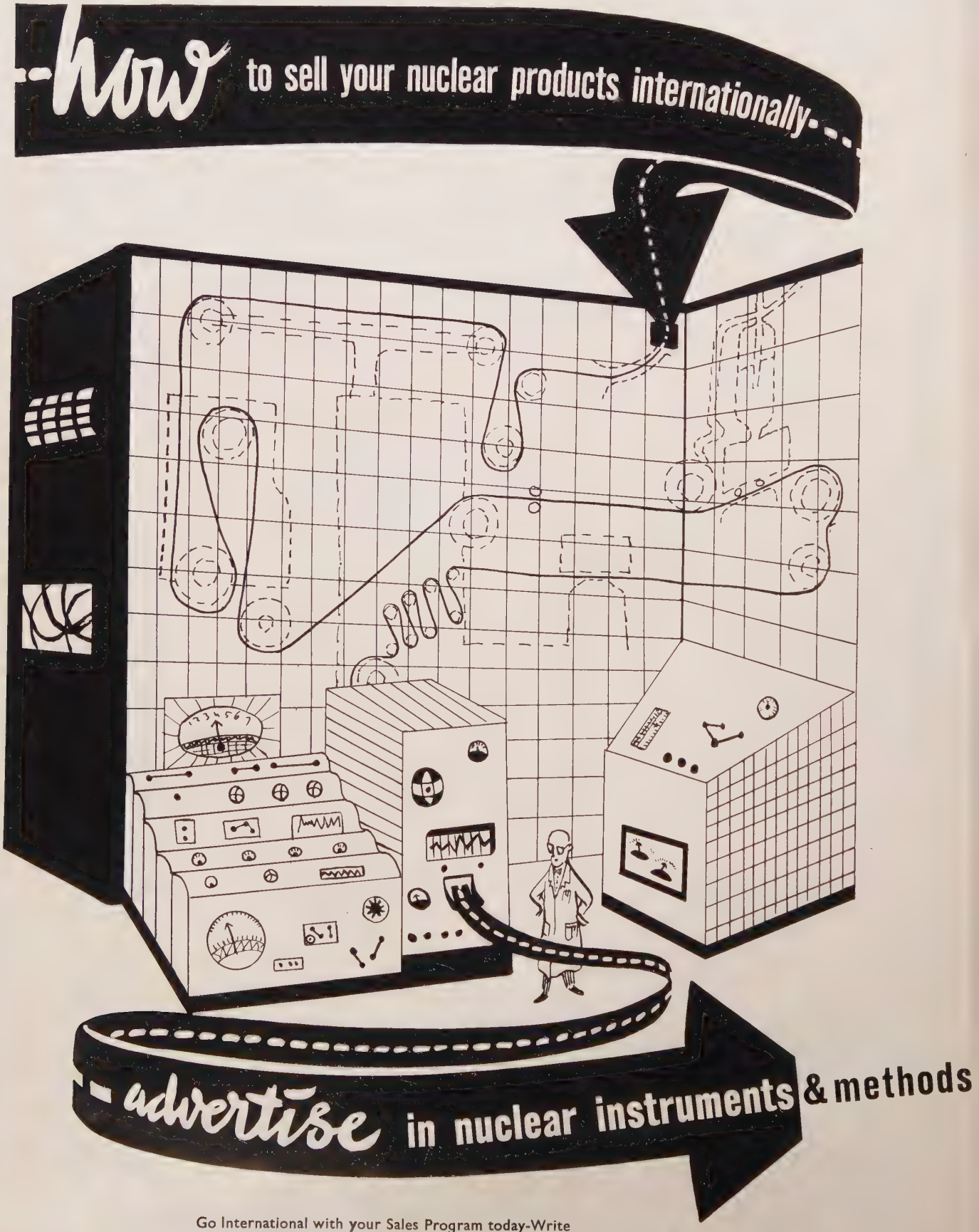


Go International with your Sales Program today-Write

**William F. Baars-Advertising Manager, North-Holland Publishing Company**

**P.O. Box 103, Amsterdam, The Netherlands**

# This is Research

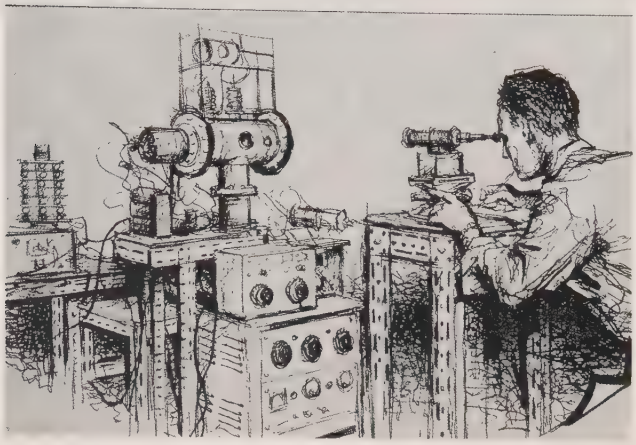

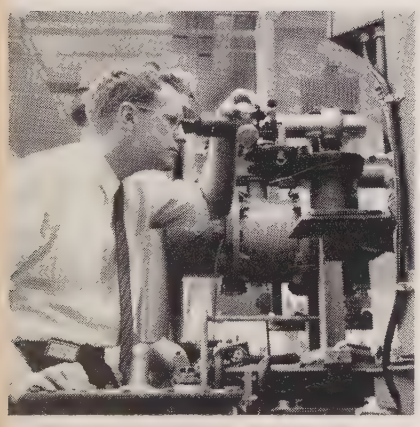

Nuclear particle accelerators designed and built by High Voltage Engineering Corporation are standard research equipment in virtually every major physics laboratory in the Free World.

The outstanding acceptance of these instruments by Science, Medicine and Industry has been due chiefly to intensive and continuing research both under Company sponsorship and in cooperation with government, academic and private institutions. This experience has given the men of High Voltage unique understanding of many phenomena which are becoming increasingly important in modern physics, nuclear engineering and space technology. Areas of research activity include:

| | |
|---|---|
| RADIATION POWER GENERATION | HIGH VACUUM |
| PARTICLE ACCELERATION | MAGNETICS |
| HIGH VOLTAGE ELECTROSTATICS | ION PROPULSION |
| ELECTRON AND ION OPTICS | RADIATION CHEMISTRY |
| MICROWAVE ELECTRONICS | NEUTRON ACTIVATION ANALYSIS |
| | PARTICLE ANALYSIS |

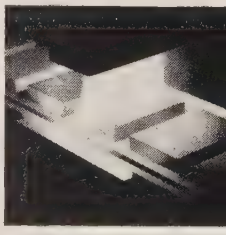

High Voltage is qualified to solve problems in these areas leading to specialized equipment for fundamental and applied research in nuclear plasma and solid state physics, chemistry and biology.

The brochure, *This is Research,* describes our research accomplishments and capabilities. Ask for a copy on your letterhead.

High Voltage Engineering (Europa) N.V.
Amersfoort, The Netherlands

**HIGH VOLTAGE ENGINEERING**
**CORPORATION**
**BURLINGTON, MASSACHUSETTS • U.S.A.**

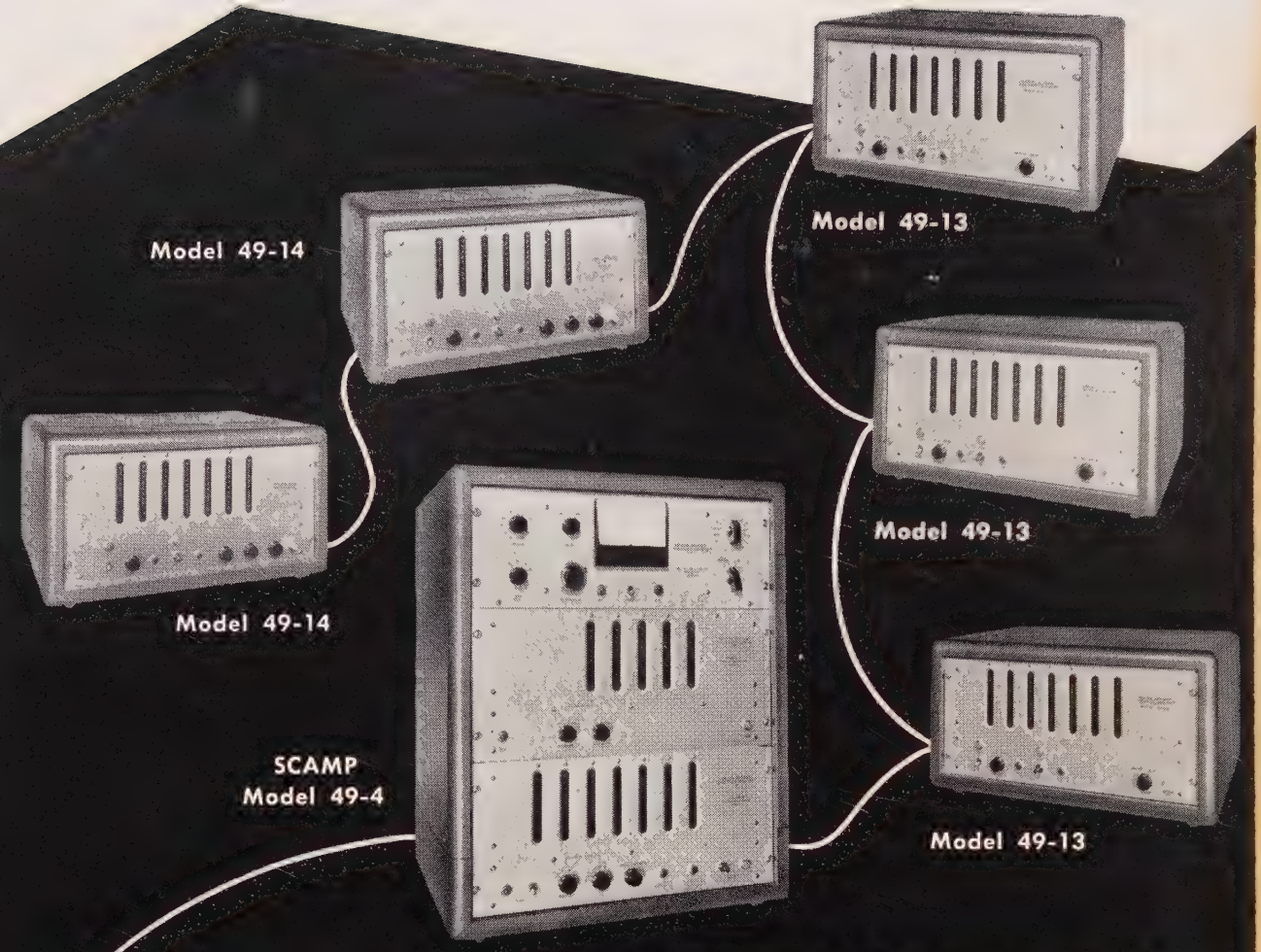


# All These Self-Programming Printing Scalers Connected to One Printer

**(two to a dozen, or more)**

FULLY AUTOMATIC OPERATION — Radiation Laboratory **automation** takes another step forward with RIDL self-programming **Printing Scalers.** Sequential data read out to any printer which accepts a 1-2-2'-4 four line binary coded decimal input makes possible the use of **any number of these printing scalers** with ONE printer.

The most popular **RIDL automatic scaling system** is the combination of the RIDL Model 49-4 SCAMP system with any number of Model 49-13 or 49-14 scalers, each connected to a different detector. Preset time, preset count, and fully automatic print out is thus available. Since these units are self-programming and adjustable for self-identification, they are interlocked — **without stepping relays and without special programming units** — for sequential read out if simultaneous printing times are reached. A tape punch may also be used to allow punched tape read out for data processing by computer methods.

*The use of RIDL printing scalers increases research potential through providing continuous, completely automatic counting operation. RIDL offers the most complete line of scalers ever available. Whatever your scaler requirements may be RIDL has a unit to fill these needs. For further information write today to Department WMB.*

RIDL INC.

*Radiation Instrument Development Laboratory, In*

5737 SOUTH HALSTED STREET • CHICAGO 21, ILLINOIS

PHONE: TRiangle 3-2345 • Cable Address: RADILAB

NUCLEAR INSTRUMENTS AND METHODS 8 (1960) 1–10; NORTH-HOLLAND PUBLISHING CO.

# FIELDS EXCITED BY BEAM CURRENTS IN CIRCULAR ACCELERATORS†

J. VAN BLADEL

*Midwestern Universities Research Association*

and

*Department of Electrical Engineering, University of Wisconsin, Madison, Wisconsin*

Received 7 March 1960

Formulas are given for the electric and magnetic fields in a circular accelerator of arbitrary cross section, excited by a non-scalloping beam of particles. Both steady-state and step-function transients are considered.

## 1. Introduction

The purpose of the present paper is to give general formulas for the electric and magnetic fields inside a beam-excited toroidal accelerator of arbitrary cross section. The configuration is shown in fig. 1. Some simplifying features will be introduced in the course of the analysis. It will be assumed, in particular:

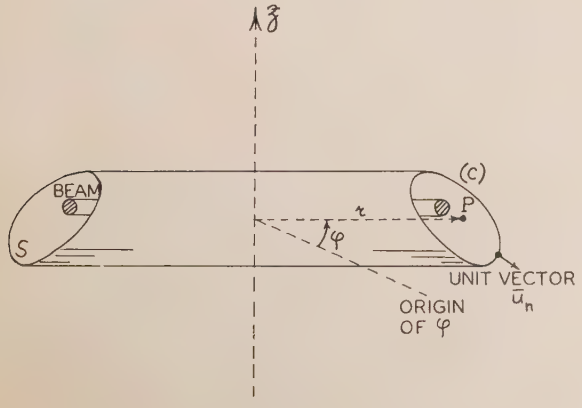


Fig. 1

(a) that the toroidal structure is bounded by a surface of revolution,

(b) that the beam current is circular, i.e., that the particles follow circular orbits (scalloping orbits are excluded),

(c) that the angular velocity $\Omega$ of all particles is the same,

(d) that the relative charge density distribution in a meridian plane is independent of the plane. (An azimuthal variation of the charge density will be allowed.)

With such a specialized beam, the volume charge density will be

$$\rho = \pi(r,z)\, g\,(\varphi - \Omega t) \tag{1}$$

and the current density

$$\boldsymbol{j} = \pi(r,z)\, g\,(\varphi - \Omega t)\, r\Omega \boldsymbol{u}_\varphi \tag{2}$$

where $\boldsymbol{u}_\varphi$ is the unit vector in the azimuthal direction.

## 2. General Formulas

Let us consider a ring-like cavity, which is not necessarily of revolution, and the current and charge densities $\boldsymbol{j}$ and $\rho$ which it contains. We are going to express the fields in terms of their expansions in electric and magnetic eigenvectors as:

$$\mathbf{e}(\mathbf{r},t) = \sum_m \sum_n \sum_p A_{mnp}(t)\, \boldsymbol{f}_{mnp}(\mathbf{r}) + \sum_m \sum_n \sum_p B_{mnp}(t)\, \mathbf{e}_{mnp}(\mathbf{r}) \tag{3}$$

$$\boldsymbol{h}(\mathbf{r},t) = \sum_m \sum_n \sum_p C_{mnp}(t)\, \boldsymbol{g}_{mnp}(\mathbf{r}) + \sum_m \sum_n \sum_p D_{mnp}(t)\, \boldsymbol{h}_{mnp}(\mathbf{r}) + c_0 \boldsymbol{h}_0 \tag{4}$$

$$\boldsymbol{j}(\mathbf{r},t) = \sum_m \sum_n \sum_p J_{mnp}(t)\, \boldsymbol{f}_{mnp}(\mathbf{r}) + \sum_m \sum_n \sum_p K_{mnp}(t)\, \mathbf{e}_{mnp}(\mathbf{r}) \tag{5}$$

$$\rho(\mathbf{r},t) = \varepsilon_0 \sum_m \sum_n \sum_p Q_{mnp}(t)\, \phi_{mnp}(\mathbf{r})\,. \tag{6}$$

† AEC Research and Development Report. Research supported by the Atomic Energy Commission, Contract No. AT (11-1)-384.

In these equations, the unknowns are the time-dependent coefficients $A, B, C$ and $D$. Coefficients $J, K$ and $Q$, on the other hand, can be calculated once $\boldsymbol{j}$ and $\rho$ are given. The various eigenvectors which appear in the formulas are defined as follows:

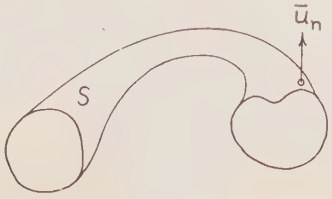


Fig. 2

1. The irrotational electric eigenvectors $\boldsymbol{f}_{mnp}$ derive from scalar potentials $\phi_{mnp}$, where

$$\nabla^2\phi_{mnp} + \lambda'_{mnp}\phi_{mnp} = 0 \quad \phi_{mnp} = 0 \text{ on } S\,. \tag{7}$$

2. The solenoidal electric eigenvectors $\boldsymbol{e}_{mnp}$ are given by

$$-\operatorname{curl}\operatorname{curl}\boldsymbol{e}_{mnp} + \lambda''_{mnp}\boldsymbol{e}_{mnp} = 0$$

$$\boldsymbol{u}_n \times \boldsymbol{e}_{mnp} = 0 \text{ on } S\,. \tag{8}$$

3. The irrotational magnetic eigenvectors $\boldsymbol{g}_{mnp}$ derive from scalar potentials $\psi_{mnp}$, where

$$\nabla^2\psi_{mnp} + \mu_{mnp}\psi_{mnp} = 0\,, \qquad \frac{\partial\psi_{mnp}}{\partial n} = 0 \quad \text{on} \quad S\,. \tag{9}$$

4. The solenoidal magnetic eigenvectors $\boldsymbol{h}_{mnp}$ are simply curl $\boldsymbol{e}_{mnp}$. They have the same eigenvalues $\lambda''_{mnp}$ as $\boldsymbol{e}_{mnp}$.

5. The "magnetostatic" eigenvector $\boldsymbol{h}_0$ is tangent to $S$, and has vanishing curl and divergence.

To find equations for the unknown coefficients, we substitute the expansions in the four Maxwell's equations and, by well-known methods[1]), obtain

$$A_{mnp} = -\frac{Q_{mnp}}{\lambda'_{mnp}}$$

$$\left(\text{from which } \varepsilon_0\frac{\mathrm{d}A_{mnp}}{\mathrm{d}t} + J_{mnp} = 0 \quad \text{follows}\right) \tag{10}$$

[1]) J. C. Slater, Microwave Electronics (Van Nostrand Co., Inc., 1950) Chs. 3 and 4;
or J. van Bladel, On Helmholtz' Theorem in multiply-bounded and multiply-connected Regions, to appear in the June 1960 issue of the Journal of the Franklin Institute.

$$\frac{\mathrm{d}C_0}{\mathrm{d}t} = \frac{\mathrm{d}C_{mnp}}{\mathrm{d}t} = 0$$

$$\left(\text{with } C_{mnp} = \frac{\iint_s \psi_{mnp}\,(\boldsymbol{h}\cdot\boldsymbol{u}_n)\,\mathrm{d}S}{\iiint_v |\,\boldsymbol{g}_{mnp}\,|^2\,\mathrm{d}V}\right) \tag{11}$$

$$B_{mnp} = -\mu_0\frac{\mathrm{d}D_{mnp}}{\mathrm{d}t} \tag{12}$$

$$\varepsilon_0\frac{\mathrm{d}B_{mnp}}{\mathrm{d}t} + K_{mnp} = \lambda''_{mnp}\,D_{mnp}\,. \tag{13}$$

The coefficients $C_0$ and $C_{mnp}$ are time-independent, and do not interest us. Furthermore, they are, and remain, zero if the beam is injected in a region where the fields are initially zero. Coefficients $B$ and $D$ are of particular importance, because of the possibility of resonance. The latter becomes evident when we write the differential equation for $D$, by use of eqs. (12) and (13), as

$$\frac{\mathrm{d}^2D_{mnp}}{\mathrm{d}t^2} + \frac{\lambda''_{mnp}}{\varepsilon_0\mu_0}D_{mnp} = \frac{\iiint_v \boldsymbol{j}\cdot\boldsymbol{e}_{mnp}\,\mathrm{d}V}{\varepsilon_0\mu_0\iiint_v |\,\boldsymbol{e}_{mnp}\,|^2\,\mathrm{d}V}\,. \tag{14}$$

Clearly, this is the equation of a resonant circuit with resonant frequency $(c/2\pi)\sqrt{\lambda''_{mnp}}$ (where $c = 1/\sqrt{\varepsilon_0\mu_0}$ is the velocity of light). Eqs. (10) to (14) transform the problem into a series of ordinary differential equations to which the usual techniques, such as Laplace transforms, can be applied. Each resonant mode $\boldsymbol{e}_{mnp}$ will be excited with a strength which depends on the value of the coupling coefficient $\iiint_v \boldsymbol{j}\cdot\boldsymbol{e}_{mnp}\,\mathrm{d}V$. The part

$$\sum_m\sum_n\sum_p A_{mnp}(t)\,\boldsymbol{f}_{mnp}(\boldsymbol{r})$$

of the electric field is rather trivial. It is simply the (non-retarded) electric field which would be found if the boundary were metallized, and the field calculated as an electrostatic field with sources corresponding to the instantaneous value of $\rho$.

At this point there is little else one could say to advance the analysis. More interesting results can be obtained by specializing the physical configuration in the manner described in the introduction.

### 3. Volumes of Revolution

In a volume of revolution, the eigenvectors take a particularly simple form because of the possibility of separation of the azimuthal dependence. More precisely[2])

1. The irrotational electric eigenvectors are the gradient of

$$\phi_{mnp} = \begin{Bmatrix} \sin m\varphi \\ \cos m\varphi \end{Bmatrix} \alpha_{mnp}(r,z) \tag{15}$$

where $\alpha_{mnp}$ is an eigenfunction of

$$\frac{\partial^2\alpha}{\partial r^2} + \frac{1}{r}\frac{\partial\alpha}{\partial r} + \frac{\partial^2\alpha}{\partial z^2} + \left(\lambda'_{mnp} - \frac{m^2}{r^2}\right)\alpha = 0 \qquad \alpha = 0 \quad \text{on} \quad C\,. \tag{16}$$

2. The solenoidal electric eigenvectors are of the form

$$\mathbf{e}_{mnp} = \begin{Bmatrix} \sin m\varphi \\ \cos m\varphi \end{Bmatrix} \mathbf{c}_{mnp}(r,z) + \begin{Bmatrix} \cos m\varphi \\ -\sin m\varphi \end{Bmatrix} \frac{r}{m} \operatorname{div} \mathbf{c}_{mnp}\, \mathbf{u}_\varphi \tag{17}$$

where $\mathbf{c}(r,z)$ is a meridian vector, with divergence ( in the $r$, $z$ plane)

$$\operatorname{div} \mathbf{c} = \frac{\partial c_r}{\partial r} + \frac{c_r}{r} + \frac{\partial c_z}{\partial z}$$

and satisfying the eigenvector problem

$$\nabla^2\mathbf{c} + \mathbf{u}_r\left(\frac{2}{r}\operatorname{div}\mathbf{c}\right) + \left(\lambda''_{mnp} - \frac{m^2}{r^2}\right)\mathbf{c} = 0 \quad \text{with} \begin{Bmatrix} \mathbf{u}_n \times \mathbf{c} = 0 \\ \operatorname{div}\mathbf{c} = 0 \end{Bmatrix} \quad \text{on} \quad (C) \tag{18}$$

where

$$\nabla^2\mathbf{c} = \left(\frac{\partial^2 c_r}{\partial r^2} + \frac{1}{r}\frac{\partial c_r}{\partial r} + \frac{\partial^2 c_r}{\partial z^2} - \frac{c_r}{r^2}\right)\mathbf{u}_r + \left(\frac{\partial^2 c_z}{\partial r^2} + \frac{1}{r}\frac{\partial c_z}{\partial r} + \frac{\partial^2 c_z}{\partial z^2}\right)\mathbf{u}_z\,.$$

These formulas are valid when $m$ is different from zero, i.e., when there is azimuthal dependence. The $\varphi$-independent modes, on the other hand, split into two simple families:

(a) "circular" modes $\beta_{0np}\mathbf{u}_\varphi$ where

$$\frac{\partial^2\beta}{\partial r^2} + \frac{1}{r}\frac{\partial\beta}{\partial r} + \frac{\partial^2\beta}{\partial z^2} + \left(\lambda''_{0np} - \frac{1}{r^2}\right)\beta = 0 \qquad \beta = 0 \quad \text{on} \quad (C) \tag{19}$$

(b) "meridian" modes curl $[\delta_{0np}\mathbf{u}_\varphi]$ where

$$\frac{\partial^2\delta}{\partial r^2} + \frac{1}{r}\frac{\partial\delta}{\partial r} + \frac{\partial^2\delta}{\partial z^2} + \left(\lambda'''_{0np} - \frac{1}{r^2}\right)\delta = 0 \qquad \frac{\partial}{\partial n}(r\delta) = 0 \quad \text{on} \quad (C)\,. \tag{20}$$

The irrotational magnetic modes, which do not appear in expansion (4), will not be listed here The solenoidal magnetic modes, on the other hand, are simply curl $\mathbf{e}_{mnp}$, curl $[\beta_{0np}\mathbf{u}_\varphi]$ and $\delta_{0np}\,\mathbf{u}_\varphi$.

To find the expansion coeffients $A$, $B$ $D$, we expand the periodic volume charge distribution $\rho$ in a Fourier series. More precisely, we write

$$g(\varphi - \Omega t) = \sum_{m=1}^{\infty} P_m \cos(m\varphi - m\Omega t + \phi_m) + g_{\text{av}} \tag{21}$$

where the amplitude $P_m$ and the phase $\phi_m$ are given, and $g_{\text{av}}$ is the D.C., non-fluctuating part of the space charge. By introducing this expansion in (10) to (14), we find:

1. .

$$A_{0np} = -\frac{1}{\varepsilon_0\lambda'_{0np}} \frac{\iint_S \pi(r,z)\,\alpha_{0np}(r,z) r\,\mathrm{d}r\,\mathrm{d}z}{\iint_S \alpha^2_{0np}(r,z) r\,\mathrm{d}r\,\mathrm{d}z}\, g_{\text{av}} = L_{0np} g_{\text{av}}\,. \tag{22}$$

[2]) For more details, see J. Van Bladel, Sets of Eigenvectors for Volumes of Revolution, to appear shortly in the IRE Transactions on Microwave Theory and Techniques.

$$2. \qquad A_{mnp} = -\frac{1}{\varepsilon_0 \lambda'_{mnp}} \frac{\iint_S \pi(r,z)\, \alpha_{mnp}(r,z) r \, \mathrm{d}r \, \mathrm{d}z}{\iint_S \alpha^2_{mnp}(r,z) r \, \mathrm{d}r \, \mathrm{d}z} P_m \begin{Bmatrix} \sin\,(m\Omega t - \phi_m) \\ \cos\,(m\Omega t - \phi_m) \end{Bmatrix} = L_{mnp} P_m \begin{Bmatrix} \sin\,(m\Omega t - \phi_m) \\ \cos\,(m\Omega t - \phi_m) \end{Bmatrix}. \quad (23)$$

The sines and cosines in the brackets correspond to the sines and cosines in formula (15). Coefficients $L$ can be calculated when $\rho$ is given. They depend solely on the cross-sectional (i.e., meridian) distribution of the space charge.

$$3. \qquad \frac{\mathrm{d}^2 D_{0np}}{\mathrm{d}t^2} + \frac{\lambda''_{0np}}{\varepsilon_0 \mu_0} D_{0np} = \frac{\Omega}{\varepsilon_0 \mu_0} \frac{\iint_S \pi(r,z)\, \beta_{0np}(r,z) r^2 \, \mathrm{d}r \, \mathrm{d}z}{\iint_S \beta^2_{0np}(r,z) r \, \mathrm{d}r \, \mathrm{d}z} g_{\mathrm{av}} = M_{0np} g_{\mathrm{av}}. \quad (24)$$

$D_{0np}$ is the expansion coefficient of the circular modes described in eq. (19). The meridian modes are not excited, because their eigenvectors are perpendicular to the current density $\boldsymbol{j}$.

$$4. \qquad \frac{\mathrm{d}^2 D_{mnp}}{\mathrm{d}t^2} + \frac{\lambda''_{mnp}}{\varepsilon_0 \mu_0} D_{mnp} = \frac{\Omega}{\varepsilon_0 \mu_0} \frac{\iint_S \pi(r,z)\, \mathrm{div}\, \mathbf{c}_{mnp} \frac{r^3}{m} \, \mathrm{d}r \, \mathrm{d}z}{\iint_S \left[ (\mathbf{c}_{mnp})^2 + \frac{r^2}{m^2} (\mathrm{div}\, \mathbf{c}_{mnp})^2 \right] r \, \mathrm{d}r \, \mathrm{d}z} \begin{Bmatrix} \cos\,(m\Omega t - \phi_m) \\ -\sin\,(m\Omega t - \phi_m) \end{Bmatrix} P_m$$

$$= M_{mnp} \begin{Bmatrix} \cos\,(m\Omega t - \phi_m) \\ -\sin\,(m\Omega t - \phi_m) \end{Bmatrix} P_m. \quad (25)$$

The upper and lower terms in the bracket correspond to the upper and lower terms in (17). Coefficients $M$ depend solely on the meridian distribution of the space charge. Factors $\lambda''_{0np}/\varepsilon_0\mu_0$ and $\lambda''_{mnp}/\varepsilon_0\mu_0$ are the squares of the resonant angular frequencies of the cavity. We shall henceforth denote them by $\omega^2_{0np}$ and $\omega^2_{mnp}$.

To find the actual field distribution in the cavity, we should solve for the $D_{mnp}$, $B_{mnp}$ and insert the results in expansions (3) and (4). Two cases are of particular interest.

### A. STEADY STATE

The term $g_{\mathrm{av}}$ gives rise to electrostatic and magnetostatic fields. These fields will be omitted, for our main interest lies in the time-dependent terms, which consist of:

(a) a non-resonant part of the electric field

$$\sum_{m=1}^{\infty} \sum_n \sum_p A_{mnp}(t)\, \mathbf{f}_{mnp}(\mathbf{r}) = \sum_{m=1}^{\infty} P_m \cos\,(m\varphi - m\Omega t + \phi_m) \left[ \sum_n \sum_p L_{mnp} \,\mathrm{grad}\, \alpha_{mnp} \right]$$

$$+ \sum_{m=1}^{\infty} P_m \sin\,(m\varphi - m\Omega t + \phi_m) \frac{m}{r} \left[ - \sum_n \sum_p L_{mnp} \alpha_{mnp} \right] \mathbf{u}_\varphi. \quad (26)$$

The first summation is a meridian vector made out of waves travelling in step with the space-charge waves. The second summation is a circular vector made out of waves travelling 90° out of phase with the space-charge waves.

(b) a resonant part of the electric field

$$\sum_{m=1}^{\infty} \sum_n \sum_p B_{mnp}(t)\, \mathbf{e}_{mnp}(\mathbf{r}) = \sum_{m=1}^{\infty} P_m \cos\,(m\varphi - m\Omega t + \phi_m)\, \mu_0 m \Omega \left[ \sum_n \sum_p \frac{M_{mnp}}{\omega^2_{mnp} - m^2\Omega^2} \mathbf{c}_{mnp} \right]$$

$$+ \sum_{m=1}^{\infty} P_m \sin\,(m\varphi - m\Omega t + \phi_m)\, \mu_0 r \Omega \left[ \sum_n \sum_p - \frac{M_{mnp}}{\omega^2_{mnp} - m^2\Omega^2} \mathrm{div}\, \mathbf{c}_{mnp} \right] \mathbf{u}_\varphi. \quad (27)$$

The first and second summations represent meridian and circular vectors respectively.

(c) the magnetic field, which consists of a resonant part only. To express the latter explicitly, we notice that

$$\boldsymbol{h}_{mnp}(\boldsymbol{r}) = \operatorname{curl} \boldsymbol{e}_{mnp} = \begin{Bmatrix} \cos m\varphi \\ -\sin m\varphi \end{Bmatrix} \left[ \frac{m}{r} (\boldsymbol{u}_\varphi \times \boldsymbol{c}_{mnp}) + \operatorname{curl} \left( \boldsymbol{u}_\varphi \frac{r}{m} \operatorname{div} \boldsymbol{c}_{mnp} \right) \right] + \begin{Bmatrix} \sin m\varphi \\ \cos m\varphi \end{Bmatrix} \operatorname{curl} \boldsymbol{c}_{mnp} . \tag{28}$$

The first term, which is a meridian vector, will, for reasons of conciseness, be written as

$$\boldsymbol{d}_{mnp} \begin{Bmatrix} \cos m\varphi \\ -\sin m\varphi \end{Bmatrix} .$$

The second term, which is a circular vector, can then be shown to be

$$- \begin{Bmatrix} \sin m\varphi \\ \cos m\varphi \end{Bmatrix} \frac{r}{m} \operatorname{div} \boldsymbol{d}_{mnp} .$$

With this notation, we find that

$$\sum_m \sum_n \sum_p D_{mnp}(t)\, \boldsymbol{h}_{mnp}(\boldsymbol{r}) = \sum_{m=1}^{\infty} P_m \cos(m\varphi - m\Omega t + \phi_m) \left[ \sum_n \sum_p \frac{M_{mnp}}{\omega_{mnp}^2 - m^2\Omega^2} \boldsymbol{d}_{mnp} \right]$$

$$+ \sum_{m=1}^{\infty} P_m \sin(m\varphi - m\Omega t + \phi_m) \left[ \sum_n \sum_p \frac{M_{mnp}}{\omega_{mnp}^2 - m^2\Omega^2} \operatorname{curl} \boldsymbol{c}_{mnp} \right] . \tag{29}$$

B. STEP-FUNCTION TRANSIENTS

Let us assume, as a convenient idealization, that the charge density (21) is suddenly injected in the accelerator at time $t = 0$, no charge being present before that time. We now find:

(a) a non-resonant part of the electric field, which is (26) augmented by a term

$$g_{av} \sum_n \sum_p L_{0np} \operatorname{grad} \alpha_{0np} \tag{30}$$

(b) a resonant part of the electric field, which is (27) augmented by

$$- \sum_{m=1}^{\infty} \mu_0 P_m \sin(m\varphi + \phi_m) \sum_n \sum_p \frac{\omega_{mnp} M_{mnp} \sin \omega_{mnp} t}{\omega_{mnp}^2 - m^2\Omega^2} \boldsymbol{c}_{mnp}$$

$$- \sum_{m=1}^{\infty} \mu_0 m\Omega P_m \cos(m\varphi + \phi_m) \sum_n \sum_p \frac{M_{mnp} \cos \omega_{mnp} t}{\omega_{mnp}^2 - m^2\Omega^2} \boldsymbol{c}_{mnp}$$

$$- \mu_0 g_{av} \sum_n \sum_p \frac{M_{0np}}{\omega_{0np}} \sin \omega_{0np} t \cdot \beta_{0np} \boldsymbol{u}_\varphi + \sum_{m=1}^{\infty} \mu_0 P_m r\Omega \sin(m\varphi + \phi_m) \sum_n \sum_p \frac{M_{mnp} \cos \omega_{mnp} t}{\omega_{mnp}^2 - m^2\Omega^2} (\operatorname{div} \boldsymbol{c}_{mnp})\, \boldsymbol{u}_\varphi$$

$$- \sum_{m=1}^{\infty} \mu_0 P_m \frac{r}{m} \cos(m\varphi + \phi_m) \sum_n \sum_p \frac{M_{mnp} \sin \omega_{mnp} t}{\omega_{mnp}^2 - m^2\Omega^2} (\operatorname{div} \boldsymbol{c}_{mnp})\, \boldsymbol{u}_\varphi . \tag{31}$$

(c) a resonant part of the magnetic field, which is (29) augmented by

$$g_{av} \sum_n \sum_p \frac{M_{0np}}{\omega_{0np}^2} (1 - \cos \omega_{0np} t) \operatorname{curl} (\beta_{0np} \mathbf{u}_\varphi) - \sum_{m=1}^{\infty} P_m \cos (m\varphi + \phi_m) \sum_n \sum_p \frac{M_{mnp} \cos \omega_{mnp} t}{\omega_{mnp}^2 - m^2\Omega^2} \mathbf{d}_{mnp}$$

$$- \sum_{m=1}^{\infty} P_m \sin (m\varphi + \phi_m)\, m\Omega \sum_n \sum_p \frac{M_{mnp} \sin \omega_{mnp} t}{\omega_{mnp}^2 - m^2\Omega^2} \frac{\mathbf{d}_{mnp}}{\omega_{mnp}}$$

$$- \sum_{m=1}^{\infty} P_m \sin (m\varphi + \phi_m) \sum_n \sum_p \frac{M_{mnp} \cos \omega_{mnp} t}{\omega_{mnp}^2 - m^2\Omega^2} \operatorname{curl} \mathbf{c}_{mnp}$$

$$- \sum_{m=1}^{\infty} P_m \cos (m\varphi + \phi_m)\, m\Omega \sum_n \sum_p \frac{M_{mnp} \sin \omega_{mnp} t}{\omega_{mnp}^2 - m^2\Omega^2} \frac{\operatorname{curl} \mathbf{c}_{mnp}}{\omega_{mnp}} . \tag{32}$$

These various formulas have been obtained under the assumption that no actual resonance took place, i.e. that $m\Omega$ was not equal to any of the $\omega_{mnp}$. In case of resonance, the fields will build up to infinite values; that is, as long as we maintain the assumption of perfectly conducting walls. In reality, however, the walls have some resistance, and the build-up will be limited by the $Q$ of the cavity. This phenomenon will be examined in more detail later on. The finite conductivity of the walls is also responsible for the decay of the transient terms, and the ultimate convergence of the fields to the values predicted by steady-state analysis.

### C. PARTICULAR CASES

1. The fields excited by a very narrow beam (a beam which can be assimilated to a fine line) are of particular importance. They have the nature of a Green's function, and allow computation by simple integrations of the fields excited by a smeared-out distribution $\pi(r,z)$. We represent the line density of the beam as:

$$\Lambda = \Lambda_{\max}\, g\,(\varphi - \Omega t) \qquad \text{Clb m}^{-1} . \tag{33}$$

where $g$ is a function which has a maximum value equal to one. Let furthermore $r_0 z_0$ be the location of the beam in the meridian plane. To find the fields excited by such a beam, it suffices to replace, in formulas (22) to (32), the $L$ and $M$ by their values

$$L_{0np} = - \frac{r_0 \alpha_{0np}(r_0,z_0)}{\varepsilon_0 \lambda'_{0np} \iint_S \alpha_{0np}^2(r,z) r \, dr \, dz} \Lambda_{\max} \tag{34}$$

$$L_{mnp} = - \frac{r_0 \alpha_{mnp}(r_0,z_0)}{\varepsilon_0 \lambda'_{mnp} \iint_S \alpha_{mnp}^2(r,z) r \, dr \, dz} \Lambda_{\max} \tag{35}$$

$$M_{0np} = \frac{\Omega}{\varepsilon_0 \mu_0} \frac{r_0^2 \beta_{0np}(r_0,z_0)}{\iint_S \beta_{0np}^2(r,z) r \, dr \, dz} \Lambda_{\max} \tag{36}$$

$$M_{mnp} = \frac{\Omega r_0^3}{m \varepsilon_0 \mu_0} \frac{\operatorname{div} \mathbf{c}_{mnp}(r_0,z_0)}{\iint_S \left[ (\mathbf{c}_{mnp})^2 + \frac{r^2}{m^2} (\operatorname{div} \mathbf{c}_{mnp})^2 \right] r \, dr \, dz} \Lambda_{\max} . \tag{37}$$

We shall not rewrite all the formulas for the narrow beam explicitly, but will restrict ourselves to those which give the steady-state resonant parts of the electric and magnetic field:

$$\mathbf{e}(\mathbf{r},t) = \Lambda_{\max}\frac{r_0\beta^2}{\varepsilon_0}\sum_{m=1}^{\infty} P_m \cos(m\varphi - m\Omega t + \phi_m)\sum_n\sum_p \frac{\mathbf{c}_{mnp}(r,z)\ \mathrm{div}\ \mathbf{c}_{mnp}(r_0,z_0)}{\left(\lambda''_{mnp} - \frac{m^2\beta^2}{r_0^2}\right)\iint_S\left[(\mathbf{c}_{mnp})^2 + \frac{r^2}{m^2}(\mathrm{div}\ \mathbf{c}_{mnp})^2\right] r\,dr\,dz}$$

$$- \Lambda_{\max}\frac{rr_0\beta^2}{\varepsilon_0}\sum_{m=1}^{\infty}\frac{P_m}{m}\sin(m\varphi - m\Omega t + \phi_m)\sum_n\sum_p \frac{\mathrm{div}\ \mathbf{c}_{mnp}(r,z)\ \mathrm{div}\ \mathbf{c}_{mnp}(r_0,z_0)}{\left(\lambda''_{mnp} - \frac{m^2\beta^2}{r_0^2}\right)\iint_S\left[(\mathbf{c}_{mnp})^2 + \frac{r^2}{m^2}(\mathrm{div}\ \mathbf{c}_{mnp})^2\right] r\,dr\,dz}\mathbf{u}_\varphi \quad (38)$$

$$\mathbf{h}(\mathbf{r},t) = \Lambda_{\max}\frac{r_0^2\beta}{(\varepsilon_0\mu_0)^{3/2}}\sum_{m=1}^{\infty}\frac{P_m}{m}\cos(m\varphi - m\Omega t + \phi_m)\sum_n\sum_p \frac{\mathbf{d}_{mnp}(r,z)\ \mathrm{div}\ \mathbf{c}_{mnp}(r_0,z_0)}{\left(\lambda''_{mnp} - \frac{m^2\beta^2}{r_0^2}\right)\iint_S\left[(\mathbf{c}_{mnp})^2 + \frac{r^2}{m^2}(\mathrm{div}\ \mathbf{c}_{mnp})^2\right] r\,dr\,dz}$$

$$+ \Lambda_{\max}\frac{r_0^2\beta}{(\varepsilon_0\mu_0)^{3/2}}\sum_{m=1}^{\infty}\frac{P_m}{m}\sin(m\varphi - m\Omega t + \phi_m)\sum_n\sum_p \frac{\mathrm{curl}\ \mathbf{c}_{mnp}(r,z)\ \mathrm{div}\ \mathbf{c}_{mnp}(r_0,z_0)}{\left(\lambda''_{mnp} - \frac{m^2\beta^2}{r_0^2}\right)\iint_S\left[(\mathbf{c}_{mnp})^2 + \frac{r^2}{m^2}(\mathrm{div}\ \mathbf{c}_{mnp})^2\right] r\,dr\,dz}. \quad (39)$$

The parameter $\beta = v/c = r_0\,\Omega/c$ measures the velocity of the beam in terms of the velocity of light.

2. The formulas for the narrow beam can be extended to include the fields of a point charge $Q$. Let the origin of azimuths be chosen at the initial position of the particle. The volume charge density is then

$$\rho = Q\frac{\delta(r - r_0)\,\delta(z - z_0)\,\delta(\varphi - \Omega t)}{r}$$

while

$$g = \delta(\varphi - \Omega t) = \frac{1}{2\pi} + \sum_{m=1}^{\infty}\frac{1}{\pi}\cos(m\varphi - m\Omega t).$$

We shall consequently replace $g_{\mathrm{av}}$ by $1/2\pi$, $P_m$ by $1/\pi$, and set $\phi_m = 0$ in all our formulas. The values of the $L$ and the $M$ can be obtained from equations (34) to (37) by replacing $\Lambda_{\max}$ by $Q/r_0$.

## 4. The Straight Tube with Periodic Currents

The formulas for the resonant parts of the fields all exhibit a factor $\omega_{mnp}^2 - m^2\Omega^2$ in the denominator. This indicates the possibility of resonance, because $m^2\Omega^2 = m^2\,v^2/r_0^2 = m^2\beta^2\,c^2/r_0^2$ can become as large as desired provided the location of the beam is sufficiently close to the axis, i.e., the inner radius is sufficiently small. To prove that this possibility of resonance is a curvature effect, we shall now present formulas for the electric and magnetic fields in a straight tube. We shall restrict ourselves to narrow beams with charge density

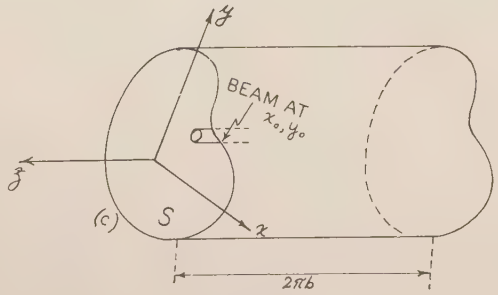


Fig. 3

$$\Lambda = \Lambda_{\max}\,g\left(\frac{z}{b} - \frac{vt}{b}\right) = \Lambda_{\max}\left[g_{\mathrm{av}} + \sum_m P_m\cos\left(\frac{mz}{b} - \frac{mvt}{b} + \phi_m\right)\right]. \quad (40)$$

The period of the beam is $2\pi b$ and the velocity $v$, We shall neglect the contribution of the D.C. component $g_{av}$, and consider the steady-state time-dependent part only. By well-known methods[1]), one obtains

$$\mathbf{e}(\mathbf{r},t) = -\frac{A_{\max}}{\varepsilon_0}\sum_{m=1}^{\infty} P_m \cos\left(\frac{mz}{b} - \frac{mvt}{b} + \phi_m\right) \sum_n \sum_p \frac{\mathscr{E}_{znp}(x_0y_0)\ \mathrm{grad}\ \mathscr{E}_{znp}(xy)}{\left[k_{np}^2 + \frac{m^2}{b^2}(1-\beta^2)\right]\iint_S \mathscr{E}_{znp}^2\,\mathrm{d}x\,\mathrm{d}y}$$

$$+ A_{\max}\frac{1-\beta^2}{\varepsilon_0 b}\sum_{m=1}^{\infty} mP_m \sin\left(\frac{mz}{b} - \frac{mvt}{b} + \phi_m\right) \sum_n \sum_p \frac{\mathscr{E}_{znp}(x_0y_0)\,\mathscr{E}_{znp}(xy)}{\left[k_{np}^2 + \frac{m^2}{b^2}(1-\beta^2)\right]\iint_S \mathscr{E}_{znp}^2\,\mathrm{d}x\,\mathrm{d}y}\,\mathbf{u}_z \tag{41}$$

$$\mathbf{h}(\mathbf{r},t) = -\frac{\beta A_{\max}}{(\varepsilon_0\mu_0)^{1/2}}\sum_{m=1}^{\infty} P_m \cos\left(\frac{mz}{b} - \frac{mvt}{b} + \phi_m\right) \sum_n \sum_p \frac{\mathscr{E}_{znp}(x_0y_0)\ (\mathbf{u}_z \times \mathrm{grad}\,\mathscr{E}_{znp})}{\left[k_{np}^2 + \frac{m^2}{b^2}(1-\beta^2)\right]\iint_S \mathscr{E}_{znp}^2\,\mathrm{d}x\,\mathrm{d}y} \tag{42}$$

where $\beta = v/c = v\sqrt{\varepsilon_0\mu_0}$, and

$$\nabla_{xy}^2 \mathscr{E}_{znp} + k_{np}^2 \mathscr{E}_{znp} = 0 \qquad \text{with} \qquad \mathscr{E}_{znp} = 0 \quad \text{on} \quad (C)\,. \tag{43}$$

All eigenvalues $k_{np}^2$ are positive and the factors $k_{np}^2 + (m^2/b^2)\,(1-\beta^2)$, which appear in the denominator, never become zero. One might wonder whether there is a threshold value of the curvature at which the possibility of resonance will appear. The answer is that this possibility will arise even for the slightest curvature, provided the value of the azimuthal quantum number $m$ is sufficiently high. Consider again eq. (18) in which the eigenvalue $\lambda''_{mnp}$ appears. There will be a resonance each time $m^2\beta^2/r_0^2$ exceeds $\lambda''_{mnp}$ or, better said, as soon as $m^2\beta^2/r_0^2$ exceeds the lowest eigenvalue $\lambda''_{m00}$ corresponding to quantum number $m$. For the lowest eigenvector $\mathbf{c}_{m00}$, the first and second order derivatives of $\mathbf{c}$ are of order $|\,\mathbf{c}\,|/D$ and $|\,\mathbf{c}\,|/D^2$ respectively, where $D$ is a typical cross-sectional dimension. In the limit of small curvature, i.e., when $D/r$ is small, the eigenvector equation (18) goes over into

$$\left(\frac{\partial^2 c_r}{\partial r^2} + \frac{\partial^2 c_r}{\partial z^2}\right)\mathbf{u}_r + \left(\frac{\partial^2 c_z}{\partial r^2} + \frac{\partial^2 c_z}{\partial z^2}\right)\mathbf{u}_z + \left(\lambda''_{m00} - \frac{m^2}{r^2}\right)\mathbf{c} = 0$$

or

$$\nabla^2\,\mathbf{c}_{m00} + \left(\lambda''_{m00} - \frac{m^2}{r^2}\right)\mathbf{c} = 0\,.$$

When, in addition, $mD/r$ is very small, the term $m^2/r^2$ becomes negligible and, to higher orders in the dimensionless quantity $mD/r$,

$$\nabla^2\mathbf{c}_{mnp} + \lambda''_{mnp}\mathbf{c}_{mnp} = 0 \qquad \text{with} \qquad \left.\begin{array}{c}\mathbf{u}_n \times \mathbf{c}_{mnp} = 0 \\ \dfrac{\partial c_r}{\partial r} + \dfrac{\partial c_z}{\partial z} = 0\end{array}\right\} \quad \text{on} \quad (C)\,. \tag{44}$$

Notice that the latter equation is valid for all quantum numbers $n$ and $p$. The higher these numbers, indeed, the stronger the derivatives of $\mathbf{c}$ will be as compared with $|\,\mathbf{c}\,|/r$ and $|\,\mathbf{c}\,|/r^2$. We have now obtained an interesting result. In the limit of vanishing values of the parameter $mD/r$, the eigenvectors $\mathbf{c}_{mnp}$ are independent of $m$. They approach, in a smooth fashion, the eigenvectors of the Helmholtz equation (44). These eigenvectors are simply $\mathrm{grad}\,\mathscr{E}_{znp}$ and $\mathbf{u}_z \times \mathrm{grad}\,\mathscr{H}_{znp}$, where $\mathscr{E}_{znp}$ is given by eq. (43), and $\mathscr{H}_{znp}$ is an eigenfunction of

$$\nabla_{xy}^2 \mathscr{H}_{znp} + \mu_{np}^2 \mathscr{H}_{znp} = 0\,, \quad \frac{\partial \mathscr{H}_{znp}}{\partial n} = 0 \quad \text{on} \quad (C)\,. \tag{45}$$

The eigenvalues $\lambda''_{mnp}$ approach $k_{np}^2$ and $\mu_{np}^2$. They are of order $1/D^2$, so that the denominator $\lambda''_{mnp} - m^2/r_0^2$ remains positive: there is no danger of resonance. One checks easily that the electric and magnetic fields in the curved tube, as given by (26), (27), (28), approach the electric and magnetic fields of the straight tube, as given by (41) and (42). The convergence, of course, takes place only for those values of $m$ for which $mD/r \ll 1$, and the period $2\pi b$ in the straight tube should be taken equal to $2\pi r_0$ while performing the comparison. The details of the latter are left to the reader.

We have reached the conclusion that the curvature effects, and the possibility of resonance, will appear when the charge density possesses ripples of such high frequency that $mD$ is of the order of $r$, i.e., when the period $L$ of a Fourier component is of the order of the cross-sectional dimensions of the tube.

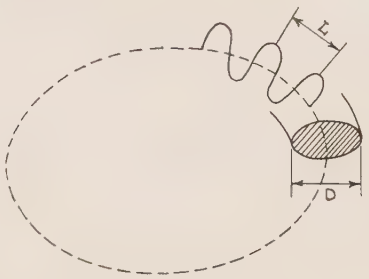

Fig. 4

## 5. Losses in the Walls

The traditional way to take the finite conductivity $\sigma$ of the walls into account is to relate the tangential components of the electric and the magnetic fields at the wall by

$$\boldsymbol{E}_{\text{tang}} = (\boldsymbol{H}_{\text{tang}} \times \boldsymbol{u}_n)\,(1 + j)\sqrt{\frac{\omega\mu}{2\sigma}} \tag{46}$$

where $\boldsymbol{u}_n$ is the unit vector pointing into the metal. The formula is valid when the conductivity is sufficiently high to make the skin depth $\delta = \sqrt{2/\omega\mu_0\sigma}$ much smaller than the wavelength and the radius of curvature of the wall. By setting $\mu = \mu_0$ in the formulas, we have assumed the walls to be nonmagnetic. When $1/\sigma$ is small the value of $\boldsymbol{H}_{\text{tang}}$ can be taken, to first order, equal to the value at a perfectly conducting wall. The power going into the walls is given by

$$\tfrac{1}{2}\,\text{Re}\iint_S \boldsymbol{u}_n\cdot(\boldsymbol{E} \times \boldsymbol{H}^*)\,dS = \tfrac{1}{2}\sqrt{\frac{\omega\mu_0}{2\sigma}}\iint_S \left|\boldsymbol{H}_{\text{tang}}\right|^2 dS \tag{47}$$

where $|\,\boldsymbol{H}_{\text{tang}}\,|$ is the magnitude of the magnetic field at the wall. Formulas (46) and (47) are valid for single-frequency fields. The magnetic field at the surface, however, contains a mixture of harmonically related frequencies. An explicit formula can be obtained from (27). For a narrow beam:

$$\boldsymbol{h}_{\text{wall}} = A_{\max}\left\{\sum_m P_m \cos(m\varphi - m\Omega t + \phi_m)\,\boldsymbol{a}_m + \sum_m P_m \sin(m\varphi - m\Omega t + \phi_m)\,b_m\,\boldsymbol{u}_\varphi\right\}$$

where $\boldsymbol{a}_m$ and $b_m$ stand for certain frequency-dependent double infinite sums. Vector $\boldsymbol{a}_m$ is tangent to the cross-sectional contour $(c)$, and both $\boldsymbol{a}_m$ and $b_m$ depend on the running coordinate $c$ along that contour. Poynting's vector along the wall is $\boldsymbol{h}\cdot(\boldsymbol{u}_n \times \boldsymbol{e})$. Using (46), we find that

$$\boldsymbol{u}_n \times \boldsymbol{e} = A_{\max}\sqrt{\frac{\Omega\mu_0}{\sigma}}\left\{\sum_m \sqrt{m}\,P_m \cos\left(m\varphi - m\Omega t + \phi_m + \frac{\pi}{4}\right)\boldsymbol{a}_m + \sum_m \sqrt{m}\,P_m \sin\left(m\varphi - m\Omega t + \phi_m + \frac{\pi}{4}\right)b_m\boldsymbol{u}_\varphi\right\}.$$

The power loss then turns out to be

$$A_{\max}^2\pi\sqrt{\frac{R\beta}{2\sigma r_0}}\int_c \left[\sum_m \sqrt{m}\,P_m^2\,(|\,\boldsymbol{a}_m\,|^2 + b_m^2)\right] r\,dc$$

where $R = \sqrt{\mu_0/\varepsilon_0} = 377\ \Omega$ is the impedance of free space.

When one mode dominates all the others in magnitude, the power loss becomes (with $M_{mnp}$ set equal to $\Lambda_{\max} K_{mnp}$ for convenience)

$$\Lambda_{\max}^2 \pi P_m \sqrt{\frac{R\beta m}{2\sigma r_0}} \frac{K_{mnp}^2}{(\omega_{mnp}^2 - m^2\Omega^2)^2} \int_c \left[ (\boldsymbol{d}_{mnp})^2 + \frac{r^2}{m^2} (\operatorname{div} \boldsymbol{d}_{mnp})^2 \right] r \, \mathrm{d}c \, .$$

Such a situation arises when the frequency is very close to the resonant frequency of the mode. The average energy which is present in the cavity is then, by classical methods

$$\iiint_V (\tfrac{1}{2}\varepsilon_0 E^2 + \tfrac{1}{2}\mu_0 H^2) \, \mathrm{d}V = \Lambda_{\max}^2 \pi \mu_0 P_m^2 \frac{K_{mnp}^2}{(\omega_{mnp}^2 - m^2\Omega^2)^2} \iint_S \left[ (\boldsymbol{d}_{mnp})^2 + \frac{r^2}{m^2} (\operatorname{div} \boldsymbol{d}_{mnp})^2 \right] r \, \mathrm{d}c \, .$$

The $Q$ of the cavity for that mode is

$$\frac{2\pi \times \text{energy}}{T \times \text{power loss}} ,$$

where $T$ is the period $2\pi/\omega_{mnp}$. It can be written as

$$Q = \frac{2}{\delta} \frac{\iint_S \left[ (\boldsymbol{d}_{mnp})^2 + \frac{r^2}{m^2} (\operatorname{div} \boldsymbol{d}_{mnp})^2 \right] r \, \mathrm{d}r \, \mathrm{d}z}{\int_c \left[ (\boldsymbol{d}_{mnp})^2 + \frac{r^2}{m^2} (\operatorname{div} \boldsymbol{d}_{mnp})^2 \right] r \, \mathrm{d}c}$$

where $\delta$ is the skin-depth at the resonant frequency. It is this value of $Q$ which will limit the build-up of the mode. Coefficient $D_{mnp}$ now satisfies the differential equation

$$\frac{\mathrm{d}^2 D_{mnp}}{\mathrm{d}t^2} + \frac{\omega_{mnp}}{Q} \frac{\mathrm{d}D_{mnp}}{\mathrm{d}t} + \omega_{mnp}^2 D_{mnp} = M_{mnp} P_m \begin{Bmatrix} \cos(m\Omega t - \phi_m) \\ -\sin(m\Omega t - \phi_m) \end{Bmatrix} .$$

The build-up of the amplitude after sudden injection of the beam at $t = 0$ is given by

$$D_{mnp} = \frac{P_m M_{mnp}}{\omega_{mnp}^2} Q \left[ \sin(\omega_{mnp} t - \phi_m) + \sin\phi_m \, \mathrm{e}^{-\omega_{mnp} t/2Q} \cos\beta t + \frac{\omega_{mnp}}{\beta} \mathrm{e}^{-\omega_{mnp} t/2Q} \sin\beta t \left( \frac{\sin\phi_m}{2Q} - \cos\phi_m \right) \right]$$

where $\cos(m\Omega t - \phi_m)$ is used as a second member (the response to $-\sin(m\Omega t - \phi_m)$ follows without difficulty). The angular frequency $\beta$ is equal to $\omega_{mnp}\sqrt{1 - 1/4Q^2}$. The transients die out after a time of the order $QT$, where $T = 2\pi/\omega_{mnp}$ is the period at resonance. For the first few cycles, an approximate value of the amplitude is given by

$$D_{mnp} \approx \frac{P_m M_{mnp}}{2\omega_{mnp}^2} [\omega_{mnp} t \sin(\omega_{mnp} t - \phi_m) + \sin\omega_{mnp} t \sin\phi_m] .$$

**Conclusion and Acknowledgement**

We have obtained general formulas for the fields excited by beams of particles in an accelerator. These formulas allow one, in principle at least, to analyze phenomena such as the interaction between two different beams which are simultaneously rotating in the accelerator. The effect of outside sources, gaps and cavities for example, has not been considered in this report, and will be the object of a future study. The use of the general formulas depends on a precise knowledge of the eigenvectors in the cavity. The latter can be written in closed analytical form for a vacuum chamber of rectangular cross section. The application of the analysis to that particularly interesting geometry will be taken up in another future report.

The author would like to acknowledge useful discussions with Drs. K. R. Symon, L. Jackson Laslett and V. K. Neil.

NUCLEAR INSTRUMENTS AND METHODS 8 (1960) 11–18; NORTH-HOLLAND PUBLISHING CO.

# $\pi^-$ STAR DETECTOR†

A. F. DUNAITZEV, YU. D. PROKOSHKIN and TANG SYAO-WEI

*Joint Institute for Nuclear Research, Dubna, USSR*

Received 25 February 1960

A scintillation detector possessing the selective sensitivity to $\pi^-$ mesons is described. The detector records the stars due to $\pi^-$ mesons coming to rest.

## 1. Introduction

Most of the $\pi^-$ mesons stopping in matter give rise to stars—the nuclear disintegrations in which a considerable amount of energy is released, its magnitude being close to the pion mass (140 MeV). This feature makes $\pi^-$ mesons distinct both from the light particles ($\mu$ mesons, electrons) which fail to produce high-energy stars, and from the positively charged nuclear-active particles (protons, $\pi^+$ mesons, etc.) producing stars only in flight and with a small probability. By using the scintillator of the scintillation counter as a substance in which the particles are brought to rest, and by recording only the pulses produced by stars, i.e., those corresponding to a large energy release in the scintillator, it is possible to accomplish a simple detector which possesses a selective sensitivity to $\pi^-$ mesons. A principle possibility of constructing such a $\pi^-$ star detector, which is not sensitive to other particles, is not doubtful since the recording efficiency for particles which do not produce high-energy stars may be obtained whatever low by increasing the threshold for the pulse amplitude discrimination at the output of the scintillation counter. However, with increasing the discrimination threshold the efficiency of the star recording also falls, although not so rapidly. Therefore, it is not clear *a priori*, whether it is possible to construct a practically usable star detector whose efficiency would be sufficiently high. To answer this question, it is necessary to investigate the amplitude spectra of pulses arising at the output of the scintillation counter when both $\pi^-$ mesons and the particles which do not produce stars (e.g. $\pi^+$ mesons) come to rest in the scintillator. An effective star detector may be accomplished only if the major part of these spectra turn out to be not overlapped.

† This detector has been described briefly in ref. [1]).

## 2. Spectra of Pulses

To measure the spectra of pulses we made use of the arrangement shown in fig. 1. A collimated beam of 170 MeV $\pi^-$ mesons from the synchro-cyclotron of the Laboratory of Nuclear Problems of JINR passed through a graphite absorber. The $\pi^-$ mesons slowing down were detected by a

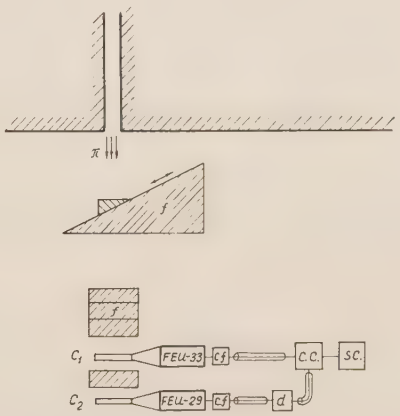


Fig. 1. Detector scheme. $C_1$ and $C_2$: scintillation counters; c.f.: cathode followers; c.c.: coincidence circuit; sc: scaler; d: variable delay (up to $5 \times 10^{-8}$ sec) to compensate the time shift of counters $C_1$ and $C_2$ with variation of $V_2$; f: moderating absorbers.

[1]) A. F. Dunaitzev, Yu. D. Prokoshkin, Tang Syao-wei. Pribory i tekhnika eksperimenta (1960) (in press); Proceedings of the International Conference on high-energy accelerators and instrumentation (1959, CERN, Geneva) p. 592.

telescope consisting of two scintillation counters in coincidence. The plastic scintillators of both counters were $6 \times 6 \times 1.5$ cm$^3$. The photomultiplier of the first counter FEU-33 worked in the regime of time resolution, the photomultiplier of the second counter FEU-29—as a spectrometric one. The coincidence circuit was

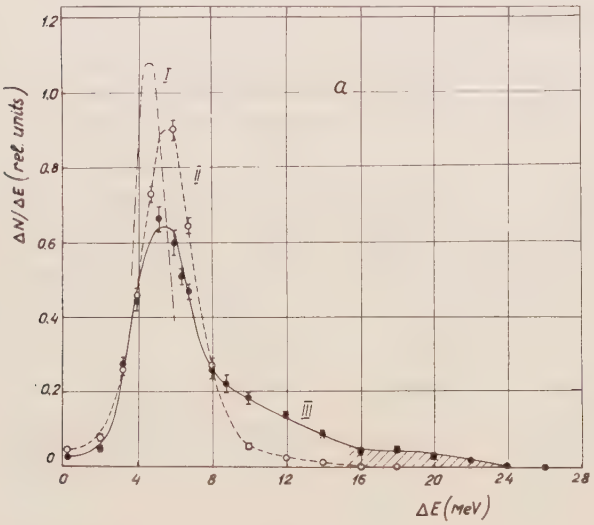


(a)

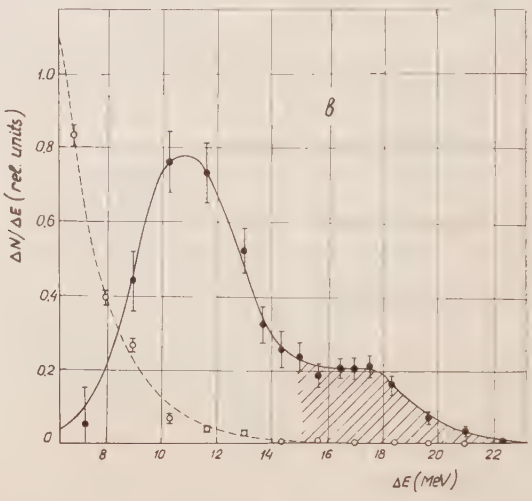


(b)

Fig. 2. Pulse spectra in counter $C_2$. The abscissa axis is the energy lost by $\pi^-$ meson in the scintillator. The spectra are normalized to equal area. Shaded is the region of the spectrum not overlapped with the "stop spectrum".

(a) I: pulse spectra from the passing relativistic $\pi^-$ mesons with the residual range 50 g/cm$^2$ of carbon and the range spread equal to $\pm$ 4 g/cm$^2$;
II: the spectrum for the residual range 10 g/cm$^2$;
III: the spectrum corresponding to zero residual range.

(b) $\frac{\text{I}}{\text{I}}$-pulse spectrum from $\pi^-$ mesons stopping in the scintillator;
$\frac{\text{I}}{\text{I}}$-a part of spectrum II.

of the bridge type and employed the semiconductor diodes D-2A. The resolving time of the telescope for the coincidences depended upon the length of the pulse-forming short-circuited cables and was equal to $10^{-8}$ sec. From the output of the coincidence circuit the pulse was fed to start the pulse height analyzer AADO-1. Simultaneously, the pulse to be analyzed from the output of the counter $C_2$ was applied to the input of this analyzer.

The amplitude spectra of pulses were obtained with three different thicknesses of the absorber (fig. 2a). The first spectrum of those measured is a comparatively narrow line corresponding to the passage of the particles with relativistic ionization losses through the scintillator. The following spectrum was obtained when such absorber was chosen so as $\pi^-$ mesons would lose almost all their energy in the detector, but they would not yet stop in $C_2$. At last, the third spectrum was measured with the thickness of the absorber corresponding to the maximum number of the stops of $\pi^-$ mesons in the scintillator $C_2$. At such a position of the absorber 20% of all the $\pi^-$ mesons incident on the scintillator stopped in it. The remaining ones passed the scintillator through. The spectrum of pulses corresponding to these passing $\pi^-$ mesons must have a shape analogous to the second spectrum in fig. 2a. Therefore, by subtracting the second spectrum from the third one (after the corresponding normalization) it is possible to single out the pulse spectra corresponding to $\pi^-$ mesons coming to rest only (fig. 2b).

When $\pi^-$ mesons stop in the scintillator, the energy is released because of the two processes occurring in succession. Firstly, a $\pi^-$ meson is slowed down losing rather large energy ($\approx$ 10 MeV in our case) for the ionization of the medium. Then it produces a nuclear disintegration, and the outgoing particles of the star

leave a part of their energy in the scintillator. The spectrum presented in fig. 2b is, therefore, a result of the superposition of two distributions: the "stop spectrum" and the "star spectrum" corresponding to the two processes mentioned above. Only the latter of these distributions is characteristic of $\pi^-$ mesons only. As to the "stop spectrum", it must be the same both for $\pi^-$ mesons and for $\pi^+$ mesons; for $\mu$ mesons it is somewhat displaced to the region of small pulses.

An experimental comparison of the spectra of pulses produced when $\pi^-$ and $\pi^+$ mesons come to rest in the scintillator has been made at the beams of $\pi^-$ and $\pi^+$ mesons having the same average energy (70 MeV) and the same spread of ranges. The comparison has shown that an approximately one third part of the stopping $\pi^-$ mesons yields the pulses exceeding the maximum pulse of the "stop spectrum". It is this part of the spectrum, shaded in fig. 2, that may be used for the work of the telescope in the regime of a star detector. It follows from what has been said that the expected recording efficiency of the stopped $\pi^-$ mesons must be rather high ($\approx 30\%$).

### 3. Efficiency

In order the telescope shown in fig. 1 could detect only the stars due to $\pi^-$ mesons it is sufficient to set at the output of the counter $C_2$ a discriminator which does not permit small pulses to reach the coincidence circuit. An analogous result may be obtained in a simpler manner by decreasing the voltage $V_2$ at the photomultiplier of this counter. Fig. 3 shows the change in the characteristics of the detector as the voltage $V_2$ decreases. (It should be, of course, borne in mind that all the values for $V_2$ given here and further have a relative character.) In this figure are plotted the results of measurements of $\pi^-$ meson counting rate $N$ as a function of the thickness of the matter $R$ they traverse (absorber and scintillators). The mean range of $\pi^-$ mesons was 62.5 g/cm² of carbon, that corresponds to an energy of 170 MeV; the range spread due to the beam being not monoenergetic and to straggling was found to be $\pm 4$ g/cm². In the region of high voltages $V_2 > 1400$ V where the recording

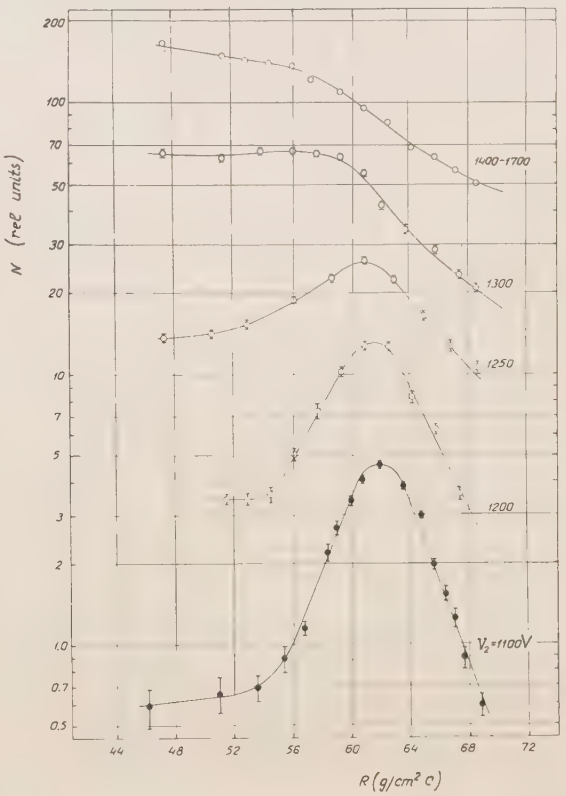


Fig. 3. The dependence of $N$ upon $R$ at various voltages $V_2$.

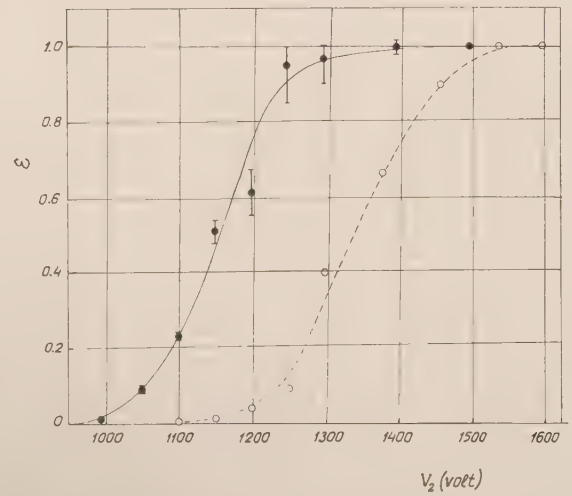


Fig. 4. Detector efficiency. ⊤ — $\varepsilon_{st}$; O — $\varepsilon_0$. The efficiency $\varepsilon_0$ was measured for $\pi^-$ mesons with residual range equal to 10 g/cm² C.

efficiencies for the passing and stopping $\pi^-$ mesons are close to unity, and, therefore, do not change by varying $V_2$, the dependence $N(R)$

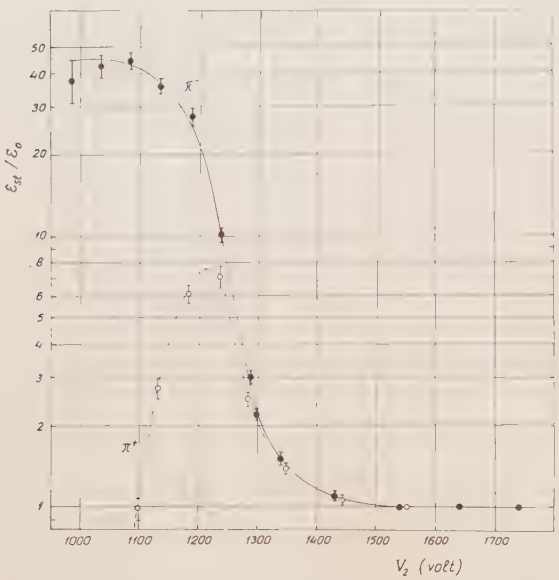


Fig. 5. The ratio $\varepsilon_{st}/\varepsilon_0$. $\frac{\top}{\perp}$-for $\pi^-$ mesons; $\frac{\vdash}{\perp}$-for $\pi^+$ mesons.

is an integral range distribution function. When $V_2 < 1400$ V, the shape of the curve $N(R)$ is essentially distorted. The counting rate $N$ in the region of thickness $R \leqslant 50$ g/cm$^2$, where the telescope detects only the traversing $\pi^-$ mesons further diminishing of the voltage the shape of the "peak" alters no longer, and only an identical decrease in the magnitudes of $N$ takes place for all the values of $R$. In this voltage region the curve practically coincides with the differential range distribution function.

Being aware of the range distribution function of $\pi^-$ mesons it is not difficult to obtain from the dependences $N(R)$ the magnitudes of the recording efficiency of the passing ($\varepsilon_0$) and stopping ($\varepsilon_{st}$) $\pi^-$ mesons. In calculating these efficiencies (fig. 4) use was made both of the curves from fig. 3 and of an analogous ones measured at the 67 MeV $\pi^-$ meson beam. As is seen from fig. 4, at first the efficiency $\varepsilon_0$ drops with decreasing the voltage $V_2$ much quicker than $\varepsilon_{st}$ in agreement with the spectra given in fig. 2. However, at low voltages the rise of the ratio $\varepsilon_{st}/\varepsilon_0$ becomes slower, and for $V_2 \leqslant 1100$ V, the magnitude of this ratio is no longer dependent upon $V_2$ (fig. 5). Such a behaviour of $\varepsilon_{st}/\varepsilon_0$ can be easily understood if we take into account that $\pi^-$ mesons produce stars both when they are brought to rest in matter and in flight. The ratio of the probabilities for these two processes for our scintillator equals approximately 50, that is close to the value of $\varepsilon_{st}/\varepsilon_0$

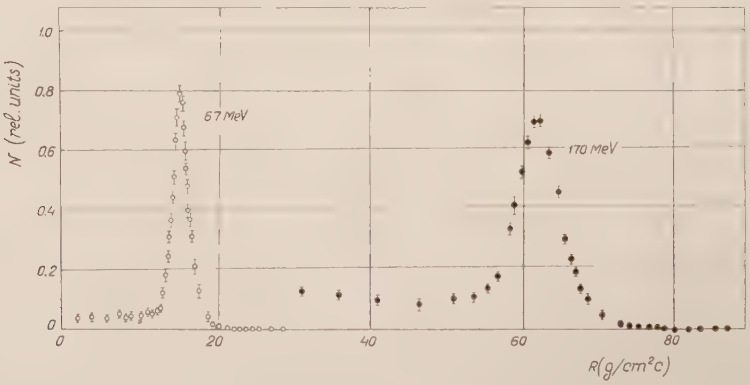


Fig. 6. Range curves for $\pi^-$ meson beams at energies of 67 ($\frac{\top}{\perp}$) and 170 MeV ($\frac{\top}{\perp}$); $V_2 = 1100$ V.

drops considerably more rapidly with decreasing $V_2$ than in the region $58 \leqslant R \leqslant 66$ g/cm$^2$, where besides the passing $\pi^-$ mesons, those stopped in the scintillator $C_2$ are detected. The variation of the shape of the curve $N(R)$ with the decrease of $V_2$ is going on up to $V_2 = 1100$ V. By a obtained for small voltages where the detector is sensitive only to stars.

The ratio $\varepsilon_{st}/\varepsilon_0$ changes with decreasing $V_2$ in another way when the detector records $\pi^+$ mesons (fig. 5). In contrast to $\pi^-$ mesons, $\pi^+$ mesons give rise to stars only in flight. Therefore,

the magnitudes of $\varepsilon_{st}/\varepsilon_0$ for $\pi^-$ and $\pi^-$ mesons coincide only in the range of large values for $V_2$, where the detector effectively records the pulses belonging to the "stop spectrum". When one goes over to the region of voltages where the detector is sensitive only to stars, the efficiency $\varepsilon_{st}$ for $\pi^+$ mesons falls, and the ratio $\varepsilon_{st}/\varepsilon_0$ decreases rapidly.

A comparison of the curves given in fig. 5 shows that the telescope begins to work in the regime of a star detector at the voltages $V_2 \approx 1100$ V. The efficiency $\varepsilon_{st}$ corresponding to this voltage is equal approximately to 30%, what is close to the estimate obtained earlier from the analysis of the spectra. The recording efficiency for the $\pi^-$ mesons coming to rest in the scintillator $\varepsilon_{st}$ should not be confused with that for $\pi^-$ mesons incident on the detector input $w$, which, in our case, is considerably lower than $\varepsilon_{st}$ due to the disappearance of mesons when they are passing through the absorber of the detector, and due to a comparatively small thickness of the scintillator. If we use a thick scintillator, i.e., whose thickness is close to the spread of $\pi^-$ meson ranges, then the latter factor from those mentioned above is removed. In this optimal case the ratio $w/\varepsilon_{st}$ is found to be 70% at an energy of $\pi^-$ mesons being 65 MeV, and 40%—at 170 MeV.

A star detector employing a thick scintillator may be used in experiments where a high efficiency of $\pi^-$ meson recording is required. If the range curve of $\pi^-$ mesons is necessary to be measured, the thickness of the scintillator should be taken small compared with the range spread. Typical range curves which are available when the telescope works as a star detector are presented in fig. 6. These curves have been measured at two different beams of $\pi^-$ mesons with the mean energies of 67 and 170 MeV.

## 4. Selection Characteristics of the Detector

Since the star detector detects only high energy stars produced by stopping $\pi^-$ mesons, it is little sensitive to other particles which do not create such stars. The selection ability of the star detector is convenient to be characterized by a selection coefficient $K$, which is the ratio of the recording efficiency for $\pi^-$ meson stops to that of other particles both coming to rest in the scintillator ($K_{st}$) and those passing through the detector ($K_0$).

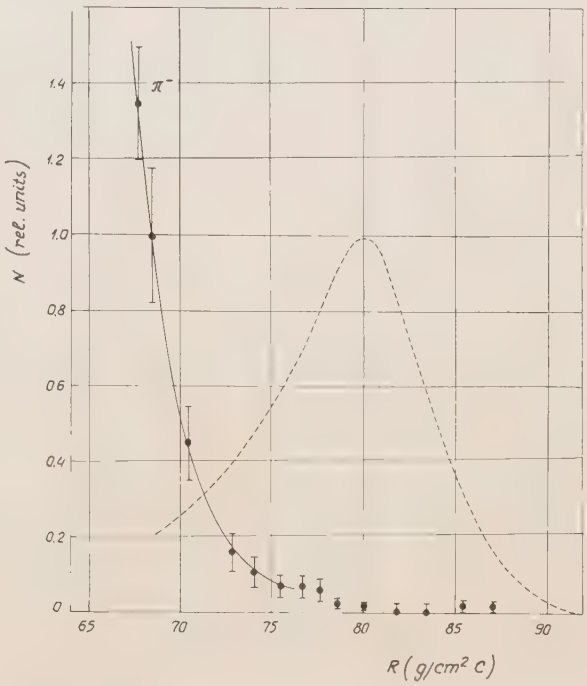


Fig. 7. Inefficiency of the star detector to $\mu^-$ mesons. $\overline{\overline{\cdot}}$-the measured range curve. The real $\mu^-$ meson range curve is shown by the dashed line. $V_2 = 1100$ V.

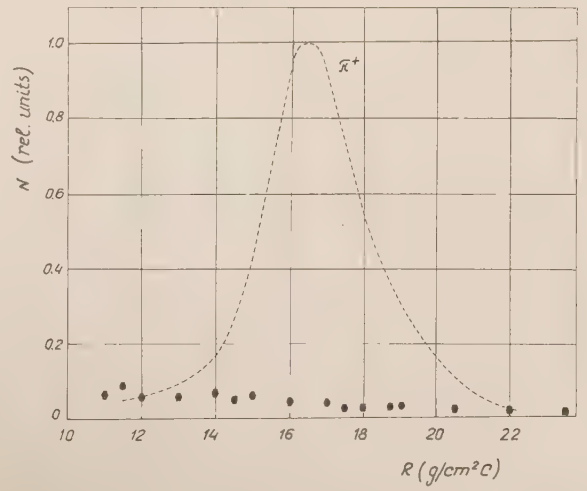


Fig. 8. The same as in fig. 7, but for $\pi^+$ mesons of 67 MeV mean energy.

$\mu$ mesons and electrons fail to produce high energy stars either in flight, or by the stopping. (When coming to rest in matter possessing large atomic weight $\mu^-$ mesons may give rise to stars, but with a small energy release.) Therefore, the selection coefficients $K_{st}$ and $K_0$ for light particles may be made whatever large by decreasing the voltage $V_2$, with $K_0 \gg K_{st}$. Fig. 7 shows a part of the measured by the star detector range curve of 170 MeV $\pi^-$ mesons and $\mu^-$ mesons contaminating this beam. If the efficiency of $\mu^-$ meson detection were the same like for $\pi^-$ mesons, i.e., $K_{st} = 1$, then the measured range curve in the region of large thickness would coincide with the dashed line drawn in the figure. As is seen from this figure, in this region there is no maximum, here $K_{st} \geqslant 30$. So, already at the voltage $V_2$ being 1100 V, i.e., near the limit of the regime of the star detector, the selection for $\mu^-$ mesons is characterized by a large magnitude of $K$. This result is likely to concern $\mu^+$ mesons as well. The magnitude of $K$ for electrons must be still greater than for $\mu$ mesons in view of small energy release when the electrons pass through the scintillator.

The selection in case of the passing $\pi^+$ mesons is characterized, according to the measurements, by the same magnitude of $K_0 \approx 50$, as in case of $\pi^-$ mesons. Note, that the magnitude of $K_0$ must be analogous for other nuclear-active particles since all of them are responsible for star production in flight with about the same probability. The magnitude of $K_{st}$ for $\pi^+$ mesons was found to be close to that obtained for $\mu$ mesons (see fig. 8). Like in case of $\mu$ mesons it may be made very large by decreasing $V_2$.

The sensitivity of the star detector to the particles heavier than $\pi$ mesons has not been investigated. Here we only note that the magnitude of $K_{st}$ must decrease with the rise of the particle mass.

## 5. Modifications of the Detector

As it was pointed out above, the upper limit of the voltage where the telescope can work as a star detector turns out to be $V_2 = 1100$—$1150$ V. If we increase the voltage by 50—100 V, the detector starts to record the pulses due to the "stop spectrum". Here, as is seen from figs. 4 and 5, the recording efficiency for the stops $\varepsilon_{st}$ may be found to be close to unity while the ratio $\varepsilon_{st}/\varepsilon_0$ remains still large. The telescope working in this regime (we shall call it a "stop detector" unlike the star detector is equally sensitive to $\pi^-$ mesons and to $\pi^+$, $\mu^-$ and $\mu^+$ mesons (fig. 9

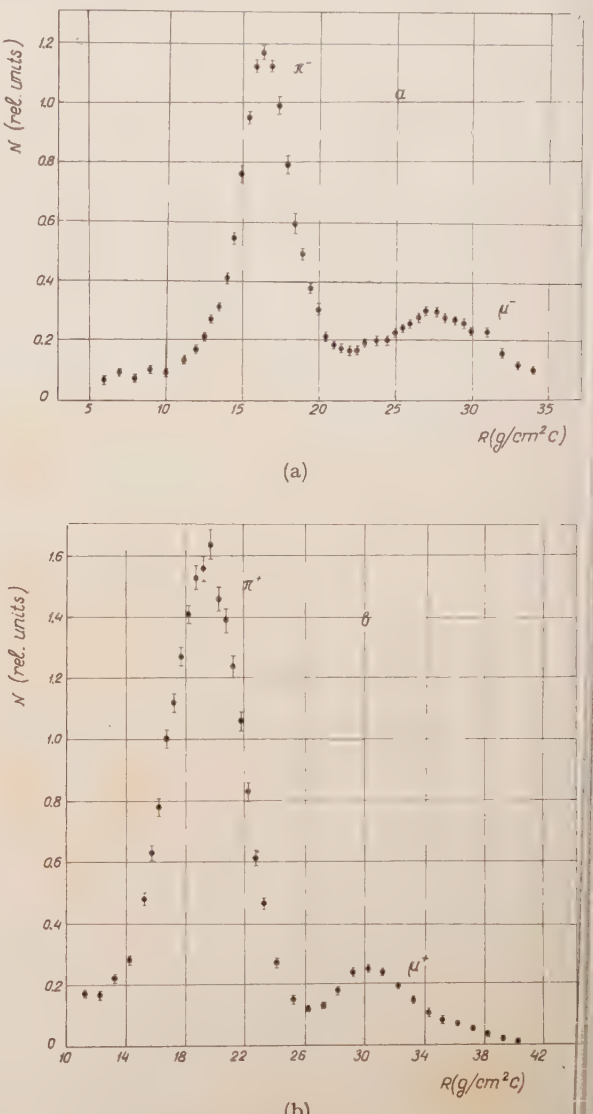


Fig. 9
Range curves measured by means of the stop detector.
(a): for the beam of $\pi^-$ and $\mu^-$ mesons with the momentum 150 MeV/$c$. ($\pi^-$ meson energy is 67 MeV).
(b): for the beam of $\pi^+$ and $\mu^+$ mesons with the momentum 163 MeV/$c$. $V_2 = 1250$ V.

When the intensity of the $\pi$ meson beam is $\approx 10^4\,\mathrm{sec}^{-1}$, the counting rate of the stop detector amounts to some hundred counts per second. Such large counting rate allows to make the measurements of the range curves $N(R)$ of only one counter, was found to be not very much different from the real range curve. However, the star detector consisting of only one counter could be hardly used for work under more difficult background conditions

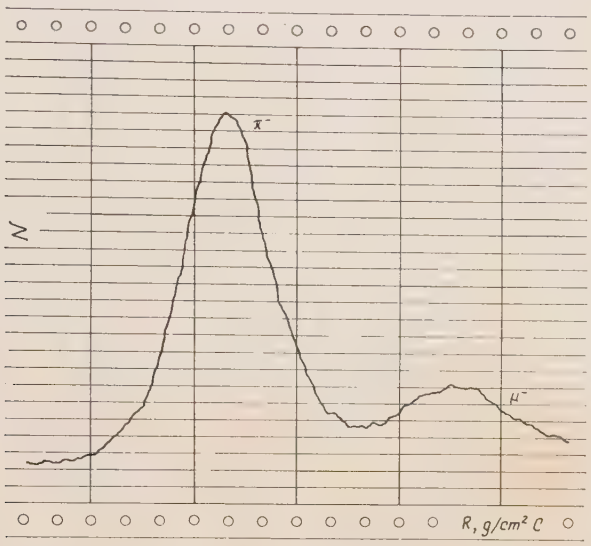


Fig. 10. Range curve registered on the record chart of the self-recording integrator. $V_2 = 1250$ V.

automatic. This presents considerable advantages in the case when in the course of an experiment it becomes necessary to control the magnitude of the beam energy frequently and quickly. For registering the range curve a self-recording integrator was connected to the output of the coincidence circuit. The motor of this integrator rotated synchronously with that moving the wedge-shaped absorber (fig. 1). A typical range curve thus measured is given in fig. 10. All the measurement procedure takes some minutes only.

The pulses in the counter $C_2$ detected in the regime of a star detector are so large that they essentially exceed all the outside pulses due to the background which is present in the experimental hall of the accelerator when working with the $\pi^-$ meson beams. This allows to simplify the scheme of the star detector by excluding the counter $C_1$ and by connecting the input of the scaler directly with the output of the counter $C_2$. The range curve of 70 MeV $\pi^-$ mesons measured by means of such a simplified detector consisting than in our case (e.g., in the proton or neutron beam).

Finally, let us point to one more modification of the star detector scheme. This modification consists in replacing the counter $C_2$ for the counter analogous to $C_1$, i.e., with a good time resolution but having a comparatively bad spectrometric characteristics. In this case so large a value for the ratio $\varepsilon_{st}/\varepsilon_0$ as that presented in fig. 5 is impossible to obtain; it is found to be 10—20. However, the star detector of such a simplified form has a practical advantage. It does not differ in anything from "standard" scintillation telescopes. So, the latter ones may be used as a star detector without essential changes for rough measurements of the range curve of $\pi^-$ mesons.

## 6. Conclusion

An investigation of the characteristics of the detector shows that the region of its working voltages is separated into three essentially different parts. When the voltages are low, the

telescope works in the regime of a star detector, distinguishing $\pi^-$ mesons coming to rest in the scintillator from other stopping and passing particles. The region of voltages corresponding to this regime is 150—200 V for the type of the photomultiplier we have chosen. Higher voltages of 1200—1270 V correspond to the regime of the stop detector. In this case the detector records the stops of $\pi$ and $\mu$ mesons of both signs equally well. Finally, in the region of still higher voltages ($V_2 > 1400$ V) the detector works as a "usual" telescope which does not possess any selection properties.

The detector described may be used as a spectrometer which allows to measure the spectra of $\pi^-$ mesons under the conditions of large outside background. It is most reasonable to apply this detector for investigating the spectra of $\pi^-$ mesons in the low energy region ($< 50$ MeV) where the magnetic spectrometer is usually difficult to apply because of the large $\mu$ meson background.

It should be noted in conclusion that because of its simplicity the star detector possesses good operation characteristics. It can be easily adjusted and works stably; for the time of its operation (about a year) its parameters do not undergo any noticeable changes.

NUCLEAR INSTRUMENTS AND METHODS 8 (1960) 19–22; NORTH-HOLLAND PUBLISHING CO.

# SPACE-CHARGE EFFECTS IN CYLINDRICAL BEAMS WITH UNIFORM ACCELERATION

C. D. MOAK†

*Atomic Energy Research Establishment, Harwell, Didcot, Berks., England*

Received 25 February 1960

The profiles of cylindrical beams of charged particles undergoing uniform acceleration have been derived for a large number of beam intensities, configurations and energies, for the case where the emergent beam is parallel. Derivations of the results are presented and their uses are illustrated. Use of the results for certain cases of non-parallel emergence is outlined. Tables of the integral required in the calculations are available as a Harwell report No. AERE-R. 3255.

## 1. Introduction

Profiles for mono-energetic cylindrical beams of charged particles in free flight were derived originally for use in the study of electron beams[1,2,3]), and these derivations are listed in a number of texts[4,5,6]). The initial assumptions are as follows:

1. The density of the beam is uniform and has an initial radius $r_0$ at $z = 0$.

2. The particles all have equal axial velocity and zero initial radial velocity.

3. The axial component of the field due to space charge is assumed to be negligible throughout.

The equation of motion of a particle on the edge of a beam of radius $r$ (cm) is given by

$$MM_{\mathrm{p}}\frac{\mathrm{d}^2r}{\mathrm{d}t^2} = \frac{2QeI}{vr} \qquad (1)$$

where $I$ is the current (e.s.u. per sec) of particles of axial velocity $v$ (cm per sec) each having a mass of $M\,M_{\mathrm{p}}$ (grams) where $M$ is the atomic weight number and having an effective charge of $Qe$ (e.s.u.) where $Q$ is the charge state of the particles. Substituting the values of $e$ and $M_{\mathrm{p}}$, and changing units, we have

$$5.8 \times 10^{-22}\left(\frac{M}{QI_{\mathrm{mA}}}\right) r\frac{\mathrm{d}^2r}{\mathrm{d}t^2} = \frac{1}{v} \qquad (2)$$

where $I_{\mathrm{mA}}$ is the current in milliamperes and $v$ is in cm per sec.

† On leave from Oak Ridge National Laboratory, Oak Ridge, Tennessee, U.S.A.

For the case of a beam in free flight $v$ is a constant which can be related to the voltage to which the particles have been accelerated. The following substitutions can be made:

$$R = \frac{r}{r_0};\; R' = \frac{\mathrm{d}R}{\mathrm{d}z};\; R'' = \frac{\mathrm{d}^2R}{\mathrm{d}z^2};\; v = \frac{\mathrm{d}z}{\mathrm{d}t} = \sqrt{\frac{2QeV}{M}}\,. \qquad (3)$$

With these substitutions eq. (2) reduces to

$$Kr_0^2(R')^2 = \ln R \qquad (4)$$

where

$$K = 24.33\left(\frac{Q}{M}\right)^{\frac{1}{2}} V_{\mathrm{kV}}^{\frac{3}{2}} I_{\mathrm{mA}}^{-1}$$

and $V_{\mathrm{kV}}$ is the potential in kilovolts to which the particles have been accelerated. Integration of eq. (4) gives

$$K^{-\frac{1}{2}}\frac{z}{r_0} = Z = \int_1^{R_f}\frac{\mathrm{d}R}{\sqrt{\ln R}}\,. \qquad (5)$$

Values of $Z$ as a function of $R$ have been given by Lash-Miller and Gordon[7]). From these values the beam radius (in units of initial beam

[1]) E. E. Watson, Phil. Mag. **3** (1927) 849.

[2]) B. v. Borries and J. Dosse, Arch. Electrotech. **32** (1938) 221.

[3]) A. V. Haeff, Proc. Inst. Radio Engrs. **27** (1939) 586.

[4]) O. Klemperer, Electron Optics (Cambridge Univ. Press, 1953) p. 202.

[5]) Zworykin, Morton, Ramberg, Hillier and Vance, Electron Optics and the Electron Microscope (John Wiley and Sons, New York, 1945) p. 591.

[6]) J. R. Pierce, Theory and Design of Electron Beams (D. van Nostrand Company, Inc., New York, 1954) Ch. IX.

[7]) W. Lash-Miller and A. R. Gordon, J. Phys. Chem. **37** (1931) 2785.

radius) can be plotted as a function of distance (in units of initial beam radius) with a scale factor, contained in $K^{-\frac{1}{2}}$, which depends upon beam current, voltage and particle charge to mass ratio. With the curves available, the requirement that the beam be parallel initially is no longer necessary. It remains necessary only that the initial radial velocity of each particle be proportional to its initial radius in cases where initial radial velocities are non-zero.

## 2. Discussion

For the case where the axial velocity is not constant, the derivations must differ beyond eq. (2). Certain special cases of this problem have been worked out. Moss has shown a small number of profiles for electron-beam focusing in a post-acceleration cathode-ray tube[8]). Special cases have been worked out by King, Hobbis and Harrison in design studies for a proton linear accelerator at Harwell[9]). In both these instances as well as in the present paper, uniform acceleration will be assumed. The calculations presented here will pertain to most cases of beams converging in the direction of positive acceleration. By starting with the same initial conditions as before and decelerating the particles uniformly towards rest, it turns out that a wide range of design conditions may be covered with a fairly complete set of beam profiles. This procedure is equivalent to assuming a final beam-condition in an accelerator, (viz. emergent beam parallel and final voltage $V_{\mathrm{kV}}$) and deriving the profile of the beam back through the accelerator toward the source. In this case the velocity may be written as

$$v = \left(\frac{2QeV_{\mathrm{kV}}}{M}\right)^{\frac{1}{2}} \left(1 - \frac{z}{L}\right)^{\frac{1}{2}} \tag{6}$$

where $V_{\mathrm{kV}}$ is the final or maximum voltage to which the particles are accelerated; working backward through the accelerator. $V_{\mathrm{kV}}$ becomes the starting potential. The number $L$ is the axial distance in which the particles come to rest. Making this substitution, eq. (2) becomes

$$DL^{-\frac{3}{2}} (L - z)\, r \frac{\mathrm{d}}{\mathrm{d}z}\left[(L - z)^{\frac{1}{2}} \frac{\mathrm{d}r}{\mathrm{d}z}\right] = 1 \tag{7}$$

where

$$D = 5.8 \times 10^{-22} \left(\frac{M}{QI_{\mathrm{m\,A}}}\right) \left(\frac{2QeV_{\mathrm{kV}}}{M}\right)^{\frac{3}{2}}.$$

If now we make the substitution that $x^2 \equiv (L - z)$ we have

$$r \frac{\mathrm{d}^2 r}{\mathrm{d}x^2} = \frac{4L^{\frac{3}{2}}}{Dx}. \tag{8}$$

If we make an additional substitution that $r \equiv 2L^{\frac{3}{4}} D^{-\frac{1}{2}} x^{\frac{1}{2}} q$, we have

$$q\left[x^2 \frac{\mathrm{d}^2 q}{\mathrm{d}x^2} + x \frac{\mathrm{d}q}{\mathrm{d}x} - \tfrac{1}{4} q\right] = 1\,. \tag{9}$$

A final substitution $u \equiv x\, \mathrm{d}q/\mathrm{d}x$ gives

$$u\, \mathrm{d}u = \frac{\mathrm{d}q}{q}\left[1 + \tfrac{1}{4} q^2\right]. \tag{10}$$

Eq. (10) integrates to

$$u = \pm \sqrt{2 \ln q + \tfrac{1}{4} q^2 - B}\,. \tag{11}$$

From the condition that initial radial velocity is zero (beam emerging parallel) we can evaluate $B$ and eq. (11) reduces to

$$u = -\left(2 \ln \frac{2L}{r_0 D^{\frac{1}{2}}} q + \tfrac{1}{4} q^2\right)^{\frac{1}{2}}. \tag{12}$$

Returning to variables $x$ and $q$ we have

$$\left(2 \ln \frac{2L}{D^{\frac{1}{2}} r_0} q + \tfrac{1}{4} q^2\right)^{-\frac{1}{2}} \mathrm{d}q = \frac{\mathrm{d}x}{x} \tag{13}$$

and

$$\ln x + C = -\int_{\frac{r_0 D^{\frac{1}{2}}}{2L}}^{\frac{D^{\frac{1}{2}} r}{2L^{\frac{3}{4}}(L-z)^{\frac{1}{4}}}} \left(2 \ln \frac{2L}{D^{\frac{1}{2}} r_0} q + \tfrac{1}{4} q^2\right)^{-\frac{1}{2}} \mathrm{d}q \tag{14}$$

$$C = -\ln x_0 = -\ln L^{\frac{1}{2}} \tag{15}$$

$$\ln \left(\frac{L - z}{L}\right)^{\frac{1}{2}} = -\int_{\frac{r_0 D^{\frac{1}{2}}}{2L}}^{\frac{D^{\frac{1}{2}} r}{2L^{\frac{3}{4}}(L-z)^{\frac{1}{4}}}} \left(2 \ln \frac{2L}{D^{\frac{1}{2}} r_0} q + \tfrac{1}{4} q^2\right)^{-\frac{1}{2}} \mathrm{d}q\,. \tag{16}$$

If we set $w \equiv q/q_0$ and $L/(L - z) \equiv s$ we have

$$\ln (s^{\frac{1}{4}}) = \int_1^A (\omega^2 + a^{-2} \ln \omega^2)^{-\frac{1}{2}}\, \mathrm{d}\omega = y \tag{17}$$

where

$$A = \frac{r}{r_0} s^{\frac{1}{4}} \quad \text{and} \quad a = \frac{K^{\frac{1}{4}}}{2\sqrt{2}} \frac{r_0}{L}$$

where $K$ is given in eq. (4).

[8]) H. Moss, Wireless Eng. 22 (1945) 316.

[9]) King, Hobbis and Harrison, Harwell report AERE GP/R. 1748 (1955).

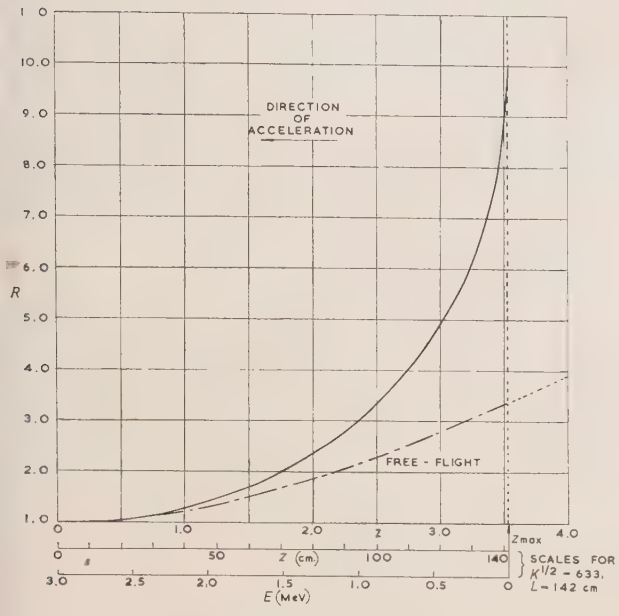


Fig. 1

For any specific problem the value of $a$ will be a fixed parameter. If, for that value of $a$, the integral of eq. (17) is tabulated, then we will have values of $s$ (and thus $z$) as a function of $(r/r_0)\, s^{\frac{1}{4}}$. From these values, $r$ as a function of $z$ may be derived and the profile of the beam will be mapped out. A particularly useful set of numbers derivable from the values of the integral of eq. (17) are the values of $R$ as a function of $Z$ where $R$ and $Z$ are defined exactly as in eq. (5) for the case of a beam in free flight.

A set of calculations has been carried out on the Mercury computer at Harwell. A wide range of values of $a$ has been used; in the cases of small $a$ (i.e. relatively gentle accelerations of rather intense beams) the profiles approach that of the free-flight case. For each value of $a$, the integral has been evaluated for enough values of $A$ to give a particle energy variation of a factor of $10^4$ except in cases of extreme radius variation. Only illustrative examples will be given here; a set of tables of $y/a$, $R$ and $Z$ as a function of $A$ for various values of $a$ is available as Harwell Report No. AERE R-3255.

## 3. Examples

An example which illustrates the use of the values of $R$ and $Z$ is the following accelerator situation:

Emergent beam: protons ($M = 1$, $Q = 1$); final beam energy 3 MeV ($V_{\mathrm{kV}} = 3000$); beam current 10 mA; final beam radius 0.063 cm.

Accelerator tube length, $L = 142$ cm.

$$K^{\frac{1}{2}} = 4.933 \left(\frac{Q}{M}\right)^{\frac{1}{4}} V_{\mathrm{kV}}^{\frac{3}{4}}\, I_{\mathrm{mA}}^{-\frac{1}{2}} = 633$$

$$a = \frac{K^{\frac{1}{2}}}{2\sqrt{2}} \frac{r_0}{L} = 0.1\ .$$

The curve for the case $a = 0.1$ is given in fig. 1. For comparison, a free-flight profile is shown for a beam of the same current and initial radius, but with no deceleration along the axial direction. The curve shown for $a = 0.1$ would clearly apply to the case where both the accelerator length and the initial radius were changed by any factor; in the new case, only the scale of $z$ would have to be changed. If current and voltage were changed so as to maintain the same ratio of $I_{\mathrm{mA}}^{\frac{1}{2}}/V_{\mathrm{kV}}^{\frac{3}{4}}$ and if $r_0$ and $L$ were kept

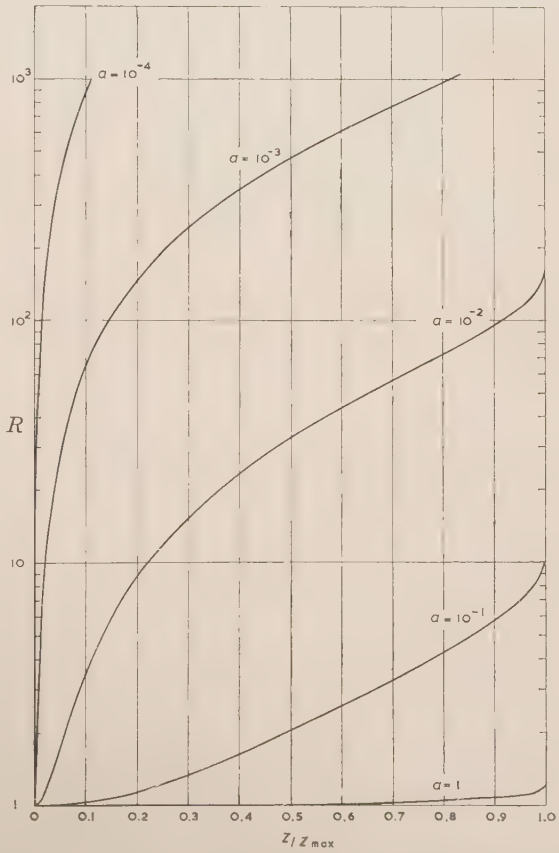


Fig. 2

fixed, then only the $E$ scale would need to be changed. In general, any changes of $I_{\mathrm{mA}}$, $V_{\mathrm{kV}}$, $r_0$ and $L$ which left $a = 0.1$ would be described by the solid curve of fig. 1, with appropriate scale changes in $z$ and $E$.

The profiles, reading from right to left, may be terminated before reaching the origin and thus the beam will emerge in a converging condition. The terminated profile may then be joined to a free-flight profile appropriate to the energy at which the curve was terminated. In this way, beam radii at targets positioned away from the end of the accelerator may be derived. The calculations do not provide for cases where beams are diverging in the direction of positive acceleration.

In order to present several representative curves on one figure, the variables $R$ vs $Z/Z_{\mathrm{max}}$, have been plotted for several values of $a$ and these are shown in fig. 2. For more accurate work, the reader is referred to the tables presented in the report.

**Acknowledgements**

The author is indebted to Dr. T. H. R. Skyrme for helpful discussions on the reduction of the problem to a form most suitable for computation and to Mr. P. D. Preston, both for carrying out the computations on the Mercury computer and for discussions concerning the most useful ranges for the parameters involved.

NUCLEAR INSTRUMENTS AND METHODS 8 (1960) 23–26; NORTH-HOLLAND PUBLISHING CO.

# ON THE CONSTRUCTION AND LONG-TERM PERFORMANCE OF MEDIUM PRESSURE $BF_3$ PROPORTIONAL COUNTERS USED FOR COSMIC-RAY RECORDING

P. H. STOKER

*Department of Physics, Potchefstroom University for C.H.E., Potchefstroom, South Africa*

Received 10 February 1960

Construction and filling procedure of $BF_3$ proportional counters for a cosmic-ray neutron monitor is outlined. The method of improvement of the operational characteristics of the counters necessitated by deterioration over the first years of continuous operation is given.

## 1. Introduction

We have made[1]) $BF_3$ counters during 1955/56 for a neutron monitor constructed according to the standard design proposed by Simpson[2]) for the I.G.Y. These counters are in continuous operation, recording cosmic-radiation since early 1956. The essential features of the method of construction and of the performance of the counters since then will be reported.

Fowler and Tunnicliffe[3]) have observed a deterioration of their counters after the first filling, but stable performance was obtained by refilling the counters after three months. Other authors[4–6]) have reported on the deterioration of $BF_3$ counters caused by heavy neutron and gamma irradiation.

Properties of medium and high pressure $BF_3$ counters are strongly affected by electronnegative constituents in the filling gas[7,8]). In the presence of electronnegative constituents, electrons produced in the gas far from the central wire have less change in reaching the wire to initiate a gas discharge than those produced near the wire. The number of electrons lost in travelling toward the anode wire depends on the purity of the $BF_3$ gas with respect to electronnegative constituents and on the characteristics of the counter, viz. gas pressure, operating voltage, counter and wire diameters. Using the experimental results which Bistline[9]) obtained for his $BF_3$ gas, Tongiori *et al.*[7]) calculated the survival probabilities of electrons in counters with different characteristics. According to these calculations a reasonable survival probability is obtained for the counters with the characteristics proposed by Simpson[2]). Although very small amounts of electronnegative constituents in the counter gas would, therefore, not be fatal for the operation of the counters, such constituents will still affect the operational characteristics considerable. It is, therefore, essential to exercise the utmost care to construct clean counters and to fill them with purified $BF_3$.

## 2. Construction

The neutron counters were made of seamless copper tubing with diameter of about 1.5 inches and wall thickness of $\frac{5}{64}$ inches. These tubes were cleaned on a lathe by cotton soaked with

[1]) P. J. Kruger, M. Sc. Thesis (1955).

[2]) J. A. Simpson, Cosmic radiation neutron intensity monitor, (published by the Institute for Nuclear Studies, The University of Chicago, January, 1955).
J. A. Simpson, W. Fonger and S. B. Treiman, Phys. Rev. **90** (1953) 934.

[3]) I. L. Fowler and P. R. Tunnicliffe, Rev. Sci. Inst. **21** (1950) 734.

[4]) W. Abson, P. G. Salmon and S. Pyrah, Proc. Inst. Electrical Eng. **105B** (1958) 357.

[5]) O. F. Swift and R. T. Bayard, Nucleonics **17** (5) (1959) 122.

[6]) R. K. Soberman, S. A. Korff, S. S. Friedland and H. S. Katzenstein, Rev. Sci. Inst. **24** (1953) 1058.

[7]) V. Cocconi Tongiori, S. Hayakawa and M. Widgoff, Rev. Sci. Inst. **22** (1951) 899.

[8]) R. B. Mendell and S. A. Korff, Rev. Sci. Inst. **30** (1959) 442.

[9]) J. A. Bistline, Rev. Sci. Inst. **19** (1948) 842.

benzine and finally polished by dry cotton jammed in the tube. The 1 mil tungsten wire was silver-soldered into small brass rods with rounded edges, as illustrated in fig. 1. Before

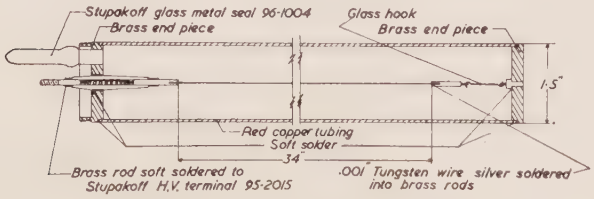


Fig. 1. The construction of the $BF_3$ proportional counters.

assembling the counter all the pieces were thoroughly cleaned in boiling water followed by washing with alcohol and benzine. After removal of cloth fibres and dust particles the pieces were assembled and the tinned end-pieces of brass soft-soldered to the tube. An assembled counter was immediately sealed to the vacuum and filling system, which was of glass tubing, Apiezon M grease being used for the stopcocks.

All the counters had good vacuum properties. A batch of four counters was pumped for about four days while heated to 100° C. While the $BF_3 \cdot CaF_2$ complex† was outgassed at about 150° C, the counters were filled with argon to a few centimetres of Hg pressure to "soak" the walls of the counters. The generated $BF_3$ obtained by raising the temperature of the complex was purified by passing the gas through a trap at dry ice temperature and filled with sodium fluoride to remove hidrofluoric acid[4,7]) and condensible impurities. The $BF_3$ was frozen in a second trap immersed in liquid oxygen. The counters were then evacuated by pumping out the argon. Next they were filled for a few minutes with $BF_3$ by removing the liquid oxygen from the trap. The $BF_3$ was frozen again and then pumped together with the counters to a good vacuum. This temporary

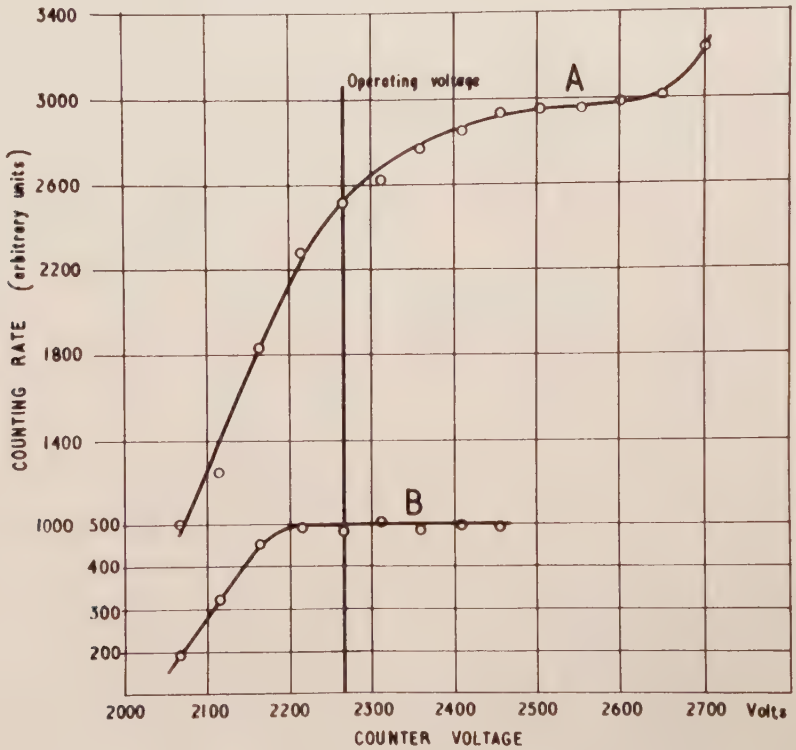


Fig. 2. Counter voltage characteristics after about a year of operation, curve A for a batch of six counters with anode wires connected together, curve B for a single counter.

† Enriched to 96% in the $B^{10}$ isotope as obtained from Carbide and Carbon Chemical Division, Oak Ridge, Tennessee.

filling procedure was repeated once. With the final filling the pressure in the system was adjusted to 45 cm Hg, the counters sealed off and removed.

### 3. Performance of the Counters

With a narrow neutron beam from a radium-beryllium source (the gamma-rays were absorbed by lead) directed along the counter wire, a double peaked pulse distribution similar to that reported by Fowler *et al.*[3]) and by Abson *et al.*[4]) for good counters, was obtained with no deterioration noticable after three months[1]). After about a year of continuous operation at the Magnetic Observatory at Hermanus, deterioration in the counting rate-voltage characteristics of a batch of six counters was observed. With the anode wires of the six counters connected together to the same head cathode follower, the plateau shifted to a higher voltage (see fig. 2). For single counters a plateau was still obtained at the operating voltage. This deterioration caused a steady decrease in the calibration intensity by a 2 mg Ra–Be neutron source and registered cosmic ray neutron intensity with time. Some improvement was obtained by increasing the amplification of the amplifying unit, which had an amplification factor of about 1000 and a clipping time of several microseconds[2]). A steady performance and a return to the original intensity was only obtained by connecting the anode wire of each counter to an amplifying tube before mixing the pulses, thus decreasing the capacity on the wires of the single counters. The wiring diagram is shown in fig. 3. The mixing is done in the common plate circuit of the six halves of the 12AT7 tubes. The first halve of the 12AU7 reverses the pulse with some amplification and the second halve serves as cathode follower. The feed-back action of the cathode resistors is sufficient to ensure linearity and stability of this amplifying and mixing unit. The anode voltage can, therefore, be supplied by an unstabilized filtered rectifying unit.

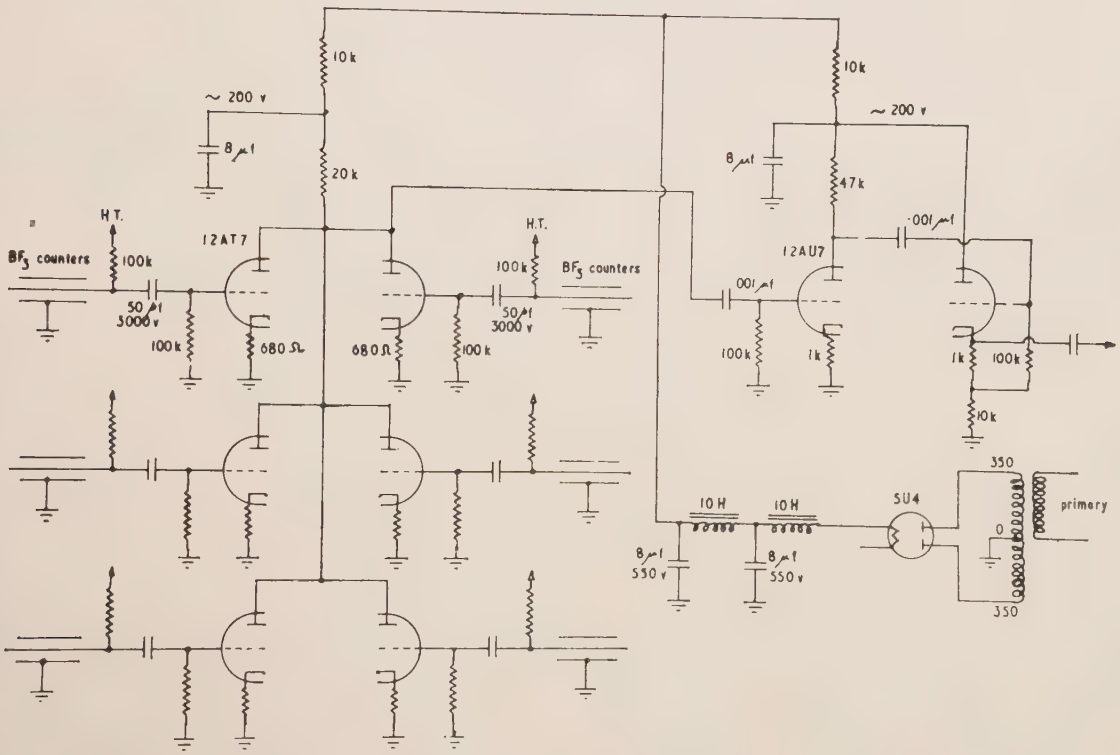


Fig. 3. The circuit for mixing and preamplifying the pulses of a batch of six $BF_3$ counters.

A batch of six counters showed with this amplifying and mixing unit the same characteristic counting rate-operating voltage curve as obtained for the single counters (fig. 2, curve B). Fig. 4 represents the integral-discriminator bias curve for a batch of six counters.

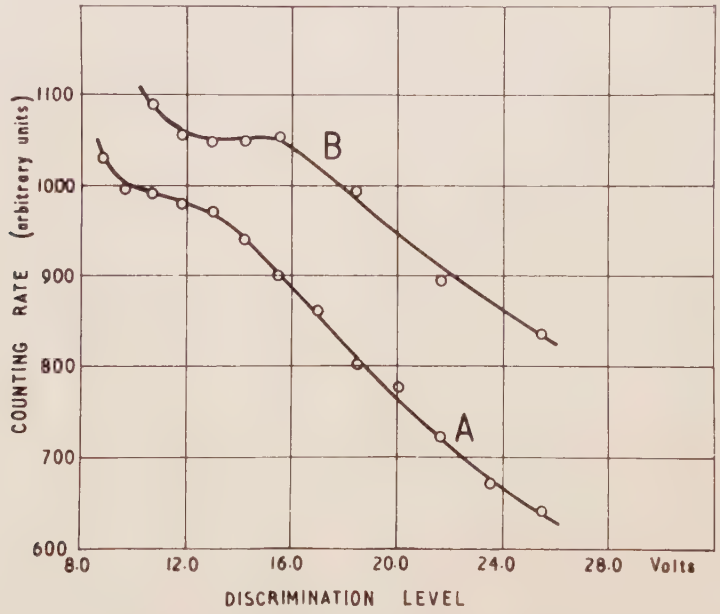


Fig. 4. The integral-discriminator bias curve for a batch of six counters, curve A with the anode wire connected together and curve B with the amplifying and mixing unit.

Recent measurements on the pulses of the counters at the grids of the 12AT7 tubes showed a rise time (taken from 10% to 90% of the height of the pulses) of 0.3 microseconds, decay times from 2 to 3 microseconds, and a pulse height distribution from 10 to 20 mV with a maximum at about 15 mV, as viewed on an oscillograph screen. The operation voltage of the counters was always 2260 volts.

A test of the temperature dependence of the neutron monitor set-up and registering units was made by varying the temperature of the room from 18° C to nearly 40° C, but no significant dependence was found under the neutron irradiation of a 2 mg Ra–Be source.

**Acknowledgements**

This publication is largely the result of the effort of Mr. A. M. van Wijk and his staff, who are operating the neutron monitor at the Magnetic Observatory, Hermanus, Cape. Thanks are due to Messrs. A. M. van Wijk and R. van der Walt for the information provided, and to Messrs. G. C. Snyman, P. I. Jongbloed and C. R. Smith for technical assistance.

The author wish to acknowledge the financial support provided by the South African C.S.I.R. for the construction of the monitor.

NUCLEAR INSTRUMENTS AND METHODS 8 (1960) 27–39; NORTH-HOLLAND PUBLISHING CO.

# THE UTRECHT 850 kV CASCADE GENERATOR

## I. BEAM DEFLECTION AND ENERGY CONTROL

C. M. BRAAMS and P. B. SMITH

*Fysisch Laboratorium der Rijksuniversiteit te Utrecht, Nederland*

Received 9 March 1960

The beam deflection magnet and energy control system of the Utrecht cascade generator are described. The uniform-field magnet has entrance and exit slits located outside the magnetic field. Since the cascade generator produces a vertical beam, the most convenient choice for the angle of deflection was 90 degrees. The radius of curvature of the beam in the region of the uniform field is 20 cm, which makes it possible to deflect a one-MeV beam of $He^+$ or $D_2^+$ ions with a field of 14.5 kilogauss. The whole assembly of the magnet and slits can be rotated about the incoming beam in order to direct the beam to different experimental arrangements. Energy control is achieved in two steps; first the exciting current of the magnet is stabilized, the magnetic field being measured with a proton magnetic resonance fluxmeter, and second the high tension is controlled so as to maintain the deflected beam centered on the exit slit of the magnet. The expected energy resolution of the system has been verified down to an energy spread (full width at half maximum) of 0.15% in proton energy. At this resolution a useful beam ($\approx 2\ \mu$A) is obtainable with a high-frequency ion source delivering a total beam of about 40 $\mu$A protons.

## 1. Introduction

The Utrecht 850 kV cascade generator has been described previously in several communications[1,2,3]). The latest of these dates from 1955. Since then numerous changes have been made in the associated equipment of the generator, and the generator itself has been converted from 50 Hz to 500 Hz operation. As a result it is now quite suitable for precision work. Since several of the improvements have not been adequately described in published form and since it is felt that such a publication may serve a useful purpose, this, and a companion publication have been prepared. In this article improvements in the beam deflecting and energy control systems will be described. In the second article[4]) will be found details on the beam current integration and measurement.

[1]) W. Maas, Thesis, Utrecht (1948).

[2]) Veenstra, Jongerius, Paris and Valckx, Physica **18** (1952) 378.

[3]) C. H. Paris, Thesis, Utrecht (1955).

[4]) P. J. M. Smulders and P. B. Smith, Nucl. Instr. & Meth. **8** (1960) 40.

[5]) K. T. Bainbridge, Part V, Experimental nuclear physics, editor E. Segrè (John Wiley and Sons, Inc., New York, 1953).

## 2. The Deflection Magnet

In the following the characteristics of the magnet and its design considerations will be discussed.

### 2.1. FOCUSSING OF TRAJECTORIES IN THE CENTRAL PLANE

The first-order focal properties of uniform-field sector magnets have been reviewed by Bainbridge[5]). The conditions for stigmatic focussing were first obtained by Cross[6]), and have been worked out in more detail by one of us[7]). We will here summarize some points which are relevant to the construction of the present beam analyzer. Our notation is illustrated in fig. 1. The plane which lies halfway between the parallel pole faces is called the central plane. One of the rays passing through the centers of the entrance- and the exit-slit is called the central ray, and we assume that all other rays make small angles with this central ray. Since the divergence of the incoming beam is small and its direction well determined, the

[6]) W. Cross, Rev. Sci. Instr. **22** (1951) 717.

[7]) C. M. Braams, Thesis, Utrecht (1956).

aperture, $2\alpha$, of the analyzer is made so small that we can neglect aberrations of second- and higher order in $\alpha$ and will treat only first-order focussing conditions. We also neglect effects of higher order in the quantities $s'/r$ and $s''/r$, where $s'$ and $s''$ are the entrance- and exit-slit openings.

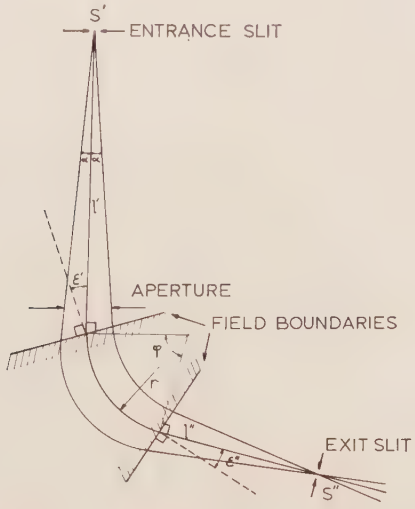


Fig. 1. Schematic representation of deflection magnet, illustrating notation used.

We further use the approximation that the field is uniform within sharp boundaries and zero outside. The entrance- and exit-slits are located at distances $l'$ and $l''$ from the field boundaries; the normals to the field boundaries at the points of entrance and exit make angles $\varepsilon'$ and $\varepsilon''$ with the central ray; in fig. 1 are indicated the directions in which $\varepsilon'$ and $\varepsilon''$ are defined as positive. We call $\tan\varepsilon' = a'$ and $\tan\varepsilon'' = a''$. The radius of curvature of the central ray is $r$ and the angle of deflection, $\varphi$.

If $\varepsilon' = \varepsilon'' = 0$, i.e., if the field boundaries are perpendicular to the central trajectory at the points of entrance and exit, the condition for the focussing of monoenergetic particles from the entrance slit on the exit slit is expressed by Barber's rule:

$$\tan\varphi = \frac{m' + m''}{r^2 - m'm''}, \tag{1}$$

or, with $\varphi = \frac{1}{2}\pi$:

$$m'm'' = r^2, \tag{1a}$$

where, for normal field boundaries, $m' = l'$ and $m'' = l''$. If $\varepsilon'$ and $\varepsilon'' \neq 0$, i.e. for oblique field boundaries, eqs. (1) and (1a) are satisfied by virtual source and image distances, $m'$ and $m''$, related to the true source and image distances, $l'$ and $l''$, by the thin-lens formulae

$$\frac{1}{l'} - \frac{1}{m'} = -\frac{a'}{r} \quad \text{and} \quad \frac{1}{l''} - \frac{1}{m''} = -\frac{a''}{r}. \tag{2}$$

From (1) and (2) the condition for focussing follows:

$$\tan\varphi = \frac{l'(a''l'' + r) + l''(a'l' + r)}{(a'l' + r)(a''l'' + r) - l'l''} \tag{3}$$

which, for $\varphi = \frac{1}{2}\pi$, reduces to

$$\left(a' + \frac{r}{l'}\right)\left(a'' + \frac{r}{l''}\right) = 1. \tag{3a}$$

In what follows we will assume that eq. (3a) is satisfied, i.e., that the slits are located in such a way that monoenergetic particles from a point of the entrance slit are focussed in a point of the exit slit.

If we define the dispersion, $D''$, as the distance between the central ray with radius of curvature $r + \Delta r$ and the focus for rays with radius $r$, divided by $\Delta r$, this quantity is given by

$$D'' = (l''/r)(\sin\varphi + a'' - a''\cos\varphi) + 1 - \cos\varphi \tag{4}$$

or, if $\varphi = \frac{1}{2}\pi$,

$$D'' = (l''/r)(1 + a'') + 1. \tag{4a}$$

Similarly, we can define a quantity $D'$, which we call the resolution factor, by changing double primes into primes in eqs. (4) and (4a). The total relative momentum spread of particles passing through entrance and exit slits of widths $s'$ and $s''$ is then given by

$$\frac{\Delta r}{r} = \frac{s'}{D'r} + \frac{s''}{D''r}. \tag{5}$$

A beam analyzer often serves both to collimate the beam and to select the particle momentum. This implies that the entrance slit is fully illuminated by the incoming beam, and that the momentum spread in the unanalyzed beam is greater than that selected by the analyzer. Under these conditions, the intensity of the analyzed beam is proportional to $s's''/D''$,

which for a given analyzer and a given maximum energy spread, i.e., if only $s'$ and $s''$ are variable, is at a maximum if $s'/D' = s''/D'' = \frac{1}{2}\Delta r$. At this maximum, $s's''/D'' = \frac{1}{4}D'r^2\,(\Delta r/r)^2$, which shows that under the conditions stated above, it is advantageous to choose a design in which $D'$ and $r$ are as large as possible. The design of an analyzer will generally be governed by many, perhaps conflicting, considerations, and no general rules can be given which are valid under all conditions and for all experimental requirements. We feel, however, that in most applications the value of the resolution factor, $D'$, rather than that of the dispersion, $D''$, is decisive for the performance of our analyzer. The quantities $D'$ and $D''$ are related to the image magnification, $M$, by the equation: $M = D''/D'$.

By changing double primes into primes in eq. (4a), one sees that $D'$ increases with $l'/r$ and with $a'$.

### 2.2. TWO-DIRECTIONAL FOCUSSING

In section 2.1, we have required without further justification that monoenergetic particles whose trajectories lie in the central plane must produce an image of the entrance slit on the exit slit. The reason is, of course, that this is the condition under which the momenta of the selected rays are independent of their directions. Since the analyzer has no dispersion in the perpendicular, or $Z$-direction, this does not imply that it should also bring particles whose trajectories make different angles with the central plane to a focus. We have considered three possible requirements with respect to focussing in the $Z$-direction: a parallel incoming beam may be required to produce either a parallel outgoing beam or a focus at the exit slit, or a source at the entrance slit may be required to be focussed on the exit slit. The first two alternatives may be chosen if the incoming beam is nearly parallel; the last one must be considered if the beam from the accelerator can be focussed on the entrance slit. The present analyzer was designed to produce a stigmatic image of the entrance slit on the exit slit.

Deflection in the $Z$-direction occurs in the fringing field unless the beam enters and leaves the magnetic field along lines prependicular to the field boundaries. The effect can again be described by thin-lens formulae, stating that $Z$-deflection occurs in lenses with focal lengths $r/a'$ and $r/a''$, placed at the points of entrance and exit, respectively. We note that these lenses have the same absolute strengths, but opposite signs as those which, according to eq. (2), describe the effect of oblique field boundaries on the focussing in the central plane. Hence, oblique boundaries act very much like quadrupole lenses. An advantage of the latter is that one has more freedom in choosing their location and strength; a disadvantage, however, that special care is required to assure that their field strength varies proportionally with that in the main magnet, independent of hysteresis and saturation.

Applying the above-mentioned thin-lens formulae, one finds the following relation between the source distance $l'$ and the distance $L''$, at

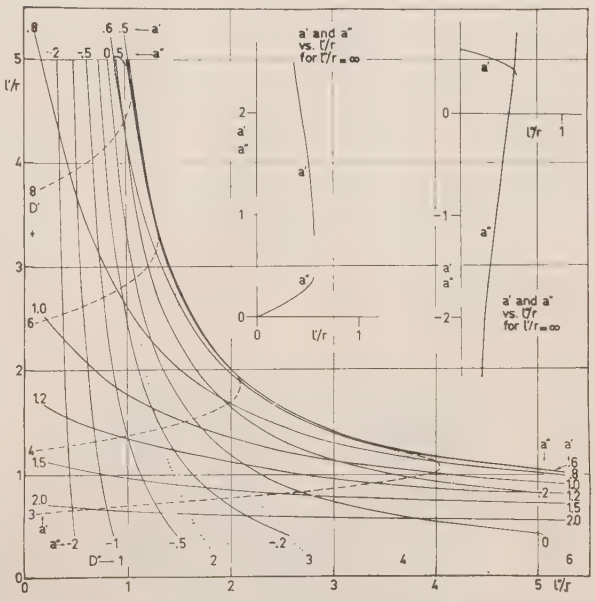


Fig. 2. The focussing condition presented as a family of curves of object distance ($l'/r$) against image distance ($l''/r$) for various values of the angles between the normals to the field boundaries and the beam (central ray). The radius of curvature of the central ray is given by $r$. For the entering beam this angle is given by $\varepsilon' = \tan^{-1}a'$, and for the beam at the exit the single primes are replaced by double primes.

which particles with different velocity components in the $Z$-direction come to a focus:

$$\frac{1}{a' - r/l'} + \frac{1}{a'' - r/L''} = \qquad (6)$$

or, for 90-degree deflection:

$$\frac{1}{a' - r/l'} + \frac{1}{a'' - r/L''} = \tfrac{1}{2}\pi . \qquad (6a)$$

The condition for stigmatic focussing with a 90-degree deflector is obtained by putting $L'' = l''$ in eq. (6a) and combining it with eq. (3a).

In fig. 2 are shown graphs of $l'/r$ vs $l''/r$ with $a'$ and $a''$ as parameters. The asymptotic values are plotted in the inserts marked $l'/r = \infty$ and $l''/r = \infty$. This figure is not complete in that curves for $a' < 0.5$ and $a'' > 0.5$ are omitted, while the curves $a' = 0.5$ and $a'' = 0.5$ are only drawn to the left of the point $l'/r = l''/r = 2$, where they touch the envelope. The figure is completed by reflecting it in the line $l' = l''$ and interchanging primes and double primes. We then obtain two sets of values of $a'$ and $a''$ for every allowed combination of $l'$ and $l''$.

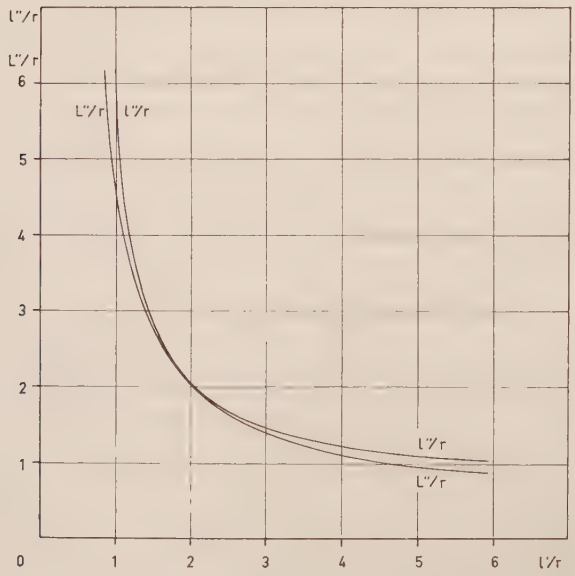


Fig. 3. The image distance in the central plane ($l''/r$) and in the $Z$-direction ($L''/r$) as a function of object distance ($l'/r$) for the choice of $a' = a'' = 0.5$ used in the design of our magnet. As can be seen the focussing is stigmatic over a relatively large range of values of the object distance.

Dashed and dotted lines in fig. 2 indicate values of $D'$ and $D''$, respectively.

It is interesting to note that the curves for $a' = 0.5$ and $a'' = 0.5$ run very close together. This suggests that it is possible to obtain approximately stigmatic focussing over a wide range of values of $l'$ and $l''$ by choosing $a' = a'' = 0.5$. This is borne out by a comparison between the astigmatic image distances $l''$ and $L''$ as functions of $l'$, shown in fig. 3. Since moderate deviations from correct $Z$-focussing do not affect the performance of the analyzer, we have chosen oblique field boundaries with $a' = a'' = 0.5$ for our instrument. This leaves appreciable freedom in the choice of $l'$ and $l''$ without necessitating the use of adjustable elements, such as a quadrupole lens or semicircular blocks, inserted in the pole faces at the points of entrance and exit.

### 2.3. DESIGN OF MAGNET AND SLIT SYSTEM

Because of space limitations and also for economy, the analyzer was made as compact as was compatible with the requirement that it should be able to bend a one-MeV beam of singly charged ions of mass number four, which has a momentum of 290 kilogauss-cm. The radius of curvature was, therefore, chosen to be 20 cm. The energy-defining slits were placed at $l' = l'' = 40$ cm; this is a compromise between the requirements that the exit slit and the target, on one hand, be placed as far as possible from the magnet to make room for measuring equipment around the target, and that the entrance slit, on the other hand, be placed at the largest possible value of $l'$, in order to obtain the best possible energy resolution.

The shape of the magnet is shown in fig. 4. The yoke was machined from forged Armco iron and annealed in an inert atmosphere before the final grinding of precision surfaces. The two coils each consist of 1000 turns of 1.5 mm round copper wire, wound on 3 mm thick copper bobbins with 3 mm i.d. copper tubing soldered to the side plates for water cooling. Copper foil of 0.1 mm thickness was wound between successive layers of winding to improve heat conduction from the interior of the coil to the side

plates. The field in the 16 mm wide air gap is 1500 gauss per ampère up to about 10 A; the

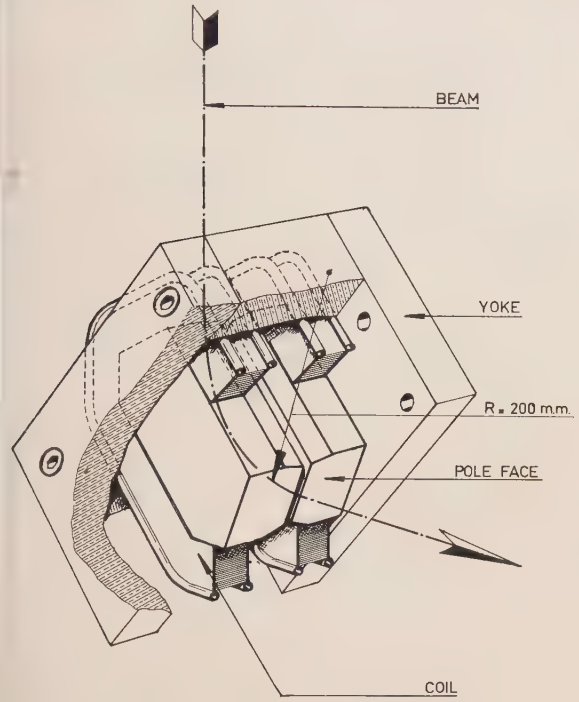


Fig. 4. Cutaway drawing of the magnet construction. See section 2.3 of the text.

coils have run continuously with a current of 12 A, which corresponds to a current density of 3.0 A/mm² averaged throughout the whole cross section of the coil, or 6.8 A/mm² in the windings.

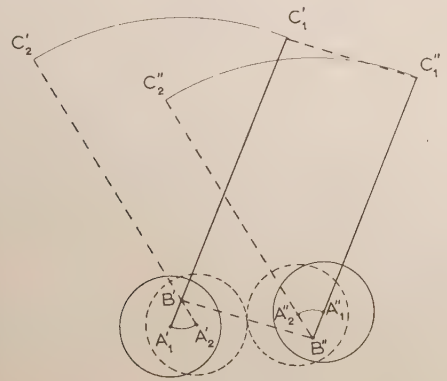


Fig. 5
Operation of the slit system. See section 2.3 of the text.

The design of the pole faces was based on the estimate that the deflection in the fringing field

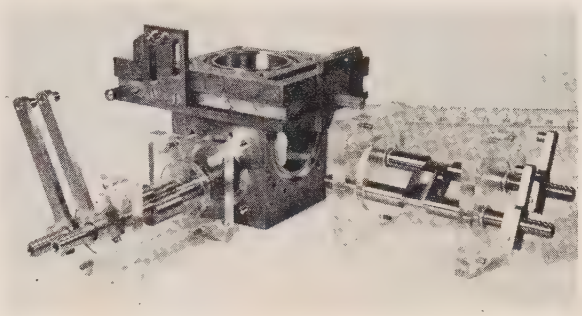

Fig. 6. Photograph of dismounted slit box.

can be accounted for by assuming the uniform field to drop sharply to zero at a boundary lying one gap width outside the pole-face edges. No detailed investigation of the validity of this procedure was made, but provisions have been made for adjusting the position of the slit system with respect to the magnet in case that the focussing should prove to be incorrect.

The slits consist of pairs of cylindrical jaws, which extend into hollow, liquid-cooled shafts, parallel to the cylindrical surfaces. Rotation of the shafts results in a displacement of the excentric jaws and, hence, opens or closes the slits. The operation is shown schematically in fig. 5, which represents a cross section through the slit jaws. The axes of the jaws pass through A′ and A″, the axes of rotation, through B′ and B″. The lever arms B′C′ and B″C″ are of equal lengths and the points C′ and C″ are constrained to move together, the distance C′C″ remaining equal to B′B″. The horizontal projection of the

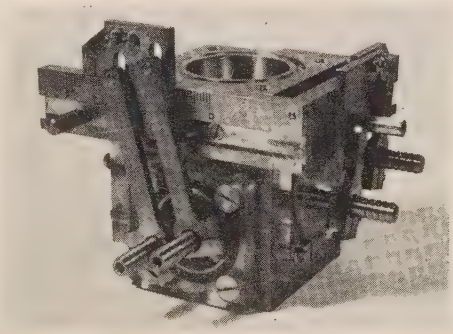

Fig. 7. Photograph of mounted slit box.

displacement of C′ and C″ is proportional to the corresponding variation in the slit opening, as

seen by a vertical beem. This construction also makes the slits open and close symmetrically. The jaws are mounted in lucite plates so that the beam current to each one can be measured or used to stabilize the accelerator voltage. Vacuum seals are made by rubber "o"-rings. An assembly of two perpendicular slits is shown in figs. 6 and 7; the energy-defining slit has a maximum opening of 5 mm and is adjustable with an accuracy of 0.1 mm, while the slit which opens in the $Z$-direction has a maximum opening of 10 mm, and is adjustable with an accuracy of 0.5 mm. It follows from eq. (5), that the relative energy spread (full width at half maximum), $\Delta E/E = 2\Delta r/r = (s' + s'')/800$, where $s'$ and $s''$ are the entrance and exit slit openings, measured in mm. The slit jaws were originally made of stainless steel. This proved to be a mistake since the accelerator beam melted them very quickly. After the stainless steel was replaced by silver no further trouble has been found from this source even when sharply focussed 800 keV beams approaching one mA are used.

### 2.4. ADJUSTMENTS

The following adjustments of the positions of the slit systems with respect to the magnet are possible (fig. 8):

1. each one of the two blocks holding a slit assembly can be rotated slightly about the direction of the beam, so that the energy-defining slits can be placed perpendicular to the central plane;

2. each one can be moved in the $Z$-direction, so that the center of the slit system can be adjusted to lie in the central plane;

3. the whole frame holding the two slit systems can be moved in the direction of the line in the central plane bisecting the angle between the field boundaries, so that the ratios $l'/r$ and $l''/r$ can be varied simultaneously in the same sense to make them satisfy the focussing condition of eq. (3a);

4. the frame can be rotated about an axis, perpendicular to the central plane and going through the intersection of the lines perpendicular to the field boundaries at the points of entrance and exit, so that the angle of deflection can be adjusted, without the calibration or the focussing being affected.

The first two possibilities for adjustment need little comment except, perhaps, that they are only necessary for one block but were put in for both to preserve symmetry. The third one was necessary because the uncertainty in the fall-off of the field strength near the pole-edge made it impossible to predict with accuracy where the slits should be located for focussing. This adjustment alters the radius of curvature which, however, has to be determined by a calibration, anyhow. The fourth, finally, was put in mainly to make it possible to adjust the direction of the analyzed beam within the central plane without change of calibration or focussing. This is illustrated in fig. 9 where $P_1$ and $Q_1$ are one set of positions of the entrance and the exit slit, and $P_2$ and $Q_2$, another. The center about which the assembly is rotated is C, and the angle of rotation is $\beta$. The point C is chosen so, that by this rotation the ray $r_1$ transforms into the congruent ray $r_2$. Hence, if we consider $r_1$ and $r_2$ as the central rays for the two situations, the rotation leaves $l'$, $r$, and $l''$ unchaged. The angles of entrance and exit, however, change by opposite amounts, but it is seen from eq. (3a) that this does not affect the focussing. The ray $r_3$, which enters through $P_2$ in a direction parallel to $r_1$, therefore leaves through $Q_2$, and it is seen from fig. 9 that it does this under an angle $2\beta$ with $r_1$, except for terms of higher order in $\beta$.

The whole assembly of the magnet with its slit system can be moved in the following ways:

5. the analyzer can rotate about a vertical axis, which makes the analyzed beam swing in the horizontal plane;

6. the position of the analyzer on the turntable can be adjusted in two perpendicular horizontal directions to make the entrance slit lie on the axis of rotation;

7. the position of the turntable can be adjusted in two perpendicular horizontal directions to make the beam from the accelerator pass through the entrance slit;

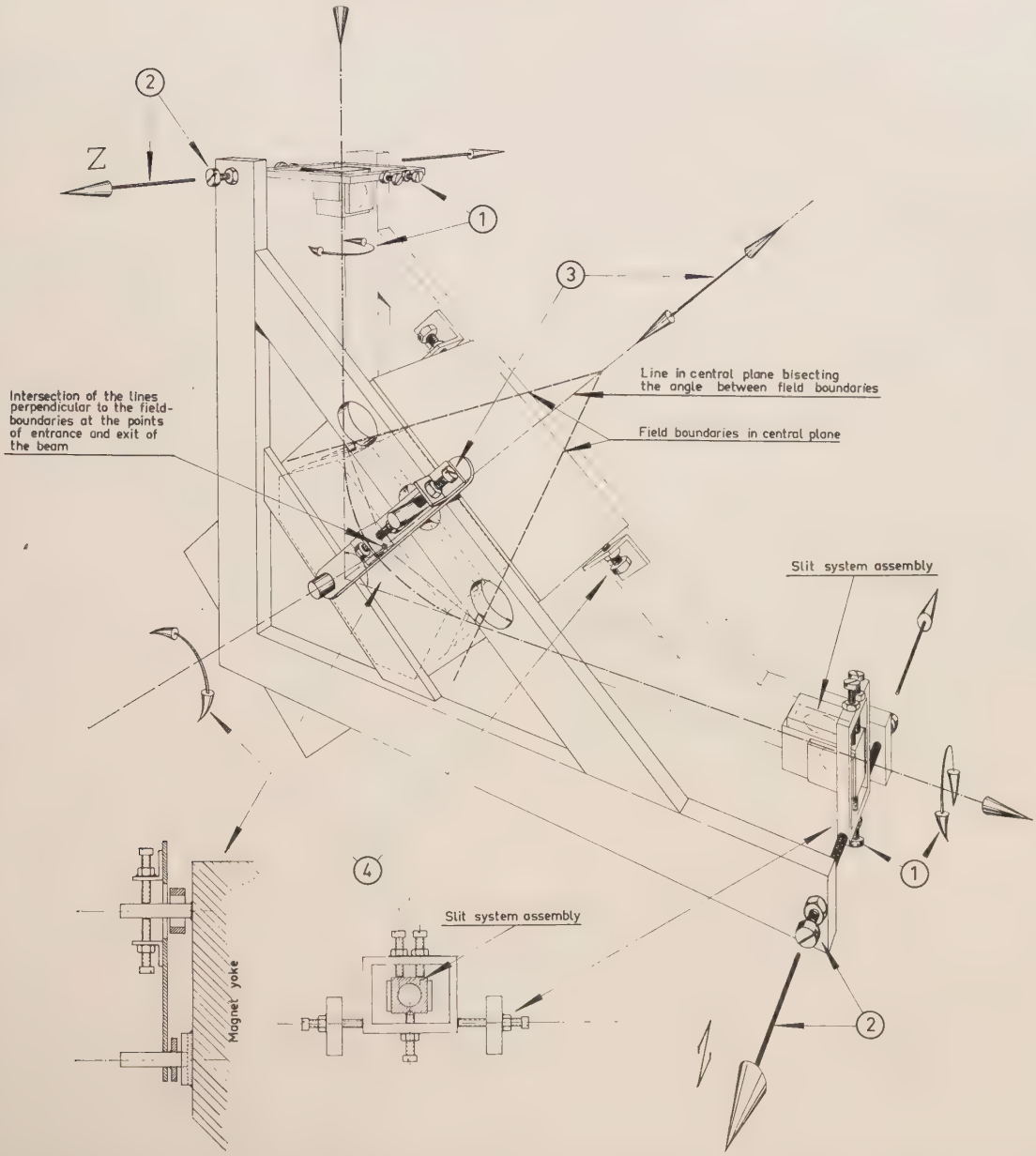
Z
Intersection of the lines perpendicular to the field-boundaries at the points of entrance and exit of the beam
Line in central plane bisecting the angle between field boundaries
Field boundaries in central plane
Slit system assembly
Slit system assembly
Magnet yoke

Fig. 8. Representation of the various adjustments possible of the slits with respect to the magnet. See section 2.4 of the text.

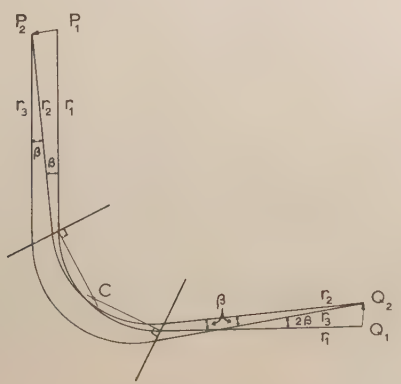


Fig. 9. Representation of the turning of rays in the central plane as a result of the fourth motion possibility discussed in section 2.4 of the text.

8. the turntable rests on four screws, by which the axis of rotation can be set vertical.

A very simple and compact design of the turntable with its horizontal adjustments was obtained by making use of a commercial ball race with ground flat end-surfaces on which the sliding motions (6 and 7) occur.

## 3. The Control System

The present control system, while not original in principle does not seem to have been applied previously to machines of this type, despite the obvious advantage that it presents of delivering to the target monoenergetic ions whose energy is determined by one control knob. The occasion for the development of this system was the conversion of the Utrecht cascade generator from 50 Hz to 500 Hz in the summer of 1957. Previously the ripple on the high tension had been so large (up to 1% at the highest tension) that no practical advantage would have accrued from stabilization.

### 3.1. PRINCIPLES OF THE CONTROL SYSTEM

A block diagram of the control system is shown in fig. 10. The fundamental comparison voltage is derived from two mercury cells. This is compared to the voltage developed across a mixed, providing, in principle, an ideal integral-plus-proportional controller with no zero setting and essentially infinite zero-frequency gain. This combined output is used to control the field of the dc generator which supplies the main magnet current.

The magnetic field is, of course, not a unique function of the current in the exciting coils. The field varies extemely slowly, however, if this current is maintained constant. The field is measured by a continuous reading nuclear magnetic resonance fluxmeter. Usually the frequency of the fluxmeter is set to the desired value and the magnet current varied so as to centre the absorption dip on a sweep variable in amplitude from zero to about 10 gauss. The field variations encountered are those to be expected in such a system; the long-term stability is within one part in 20 000 for many hours, but the inadequate band-pass of the generator

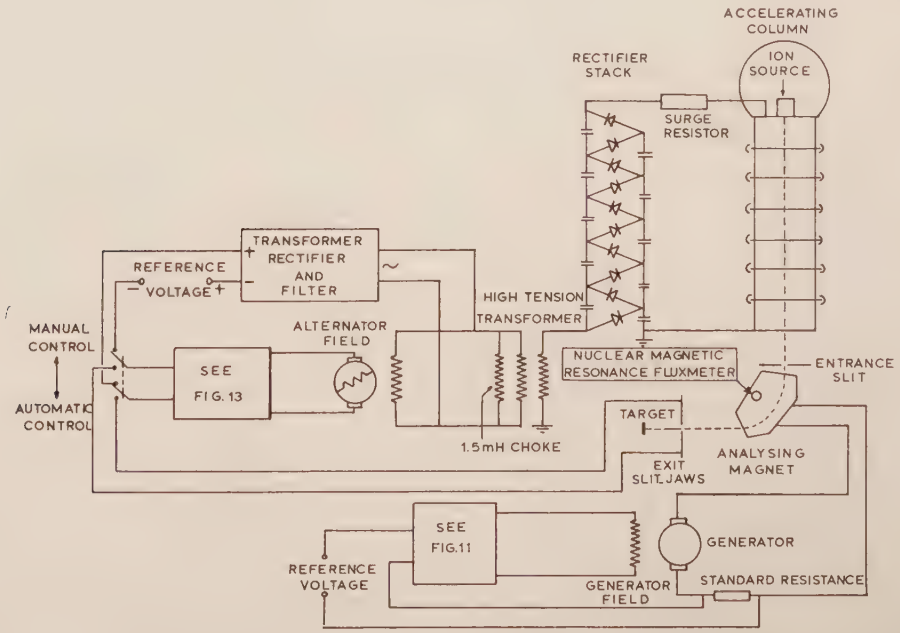


Fig. 10. Block diagram of the complete control and stabilization system of the cascade generator.

standard resistance by the magnet current. The error signal is impressed upon the inputs of two amplifiers in parallel, one an ordinary dc balanced amplifier, and the other a commercial "chopper" type amplifier driving a two-phase motor. The outputs of these two amplifiers are additively permits the occurence of high frequency fluctuations of about one part in 5 000 (average value) most of which are caused by the generator itself.

A 200 V, 500 Hz, alternator powers the primary of the high-tension transformer of the

cascade generator. The multiplier components, surge resistor, and accelerating tube were not modified during the frequency conversion. The transformer had to be replaced, of course. The new transformer was designed and constructed by N.V. Philips Gloeilampenfabrieken, constructors of the original machine. The large negative reactance reflected into the primary by the multiplying circuit load is partially cancelled by a 1.5 mH air-cored inductance designed and constructed by the Electronics Dept. of the Utrecht Physics Laboratory.

The high tension is controlled by the differential signal developed between the insulated magnet exit slit jaws by the impinging beam. This signal is heavily compensated and then used to control the field of the above mentioned alternator. With this arrangement the beam is controlled by the magnet current, making for extreme simplicity of operation. Alternative manual control of high tension is provided to permit "finding" the beam. Once the beam is through the slits, the high tension may be varied over its entire range by merely changing the magnet current. The system gain is high enough so that no zero setting is necessary, the beam always being at least as great as is obtainable by manual control, and usually greater.

### 3.2. THE MAGNET CURRENT STABILIZER

The stabilization principle used here is that of paralleling an integrator and an amplifier. In this section it will be shown that analysis of such systems is quite easy, and that a criterion may be found which permits rapid determination of the required gain of the dc amplifier before additive mixing.

The circuit diagram is shown in fig. 11. The analysis is carried out in the complex-frequency ($s$-) plane. In fig. 11 the transfer functions appropriate to each section of the system are indicated. The additive mixing is accomplished in such a way that, at least to first order, the transmission of each block is unaffected by signal in the other block. Thus the transfer function of the combined amplifiers from the error signal input to the grids marked A and B is given quite accurately by $(A_1 + p_B p_0/s(s+p_0))$. The open-loop pole-zero configuration is shown for the system with $A_1 = 0$, in fig. 12(a). For reasonable values of overall gain the system is unstable, as can be seen by the early crossing of the imaginary axis by the loci of the principal roots of the closed system response.

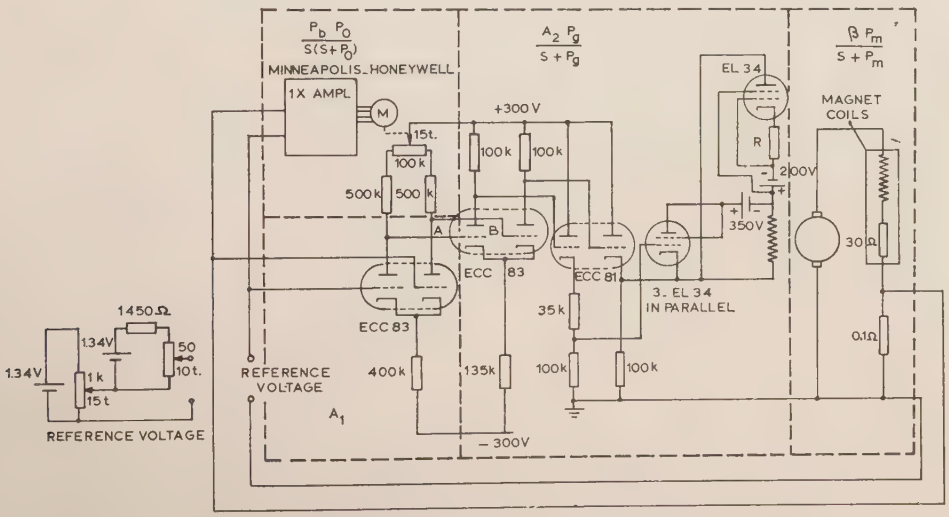


Fig. 11. Circuit diagram of the stabilization circuit of the deflection magnet.

In fig. 12(b) the pole-zero configuration and root loci are shown of the system with $A_1 \neq 0$. It can be seen that for high gain the system is stable due to the two complex zeros arising

from the parallel combination of the two types of amplifiers. Under these conditions the closed loop poles are given approximately by the triangles in fig. 12(b). It can be seen that the

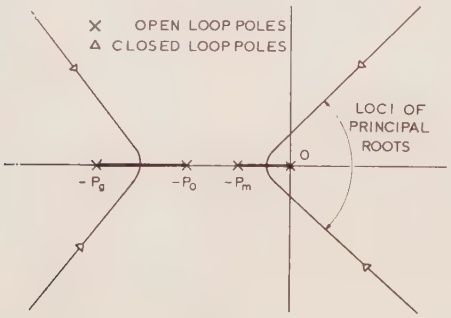


Fig. 12(a). Root loci of the stabilization circuit of the deflection magnet for the case of zero gain of the fast (direct-coupled) amplifier.

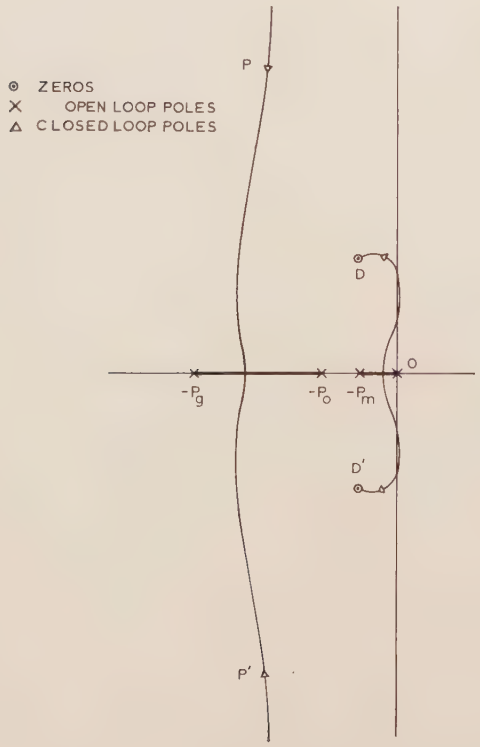


Fig. 12(b). The root loci of the system for $A_1 \neq 0$.

response is governed principally by the high frequency complex conjugate poles P and P'. The dipoles D and D' are quite weak for very high gain, and, although of low frequency, contribute very little to the response of the system (they are, of course, responsible for the high precision). Caution must be exercised in the choice of values of $A_1$, $p_0$, and $p_B$, however. This can be seen by considering the position of the complex zeros as a function of these variables. They are found at $\frac{1}{2}p_0\,(-1 \pm j\sqrt{\gamma - 1})$ where $\gamma = 4p_B/A_1p_0$. It can be seen from the sketch in fig. 12(b) that for any values of the parameters the system is stable for very high gain. However, if the imaginary part of the coordinates of zeros is too large, the root loci will go very far into the right half-plane before returning to the zeros. This results in a conditionally stable system which may break into sustained oscillation if a temporary overload drives the system into a region where one or more elements become saturated, thus lowering the gain so that the right-hand poles move into the right half of the plane. It is probable that a similar system described by Havill and Rubins[8]) displays this type of behaviour. In their case, $A_1 = 1$ which will result in complex zeros located very far from the real axis for usual values of $p_B$ and $p_0$.

In view of the above consideration, measurements of $p_B$ and $p_0$ were made on the integrator used, before the circuit was designed. The quantity $\gamma = 4p_B/A_1p_0$ was made equal to approximately ten, resulting in the configuration sketched in fig. 12(b). For high gain the response is apparently quite independent of the value of $\gamma$, but a more realistic analysis shows this not to be strictly true. The reason that $\gamma$ cannot be made very small is that the integrator corrects for drifts and low frequency flutter noise at the grid of the first amplifier tube. If $A_1$ is made too large this drift overcomes the correcting capacity of the integrator, and furthermore, the amplifier can drift out of its correct operating range or the limit of the range of correction afforded by the integrator.

Thus a correct compromise must be found for a given case. Fortunately $\gamma$ can be arbitrarily varied over an enormous range by changing the amplification of the amplifier ($A_1$) or the gear reduction factor of the integrator ($p_B$). The

[8]) J. R. Havill and S. Rubin, Rev. Sci. Instr. **26** (1955) 515 (N).

behaviour of a correctly designed system is seen to depend principally on the location of the poles P and P′, and to a much lesser extent on the weak dipoles D and D′. In other words this system retains fully the advantages of speed and stability of a simple dc feedback amplifier, while possessing the precision of a chopper type integrating feedback system.

The weak point in the system is the generator. The ripple and noise introduced by this source could be corrected by static or dynamic filters applied to the output. Several such circuits have been described. In this case, however, it would have been better to use direct feed by vacuum tubes or transistors†, since the power consumption is not excessive (less than 5 kW). The generator was used in the present circuit because it already existed when the design was started. The magnetic field variations observed

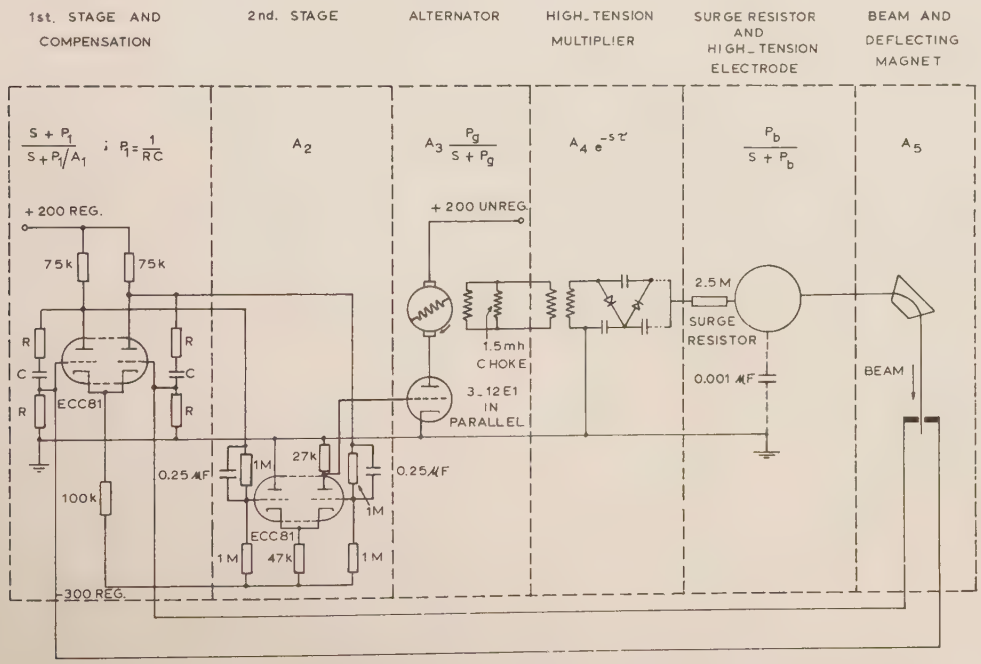


Fig. 13. Circuit of high-tension stabilizer.

are a factor of five less than the minimum instrumental width utilizable with the cascade generator, and so cause no inconvenience. For that reason no filters (of the types mentioned above) were tried.

### 3.3. THE HIGH-TENSION STABILIZER

As can be seen from fig. 10, the high tension stabilizer can be operated in two completely diverse manners. The manual control requires no special discussion since the circuit is stable for practically any value of gain. The high tension itself is seen not to be stabilized by this mode of control. In practice it is therefore used only in putting the generator into operation. The automatic control mode would be unstable with any reasonable value of gain and so a discussion is given of the compensation used.

The circuit of the high-tension stabilizer is shown in fig. 13. Only the automatic control mode is shown. The various transfer functions are indicated. It is to be noted that the transfer function of the high-tension rectifier stack is treated as a pure time delay of $\frac{1}{2}$ of one cycle, that is 0.001 sec ($\tau$). This approximation is valid for either increasing or decreasing voltage providing the load is adequate. For small load,

† Such a system has since been built at this laboratory for the deflection magnet of the 3 MeV Utrecht Van de Graaff generator. As expected, it shows neither long nor short term fluctuations greater than one part in 25 000.

or large, rapid, changes it ceases to be valid for falling voltage. From the point of view of stability only small changes are usually of importance, however. The generator field time-constant ($1/p_g$) is about 1 sec, and there is also a $2\frac{1}{2}$ millisecond time constant ($1/p_B$) formed by the surge resistor and high-tension electrode capacity.

The various factors shown in fig. 13 are self-explanatory except for $A_5$, the effective amplification factor of the beam. This is the relationship between the change of the high tension and the voltage caused thereby on the slit jaws, through the deflecting action of the magnet. This factor may differ by several orders of magnitude under different circumstances and for this reason the effective resistance to ground of the slit jaws can be changed by the operator to suit conditions.

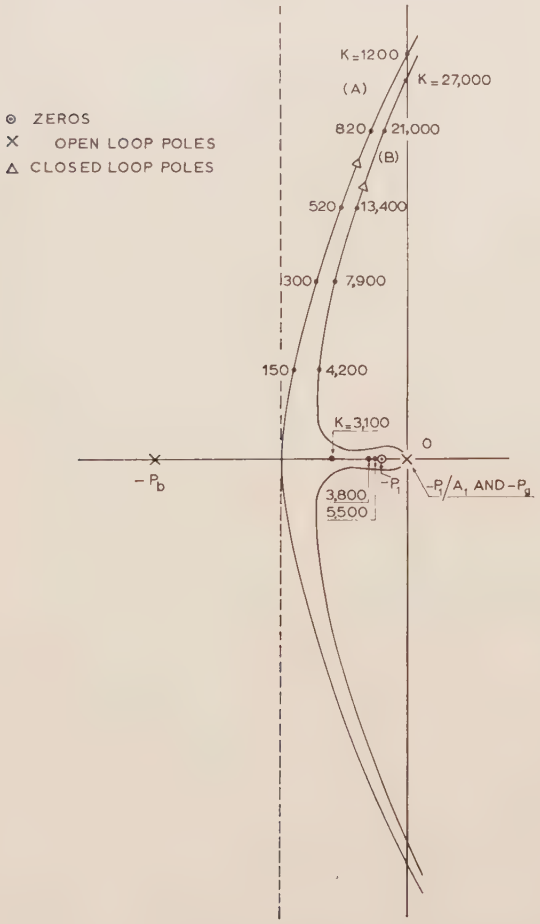


Fig. 14 Root loci for the uncompensated (A) and compensated (B) system.

In order to describe the theory of the circuit, a value of $A_5$ must be specified. In the discussion that follows a typical value will be assumed, which renders the zero-frequency loop gain equal to $10^4$. This loop gain ($K$) is given by the product $A_1A_2A_3A_4A_5$. For a value of $K = 10^4$ the expected deviation of the beam from the center of the exit slit is negligible in comparison with the slit width and the machine ripple.

In fig. 14 the root loci are shown for the uncompensated system (A) (with the condensers, C, removed) and for the complete system (B). Without the time-lag factor $e^{-s\tau}$, the uncompensated root loci would be given by the dashed line. This factor contributes phase-shift which limits the usable gain.

The necessity for the compensation is obvious from an examination of the values of $K$ indicated on the compensated and uncompensated loci. On the scale of fig. 14 it is not possible to show the relative locations of the poles closest to the imaginary axis. These positions and the exact loci in this region are not important, however. For high gain the loci of the principal roots are essentially unmodified by the compensator, the value of $K$ being simply multiplied by $A_1$ at any given point as a result of the compensation. The values of $K$ indicated on the negative real axis refer to the position of the extra root introduced by the compensation. For $K = 10^4$ this root forms a weak dipole together with the zero at $-p_1$.

Two further details deserve mention. The first is that a provision (not shown) is also made for automatic switching in and out of the control circuit by the beam itself. Circuits to accomplish this are simple to incorporate in the design but should be adapted to conditions likely to be met in the operation of a given machine. Secondly, two phase-lead condensers were incorporated in the coupling networks between the two stages of voltage amplification (fig. 13). These are not strictly necessary (nor very effective) but do produce a desirable effect of speed-up, at least in the manual control mode.

3.4. PERFORMANCE

The magnet, magnet current stabilizer, and high-tension stabilizer have been in operation of

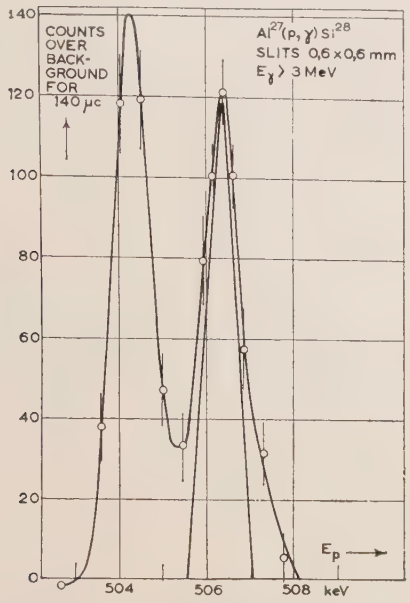


Fig. 15

Gamma-ray yield curve taken with the system described in this article. The reaction under study was $Al^{27}(p,\gamma)Si^{28}$ at the 504–506 keV doublet. See section 3.4 of the text.

a period of more than one year. The most difficult resolution problem encountered in this interval was the study of the 504–506 keV doublet in the $Al^{27}$ (p,$\gamma$) reaction. In fig. 15 is shown the yield curve obtained at the time the upper of the two resonances was under study. The triangular resolution curve drawn underneath this resonance is the predicted shape of the yield curve for the slit opening used (0.75 mm) (see section 2.3). The extra width observed is accounted for by the target thickness of several hundred eV (the precise value was not determined). At this slit opening a beam of approximately 2 $\mu$A is available on the target located 40 cm beyond the exit slits of the magnet.

**Acknowledgements**

This investigation is part of the research program of the "Stichting voor Fundamenteel Onderzoek der Materie", and was made possible by financial support from the "Nederlandse Organisatie voor Zuiver Wetenschappelijk Onderzoek".

The authors wish to acknowledge the help and encouragement of their colleagues Prof. Dr. P. M. Endt and Dr. A. M. Hoogenboom. The magnet was constructed in the workshop of the Utrecht Physical Laboratory by Mr. F. A. Meeuwissen, and the stabilization circuits by Mr. A. Veenenbos.

NUCLEAR INSTRUMENTS AND METHODS 8 (1960) 40–45; NORTH-HOLLAND PUBLISHING CO.

# THE UTRECHT 850 kV CASCADE GENERATOR

## II. THE BEAM INTEGRATOR AND GALVANOMETER

P. J. M. SMULDERS and P. B. SMITH

*Fysisch Laboratorium der Rijksuniversiteit te Utrecht, Nederland*

Received 9 March 1960

A current integrator is described for the integration of currents from 0.01 to 500 $\mu$A with an accuracy of 0.1%. The principle used is essentially the same as that of the excellent circuit described earlier by Helmer and Hemmendinger. The modifications effected result in a considerable reduction in expense, as well as a lower input impedance. Due to increased high frequency gain much smaller condensers are necessary in order to maintain the input voltage within some hundredths of a volt of ground, at all times. The integrated current is measured as the number of output pulses, each pulse representing a fixed amount of charge. Except for the condensers, no special components are used. A low-impedance electronic galvanometer for operation in series with this integrator is also described. This circuit combines the advantages of imperceptible zero drift, fixed calibration, and essentially absolute protection against burn-out.

## 1. The Current Integrator

In section 1 follows a description of the new current integrator as well as a short discussion (section 1.1) of the motives underlying its development.

### 1.1. INTRODUCTION

In recent years great progress has been made in constructing current integrators, combining the qualities of accuracy (accurately quantized charge removal), low input impedance and high switching rate[1,2]). To date, the instrument which best satisfies these requirements is that of Helmer and Hemmendinger. These authors utilize a vibrating reed electrometer to detect input error. The removal of charge is accomplished in their circuit by a reversing condenser connected between the input and a precision voltage, the reversing rate being controlled by a variable frequency multivibrator. In addition the feedback connection of the vibrating reed electrometer is connected to the input through a condenser, thus lowering the input impedance. In the description of the circuit the suggestion is made that it should be possible to build a similar integrator without the use of such an expensive device as the vibrating reed electrometer. The present integrator is the direct result of this suggestion. It is felt that it is worth while to report upon the results obtained since an extremely accurate, wide-range instrument has been built at very low cost. Furthermore an improvement has been effected over the original circuit by feeding back with a low enough impedance and a high enough high-frequency gain, so that the input is maintained virtually at ground even during the switching pulses. Since the feedback condenser is effectively increased by the gain of the amplifier it is possible to use switching condensers one-fourth or one-fifth of the feedback condenser (in comparison with 1/600 in the circuit of Helmer and Hemmendinger). This has permitted an increase of the current range to fifteen times that of the original circuit, although using smaller condensers.

[1]) R. J. Helmer and A. Hemmendinger, Rev. Sci. Instr. **28** (1957) 649.

[2]) I. A. D. Lewis and B. Collinge, Rev. Sci. Instr. **24** (1953) 1113.

### 1.2. PRINCIPLE

The principle of operation may be seen from fig. 1. The beam current enters at the input of a two-stage direct-coupled balanced amplifier with

negative feedback condenser $C_2$. This feedback holds the input close to ground potential while the output voltage is $e_2 \approx -1/C_2 \int i\,dt$. When this voltage reaches the trigger level a pulse goes to the scale of two and the relay is closed or opened, which results in a reversal of the condenser $C_1$. By this action a charge $2BC_1$, where $B$ is a precision reference voltage, is removed from the input. Thus the output raises by about $2BC_1/C_2$, and the trigger flips back to its original position. Meanwhile, the beam current goes on charging $C_2$ and the process described is repeated when the trigger level is reached again. The trigger pulses are also fed to a scaler. If the number of pulses is $n$, the integral of the current is $2nBC_1$.

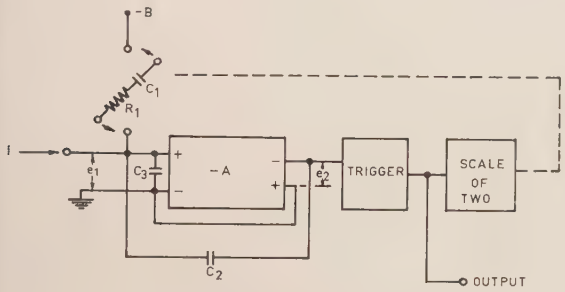


Fig. 1. Block diagram of the integrator.

The resistor $R_1$ in series with $C_1$ limits the current flow during the switching to a value low enough that the amplifier may cope with it. The condenser $C_3$ is necessary only in order to handle the surge of current before the amplifier has had time to act. Its value is not critical, and the charge flowing into it is very small compared to that flowing into $C_2$. The precision with which the output is given by the integral of the input, depends upon the gain, output impedance and frequency response of the amplifier. Under favorable conditions rather high precision is obtainable and a useful integrator can be made by determining the limits over which the output varies by a trigger tube[3]). The precision is normally limited by drifts of the trigger tube. Furthermore, to extend the range to more than one cycle (which is usually essential for general use) further errors are inevitably introduced by the time needed for the recycling procedure.

The present circuit uses the relationship between input and output only incidentally as a means of determining the rate at which charge should be removed from the input. Since at the moment of each trigger pulse the value of $e_2$ and so the charge on $C_2$ is the same, the charge which has flowed into the integrator must be equal to the charge removed per count and so the precision ultimately depends on the constancy of this charge "quantum". This is given by:

$$Q = 2BC_1\left(1 + \frac{V}{B}\right), \tag{1}$$

if $V$ is the input voltage at the moment $C_1$ is reversed. The delay time $\tau$ of the relay and the output impedance $R_0$ cause this voltage to depend somwehat on current:

$$V = V_0 + \frac{i\tau}{AC_2} + \frac{iR_0}{A}, \tag{2}$$

if $V_0$ is the voltage that would obtain at the input when the output reaches the trigger level, under conditions of very small current. Differentiation of (1) (assuming that $B \gg V$) gives for the relative error in $Q$:

$$\frac{\Delta Q}{Q} = \frac{\Delta B}{B} + \frac{\Delta V_0}{B} + \left(\frac{\tau}{ABC_2} + \frac{R_0}{AB}\right)\Delta i\,. \tag{3}$$

The first term on the right hand represents instability of the constant voltage source, the second term drift at the amplifier input, and the last term is the current dependent error. The last two terms can be made negligible compared to $\Delta B/B$ by choosing suitable values of $A$, $B$, $C_2$ and $R_0$, so that the precision depends wholly on the stability of $B$. An interesting fact is, that for a given current the error is independent of the switching frequency, so one can go to the highest frequency where the relay will operate safely. In our apparatus $B = 85$ V, $A = 1200$, $R_0 \approx 2\,\text{k}\Omega$, $\tau = 6$ and 4 msec resp., for opening and closing the relay. The sum of the factors $i\tau/ABC_2$ and $iR_0/AB$ is smaller than $3 \times 10^{-4}$ for all currents to be measured.

[3]) W. A. Higinbotham and S. Rankowitz, Rev. Sci. Instr. 22 (1951) 688.

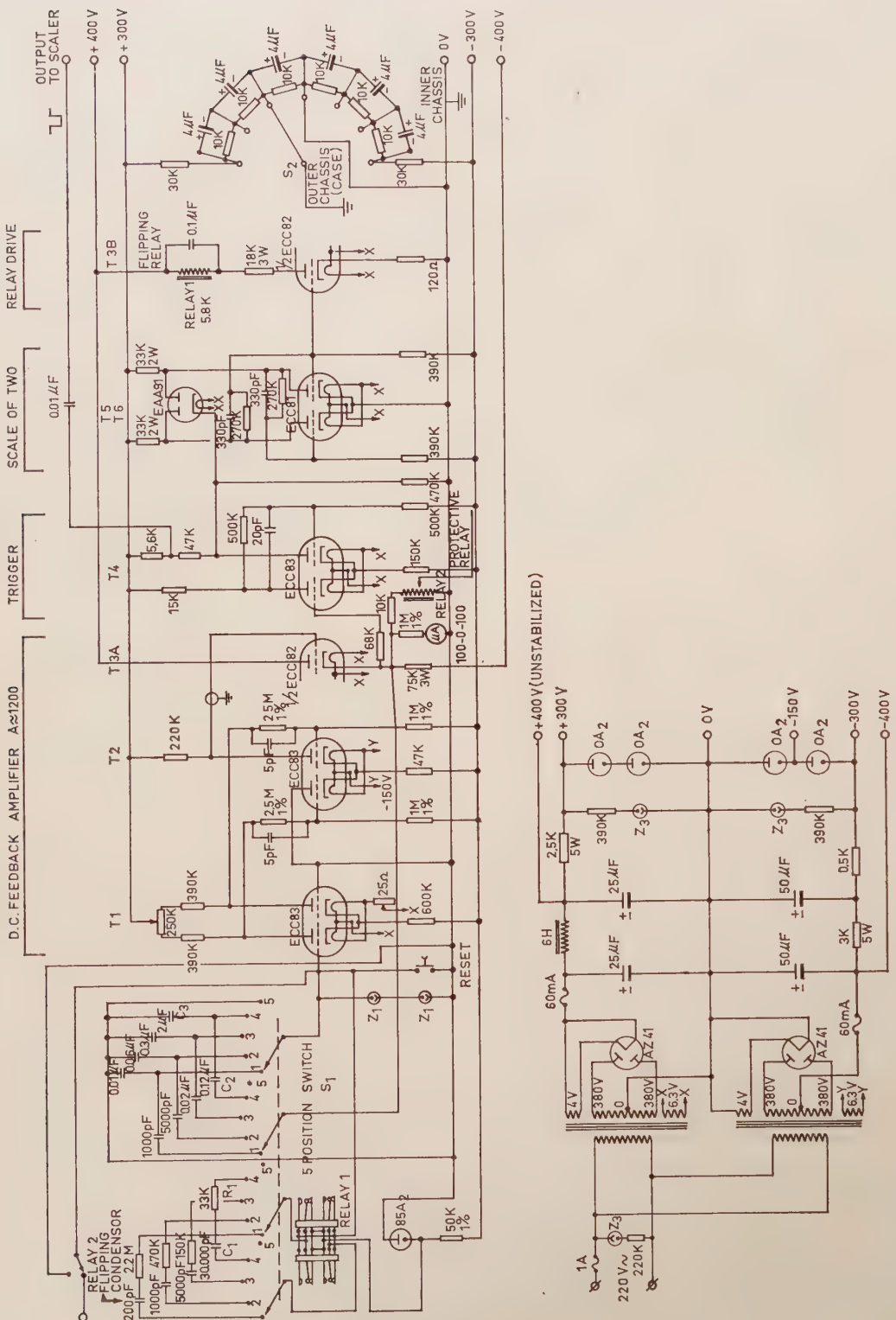


Fig. 2. Circuit diagram of the integrator.

The drift of the amplifier input is smaller than 0.01 V in several hours, resulting in a value of $\Delta V_0/B$ of the order of $10^{-4}$. The ultimate stability thus depends on the 85 A2 voltage reference tube, which, according to the manufacturer, should give 0.1% stability under suitable conditions.

The peak to peak value of the input voltage is in our apparatus about 0.04 V. The mean input level however does not exceed a value of 0.02 V from ground for all currents to be measured. This value determines the leakage which may be permitted between target and ground. If, for instance, one wants to measure a current of 10 $\mu$A with 0.1% precision the leakage resistance must be higher than 2 M$\Omega$, which is low enough to make use of watercooled targets.

### 1.3. CONSTRUCTION

A complete circuit, including plate voltage supplies, is given in fig. 2. Tubes $T_1$ and $T_2$ form the dc-amplifier. The heater voltage on the first tube is 4 V. By varying the cathode resistor a working point has been found where the grid current is $\approx 1.5 \times 10^{-11}$ A in the whole range used. This limits the practical use of the apparatus to currents higher than $10^{-9}$ A, which is low enough for practically all applications in nuclear physics. Tube $T_3A$ is a cathode follower used to reduce the output impedance. This stage may be omitted when only the first three ranges of the apparatus are used. This fact is mentioned since currents above 85 $\mu$A (maximum permissible on scale 3) are not needed frequently and the elimination of the cathode follower results in a circuit which is absolutely stable. The phase-advance condensers in the grids of $T_2$ have been found, however, to produce complete stability when the cathode follower is included in the feedback loop. Admittedly a solution to the stability problem possessing a higher degree of safety could be found (the values of these condensers are quite critical), but further work was not deemed worthwhile since no trouble has been experienced with incipient or recurring oscillations. Through the four pole five position switch, $S_1$, one can choose four different sets of $R_1, C_1, C_2$ and $C_3$ while in the fifth position the input is short circuited. The time constant $R_1C_1$ is kept smaller than one eighth of the smallest time between two switchings, so that $C_1$ is always discharged to less than 0.03% of its original charge.

Tube $T_4$ is wired as a Schmitt trigger. The trigger level is about — 15 V and the hysteresis is 10 V. Tubes $T_5$ and $T_6$ form the scale of two, while $T_3B$ is the relay driving tube. The reference voltage, $B$, is delivered by an 85 A 2 tube $T_7$ fed through precision resistors. The circuit is never turned off so as to guarantee the highest possible constancy of ambient conditions, and thus voltage, for this tube. The apparatus is protected in two ways: if the absolute value of the output of the amplifier becomes higher than 60 volts the relay 2 falls in and disconnects the input. If this relay does not work, for instance because the voltage supplies are out of order, two neon tubes connected between the input and ground protect the condensers against overvoltage.

All condensers connected to the input are Leclanché polystyrene condensers except the 2 $\mu$F condenser. Since the voltage across it is so small (maximum 0.04 V) soakage effects will not be important. Switch S1 is an E.B.E. switch with silicone deck. The relays are Siemens Trls 151/71e. The two halves of relay 1 are connected in parallel. Its insulation proved to be good enough, the leakage current being less than $10^{-11}$ A. The noise of this relay was reduced to an agreeable level by mounting it in a foam rubber house.

The integrator is mounted on a chassis which is insulated with perspex. The chassis level with respect to ground may be varied from + 150 to — 150 V by means of the seven position switch S2. This may be used as a check on the working of the suppressor used to retain secondary electrons on the target and also to measure the resistance between target and ground. The meter connected to the output of the amplifier is used to control the amplifier balance and may also be used to measure the grid current.

1.4. DISCUSSION

The performance of this integrator has been such as to warrant the construction of a duplicate for the Utrecht 3 MeV electrostatic accelerator. Both have been in daily use for many months and have shown themselves to be extremely flexible and reliable. Calibration checks have disclosed that the linearity is better than 0.1%.

## 2. The Galvanometer

In the following an electronic galvanometer suitable for use in combination with the integrator is described.

2.1. INTRODUCTION

The integrator just described makes it possible to perform high precision charge measurements even if the insulation of the target is not especially good. In order to take advantage of this property a low-impedance galvanometer must also be used since the galvanometer is usually in series with the integrator. Conventional moving-coil galvanometers of adequate sensitivity are generally of very low resistance, but possess several practical disadvantages. They are seldom robust, usually cumbersome, and of course, quite expensive, while subject to easy burnout. In addition the limited frequency response of such instruments sometimes deprives the accelerator operator of essential information on fast beam fluctuations.

For these reasons an electronic galvanometer has been constructed, combining in a simple circuit the following advantages:

(a) An input impedance given by 20 k$\Omega$ divided by the number of microamperes for full-scale deflection;

(b) A non-adjustable deflection sensitivity which is at least as precise and constant as a high-quality commercial galvanometer;

(c) No zero-set adjustment; the zero does not drift nor change perceptibly for scale changes from 0.1 $\mu$A to 1 mA full-scale deflection; and

(d) Essentially complete safety from burnout even if quite high positive or negative voltages are accidentally connected to the input.

2.2. DESCRIPTION

The circuit makes use of unity voltage feedback around a two-stage balanced amplifier. The operation may be understood by reference to fig. 3. The amplifier is adequately represented by a real voltage gain, $A$, an infinite input impedance, and an output impedance, $R_0$. The input impedance is given by $R_f/A$ (within an error of $1:A$, i.e., 1:1000 in our circuit). The meter current is $iR_f/R_m$†, where $i$ is the input current. Thus the deflection sensitivity depends only upon precision resistors and a robust meter whose calibration can be expected to be extremely constant since it can never be subjected to serious overload (see below for further discussion of this point).

The lack of zero-drift is perhaps the most important innovation involved in this circuit. Because of the unity feedback the drift at the

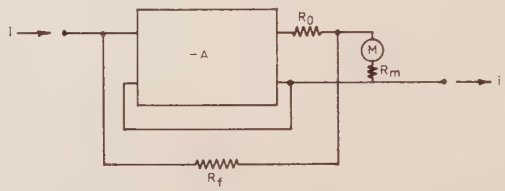


Fig. 3. Block diagram of the electronic galvanometer

output is just equal to the drift at the input. Since the input is a balanced stage operating under essentially ideal conditions, we can expect this drift never to exceed 50 mV. Full-scale deflection of the meter corresponds to an output voltage of 20 volts, hence the zero drift should never exceed 1/400 of full scale, an undetectable deflection. It should be noted that in designing such a circuit there is considerable latitude in the parameters, but that vanishingly small zero-shift must be purchased for the price of increasing the input impedance. This could be circumvented by increasing the circuit gain, however in order to hold the circuit to two

† The correct expression is actually

$$i\frac{R_f}{R_m}\frac{\left(1+\frac{R_0}{AR_f}\right)}{\left(1-\frac{1}{A}-\frac{R_0}{AR_m}\right)}.$$

The correction terms can at most amount to 0.2%, or less than a detectable deflection.

double triodes this expedient was not resorted to in this case.

The circuit is outstanding as to capacity to withstand overload. This can be of importance in accelerator use where short circuits (or gas discharges) between target and secondary-

### 2.3. CIRCUIT DIAGRAM

The complete circuit diagram is shown in fig. 4. The power is provided by a transformer insulated with perspex, so that the insulation to ground is quite as good as that required for the input of the integrator. The entire circuit, in-

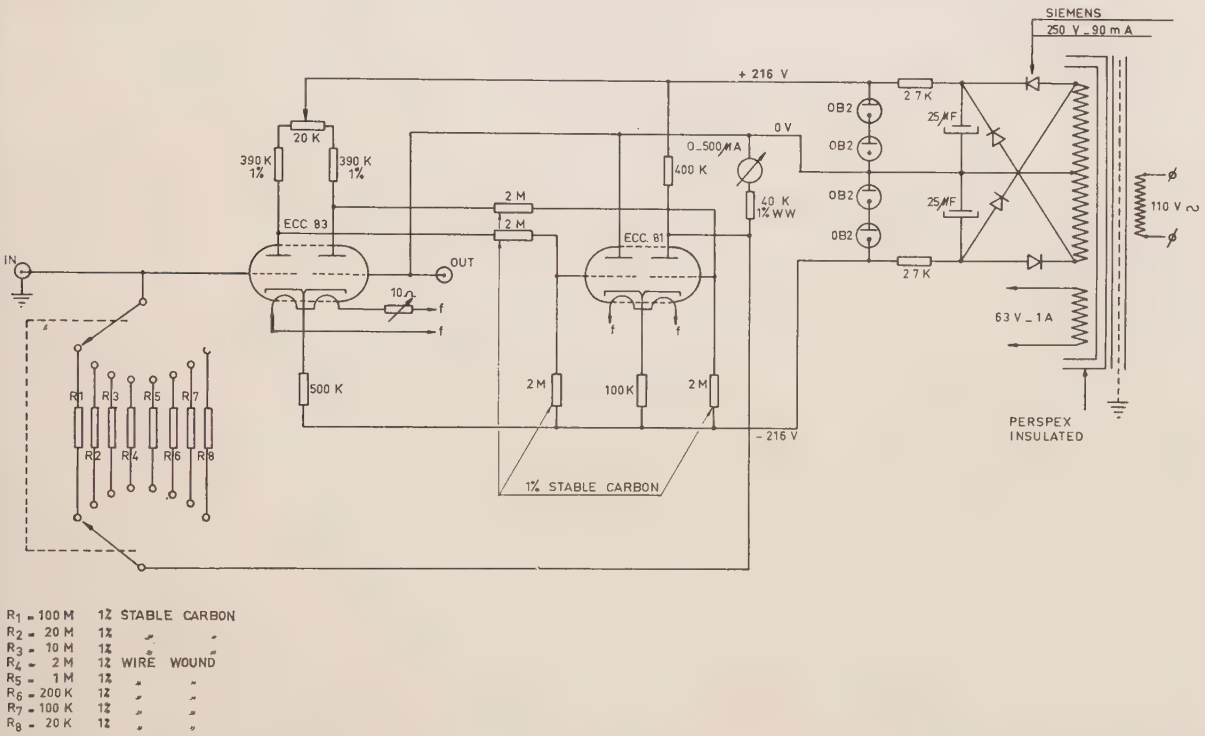


$R_1$ = 100 M 1% STABLE CARBON
$R_2$ = 20 M 1% " "
$R_3$ = 10 M 1% " "
$R_4$ = 2 M 1% WIRE WOUND
$R_5$ = 1 M 1% " "
$R_6$ = 200 K 1% " "
$R_7$ = 100 K 1% " "
$R_8$ = 20 K 1% " "

Fig. 4. Circuit diagram of the electronic galvanometer.

electron suppressor are a possibility. Under overload conditions (that is, with the voltage measured at the input more than a few tenths of a volt) the amplifier itself can deliver no more than 1 mA to the meter, this amounting to only a factor of two overload. Increasing the applied input voltage up to 40 volts on the 1 mA scale and up to more than 200 volts on all other scales decreases the overload since the input current flows through the meter in the opposite direction to that of the amplifier output current. The input tube itself, since the cathode resistor is very high, can easily follow positive input voltages of as much as 200 volts without destructive grid current, and in most cases can tolerate a negative grid voltage of 200 volts for a short time without breaking down.

cluding power supply, is built onto the back of the meter itself, thus making for an extremely compact unit.

### 2.4. CONCLUSION

As in the case of the integrator, identical circuits have been built for both the Van de Graaff accelerator and the cascade generator. The operation of both has been completely trouble free for several months.

**Acknowledgements**

This investigation is part of the research program of the "Stichting voor Fundamenteel Onderzoek der Materie", and was made possible by financial support from the "Nederlandse Organisatie voor Zuiver Wetenschappelijk Onderzoek".

NUCLEAR INSTRUMENTS AND METHODS 8 (1960) 46–54; NORTH-HOLLAND PUBLISHING CO.

# TRANSISTORIZED APPARATUS FOR ACCUMULATION AND BINARY-DECIMAL CONVERSION

D. BRINI, A. GANDOLFI and G. L. TABELLINI

*Istituto di Fisica dell'Università di Bologna. Istituto Nazionale di Fisica Nucleare. Sezione di Bologna*

Received 28 March 1960

We describe an apparatus capable of adding binary numbers and of converting the sum into decimal form.

The fundamental unit is a decade element having four inputs corresponding to the numbers 1, 2, 4, 8 and an output $Z$ corresponding to the carry. The number which is stored in the decade element can be read directly on an instrument.

(I) It is well known that the binary system of numbering is considered the most convenient and practical for electronic computing and for memorizing data. Furthermore we are so accustomed to using the decimal numbering that we often regard the conversion of a written binary number into a decimal form as indispensable.

In particular the apparatus described here will be utilized in conjunction with the memorisation and registration system for various counting channels, in the Cosmic Rays station at the Institute of Physics of the Bologna University. Each of the counting channels corresponds to a fixed time-interval.

This apparatus, besides being capable to convert a memorised number in a binary form into a decimal form, gives the possibility to accumulate an *a priori* fixed number of data of each channel.

Obviously the first requirement of such an apparatus corresponds to the most common case, the conversion of the counting of a binary scaler into a decimal form.

This problem has already been dealt with by various authors[1–6]). Since in our case we require also the addition operation, we thought, for reasons of economy, of an apparatus capable of making simultanously both accumulation and conversion of data.

† The numbers from $2^0$ at $2^n$ are sent as pulses following in the corresponding inputs.

The system has $n$ inputs, each corresponding to a fixed power of two, as shown in fig. 1†.

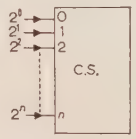


Fig. 1

For instance, if 1011 is the number to be converted (and to be summed to the numbers previously sent into the system) we shall have, successively in time, a pulse on 0 input, a second pulse on input 1 none on 2 and a last pulse on input 3.

In our case, we have 17 inputs, the $17^{th}$ corresponding to $2^{16} = 65536$ units.

(II). The fundamental unit of the apparatus is a particular decade element with 10 stable states capable, therefore, to store a decimal number. It has four inputs $X_1$, $X_2$, $X_3$, $X_4$, and

[1]) R. K. Richards, Arithmetic Operations in Digital Computers (D. Van Nostrand Company, 1955).

[2]) J. F. Couleur, BIDEC, A Binary-to-Decimal or decimal-to-Binary Converter (I.R.E. Trans. Elect. Comp. Vol. EC7 N.4, Dec. 1958).

[3]) L. Dadda, Le conversioni automatiche nella calcolatrici Elettroniche binarie, Energia Elettrica 1 (1959).

[4]) S. H. Caldwell, Switching Circuits and Logical Design (J. Wiley and Sons, 1958).

[5]) J. Millman and H. Taub, Pulse and Digital Circuits (McGraw-Hill Book Company, 1956).

[6]) A. W. Lo *et al.*, Transistor Electronics (Prentice-Hall, Inc., 1955.)

TABLE 1

| (a) | (b) | | | | (c) | | | | | (d) | | | | | (e) | | | | | (f) | | | | |
|---|---|---|---|---|---|---|---|---|---|---|---|---|---|---|---|---|---|---|---|---|---|---|---|---|
| | | | | | $X_1(+1)$ | | | | | $X_2(+2)$ | | | | | $X_3(+4)$ | | | | | $X_4(+8)$ | | | | |
| | $Y_4$ | $Y_3$ | $Y_2$ | $Y_1$ | $\tau_4$ | $\tau_3$ | $\tau_2$ | $\tau_1$ | Z | $\tau_4$ | $\tau_3$ | $\tau_2$ | $\tau_1$ | Z | $\tau_4$ | $\tau_3$ | $\tau_2$ | $\tau_1$ | Z | $\tau_4$ | $\tau_3$ | $\tau_2$ | $\tau_1$ | Z |
| 0 | 0 | 0 | 0 | 0 | 0 | 0 | 0 | 1 | 0 | 0 | 0 | 1 | 0 | 0 | 0 | 1 | 0 | 0 | 0 | 1 | 0 | 0 | 0 | 0 |
| 1 | 0 | 0 | 0 | 1 | 0 | 0 | 1 | 1 | 0 | 0 | 0 | 1 | 0 | 0 | 0 | 1 | 0 | 0 | 0 | 1 | 0 | 0 | 0 | 0 |
| 2 | 0 | 0 | 1 | 0 | 0 | 0 | 0 | 1 | 0 | 0 | 1 | 1 | 0 | 0 | 0 | 1 | 0 | 0 | 0 | 0 | 0 | 1 | 0 | 1 |
| 3 | 0 | 0 | 1 | 1 | 0 | 1 | 1 | 1 | 0 | 0 | 1 | 1 | 0 | 0 | 0 | 1 | 0 | 0 | 0 | 0 | 0 | 1 | 0 | 1 |
| 4 | 0 | 1 | 0 | 0 | 0 | 0 | 0 | 1 | 0 | 0 | 0 | 1 | 0 | 0 | 1 | 1 | 0 | 0 | 0 | 0 | 1 | 1 | 0 | 1 |
| 5 | 0 | 1 | 0 | 1 | 0 | 0 | 1 | 1 | 0 | 0 | 0 | 1 | 0 | 0 | 1 | 1 | 0 | 0 | 0 | 0 | 1 | 1 | 0 | 1 |
| 6 | 0 | 1 | 1 | 0 | 0 | 0 | 0 | 1 | 0 | 1 | 1 | 1 | 0 | 0 | 0 | 1 | 1 | 0 | 1 | 0 | 0 | 1 | 0 | 1 |
| 7 | 0 | 1 | 1 | 1 | 1 | 1 | 1 | 1 | 0 | 1 | 1 | 1 | 0 | 0 | 0 | 1 | 1 | 0 | 1 | 0 | 0 | 1 | 0 | 1 |
| 8 | 1 | 0 | 0 | 0 | 0 | 0 | 0 | 1 | 0 | 1 | 0 | 0 | 0 | 1 | 1 | 0 | 1 | 0 | 1 | 1 | 1 | 1 | 0 | 1 |
| 9 | 1 | 0 | 0 | 1 | 1 | 0 | 0 | 1 | 1 | 1 | 0 | 0 | 0 | 1 | 1 | 0 | 1 | 0 | 1 | 1 | 1 | 1 | 0 | 1 |

an output $Z$. A pulse on $X_1$ (equal number 1) increases the stored number from $n$ to $n + 1$, a pulse on $X_2$ (equal number 2) increases the stored number from $n$ to $n + 2$, a pulse on $X_3$ (equal to number 4) increases the number from $n$ to $n + 4$, lastly a pulse on $X_4$ (equal to number 8) increases the stored number from $n$ to $n + 8$.

If these operation give a carry, a pulse appears on output $Z$ and the number of lowest order is stored in the decade element.

The choice of the 4 inputs corresponding to the four numbers 1, 2, 4, 8 has been determined by making a compromise as discussed in Appendix A.

The whole apparatus is made by 6 decade elements, capable therefore to sum and convert numbers up to $10^6$. The 6$^{th}$ decade element is used only to store the carries; it will have therefore only input $X_1$.

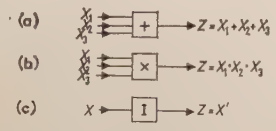


Fig. 2

(III). The scheme of the decade element is based on 4 bistable symmetric multivibrators (flip-flop), used as a memorising element, and on the principle that two pulses cannot exist simultanously on different inputs.

Table 1 summarises the conditions which the decade must satisfy. The columns show:

(a) the stored decimal numbers;

(b) $Y_1$, $Y_2$, $Y_3$, $Y_4$ the states of the four memorising elements corresponding to the stored number of (a);

(c) which of the four flip-flops corresponding to column (b) should change its state after the pulse on $X_1$ (= 1) in order to obtain the number $n + 1$ and also whether there is $Z$ carry†;

(d), (e), (f) which of the four flip-flops should change its state after a pulse on $X_2$ (= 2), on $X_3$ (= 4) and on $X_4$ (= 8) respectively.

By using table 1 and the Boole algebra

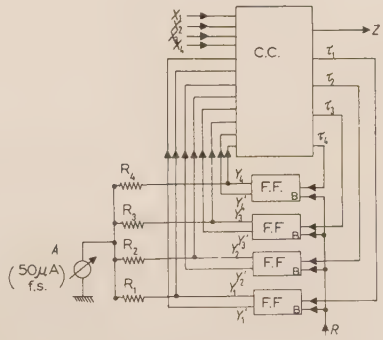


Fig. 3

(see appendix B) the following equations describing the behaviour of the decade element are obtained:

† The change of state of the $i$-th flip-flop takes place when $\tau_i = 1$.

$$\tau_1 = X_1$$

$$\tau_2 = X_1 Y_1 Y_4' + X_2 Y_4' + X_3(Y_2 Y_3 + Y_4) + \\ + X_4 (Y_2 + Y_3 + Y_4)$$

$$\tau_3 = X_1 Y_1 Y_2 + X_2 Y_2 + X_3 Y_4' + X_4 (Y_2' Y_3 + Y_4)$$

$$\tau_4 = X_1 Y_1 (Y_2 Y_3 + Y_4) + X_2 (Y_2 Y_3 + Y_4) + \\ + X_3 (Y_2' Y_3 + Y_4) + X_4 Y_2' Y_3'$$

$$Z = X_1 Y_1 Y_4 + X_2 Y_4 + X_3 (Y_2 Y_3 + Y_4) + \\ + X_4 (Y_2 + Y_3 + Y_4) \qquad (1)$$

where the $Y_i'$ represent the complementary outputs of $Y_i$ (es. $Y_1 = 1$, $Y_1' = 0$). The (1) indicate therefore the logic operations necessary to satisfy the conditions required by the apparatus.

Precisely three types of elementary circuits are necessary. They are sketched in fig. 2:

(a) logic circuit for addition;

(b) logic circuit for multiplication;

(c) inverter circuit.

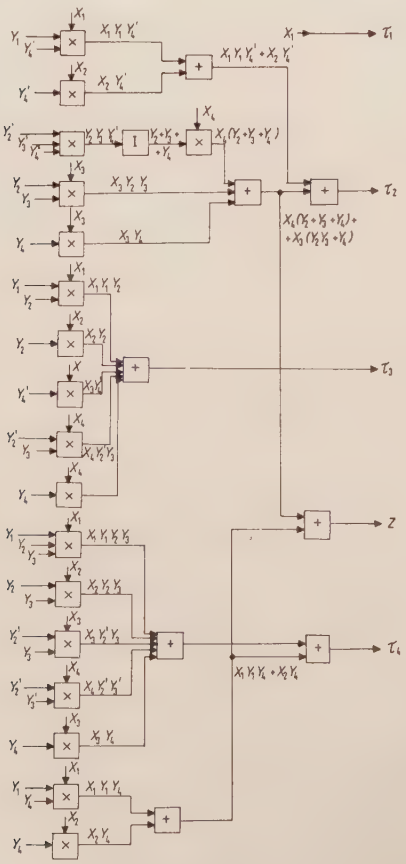

Fig. 4

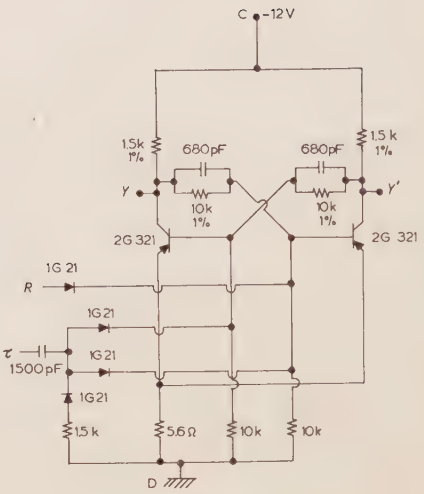


Fig. 5 (a)

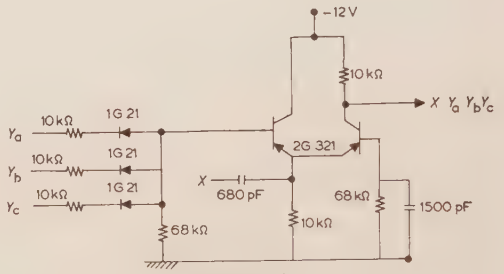


Fig. 5 (b)

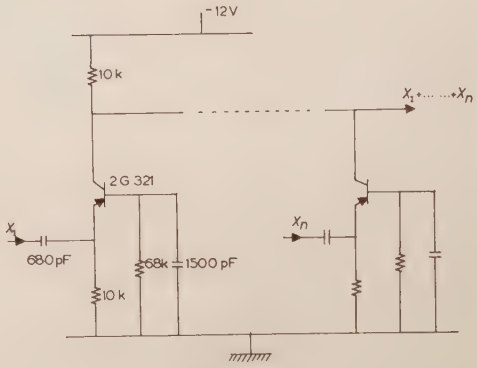


Fig. 5 (c)

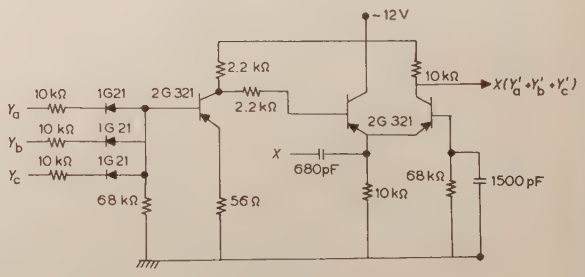


Fig. 5 (d)

The whole scheme of the decade element could be of the type shown in fig. 3, where C.C. indicates the block of combinational circuit made essentially of the three elementary circuits of fig. 2.

The stored decimal counting of the decade element can be read with the instrument A, by taking the voltage levels of the four flip-flops through $R_1$, $R_2$, $R_3$, $R_4$.

The block diagram of fig. 4 shows how the combinational circuit was made.

Fig. 5 shows the detailed schemes of the elementary circuits used. Their mounting was made on printed circuits. The elementary circuits are:

(a) Flip-flop, where $R$ represents the positive input pulse for reset, $\tau$ is the triggering positive input pulse, $Y$ and $Y'$ give the complementary states of the circuits;

(b) the circuit for multiplication, where $Y_a$, $Y_b$, $Y_c$ and $X$ correspond to the 4 inputs to be multiplied and $(Y_a \cdot Y_b \cdot Y_c \cdot X)$ is the output;

(c) the circuit for addition, where the $X_i$ are the pulses to be summed and $\Sigma X_i$ is the output;

(d) the combinational circuit of multiplication, inversion and successive multiplication. The first transistor makes the inversion of the input $Y_a \cdot Y_b \cdot Y_c$ giving $Y_a' + Y_b' + Y_c'$. The output will be given by $(Y_a' + Y_b' + Y_c') \cdot X$.

We point out that the inputs $X_i$ are pulses, while $Y_i$ or $Y_i'$ are voltage levels corresponding to two states.

(IV) The checks of the decade element have been made by sending separately pulses into the four inputs $X_1$, $X_2$, $X_3$, $X_4$, and by observing in a synchroscope the distribution of the outputs with respect to the inputs. If the apparatus works correctly the distribution corresponding to the waveform chart shown in fig. 6 must appear. In this figure:

(a) represents the sequency of the input pulses;

(b) gives the distribution of $Z$ outputs if the input (a) is sent into $X_1$;

(c), (d), (e) give the distribution of the $Z$ outputs if the triggering pulses are sent respectively into $X_2$, $X_3$, $X_4$.

A further check could be carried out by observing the waveforms on the instrument A of fig. 3 when the pulses are sent to the four inputs separately. Then one should observe the waveforms as shown in fig. 7, represented by (a), (b), (c), (d) and corresponding to the four inputs $X_1$, $X_2$, $X_3$ and $X_4$.

TABLE 2

| $n$ | 0 | 1 | 2 | 3 | 4 | 5 | 6 | 7 | 8 | 9 | 10 | 11 | 12 | 13 | 14 | 15 | 16 |
|---|---|---|---|---|---|---|---|---|---|---|---|---|---|---|---|---|---|
| $2^n$ | 1 | 2 | 4 | 8 | 16 | 32 | 64 | 128 | 256 | 512 | 1.024 | 2.048 | 4.096 | 8.192 | 16.384 | 32.768 | 65.536 |
| 10 | $X_1$ | $X_2$ | $X_3$ | $X_4$ | $X_2$ $X_3$ | $X_2$ | $X_3$ | $X_4$ | $X_2$ $X_3$ | $X_2$ | $X_3$ | $X_4$ | $X_2$ $X_3$ | $X_2$ | $X_3$ | $X_4$ | $X_2$ $X_3$ |
| $10^2$ | — | — | — | — | $X_1$ | $X_1$ $X_2$ | $X_2$ $X_3$ | $X_2$ | $X_1$ $X_3$ | $X_1$ | $X_2$ | $X_3$ | $X_1$ $X_4$ | $X_1$ $X_4$ | $X_4$ | $X_2$ $X_3$ | $X_1$ $X_2$ |
| $10^3$ | — | — | — | — | — | — | — | $X_1$ | $X_2$ | $X_1$ $X_3$ | — | — | — | $X_1$ | $X_1$ $X_2$ | $X_1$ $X_2$ $X_3$ | $X_1$ $X_3$ |
| $10^4$ | — | — | — | — | — | — | — | — | — | — | $X_1$ | $X_2$ | $X_3$ | $X_4$ | $X_2$ $X_3$ | $X_2$ | $X_1$ $X_3$ |
| $10^5$ | — | — | — | — | — | — | — | — | — | — | — | — | — | — | $X_1$ | $X_1$ $X_2$ | $X_2$ $X_3$ |
| | 0 | $R$ | $R$ | $R$ | $R$ | $3R$ | $3R$ | $3R$ | $3R$ | $5R$ | $4R$ | $3R$ | $3R$ | $5R$ | $5R$ | $7R$ | $9R$ |

Total = $57R$.

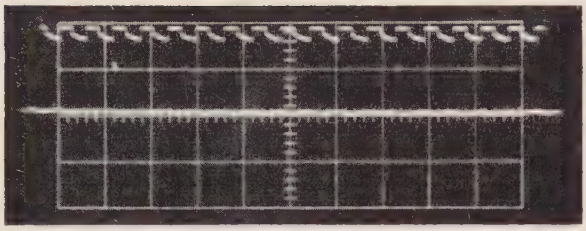

Fig. 6 (a)–(b)

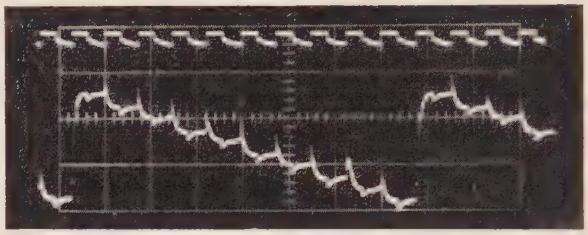

Fig. 7 (a)

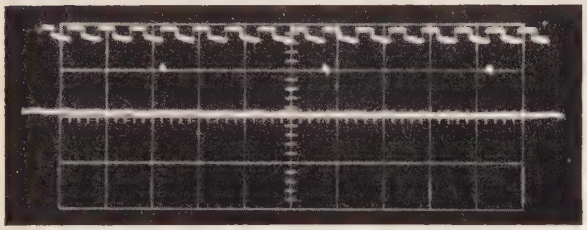

Fig. 6 (a)–(c)

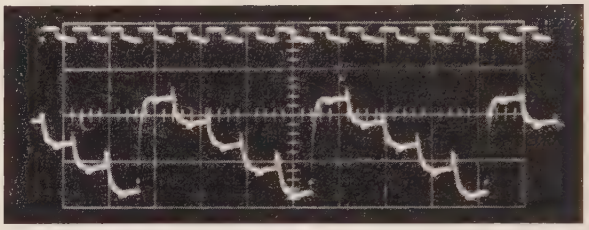

Fig. 7 (b)

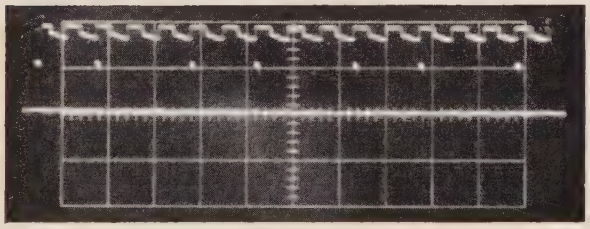

Fig. 6 (a)–(d)

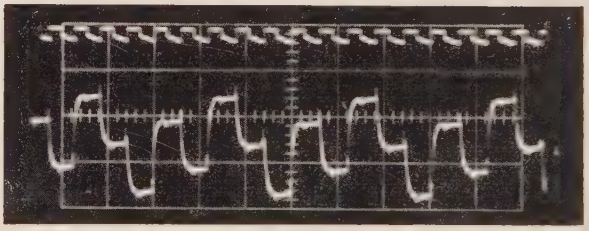

Fig. 7 (c)

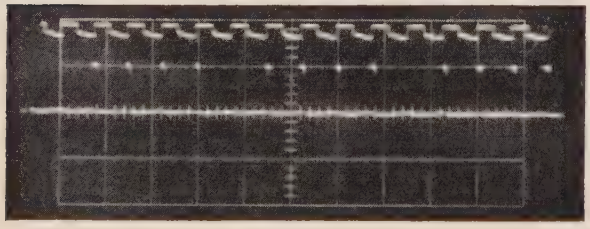

Fig. 6 (a)–(e)

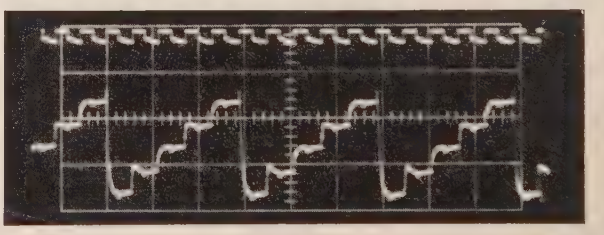

Fig. 7 (d)

The average resolution obtained is about 10 $\mu$s, using positive pulses of few volts coming from a convenient former.

The power required for a decade element is about 170 mA $\times$ 12 volts.

(V) The whole apparatus consists of 6 decades, as pointed out above. The distribution of the pulses on the various inputs of the 6 decades is shown in table 2.

As no input of any decade element can be simultaneous to another input, it is necessary to delay conveniently each trigger with an $R$ delay which should not be lower than the resolution of the apparatus.

The last line of table 2 shows the delays to be fixed between each input. As one can see, the complete elaboration of a number of 17 binary figures can be made in a time of $57R$, which, considering the resolution of the apparatus, correspond to about 0.5 ms.

The block diagram of the triggers distribution is shown in fig. 8, where $R$ or $nR$ delays are obtained by monostable multivibrators made as indicated in fig. 9.

The test of the whole apparatus can be carried out simply by sending $N$ pulses into any

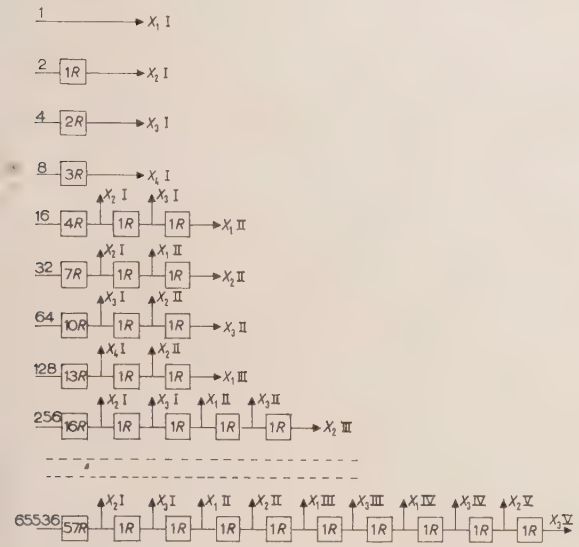


Fig. 8

of the inputs corresponding to a given power of two ($2^i$). The counting stored by the apparatus (measured by $A$ instruments) should be $N2^i$.

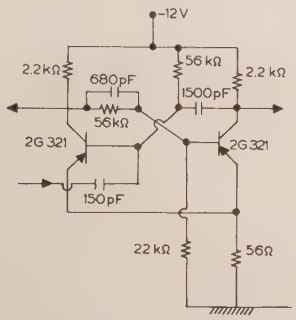


Fig. 9

We wish to thank, Mr. Merli for his help in mounting our apparatus.

## Appendix A

The choice of the four inputs $X_1\,X_2\,X_3\,X_4$ was suggested by a compromise. In fact only one input $X_1$ could have been taken into account. In this way we would have simplified the circuit of the decade element but we would have complicated the distribution of the pulses for each decimal number to be elaborated, and it would have increased very much the time of elaboration. On the other hand, in order to obtain a shorter operation time, we could have taken nine inputs each corresponding to nine numbers 1.....9, but in this case we would have to increase considerably the number of the components in each decade element.

The choice of the four inputs $X_1$, $X_2$, $X_3$, $X_4$ allows therefore a reasonable compromise between good operation-time and economy in the apparatus. The choice of the numbers corresponding to the four inputs was suggested by the idea to obtain a minimum operation time. The latter is proportional to the number of the pulses, following in the time, to be sent into the apparatus.

Table 3 shows in columns (a), (b) the frequencies of the decimal numbers corresponding to a given power of two, up to the maximum power $2^{16}$. As it appears, the most frequent numbers are 2, 1, 6, 4 and 8. Therefore it is evident that it is more convenient to choose the four inputs within these five numbers. Column (c) shows the pulses necessary to elaborate all the 17 powers of 2, considering the groups 1–2–4–8, 1–2–4–6, 1–2–6–8. As can be seen, the number of pulses needed and consequently the operating time does not depend on the choice of the group of the four numbers. Columns (d) and (e) show, for a comparison, the cases corresponding to the five most convenient inputs, and to a single input corresponding, of course, to number 1. In the first case, the operating time is 15% shorter, in the second one it increases by about 300%.

## Appendix B

The logic algebra (or Boole algebra) takes into account only the variables which two different values (or states) corresponding to 0 or to 1 can assume. It is therefore useful to study the circuits which elaborate codified data in a binary form.

The fundamental logic operations (to which, in practice, real circuits must correspond) are the following:

(a) addition:

$$0 + 0 = 0; \quad 1 + 0 = 0 + 1 = 1; \quad 1 + 1 = 1;$$

TABLE 3

| (a) | (b) | | | | | | | | | | | | | | | | | | (c) | | | (d) | (e) |
|---|---|---|---|---|---|---|---|---|---|---|---|---|---|---|---|---|---|---|---|---|---|---|---|
| decimal numbers | binary numbers to elaborate | | | | | | | | | | | | | | | | | | | | | | |
| | $2^0 = 1$ | $2^1 = 2$ | $2^2 = 4$ | $2^3 = 9$ | $2^4 = 16$ | $2^5 = 32$ | $2^6 = 64$ | $2^7 = 128$ | $2^8 = 256$ | $2^9 = 512$ | $2^{10} = 1024$ | $2^{11} = 2048$ | $2^{12} = 4096$ | $2^{13} = 8192$ | $2^{14} = 16.384$ | $2^{15} = 32.768$ | $2^{16} = 65.536$ | Total | 1, 2, 4, 8 | 1, 2, 4, 6 | 1, 2, 6, 8 | 1, 2, 4, 6, 8 | 1 |
| 1 | 1 | 0 | 0 | 0 | 1 | 0 | 0 | 1 | 0 | 1 | 1 | 0 | 0 | 1 | 1 | 0 | 0 | 7 | 7 | 7 | 7 | 7 | 7 |
| 2 | 0 | 1 | 0 | 0 | 0 | 1 | 0 | 1 | 1 | 1 | 1 | 1 | 0 | 1 | 0 | 1 | 0 | 9 | 9 | 9 | 9 | 9 | 18 |
| 3 | 0 | 0 | 0 | 0 | 0 | 1 | 0 | 0 | 0 | 0 | 0 | 0 | 0 | 0 | 1 | 1 | 1 | 4 | 8 | 8 | 8 | 8 | 12 |
| 4 | 0 | 0 | 1 | 0 | 0 | 0 | 1 | 0 | 0 | 0 | 1 | 1 | 1 | 0 | 1 | 0 | 0 | 6 | 6 | 6 | 12 | 6 | 18 |
| 5 | 0 | 0 | 0 | 0 | 0 | 0 | 0 | 0 | 1 | 1 | 0 | 0 | 0 | 0 | 0 | 0 | 2 | 4 | 8 | 8 | 12 | 8 | 20 |
| 6 | 0 | 0 | 0 | 0 | 1 | 0 | 1 | 0 | 1 | 0 | 0 | 0 | 1 | 0 | 1 | 1 | 2 | 8 | 16 | 8 | 8 | 8 | 48 |
| 7 | 0 | 0 | 0 | 0 | 0 | 0 | 0 | 0 | 0 | 0 | 0 | 0 | 0 | 0 | 0 | 1 | 0 | 1 | 3 | 2 | 2 | 2 | 7 |
| 8 | 0 | 0 | 0 | 1 | 0 | 0 | 0 | 1 | 0 | 0 | 0 | 1 | 0 | 1 | 1 | 1 | 0 | 6 | 6 | 12 | 6 | 6 | 48 |
| 9 | 0 | 0 | 0 | 0 | 0 | 0 | 0 | 0 | 0 | 0 | 0 | 0 | 1 | 1 | 0 | 0 | 0 | 2 | 4 | 6 | 4 | 4 | 18 |
| | | | | | | | | | | | | | No. pulses | | | | | | 67 | 66 | 68 | 58 | 196 |

(b) multiplication:

$$0\times1 = 1\times0 = 0; \quad 1\times1 = 1; \quad 0\times0 = 0;$$

(c) inversion:

$$0' = 1; \quad 1' = 0\,. \tag{1}$$

From these we get the important rules:

$$X + X' = 1 \quad \text{and} \quad (X_1\cdot X_2\cdots X_4)' = X_1' + X_2' + \cdots + X_n'\,. \tag{2}$$

It is clear therefore that if we want to assembly an apparatus with one or more variable inputs, capable to satisfy a whole combination of inputs and to give an output 1, it will be enough to sum up the outputs of various circuits, each satisfying separately and univocally one single required combination.

Actually these circuits carry out only the inversion and logic multiplication operations. In fact, for instance, the combination $Y_1 = 0$, $Y_2 = 0$ and $Y_3 = 1$, can be represented by $Z = Y_1'\,Y_2'\,Y_3'$.

To make a synthesis of a combinational circuit means then to obtain the whole of the required combinations.

Let us assume, for instance, that these are given by table 4

TABLE 4

| | $Y_1$ | $Y_2$ | $Y_3$ | $Z$ |
|---|---|---|---|---|
| a | 0 | 0 | 1 | 1 |
| b | 0 | 1 | 1 | 1 |
| c | 1 | 0 | 0 | 1 |

We shall have $Z(a) = Y_1'Y_2'Y_3'$; $Z(b) = Y_1'Y_2Y_3$; $Z(c) = Y_1Y_2'Y_3'$. Then the required equation is:

$$Z = Z(a) + Z(b) + Z(c)\,. \tag{3}$$

Taking into account (1) and (2) we can simplify eq. (3). This is of great importance in practice, because it reduce the number of circuits and consequently of the utilised components. We shall have:

$$Z = Y_1'Y_3(Y_2 + Y_2') + Y_1Y_2'Y_3' = = Y_1'Y_3 + Y_1Y_2'Y_3\,.$$

If there are no more than 4 variables, it is useful to use the so called Karnaugh map, which consists of a square divided into 16 cells, each representing one of the 16 possible combinations of the variables of input ($2^4 = 16$). With this method, the simplifications appear immediate, considering the following most common cases:

(a) Two adjacent cell case.

| $(Y_1Y_2)$ \ $(Y_3Y_4)$ | 00 | 01 | 11 | 10 |
|---|---|---|---|---|
| 00 | 0 | 0 | 0 | 0 |
| 01 | 0 | 1 | 1 | 0 |
| 11 | 0 | 0 | 0 | 0 |
| 10 | 0 | 0 | 0 | 0 |

(b) four adjacent cell case.

| $(Y_1Y_2)$ \ $(Y_3Y)_4$ | 00 | 01 | 11 | 10 |
|---|---|---|---|---|
| 00 | 0 | 0 | 0 | 0 |
| 01 | 1 | 1 | 0 | 0 |
| 11 | 1 | 1 | 0 | 0 |
| 10 | 0 | 0 | 0 | 0 |

(c) Eight adjacent cell case.

| $(Y_1Y_2)$ \ $(Y_3Y_4)$ | 00 | 01 | 11 | 10 |
|---|---|---|---|---|
| 00 | 0 | 0 | 0 | 0 |
| 01 | 1 | 1 | 1 | 1 |
| 11 | 1 | 1 | 1 | 1 |
| 10 | 0 | 0 | 0 | 0 |

(a)
We have: $Z = Y_1'Y_2(Y_3'Y_4 + Y_3Y_4) = Y_1'Y_2Y_4$.
The variable for which the two cells differ, disappears.

(b)
We have: $Z = Y_1'Y_2Y_3' + Y_1Y_2Y_3' = Y_2Y_3'$
The two variables for which the four cells differ, disappear.

(c)
We have $Z = Y_2Y_3' + Y_2Y_3 = Y_2$.
The three variables which differ going from one cell to another disappear.

TABLE 5

| | | $X_1$ | $X_2$ | $X_3$ | $X_4$ |
|---|---|---|---|---|---|
| $Y_2Y_1$ | $Y_4Y_3$ | 00—01—11—10 | 00—01—11—10 | 00—01—11—10 | 00—01—11—10 |
| $\tau_1$ | 00 | 1 1 0 or 1 1 | 0 0 0 or 1 0 | 0 0 0 or 1 0 | 0 0 0 or 1 0 |
| | 01 | 1 1 0 or 1 1 | 0 0 0 or 1 0 | 0 0 0 or 1 0 | 0 0 0 or 1 0 |
| | 11 | 1 1 0 or 1 0 or 1 | 0 0 0 or 1 0 or 1 | 0 0 0 or 1 0 or 1 | 0 0 0 or 1 0 or 1 |
| | 10 | 1 1 0 or 1 0 or 1 | 0 0 0 or 1 0 or 1 | 0 0 0 or 1 0 or 1 | 0 0 0 or 1 0 or 1 |
| $\tau_2$ | 00 | 0 0 0 or 1 0 | 1 1 0 or 1 0 | 0 0 0 or 1 1 | 0 1 0 or 1 1 |
| | 01 | 1 1 0 or 1 0 | 1 1 0 or 1 0 | 0 0 0 or 1 1 | 0 1 0 or 1 1 |
| | 11 | 1 1 0 or 1 0 or 1 | 1 1 0 or 1 0 or 1 | 0 1 0 or 1 0 or 1 | 1 1 0 or 1 0 or 1 |
| | 10 | 0 0 0 or 1 0 or 1 | 1 1 0 or 1 0 or 1 | 0 1 0 or 1 0 or 1 | 1 1 0 or 1 0 or 1 |
| $\tau_3$ | 00 | 0 0 0 or 1 0 | 0 0 0 or 1 0 | 1 1 0 or 1 0 | 0 1 0 or 1 1 |
| | 01 | 0 0 0 or 1 0 | 0 0 0 or 1 0 | 1 1 0 or 1 0 | 0 1 0 or 1 1 |
| | 11 | 1 1 0 or 1 0 or 1 | 1 1 0 or 1 0 or 1 | 1 1 0 or 1 0 or 1 | 0 0 0 or 1 0 or 1 |
| | 10 | 0 0 0 or 1 0 or 1 | 1 1 0 or 1 0 or 1 | 1 1 0 or 1 0 or 1 | 0 0 0 or 1 0 or 1 |
| $\tau_4$ | 00 | 0 0 0 or 1 0 | 0 0 0 or 1 1 | 0 1 0 or 1 1 | 1 0 0 or 1 1 |
| | 01 | 0 0 0 or 1 1 | 0 0 0 or 1 1 | 0 1 0 or 1 1 | 1 0 0 or 1 1 |
| | 11 | 0 1 0 or 1 0 or 1 | 0 1 0 or 1 0 or 1 | 0 0 0 or 1 0 or 1 | 0 0 0 or 1 0 or 1 |
| | 10 | 0 0 0 or 1 0 or 1 | 0 1 0 or 1 0 or 1 | 0 0 0 or 1 0 or 1 | 0 0 0 or 1 0 or 1 |
| $Z$ | 00 | 0 0 0 or 1 0 | 0 0 0 or 1 1 | 0 0 0 or 1 1 | 0 1 0 or 1 1 |
| | 01 | 0 0 0 or 1 1 | 0 0 0 or 1 1 | 0 0 0 or 1 1 | 0 1 0 or 1 1 |
| | 11 | 0 0 0 or 1 0 or 1 | 0 0 0 or 1 0 or 1 | 0 1 0 or 1 0 or 1 | 1 1 0 or 1 0 or 1 |
| | 10 | 0 0 0 or 1 0 or 1 | 0 0 0 or 1 0 or 1 | 0 1 0 or 1 0 or 1 | 1 1 0 or 1 0 or 1 |

By using the requirements of the decade element given in table 1, it is possible to build the 20 maps of table 5 relative to the five outputs $\tau_1$, $\tau_2$, $\tau_3$, $\tau_4$ and $Z$, and the four inputs $X_1, X_2, X_3, X_4$. 0 or 1 indicates the flip-flop states which in a normal working condition are not possible (corresponding as they do to the decimal numbers from 10 to 15).

Taking into account the above mentioned rules and choosing 1 or 0 for the not allowed states, according to the best obtainable simplification, we can write the equation describing the behaviour of the decade element. We shall have:

| | Not allowed states chosen as 1 |
|---|---|
| $\tau_1 = X_1$ | $X_1$ map |
| $\tau_2 = X_1Y_2Y_4' +$ | |
| $+ X_2Y_4' +$ | 1100, 1101, 1111, 1110, 1011 |
| $+ X_3Y_2Y_3 + X_3Y_4 +$ | 1010 |
| $+ X_4(Y_2 + Y_3 + Y_4) =$ | 1100, 1100, 1111, 1110, 1011<br>1010 |
| $= X_1Y_1Y_4' + X_2Y_4' + X_3(Y_2Y_3 + Y_4) +$ | |
| $+ X_4(Y_2'Y_3'Y_4')$ | |
| $\tau_3 = X_1Y_1Y_2 +$ | 1111, 1011 |
| $+ X_2Y_2 +$ | 1111, 1110, 1010 |
| $+ X_3Y_4' +$ | |
| $+ X_4(Y_2Y_3 + Y_4) =$ | 1100, 1101, 1111, 1011, 1010 |
| $= X_1Y_1Y_2 + X_2Y_2 + X_3Y_4' + X_4(Y_2'Y_3 + Y_4)$ | |
| $\tau_4 = X_1Y_1(Y_2Y_3 + Y_4) +$ | 1101, 1111, 1011 |
| $+ X_2(Y_2Y_3 + Y_4) +$ | 1100, 1101, 1111, 1110, 1011, 1010 |
| $+ X_3(Y_2'Y_3 + Y_4) +$ | 1100, 1101, 1111, 1110, 1010 |
| $+ X_4Y_2'Y_3' =$ | |
| $= X_1Y_1(Y_2Y_3 + Y_4) + X_2(Y_2Y_3 + Y_4) +$ | |
| $+ X_3(Y_2'Y_3 + Y_4) + X_4Y_2'Y_3'$ | |
| $Z = X_1Y_1Y_2 +$ | 1101, 1111, 1011 |
| $+ X_2Y_4 +$ | 1100, 1101, 1111, 1110, 1011, 1010 |
| $+ X_3(Y_2Y_3 + Y_4) +$ | 1100, 1101, 1111, 1110, 1011, 1010 |
| $+ X_4(Y_2 + Y_3 + Y_4) =$ | 1100, 1101, 1111, 1110, 1011, 1010 |
| $= X_1Y_1Y_2 + X_2Y_4 + X_3(Y_2Y_3 + Y_4) +$ | |
| $+ X_4Y_2'Y_3'Y_4'$ | |

NUCLEAR INSTRUMENTS AND METHODS 8 (1960) 55–60; NORTH-HOLLAND PUBLISHING CO.

# APPARATUS AND LABORATORY FOR PROCESSING NUCLEAR EMULSION STACKS

H. ENGELHARDT, I. HAUSER and U. KRECKER

*Deutsche Akademie der Wissenschaften zu Berlin, Kernphysikalisches Institut Zeuthen*

Received 9 January 1960

In the following an apparatus is described for processing nuclear emulsion stacks with an area up to 35 × 45 cm². The apparatus is so constructed that 3.5 l of emulsion, thickness 400 μ, can be processed during 5 days. The procedure for developing nuclear emulsions of type NIKFI R is represented.

## 1. Introduction

When the construction of the Synchrophasotron at the Joint Institute of Nuclear Research, Dubna U.S.S.R., was completed, there arose the need to have enough capacity for the development of nuclear emulsion stacks. To meet this requirement in the Kernphysikalisches Institut der Deutschen Akademie der Wissenschaften, Zeuthen, a laboratory was built which works for all the member states of the Joint Institute of Nuclear Research. The new apparatus used in this laboratory makes it possible to treat emulsion pellicles up to 35 × 45 cm². This apparatus and the procedure are described in this paper.

## 2. Development Procedure

The method of development used in this apparatus is based on the temperature cycling method by Dilworth *et al.*[1]) with dry hot stage. The procedure and the composition of the solutions are adapted to the development of emulsions type NIKFI R, 400 μ thick[2–4]). All emulsions are mounted before processing. The development procedure consists of the following steps:

### 2.1. PREPARATION OF THE GLASS

The cleaned glass plates, 1.2—1.3 mm thick, are immersed three times in a solution of the following composition:

| | | |
|---|---|---|
| 4 | g | Gelatine |
| 10 | g | Sodium silicate |
| 0.75 | g | Alum chronium |
| 0.5 | g | Thymol |
| 60 | ml | Ethyl alcohol |
| to 1000 | ml | Distilled water |

Henceforth it is possible to get special glass for mounting NIKFI R emulsions.

### 2.2. MOUNTING

Before mounting, that surface of the pellicle which is to be mounted must be rubbed down with an alcohol-water solution of 25% or 30% according to the time elapsed between the manufacture of the emulsion and its use. Otherwise a black sediment will be formed during the processing upon the surface of the emulsion. In this way 3—4 μ has to be removed. Then the pellicles are mounted on glass in the same solution as described before. In this solution the pellicle must be laid down on the glass plate and moved back and forth, until it sticks to the glass. This procedure lasts about 3—5 sec. Then the emulsion must immediately be taken out of the solution, cleaned, and then rolled with a machine-roller. After mounting, the pellicles are air dried for about 2 h and simultaneously cooled down from room temperature to 3° C.

[1]) C. C. Dilworth, G. P. S. Occhialini and L. Vermaesen, Bulletin du Centre de Physique Nucléaire de Bruxelles No. 13a, (Febr. 1950).

[2]) D. M. Samoilowitsch and I. S. Pissanko, J. Techn. Phys. No. 2 (1956) 45.

[3]) J. Beljakow, L. G. Koslowa, L. N. Iwanowa and K. D. Tolstow, J. Sci. Appl. Photogr. Cinema 2 (1957) 325.

[4]) S. J. Ljubomilow, private communication.

### 2.3. PRESOAKING

The emulsions are soaked in distilled water of 3° C for 2.5 h.

### 2.4. SOAKING WITH COLD DEVELOPER

The emulsions are taken out of the presoaking bath and put for 2.5 h in the cold developer solution (3° C), having the following composition:

2.5 g Amidol
12 g Sodium sulphite (anhydrous)
ca. 2 g Citric acid, in order to have a *p*H-value of 6.6 to 1000 ml distilled water.

### 2.8. FIXING

The fixing bath consists of a 30% hypo solution to which potassium metabisulphite is added in order to have a *p*H of 6.9. The flow of hypo over the emulsions amounts to nearly 6 cm/min i.e. 1.5 l/min through one tray containing 0.176 l emulsion and 20 l hypo. The fixing time is 50% longer than that of the clearing time. This corresponds to a time of about 40 h. The temperature is approximately 5° C. At the beginning the fixing solution contains no silver but at the end the concentration amounts to

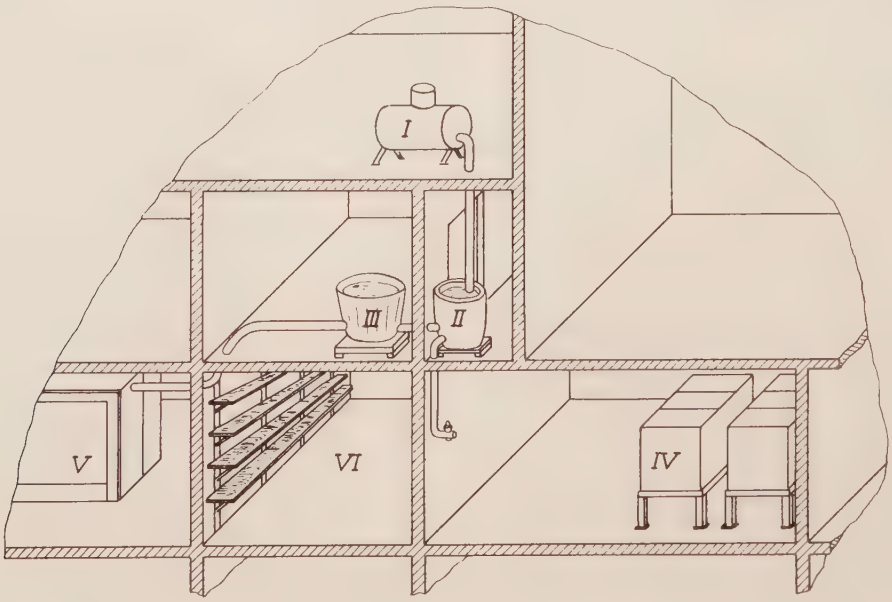


Fig. 1. Scheme of location of the rooms for processing.
I. water destillator, II. containers for distilled water, III. preparation of fixing solution, IV. development, V. fixing room, VI. drying room.

### 2.5. DRY HOT STAGE

After the plates have been taken out of the developer the surfaces of the emulsions are gently wiped off with filterpaper and then the plates are put immediately into a thermostat of 24° C for a period of 40 min.

### 2.6. STOP BATH

The development is interrupted by immersing the emulsions into a solution of 0.5% acetic acid of 3° C for 2.5 h.

### 2.7. INTERMEDIATE WASHING

The stop bath is let off and replaced by distilled water of 3° C for 2.5 h.

8 g/l. This is the greatest concentration attainable in our fixing unit with emulsions of 400 $\mu$ thickness. Corrosion is not found.

### 2.9. DILUTION AND WASHING

At the end of fixing the hypo is diluted with tap water over a period of 12 h, so that the concentration decreases proportionally to time until it reaches less than 1%. Simultaneously the temperature increases to the temperature of the tap water of approximately 13—15° C. Then the washing is started and is continued over a period of 24 h with running tap water by the same flow as during fixing.

2.10. DRYING

The emulsions are soaked for a time of 2 h in each of the five alcohol-water solutions with increasing concentrations of the successive baths by steps of 20%, beginning with 10%. To each solution 5% glycerin is added. Afterwards the emulsions are dried in air of room temperature and about 60—70% atmospheric humidity.

## 3. Apparatus

The laboratory for processing nuclear emulsion stacks consists of six rooms with an area of 162 $m^2$ for mounting, processing, fixing and for the preparation and storage of distilled water and fixing solution (fig. 1).

For mounting the pellicles on the glass a double wall tank of stainless steel is used through which temperature conditioning water can circulate (fig. 2). The dimensions of the inside tank are 65 × 55 $cm^2$. During mounting the glass plates are placed on a lattice (a) of PVC. When the dimensions of pellicles are smaller another smaller tank is used. After mounting the plates are passed through a machine-roller (fig. 3). It consists of a roller (a) coated with soft rubber of 0.4 cm thickness. The roller is driven slowly forward and backward by means of a small motor. The pressure between the roller and the tabletop can be adjusted with four springs (b). The roller can be moved up and down with a lever (c).

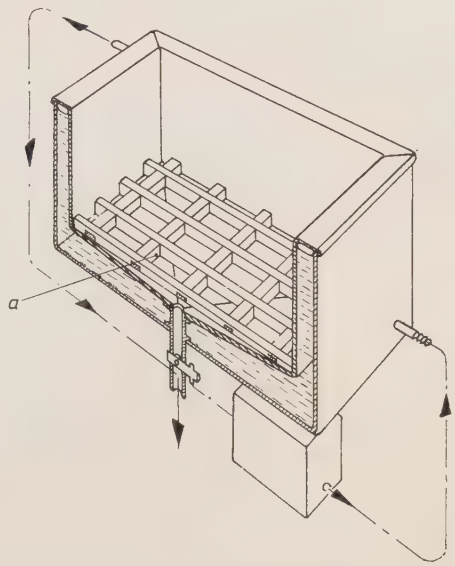


Fig. 2. Double wall tank for mounting.

After the plates have been passed through the roller they are immediately placed on trays of PVC (thickness 8 mm) and fixed there with springs in order to avoid that they swimm about while they are soaked in the diverse solutions. The area of a tray is 54 × 41 $cm^2$. Little disks are fixed on the surfaces of the trays in order to avoid that the plates will stick to the trays. The trays

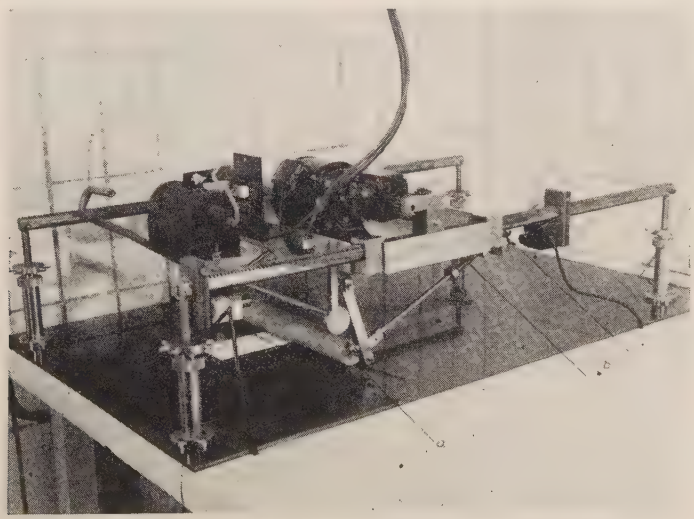

Fig. 3. Machine-roller for mounting pellicles.

(maximal 14) are placed in a rack of stainless steel one upon another and are fixed with pins. Two successive trays are separated by a distance of 1 cm (fig. 4).

3 containers. A cooling liquid circulates through the jackets of the tanks; a contact thermometer controls the function of the pumps and thus the temperature is regulated within the containers

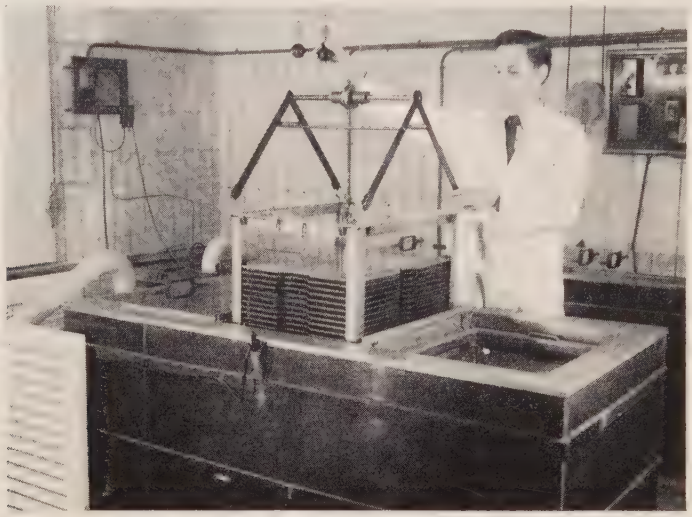

Fig. 4. Double wall tank for the processing steps of low temperature with rack withdrawn.

During the processing steps at low temperature, cooling down of the pellicles, presoaking, cold development, stopbath, and intermediate washing the emulsions are in these racks. For these steps two identical double wall tanks of stainless steel are used (figs 4 and 5). Each tank includes

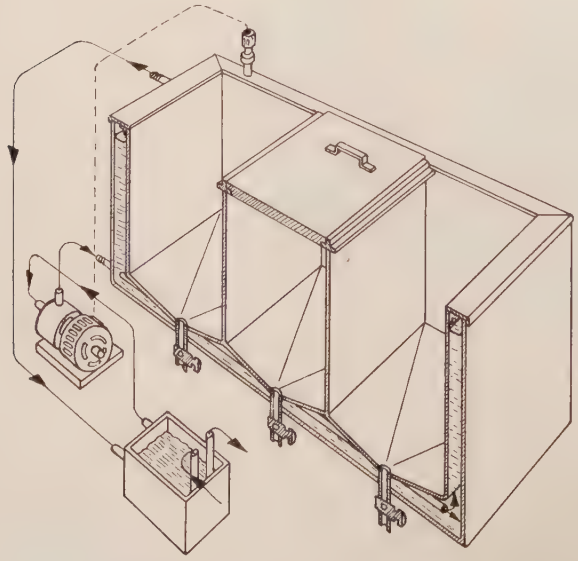

Fig. 5. Cut-away drawing of the tank of fig. 4 with cooling system (schematically).

with an accuracy of $\pm$ 0.2 °C. An electrically driven pulley is used to transport the racks from one container to the next one.

The warm stage of development takes place in a temperature controlled cupboard (fig. 6) with ten sections (each of them has an area of 59 $\times$ 52 cm$^2$). Every section consists of a metal-tub (fig. 7) over which a soft rubber membrane is stretched, so that the glass plates with the pellicles remain in close contact with the rubber kept at a controlled temperature over the whole surface. Each tub is revolving around a tubular axis allowing the water for temperature conditioning to run in and out. In order to put the emulsions in and out the cupboard every section can be opened successively by moving the tubs up or down. When closed the tubs are horizontal and the sections are protected by front plates against the surroundings. The temperature of the rubber membrane and inside the cupboard differs no more than $\pm$ 0.1° C from the fixed value. After the intermediate washing the racks are transported to the fixing room in a lighttight car. For fixing two identical apparatus are used. Each consists of a big rack with ten

trays (fig. 8), made of plastic (Haveg) which is resistant to corrosion. Every tray has an area of 150 × 48 cm². In fig. 9 the arrangement and function of the trays are shown. The fixing solution is pumped from a tank with a cooling coil into the back channel (a), runs through the holes (b) over the pellicles and flows back into the tank. The current velocity of the hypo can be regulated with cocks in front of the channels. The pipe system is similar to that shown in fig. 6. The dilution of hypo and the washing is also done in this apparatus. For the preparation of the fixing

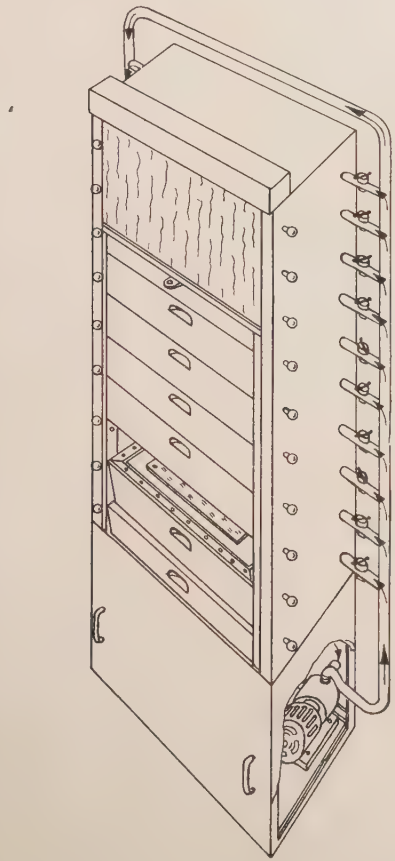

Fig. 6. Cupboard for the warm stage of development.

solution there exist two vessels. In the first vessel water and sodium thiosulphate are mixed by stirring. Then the solution is pumped through a filter into the second vessel and cooled down to a temperature of — 8° C in order to reach afterwards a temperature of about + 5° C in the fixing apparatus. For soaking the emulsions in the alcohol-water solutions they are put in two vessels. Each of them has a volume of 70 l

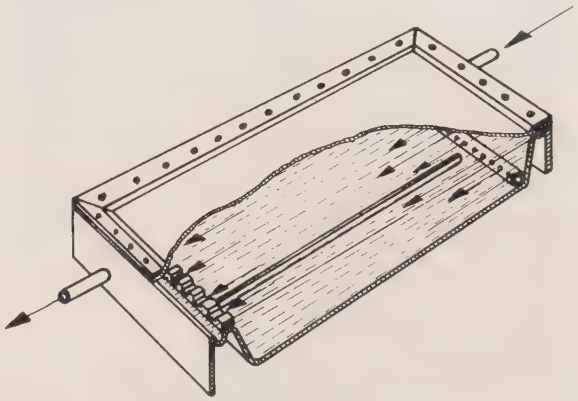

Fig. 7a. Cut-away drawing of the metal-tub of the cupboard shown in fig. 6.

and is able to take up all the emulsions fixed in one of the two fixing apparatus.

3.5 l of emulsion of 400 $\mu$ thickness can be processed simultaneously in the fixing apparatus. The capacity of the cupboard for the warm stage of development is about 0.7 l emulsion; this means that 5 developments are necessary to fill the fixing apparatus. The time difference between the first and the last development is about 15 h and the whole processing from the beginning to its last stage takes five days.

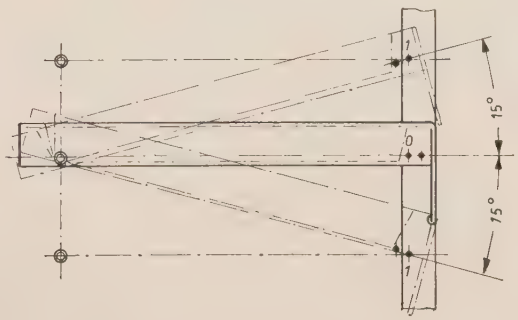


Fig. 7b. Metal-tub in the various positions.

## 4. Results

Until now a number of emulsion stacks have been developed in our laboratory and from this it is evident that the process supplies reproducible results.

After having taken out a representative stack NIKFI R, 400 $\mu$, 10 × 20 cm² we found the following values:

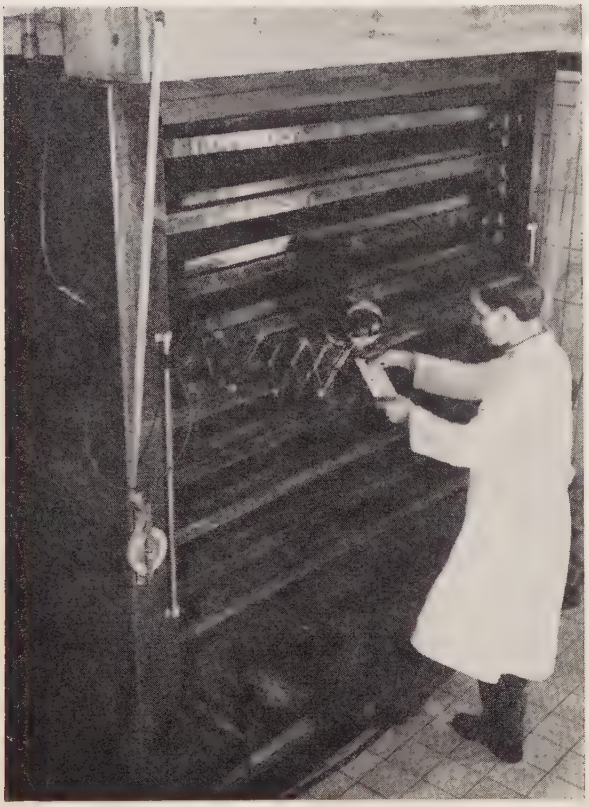

Fig. 8. Fixing apparatus (opened), below the trays the tank with the cooling coil.

The average blob density of tracks with plateau ionisation amounts to 22.7 blobs/100 $\mu$ and the fog is 1.15 grains/1000 $\mu^3$.

The gradient of development is about 5%. This value is calculated as the ratio between the difference of the blob density in the upper and the lower layers (each 30 $\mu$ thick) to the density of the upper layer.

The distortions measured by the method of Cosyns and Vanderhaeghe[5]) amount to about 20$\mu$.

The area of bubbles related to the total area of emulsion is 0.038%.

**Acknowledgement**

The authors wish to thank the autorities of the Amt für Kernforschung und Kerntechnik, der DDR, the Joint Institut for Nuclear Research, Dubna, and the Deutsche Akademie der Wissenschaften zu Berlin, especially the Direction of the Kernphysikalisches Institut for the generous help to accomplish the whole work. Thanks are also due to the Laboratoire de Physique Nucléaire, Université Libre de Bruxelles and to Dr. K. Lanius for stimulating discussions and to Dr. H. Heitler, Bristol, for his valuable correspondence. The authors express their gratitude to G. Nowatzki for the construction of the apparatus and to all those who participated in this work.

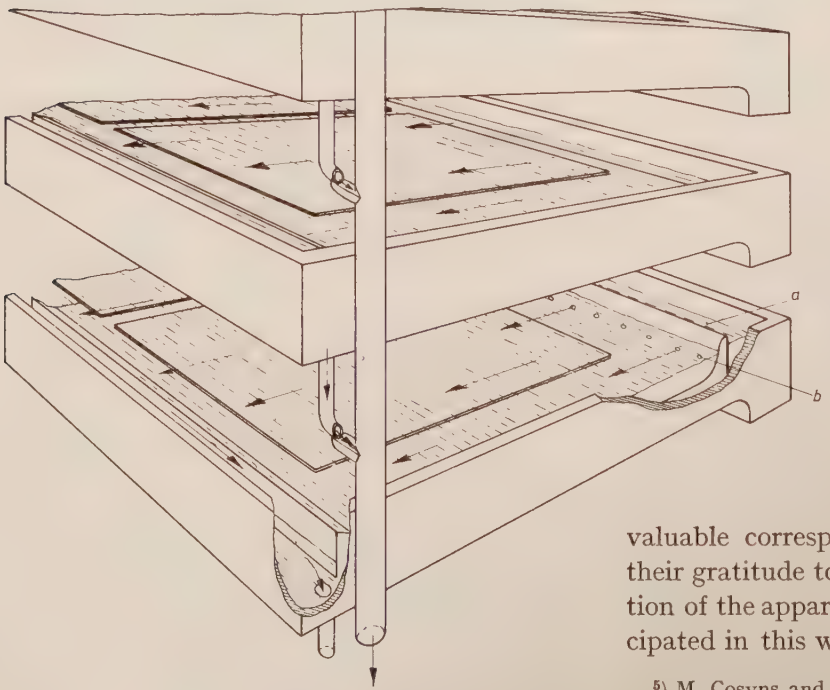


Fig. 9. Detail of fixing apparatus shown in fig. 8.

[5]) M. Cosyns and G. Vanderhaeghe, Bulletin du Centre de Physique Nucléaire de Bruxelles No. 15, (Febr. 1950).

NUCLEAR INSTRUMENTS AND METHODS 8 (1960) 61–69; NORTH-HOLLAND PUBLISHING CO.

# OPTIMUM CONDITIONS FOR DOUBLE FOCUSING BETA RAY SPECTROMETERS

MITSUO SAKAI

*Institute for Nuclear Study, University of Tokyo, Japan*

Received 1 March 1960

Formulas for theoptimum dimensions of the source and the solid angle for the double focusing spectrometer, including the sector type spectrometer, were given in function of the given resolution. The maximum luminosity derived these formulas was compared with each other. It was found that the sector type double focusing spectrometer, of which the field parameters $\alpha$ and $\beta$ are equal to $\frac{1}{2}$ and $\frac{1}{4}$, respectively, has a configuration with very good focusing properties. It has, in sense of the generalized Barber's law, such a configuration that the deflection angle is $\frac{2}{3}\pi$ and the distance between the image and the exit boundary of magnetic field is equal to the reference radius.

The results were also compared with the ordinary semicircular spectrometer, the Konopinski type semicircular spectrometer and the solenoid lens type spectrometer. These kinds of spectrometer have a nearly equal maximum luminosity, about ten times smaller than that of any type of double focusing spectrometer.

## 1. Introduction

The optimum conditions for a beta ray spectrometer have been discussed by several authors. Geoffrion[1]) discussed the optimum conditions for the uniform field semicircular spectrometer and DuMond[2]) for the solenoid lens type spectrometer, taking into account not only the solid angle but also the source dimensions. By using the same treatment, we discussed in the early article[3]) the optimum conditions for the spiral orbit spectrometer[4]) and the characteristics of three types of spectrometer, namely, semicircular, lens type and spiral orbit spectrometer were compared with each other. Verster[5]) discussed the electron optical properties of magnetic beta ray spectrometer and described transmission and luminosity versus line width for the different spectrometers.

In the present article, the theory of optimum conditions was developed and was applied to various types of double focusing beta ray spectrometer[6]), including the sector type double focusing spectrometer[7,8]). Especially the latter type was examined in details, in connection with the INS beta ray spectrometer[9]), in which, for the first time, the sector type double focusing principle was adopted. From this study, it was revealed that there existed a new geometrical setting which had as much good focusing properties as those of the ordinary $\pi\sqrt{2}$ focusing spectrometer. For comparison, the focusing properties of the ordinary semicircular spectrometer, the Konopinski type semicircular spectrometer and the solenoid lens type spectrometer were also discussed. The final results were expressed by the formulas for the optimum dimensions of the source and the solid angle in function of the given resolution. Finally, the usefulness of a spectrometer was discussed from the point of view of the maximum luminosity.

In the next section, the general treatment of the theory of optimum conditions was presented. In section 3, the aberration formula and the resolution formula of the sector type double focusing spectrometer was discussed and new setting was proposed. The aberration formula

[1]) C. Geoffrion, Rev. Sci Instr. **20** (1949) 638.

[2]) J. W. M. DuMond, Rev. Sci. Instr. **20** (1949) 160.

[3]) M. Sakai, Jour. Phys. et Radium **14** (1953) 570.

[4]) G. Miyamoto, Proc. Phys., Math. Soc. Japan, (in Japanse) **17** (1943) 587;
M. Sakai, Jour. Phys. Soc. Japan **5** (1950) 178; **5** (1950) 184.

[5]) N. F. Verster, Progress in Nucl. Phys. **2** (1952) 1.

[6]) K. Siegbahn and N. Svaltholm, Nature, Lond. **157** (1946) 872;
N. Svartholm and K. Siegbahn, Arkiv f. Mat. astro. o. fysik **33A**, No. 21 (1946).

[7]) David L. Judd, Rev. Sci. Instr. **21** (1950) 213.

[8]) E. S. Rosenblum, Rev. Sci. Instr. **21** (1950) 586;
H. Ikegami, Rev. Sci. Instr. **29** (1958) 943.

[9]) M. Sakai and H. Ikegami, Jour. Phys. Soc. Japan **13** (1958) 1076.
T. Yamazaki, H. Ikegami and M. Sakai, Jour. Phys. Soc. Japan **13** (1958) 1080.

and the resolution formula for various $\pi\sqrt{2}$ type double focusing spectrometers were treated in section 4 and those for the semicircular and lens type spectrometer were summarized in section 5. In section 6, according to the general discription presented in section 2, the mathematical formulation was derived and the optimum conditions of the different spectrometers were presented. The dependency of the slit width of the detector on the optimum condition was examined briefly in section 7. The comparison of different spectrometers was made in the last section, and their usefulness was discussed.

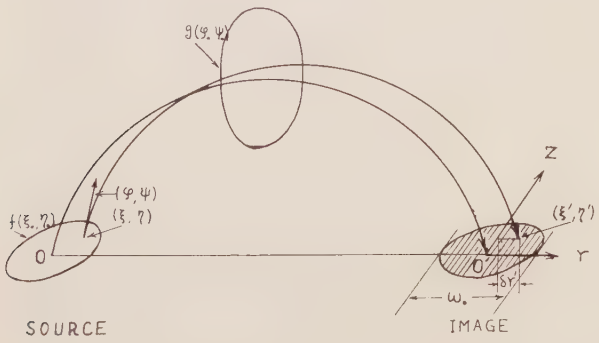


Fig. 1. Electron trajectories in a spectrometer. The coordinates used in the description are shown.

## 2. Presentation of the Problem on Optimum Conditions

For the general presentation of the problem, let us consider the schematical set-up of a spectrometer, shown in fig. 1. The source is assumed to emanate monoenergetic electrons with momentum $p$ uniformly in all directions, to have an area $A$ defined in general by $f(\xi_0,\eta_0) = 0$ and to be viewed by the solid angle $\Omega$, defined by a defining baffle which is expressed approximately by $g(\varphi_0, \psi_0) = 0$, being independent of $\xi_0$ and $\eta_0$. The defining baffle is usually placed at the middle of the electron trajectories. Then the total number of electrons coming from this source through this defining baffle reaching at the detector plane can be expressed as $A\Omega$, which is defined as the luminosity $L$, where the number of monoenergetic electrons emitted by the source in all directions per unit area per unit time is normalized to the unit intensity. In the following discussions all lengths are measured in units of the reference radius, namely, the radius of curvature of electron with momentum $p$ in the magnetic field $H_0$.

After passing though the defining baffle each electron, lavelled by $(\xi, \eta, \varphi, \psi)$, as shown in fig. 1, hits on a point $(\xi', \eta')$ in the detector plane. The assembly of this image point forms the image of the source and its density corresponds to the blackening of photographic plate in a beta ray spectrograph. These circumstances were schematically demonstrated in fig. 1 by a hatched area. In this case the $r$ coordinate is chosen along the right edge of two images of electrons differing in momentum by $\Delta p$, both of which are lavelled by (0, 0, 0, 0) and the $z$ coordinate rectangular to the $r$ coordinate. The origin of this coordinate system is chosen as the image point of the electron of momentum $p$ and the initial condition (0, 0, 0, 0). In general, the height of the detector slit is set along the $z$ coordinate.

Then, the $r$ coordinate of the image point of electron $(\xi, \eta, \varphi, \psi)$ is expressed by

$$\delta r' = a_1\xi + a_2\xi^2 + b_1\eta + b_2\eta^2 + \\ + \alpha_1\varphi + \alpha_2\varphi^2 + \beta_1\psi + \beta_2\psi^2 \\ + \text{second order cross terms of } \xi\eta,\ \varphi\psi \text{ and } \eta\psi \text{ etc.} \\ + \text{heigher order terms.} \qquad (1)$$

This is the ordinary aberration formula. And the formula for the $z$ coordinate can be also written in the same manner. The focusing study in the spectrometer is just to search for the conditions which make the coefficients of terms in eq. (1) as small as possible. Then the maximum value $w_0$ of coordinate of an image (see fig. 1) can be considered as the line width of a monoenergetic electron bundle with momentum $p$ coming from the source through the defining baffle.

Using eq. (1) and introducing the dispersion $D$, the resolution can be defined by

$$\frac{\Delta p}{p} = \frac{w_0}{D} = W_0 \qquad (2)$$

where $\Delta p$ is the difference between the momenta of two groups of monoenergetic electrons, of which the spectrometer gives two images separated just by $w_0$. The resolving power is

defined by the inverse of the resolution. Then, the problem of obtaining the optimum conditions can be reduced to achieving the greatest possible luminosity for a given resolving power. The mathematical treatment will be developed in section 6.

Strictly speaking, this problem setting is not exact, because the effect of the detector slit width should be considered. This effect is treated in section 7. It will be seen in that section that the optimum condition taking into account the effect of slit width is nearly equal to the condition without consideration of that effect. Therefore, the present problem setting might be justified.

In the following three sections, we shall deduce the formulae for $W_0$ and $L$ of the different spectrometers.

## 3. Resolution and Luminosity of Sector Type Double Focusing Spectrometer

The magnetic field in this case is assumed to exist only in a sectorial region between the planes $\vartheta = 0$ and $\vartheta = \Phi$ of a cylindrical polar coordinate system $r$, $\vartheta$ and $z$. In this region the field is assumed to be symmetric about the plane $z = 0$ and to be independent of $\vartheta$. Following Shull and Dennison's equations[10]), the axial and radial components of the field can be expressed by

$$H_z = H_0 [1 - (r-1)\alpha + (r-1)^2 \beta + z^2 (\tfrac{1}{2}\alpha - \beta)] , \quad (3)$$

$$H_r = zH_0 [-\alpha + 2\beta (r-1)] , \quad (4)$$

where $\alpha$ and $\beta$ are the field parameters and $H_0$ is the field at the reference radius. It is a well known fact that we get the double focusing spectrometer for $\alpha = \frac{1}{2}$. In the case of $\Phi = \pi\sqrt{2}$, the spectrometer becomes an ordinary double focusing spectrometer which will be discussed in the next section.

The second order aberration formula for this type of spectrometer was for the first time derived by Rosenblum[8]). Introducing the magnification $M$ into this formula, we get the following second order formula for the case of $\beta = \frac{1}{4}$:

[10]) F. Sull and D. Dennison, Phys. Rev. **71** (1947) 681; Phys. Rev. **72** (1947) 256.

$$\delta r' = +M\delta r + \tfrac{1}{6}(\cos\varphi - 1)\,(1 + \cos\varphi - 2M)\,\delta z^2 + \frac{1}{3}\frac{(2\cos\varphi + 1)}{\sin^2\varphi}\frac{M-1}{M^2}$$
$$[3M - (2\cos\varphi - 1)\,(M^2 + M + 1)]\,\delta\varphi^2 - \frac{1}{3}\frac{1 - M^3}{M^2}\delta\psi^2 - \frac{\sqrt{2}\,(\cos\varphi - 1)}{\sin\varphi}$$
$$[1 + \cos\varphi - M - M^2]\,\delta z\delta\psi , \quad (5)$$

where $M$ is defined as

$$M = \cos\varphi - \tan\varphi'' \sin\varphi , \quad (6)$$

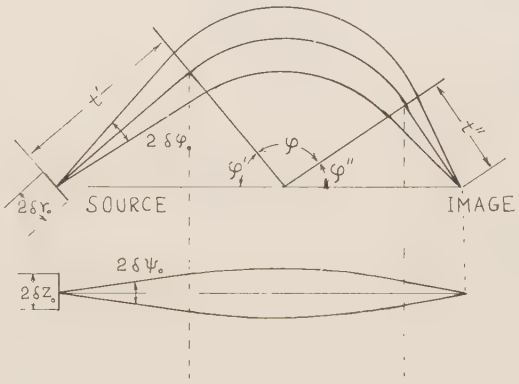


Fig. 2. Geometric relations in the generalized Barber's law. The radial and vertical focusings are presented.

and $\varphi$ and $\varphi''$ are the angles which satisfied the generalized Barber's law, i.e., $\varphi = \Phi/\sqrt{2}$ and $\tan\varphi'' = t'' = T''/\sqrt{2}$ where $\Phi$ and $T''$ are the deflection angle and the distance between the exit pole boundary and the image, respectively (see fig. 2). In this case the initial condition for the electron is denoted by ($\delta r$, $\delta z$, $\delta\varphi$ and $\delta\psi$) instead of by ($\xi$, $\eta$, $\varphi$ and $\psi$) used in section 2. For deriving this equation, $\delta r$ is assumed as the second order small quantity and the terms containing $\delta r$ except that of the first order are neglected. This neglection can be justified since the coefficient of $\delta r$ cannot vanish, and since, as we can see in section 6, in case of the optimum condition, all the terms involved in $W_0$ should be the same order of quantity and since $\delta z$, $\delta\varphi$ and $\delta\psi$ can be regarded as the first order of small quantity.

Now, let us look for the focusing conditions. The third term of eq. (5) can be vanished, no

matter how $\varphi''$ may be, if $\varphi$ satisfied the condition

$$2\cos\varphi + 1 = 0\,, \tag{7}$$

which means that $\varphi = \frac{2}{3}\pi$. Introducing this value into the coefficient of the last term, we get the following condition for vanishing this coefficient:

$$M^2 + M - \tfrac{1}{2} = 0\,. \tag{8}$$

From eq. (6), we get

$$\tan\varphi'' = 1 \tag{9}$$

that is,

$$\varphi'' = \tfrac{1}{4}\pi\,.$$

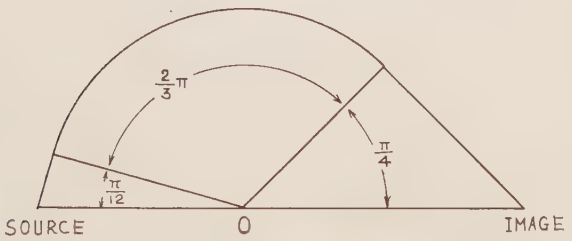


Fig. 3. New sector type double focusing setting with $\alpha = \frac{1}{2}$ and $\beta = \frac{1}{4}$.

Therefore the configuration of the generalized Barber's law becomes a very simple form as presented in fig. 3. And in this case, eq. (5) is given by

$$\delta r' = -\frac{1+\sqrt{3}}{2}\delta r - \frac{2\sqrt{3}+3}{8}\delta z^2 - \frac{3+\sqrt{3}}{2(2+\sqrt{3})}\delta\psi^2\,. \tag{10}$$

Then, the line width $w_0$ becomes

$$w_0 = (1+\sqrt{3})\delta r_0 + \frac{2\sqrt{3}+3}{8}\delta z_0^2 + \frac{3+\sqrt{3}}{2(2+\sqrt{3})}\delta\psi_0^2\,. \tag{11}$$

Since the dispersion $D$ is given by the formula[7])

$$D = 2(1 - M) \tag{12}$$

we get following resolution formula corresponding to eq. (2):

$$W_0 = \frac{1}{\sqrt{3}}\delta r_0 + \frac{2+\sqrt{3}}{8(\sqrt{3}+1)}\delta z_0^2 + \varepsilon\delta\varphi_0^2 + \frac{1}{2(2+\sqrt{3})}\delta\psi^2{}_0 \tag{13}$$

where $\varepsilon$ is the measure of error of focusing adjustment, either of the magnetic field or of the geometrical setting, and this value should be in general one order smaller than the coefficient of the other terms.

The aberration formulas for $\beta = \frac{3}{8}$ and $\beta = \frac{1}{8}$ are also derived and carefully examined. However, no interesting configuration could be obtained, except for $\beta = \frac{3}{8}$, where the aberration formula can be written as follows;

$$W_0 = \left|\frac{\cos\varphi}{(1-\cos\varphi)}\right|\delta r_0 + \left|\frac{\cos\varphi}{8}\right|\delta Z_0^2 + \left|\frac{7\cos^2\varphi + 7\cos\varphi + 4}{12\cos^2\varphi}\right|\delta\varphi_0^2 + \left|\frac{1+\cos\varphi}{4\cos\varphi}\right|\delta\psi_0^2 \tag{14}$$

if the condition

$$\varphi'' = 0$$

is satisfied.

For the INS sector type double focusing spectrometer which has the spectrometer configuration of $\alpha = \frac{1}{2}$, $\beta = \frac{1}{4}$,

$$\varphi = \pi/\sqrt{2} \qquad (\text{i.e., } \Phi = \pi) \quad \text{and} \quad \varphi'' = 0\,,$$

the resolution formula becomes:

$$W_0 = 0.38\,\delta r_0 + 0.133\,\delta z_0^2 + 0.021\,\delta\varphi_0^2 + 0.35\,\delta\psi_0^2 + 1.12\,\delta z_0\delta\psi_0\,. \tag{15}$$

The resolution formula for the same configuration but $\beta = \frac{3}{8}$ can be calculated from eq. (14) and given by

$$W_0 = 0.38\,\delta r_0 + 0.076\,\delta z_0^2 + 0.79\,\delta\varphi_0^2 + 0.192\,\delta\varphi_0^2\,. \tag{16}$$

In all cases treated in this section, the luminosity is expressed by the following equation;

$$L = \frac{4}{\pi}\delta r_0\delta z_0\delta\varphi_0\delta\psi_0\,. \tag{17}$$

## 4. Resolution and Luminosity of $\pi\sqrt{2}$ Double Focusing Spectrometer

According to the ref.[6]), the general resolution formula in this case can be written as follows;

$$W_0 = \tfrac{1}{2}\delta r_0 + \left|\frac{4\beta-3}{12}\right|\delta z_0^2 + \left|\frac{1-8\beta}{6}\right|\delta\varphi_0^2 + \left|\frac{8\beta-3}{6}\right|\delta\psi_0^2\,. \tag{18}$$

Therefore the resolution of the following 4 cases is given by:

for $\beta = \frac{1}{8}$,

$$W_0 = \tfrac{1}{2}\delta r_0 + \tfrac{5}{24}\delta z_0^2 + \varepsilon\delta\varphi_0^2 + \tfrac{1}{3}\delta\psi_0^2 , \qquad (19)$$

for $\beta = \frac{3}{8}$,

$$W_0 = \tfrac{1}{2}\delta r_0 + \tfrac{1}{8}\delta z_0^2 + \tfrac{1}{3}\delta\varphi_0^2 + \varepsilon\delta\psi_0^2 , \qquad (20)$$

for $\beta = \frac{3}{4}$,

$$W_0 = \tfrac{1}{2}\delta r_0 + \varepsilon\delta z_0^2 + \tfrac{5}{6}\delta\varphi_0^2 + \tfrac{1}{2}\delta\psi_0^2 , \qquad (21)$$

for $\beta = \frac{1}{4}$,

$$W_0 = \tfrac{1}{2}\delta r_0 + \tfrac{1}{6}\delta z_0^2 + \tfrac{1}{6}\delta\varphi_0^2 + \tfrac{1}{6}\delta\psi_0^2 . \qquad (22)$$

In the last case, all the electrons, of which the direction $(\delta\varphi, \delta\psi)$ satisfies the condition of

$$\delta\varphi^2 + \delta\psi^2 = \delta\chi^2 \qquad (23)$$

have the same aberration. Therefore, if we set a defining baffle which satisfies the condition of $\delta\varphi_0^2 + \delta\psi_0^2 = \delta\chi_0^2$, eq. (22) can be rewritten by:

$$W_0 = \tfrac{1}{2}\delta r_0 + \tfrac{1}{6}\delta z_0^2 + \tfrac{1}{6}\delta\chi_0^2 . \qquad (24)$$

The meaning of this baffle is to choose a conical electron bundle. We call this special baffle as circular defining baffle. As we shall see in section 6, the use of the circular defining baffle can improve the spectrometer properties largely. Of course, this argument can be applied also to the case of eq. (21) where we have to use an elliptical defining baffle.

The luminosity in the cases of eqs. (19), (20), (21) and (22) has the same formula:

$$L = \frac{4}{\pi}\delta r_0\delta z_0\delta\varphi_0\delta\psi_0 \qquad (25)$$

and in the case of eq. (23), it becomes

$$L = \delta r_0\delta z_0\delta\varphi_0\delta\psi_0 . \qquad (26)$$

## 5. Semicircular Spectrometer and Lens Type Spectrometer

### 5.1. SEMICIRCULAR SPECTROMETER

In this spectrometer the magnetic field is characterized by $\alpha = 0$, corresponding to radial focusing after $\pi$ and no axial focusing.

The resolution formula is given[5]) by

$$W_0 = \delta r_0 + |\beta|\,\delta z_0^2 + \left|\frac{3 + 4\beta}{6}\right|\delta\varphi_0^2 + \left|\frac{1 + (\pi^2 - 4)\beta}{2}\right|\delta\psi_0^2 + |2\pi\beta|\,\delta z_0\delta\psi_0 . \qquad (27)$$

Putting $\beta$ equal to zero, we have the ordinary homogeneous spectrometer and find the formula for $W_0$;

$$W_0 = \delta r_0 + \tfrac{1}{2}\delta\varphi_0^2 + \tfrac{1}{2}\delta\psi_0^2 . \qquad (28)$$

In this case the effect of $\delta z$ can be automatically included in the $\psi$ term in connection of the following condition

$$2\,\delta z_0 = \pi\delta\psi_0 . \qquad (29)$$

Since the solid angle $\Omega$ is $(1/2\pi)\,\delta\varphi_0\,\delta\psi_0$, the luminosity can be given by

$$L = 4\,\delta r_0\delta z_0\frac{1}{2\pi}\delta\varphi_0\delta\psi_0 = \delta r_0\delta\varphi_0\delta\psi_0^2 . \qquad (30)$$

In this case it seems worth noting that the spectrometer properties can be improved by means of a circular defining baffle instead of a ordinary rectangular baffle. It is the same reason as that in case of $\alpha = \frac{1}{2}$ and $\beta = \frac{1}{4}$ mentioned at the end of the preceeding section.

The case of $\beta = -\frac{3}{4}$ was considered by Beiduk and Konopinski[11]) in order to eliminate the radial spherical aberration. Since the dispersion remains unchanged, we obtain

$$W_0 = \delta r_0 + 0.75\,\delta z_0^2 + \varepsilon\delta\varphi_0^2 + 2.70\,\delta\psi_0^2 + 4.7\,\delta z_0\delta\psi_0 . \qquad (31)$$

The luminosity in this case can be expressed by the same formula as eq. (25).

### 5.2. LENS TYPE SPECTROMETER

In general the aberration formula is complicated. In the present article only the simple solenoid spectrometer in which the electrons start in the direction of 45 degree to the symmetrical axis was treated. According to ref. [2]), we have

$$W_0 = 1.12\,\delta r_0 + 2.5\,\delta\varphi_0^2 \qquad (32)$$

and

$$L = \frac{\pi}{\sqrt{2}}\delta r_0^2\delta\varphi_0 . \qquad (33)$$

The results on $W_0$ and $L$ obtained in section 3, 4 and 5 are summerized in table 1.

[11]) F. M. Beiduk and F. J. Konopinski, Rev. Sci. Instr. 19 (1948) 594.

TABLE 1

Dependence of initial conditions on the resolution and the luminosity.

| Setting | $W_0$ | | | | | $L$ |
|---|---|---|---|---|---|---|
| $\alpha$ $\beta$ $\Phi$ | $\delta r_0$ | $\delta z_0$ | $\delta\varphi_0$ | $\delta\psi_0$ | $\delta z_0\,\delta\psi_0$ | $\delta r_0\,\delta z_0\,\delta\varphi_0\,\delta\psi_0$ |
| | $a(n_1)$ | $b(n_2)$ | $\alpha(n_3)$ | $\beta(n_4)$ | $\gamma(1,1)$ | $l(m_1m_2m_3m_4)$ |
| $\frac{1}{2}$ $\frac{1}{4}$ $\frac{2}{3}\sqrt{2}\pi$ | $\frac{1}{\sqrt{3}}$ (1) | $\frac{2+\sqrt{3}}{8\,(1+\sqrt{3})}$ (2) | $\varepsilon$ (2) | $\frac{1}{2\,(2+\sqrt{3})}$ (2) | | $\frac{4}{\pi}$ (1, 1, 1, 1) |
| $\frac{1}{2}$ $\frac{1}{4}$ $\pi$ | 0.38 (1) | 0.133 (2) | 0.021 (2) | 0.35 (2) | 1.12 (1,1) | $\frac{4}{\pi}$ (1, 1, 1, 1) |
| $\frac{1}{2}$ $\frac{3}{8}$ $\pi$ | 0.38 (1) | 0.076 (2) | 0.53 (2) | 0.16 (2) | | $\frac{4}{\pi}$ (1, 1, 1, 1) |
| $\frac{1}{2}$ $\frac{1}{8}$ $\pi\sqrt{2}$ | $\frac{1}{2}$ (1) | $\frac{5}{24}$ (2) | $\varepsilon$ (2) | $\frac{1}{3}$ (2) | | $\frac{4}{\pi}$ (1, 1, 1, 1) |
| $\frac{1}{2}$ $\frac{3}{8}$ $\pi\sqrt{2}$ | $\frac{1}{2}$ (1) | $\frac{1}{8}$ (2) | $\frac{1}{3}$ (2) | $\varepsilon$ (2) | | $\frac{4}{\pi}$ (1, 1, 1, 1) |
| $\frac{1}{2}$ $\frac{3}{4}$ $\pi\sqrt{2}$ | $\frac{1}{2}$ (1) | $\varepsilon$ (2) | $\frac{5}{6}$ (2) | $\frac{1}{2}$ (2) | | $\frac{4}{\pi}$ (1, 1, 1, 1) |
| $\frac{1}{2}$ $\frac{1}{4}$ $\pi\sqrt{2}$ | $\frac{1}{2}$ (1) | $\frac{1}{6}$ (2) | $\frac{1}{6}$ (2) | $\frac{1}{6}$ (2) | | $\frac{4}{\pi}$ (1, 1, 1, 1) |
| $\frac{1}{2}$ $\frac{1}{4}$ $\pi\sqrt{2}$ circular baffle | $\frac{1}{2}$ (1) | $\frac{1}{6}$ (2) | $\frac{1}{6}$ (2) | | | 1 (1, 1, 1, 1) |
| 0 0 $\pi$ | 1 (1) | | $\frac{1}{2}$ (2) | $\frac{1}{2}$ (2) | | 1 (1, 0, 1, 2) |
| $0\ -\frac{3}{4}$ $\pi$ | 1 (1) | 0.75 (2) | $\varepsilon$ (2) | 2.70 (2) | 4.7 (1,1) | $\frac{4}{\pi}$ (1, 1, 1, 1) |
| lens type | 1.12 (1) | | 2.5 (2) | | | $\frac{\pi}{\sqrt{2}}$ (2, 0, 1, 0) |

## 6. Theoretical Formulation for the Optimum Conditions

The out-line of the problem setting was already described in section 2. Since the optimum conditions are those for achieving the greatest possible luminosity $L$ for a given resolution $W_0$, these conditions can be expressed mathematically, by using Lagrange's method of undetermined coefficient, as follows:

$$\frac{\partial U}{\partial \delta r_0}=0\,,\quad \frac{\partial U}{\partial \delta z_0}=0\,,\quad \frac{\partial U}{\partial \delta\varphi_0}=0\,,\quad \frac{\partial U}{\partial \delta\psi_0}=0 \tag{34}$$

where a new function

$$U=W_0+\lambda L \tag{35}$$

is introduced. As seen in table 1, $W$ and $L$ can be written in general as follows:

$$W_0=a\delta r_0{}^{n_1}+b\delta z_0{}^{n_2}+\alpha\delta\varphi_0{}^{n_3}+\beta\delta\psi_0{}^{n_4}+\gamma\delta z_0\delta\psi_0\,. \tag{36}$$

and

$$L=l\delta r_0{}^{m_1}\delta z_0{}^{m_2}\delta\varphi_0{}^{m_3}\delta\psi_0{}^{m_4}\,. \tag{37}$$

Then, the conditions of eq. (34) yield the optimum values of $\delta r_0$, $\delta z_0$, $\delta\varphi_0$ and $\delta\psi_0$ in case of $\gamma=0$. They are:

TABLE 2

Optimum dimensions and maximum luminosity

| Setting $\alpha$ | $\beta$ | $\Phi$ | $\delta r_0$ | $\delta z_0$ | $\delta\varphi_0$ | $\delta\psi_0$ | $L$ |
|---|---|---|---|---|---|---|---|
| $\frac{1}{2}$ | $\frac{1}{4}$ | $\frac{2\sqrt{2}}{3}\pi$ | $3.46\left(\frac{W_0}{5}\right)$ | $2.42\left(\frac{W_0}{5}\right)^{\frac{1}{2}}$ | $\left(\frac{1}{\varepsilon}\right)^{\frac{1}{2}}\left(\frac{W_0}{5}\right)^{\frac{1}{2}}$ | $2.74\left(\frac{W_0}{5}\right)^{\frac{1}{2}}$ | $29.2\left(\frac{1}{\varepsilon}\right)^{\frac{1}{2}}\left(\frac{W_0}{5}\right)^{\frac{5}{2}}$ |
| $\frac{1}{2}$ | $\frac{1}{4}$ | $\pi$ | $5.26\left(\frac{W_0}{5}\right)$ | $1.44\left(\frac{W_0}{5}\right)^{\frac{1}{2}}$ | $6.99\left(\frac{W_0}{5}\right)^{\frac{1}{2}}$ | $0.89\left(\frac{W_0}{5}\right)^{\frac{1}{2}}$ | $59.9\left(\frac{W_0}{5}\right)^{\frac{5}{2}}$ |
| $\frac{1}{2}$ | $\frac{3}{8}$ | $\pi$ | $5.26\left(\frac{W_0}{5}\right)$ | $3.62\left(\frac{W_0}{5}\right)^{\frac{1}{2}}$ | $1.41\left(\frac{W_0}{5}\right)^{\frac{1}{2}}$ | $2.50\left(\frac{W_0}{5}\right)^{\frac{1}{2}}$ | $85.4\left(\frac{W_0}{5}\right)^{\frac{5}{2}}$ |
| $\frac{1}{2}$ | $\frac{1}{8}$ | $\pi\sqrt{2}$ | $4\left(\frac{W_0}{5}\right)$ | $2.19\left(\frac{W_0}{5}\right)^{\frac{1}{2}}$ | $\left(\frac{1}{\varepsilon}\right)^{\frac{1}{2}}\left(\frac{W_0}{5}\right)^{\frac{1}{2}}$ | $1.73\left(\frac{W_0}{5}\right)^{\frac{1}{2}}$ | $19.3\left(\frac{1}{\varepsilon}\right)^{\frac{1}{2}}\left(\frac{W_0}{5}\right)^{\frac{5}{2}}$ |
| $\frac{1}{2}$ | $\frac{3}{8}$ | $\pi\sqrt{2}$ | $4\left(\frac{W_0}{5}\right)$ | $2.83\left(\frac{W_0}{5}\right)^{\frac{1}{2}}$ | $1.73\left(\frac{W_0}{5}\right)^{\frac{1}{2}}$ | $\left(\frac{1}{\varepsilon}\right)^{\frac{1}{2}}\left(\frac{W_0}{5}\right)^{\frac{1}{2}}$ | $25.0\left(\frac{1}{\varepsilon}\right)^{\frac{1}{2}}\left(\frac{W_0}{5}\right)^{\frac{5}{2}}$ |
| $\frac{1}{2}$ | $\frac{3}{4}$ | $\pi\sqrt{2}$ | $4\left(\frac{W_0}{5}\right)$ | $\left(\frac{1}{\varepsilon}\right)^{\frac{1}{2}}\left(\frac{W_0}{5}\right)^{\frac{1}{2}}$ | $1.10\left(\frac{W_0}{5}\right)^{\frac{1}{2}}$ | $1.41\left(\frac{W_0}{5}\right)^{\frac{1}{2}}$ | $10.6\left(\frac{1}{\varepsilon}\right)^{\frac{1}{2}}\left(\frac{W_0}{5}\right)^{\frac{5}{2}}$ |
| $\frac{1}{2}$ | $\frac{1}{4}$ | $\pi\sqrt{2}$ | $4\left(\frac{W_0}{5}\right)$ | $2.45\left(\frac{W_0}{5}\right)^{\frac{1}{2}}$ | $2.45\left(\frac{W_0}{5}\right)^{\frac{1}{2}}$ | $2.45\left(\frac{W_0}{5}\right)^{\frac{1}{2}}$ | $74.6\left(\frac{W_0}{5}\right)^{\frac{5}{2}}$ |
| $\frac{1}{2}$ | $\frac{1}{4}$ | $\pi\sqrt{2}$ circular baffle | $4\left(\frac{W_0}{5}\right)$ | $2.45\left(\frac{W_0}{5}\right)^{\frac{1}{2}}$ | $3.46\left(\frac{W_0}{5}\right)^{\frac{1}{2}}$ | | $117.3\left(\frac{W_0}{5}\right)^{\frac{5}{2}}$ |
| 0 | 0 | $\pi$ | $2\left(\frac{W_0}{5}\right)$ | $3.14\left(\frac{W_0}{5}\right)^{\frac{1}{2}}$ | $1.41\left(\frac{W_0}{5}\right)^{\frac{1}{2}}$ | $2\left(\frac{W_0}{5}\right)^{\frac{1}{2}}$ | $11.3\left(\frac{W_0}{5}\right)^{\frac{5}{2}}$ |
| 0 | $-\frac{3}{4}$ | $\pi$ | $2\left(\frac{W_0}{5}\right)$ | $0.71\left(\frac{W_0}{5}\right)^{\frac{1}{2}}$ | $\left(\frac{1}{\varepsilon}\right)^{\frac{1}{2}}\left(\frac{W_0}{5}\right)^{\frac{1}{2}}$ | $0.37\left(\frac{W_0}{5}\right)^{\frac{1}{2}}$ | $0.675\left(\frac{1}{\varepsilon}\right)^{\frac{1}{2}}\left(\frac{W_0}{5}\right)^{\frac{5}{2}}$ |
| Lens type | | | $3.57\left(\frac{W_0}{5}\right)$ | | $0.63\left(\frac{W_0}{5}\right)^{\frac{1}{2}}$ | | $17.9\left(\frac{W_0}{5}\right)^{\frac{5}{2}}$ |

$$\delta r_0 = \left\{\frac{1}{a}\frac{m_1}{n_1}\frac{W_0}{N}\right\}^{1/n_1}, \tag{38}$$

$$\delta z_0 = \left\{\frac{1}{b}\frac{m_2}{n_2}\frac{W_0}{N}\right\}^{1/n_2}, \tag{39}$$

$$\delta\varphi_0 = \left\{\frac{1}{\alpha}\frac{m_3}{n_3}\frac{W_0}{N}\right\}^{1/n_3}, \tag{40}$$

$$\delta\varphi_0 = \left\{\frac{1}{\beta}\frac{m_4}{n_4}\frac{W_0}{N}\right\}^{1/n_4}, \tag{41}$$

where

$$N = \frac{m_1}{n_1} + \frac{m_2}{n_2} + \frac{m_3}{n_3} + \frac{m_4}{n_4}.$$

The luminosity for this case can be expressed by:

$$L = \left(\frac{1}{a}\frac{m_1}{n_1}\right)^{m_1/n_1}\left(\frac{1}{b}\frac{m_2}{n_2}\right)^{m_2/n_2}\left(\frac{1}{\alpha}\frac{m_3}{n_3}\right)^{m_3/n_3} \times \times \left(\frac{1}{\beta}\frac{m_4}{n_4}\right)^{m_4/n_4}\left(\frac{W_0}{N}\right)^{N}. \tag{42}$$

In case of $\gamma \neq 0$, the derivation of the optimum values is rather complicated. However, in the cases appeared in table 1, namely, in the case of $m_2 = m_4 = 1$ and $n_2 = n_4 = 2$, we have the following simple formulas for the optimum conditions:

$$\delta r_0 = \frac{2}{a}\frac{W_0}{5} \ , \tag{38'}$$

$$\delta z_0 = \left(\frac{\beta}{b}\right)^{\frac{1}{4}} \frac{1}{\{(b\beta)^{\frac{1}{2}} + \frac{1}{2}\gamma\}^{\frac{1}{2}}} \left(\frac{W_0}{5}\right)^{\frac{1}{2}} , \tag{39'}$$

$$\delta\varphi_0 = \left(\frac{1}{\alpha}\right)^{\frac{1}{2}} \left(\frac{W_0}{5}\right)^{\frac{1}{2}} , \tag{40'}$$

$$\delta\psi_0 = \left(\frac{b}{\beta}\right)^{\frac{1}{2}} \frac{1}{\{(b\beta)^{\frac{1}{2}} + \frac{1}{2}\gamma\}^{\frac{1}{2}}} \left(\frac{W_0}{5}\right)^{\frac{1}{2}} , \tag{41'}$$

and the luminosity is

$$L = l\frac{2}{a}\left(\frac{1}{\alpha}\right)^{\frac{1}{4}} \frac{1}{\{(b\beta)^{\frac{1}{2}} + \frac{1}{2}\gamma\}} \left(\frac{W_0}{5}\right)^{\frac{5}{2}} . \tag{42'}$$

This formula demonstrates clearly the effect of $\gamma$-term on the maximum luminosity.

Introducing the values $a$, $b$, $\alpha$, $\beta$ and $l$ into eqs. (38), (39), (40), (41), (42), (38'), (39'), (40'), (41') and (42'), the optimum dimensions for the source and the solid angle and the maximum luminosity can be expressed as a function of $W_0$. The results are tabulated in table 2.

## 7. Optimum Condition for the Detector Slit Width

In the preceding sections we assumed the detector to have a slit of a very narrow width d$f$ and of very long height along $Z$ coordinate.

The intensity distribution curve taken by this detector corresponds to the electron density curve along the image width. This curve can be calculated easily[3]), and the area under it is equal to $L$. As, in reality, we use a detector with finite slit width $f$ in a spectrometer, the effective image width will be enlarged to be $w_0 + f$ and the intensity distribution curve taken by this detector can be obtained by integrating the density distribution curve, in the domain $f$ along the image width. Therefore, the problem should be presented as follows; the peak value $\mathscr{W}$ of the intensity distribution curve is as large as possible at the given effective resolution $\mathscr{W}_0$. Since $\mathscr{W}_0$ and $\mathscr{L}$ can be expressed by the following formulas:

$$\mathscr{W}_0 = W_0 + \tfrac{1}{2}af = W_0' + a\delta r_0 + \frac{1}{2}\frac{a}{|M|}f \tag{43}$$

and

$$\mathscr{L} = \varkappa L = \varkappa \delta r_0^{m_1} L' , \tag{44}$$

the optimum condition for the slit width can be derived from the following formulas:

$$\frac{\partial U'}{\partial f} = \frac{1}{2}\frac{a}{|M|} + \lambda\frac{\partial \varkappa}{\partial f}\delta r_0 m_1 L' = 0 , \tag{45}$$

$$\frac{\partial U'}{\partial \delta r_0} = a + \lambda m_1 \varkappa \delta r_0^{m_1 - 1} L' = 0 , \tag{46}$$

where

$$U' = \mathscr{W}_0 + \lambda \mathscr{L} . \tag{47}$$

Hence, we get

$$2|M|\delta r_0 \frac{\partial \varkappa}{\partial f} = m_1 \varkappa . \tag{48}$$

Since $\varkappa$ is a function of $f$, depending upon the density distribution curve, and since $\varkappa$ is equal to zero in case of $f = 0$, $\varkappa$ can be expressed, as the second order approximation, by

$$\varkappa = C_1 f + C_2 f^2 . \tag{49}$$

Introducing eq. (49) into eq. (48), we have

$$f = \frac{2|M|\delta r_0}{m_1}\left(1 + \frac{C_2}{C_1}\frac{2|M|\delta r_0}{m_1}\right) . \tag{50}$$

In practical purpose, it is sufficient to consider the $f$ value up to the first order, that is,

$$f \approx \frac{2|M|\delta r_0}{m_1} . \tag{51}$$

Since $m_1$ is equal to 1 for all spectrometers except the lens type spectrometer and since $\varkappa$ is about same order of figure in every case, we might discuss the usefulness of the spectrometer by the luminosity $L$ instead of $\mathscr{L}$.

## 8. Discussion

Although it is not exactly the case, the value $L$ numerically derived in section 6 in function of $W_0$ can be considered as a measure of the usefulness of the spectrometers, as it has been proved in the preceding section. Since we can reduce the value of $\varepsilon$ to the order of $10^{-2}$, let us substitute this value for $\varepsilon$ in the formula of $L$.

Now, it is revealed that the new setting of the sector type double focusing spectrometer has a large $L$ value and it is even larger than that in the standard $\pi\sqrt{2}$ spectrometer. Since the field distribution with $\beta = \frac{1}{4}$ can be achieved easily by using a cone type pole face[12]), and since the

[12]) E. Arbman and N. Svartholm, Arkiv. f. Fysik **10** (1956) 1.

source and the detector could be put outside the magnetic field in this type of spectrometer, this setting should be one of the powerful tool not only for the nuclear spectroscopy but also for the charged particle detector in the nuclear reaction experiment.

The INS setting has also been found to have a rather good luminosity which is comparable with that in the $\pi\sqrt{2}$ spectrometer with $\beta = \frac{1}{4}$. Since, for this setting, we can use a long arm between the source and the magnetic boundary, a spectrometer, using the INS setting, should be also one of the important spectrometers in near future, especially for the purpose of electron angular correlation measurement.

So far as the $\pi\sqrt{2}$ spectrometer is concerned, both of the spectrometers with $\beta = \frac{3}{8}$ and $\beta = \frac{1}{8}$ have about the same $L$ value which is nearly three times larger than that of the spectrometers with $\beta = \frac{3}{4}$ and $\beta = \frac{1}{4}$. In the last spectrometer ($\beta = \frac{1}{4}$), it is worth noting that we can improve the $L$ value by $\frac{1}{2}\pi$ times by means of a circular defining baffle.

In the present treatment, the lens type spectrometer has a luminosity 1.5 times larger than that of semicircular spectrometer. The reason of this lies upon the fact that the density distribution curve for the lens type has a trapezoid form while that for the semicircular spectrometer has a triangular form[3]). If the slit width of the detector is taken into consideration, $L$ of semicircular spectrometer can be about twice larger than that of the lens type spectrometer, because, according to eq. (51), the slit width for the former spectrometer can be taken twice wider than that in the latter one. Therefore, we have about the same $\mathscr{L}$ value in both of the spectrometers. This conclusion is consistent with the result obtained in ref. [3]).

It is rather suprising that the Konopinski type spectrometer has a rather small $L$ value which is comparable to that of the ordinary semicircular spectrometer. This is partly due to the large $\gamma$ value which appears in the resolution formula (eq. (31)).

The author wishes to thank Messrs. H. Ikegami and T. Yamazaki for the helpful discussions.

NUCLEAR INSTRUMENTS AND METHODS 8 (1960) 70–72; NORTH-HOLLAND PUBLISHING CO.

# CIRCUIT ALLONGEUR D'IMPULSIONS RAPIDES

A. SARAZIN, J. SAMUELI, G. DUCROS et P. RAIMBAULT

*Institut d'Etudes Nucléaires, Alger*

Reçu le 25 Mars 1960

A pulse lengthener is described meant to be used together with a multichannel analyzer, in order to study the amplitude of pulses in the nanosecond range. The circuit is linear from 0.8 to 14 volts and its recovery time is 0.5 $\mu$s.

Les discriminateurs et les analyseurs d'amplitude sont des appareils très employés dans les expériences de physique nucléaire. Or la détermination de l'amplitude maximum des impulsions électriques fournies par les détecteurs actuels (détecteurs à scintillateurs plastiques, compteurs Čerenkov) est relativement difficile, à cause de la rapidité de ces impulsions.

On demande en effet aux circuits de mesure d'amplitudes de donner une indication de l'amplitude réelle, c'est-à-dire non intégrée, de l'impulsion et ceci indépendamment, si possible, de sa durée et de son temps de montée. Les circuits discriminateurs rapides existant actuellement ne répondent qu'imparfaitement à ce problème, cependant que les analyseurs multicanaux ne peuvent que donner une indication de l'amplitude intégrée de signaux rapides.

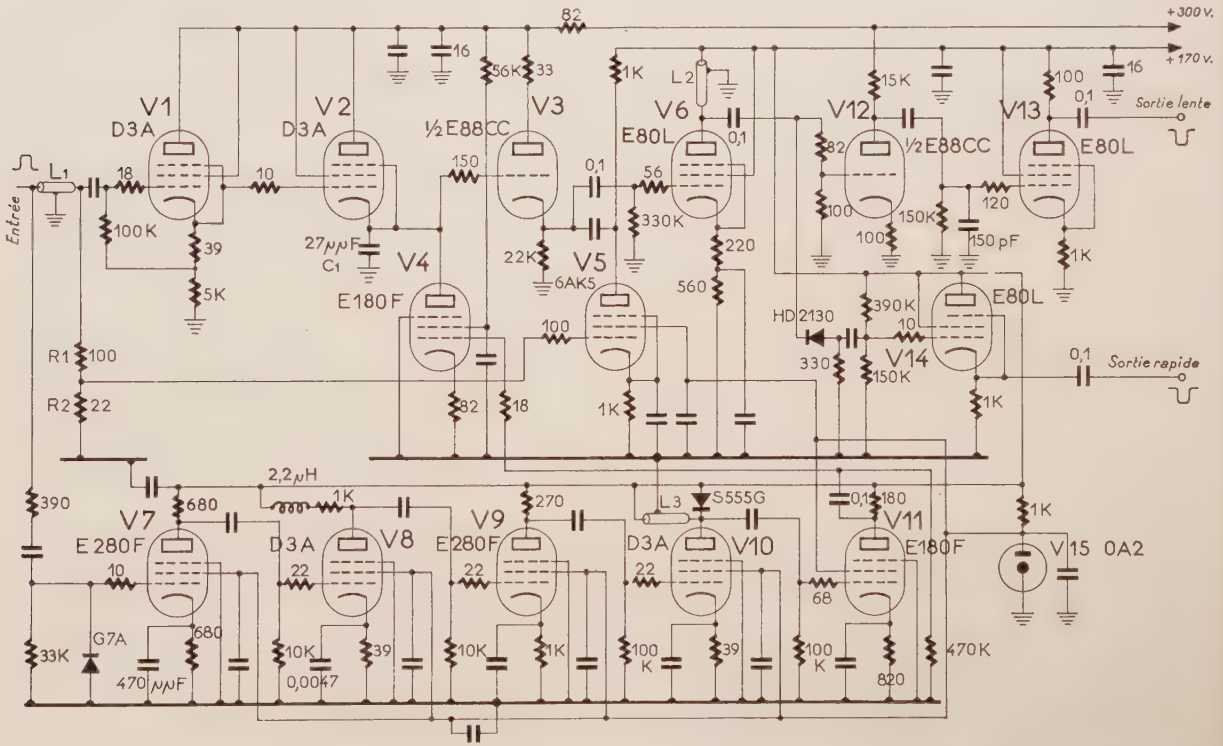


Fig. 1. Schéma général du circuit élargisseur. Toutes les capacités sont des 0.01 microfarad sauf indications contraires; $L_1$: RG 63 U, 4 m. $L_2$: RG 114 U, 12 m. $L_3$: RG 114 U, 12 m.

Une solution à ce problème consiste à réaliser un allongeur d'impulsions, c'est-à-dire un circuit convertissant des signaux rapides en impulsions longues, d'amplitude proportionnelle à l'amplitude cherchée. L'impulsion ainsi obtenue peut être alors envoyée sur un discriminateur classique ou un analyseur multicanaux.

Le circuit que nous décrivons ici est conçu pour recevoir des impulsions de largeur supérieure à $2 \times 10^{-9}$ seconde, d'amplitude comprise entre 0.8 et 14 volts et de temps de montée inférieur à $1.5 \times 10^{-8}$ seconde.

PRINCIPE

Le principe des allongeurs d'impulsions est le suivant: on charge un condensateur à l'amplitude maximum de l'impulsion. Après le passage de l'impulsion le condensateur reste chargé à la même valeur jusqu'à ce qu'on le décharge. De nombreux circuits destinés à des impulsions d'entrée dont la durée est de l'ordre de la microseconde ont été réalisés ces dernières années[1,2]).

[1]) M. A. Meyer, Nuclear Instruments **1** (1957) 62.

[2]) R. W. Schumann, J. P. MacMahon, Rev. Sci. Inst. **27** (1956) 675.

*Détail des circuits.* Le schéma général est donné figure 1. L'élargisseur proprement dit, constitué par les tubes $V_1$, $V_2$, $V_3$ et $V_4$, est prévu pour des impulsions positives. L'impédance d'entrée est de 125 ohms.

Les tubes $V_1$ et $V_2$ chargent le condensateur $C_1$ à l'amplitude maximum du signal d'entrée. Le tube $V_4$ qui contrôle la charge de $C_1$ et qui est normalement débloqué, est à cet effet amené au cut-off par une impulsion provenant d'un circuit de mise en forme déclenché par le signal d'entrée.

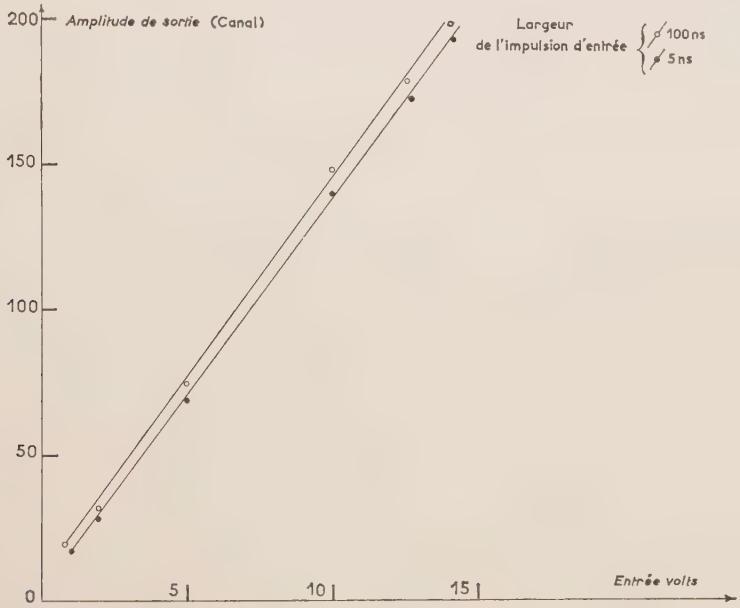


Fig. 2. Réponse du circuit.

L'emploi, pour $V_2$, du tube D3A Siemens de pente 35 mA/V permet d'obtenir une faible constante de temps de charge de $C_1$.

La ligne à retard $L_1$ permet de bloquer $V_4$ quelques millimicrosecondes avant l'arrivée de l'impulsion sur la grille de $V_2$.

Le circuit de mise en forme fournissant le signal envoyé sur la grille de $V_4$ utilise les tubes $V_7$, $V_8$, $V_9$, $V_{10}$ et $V_{11}$. Les trois premiers tubes servent à amplifier et élargir les impulsions d'entrée très courtes. Dans le cas de signaux relativement larges, les faibles valeurs des capacités de découplage de cathode des divers tubes introduisent une contre-réaction sélective qui

limite la largeur des signaux dès le second tube.

L'ensemble $V_7$, $V_8$ et $V_9$, dont $V_8$ est monté en limiteur, permet donc une première standardisation des signaux avant d'attaquer $V_{10}$ dont la charge anodique est une ligne à retard d'impédance 185 ohms. La longueur de cette ligne définit la durée de l'impulsion élargie, soit 120 ns environ. L'impulsion délivrée par la mise en forme est indépendante de la forme du signal d'entrée lorsque ses caractéristiques répondent aux conditions définies plus haut.

Le tube $V_5$ sert à soustraire du signal élargi une impulsion égale à celle qui arrive par capacité sur la grille du cathode follower $V_3$. Pour cela $V_5$ reçoit l'impulsion d'entrée atténuée par le diviseur $R_1$ — $R_2$. Le signal négatif obtenu est envoyé sur la cathode de $V_3$.

Le signal résultant est ensuite coupé par un cable, à 100 ns, dans l'anode de $V_6$. Cette opération est effectuée afin d'éviter une longue descente de l'impulsion, due à la décharge de $C_1$ qui est indésirable.

Deux sorties sont prévues: la première fournit des impulsions négatives rectangulaires allongées à 100 ns. La sortie s'effectue par le cathode follower $V_{14}$.

La seconde donne des impulsions lentes, intégrées par $V_{12}$. Le tube $V_{13}$ sert d'adapteur d'impédance. Cette sortie donne des impulsions négatives utilisables avec des sélecteurs multicanaux à mémoire magnétique.

Les caractéristiques essentielles du circuit sont les suivantes:

Linéarité: le circuit est linéaire entre 0.8 et 14 volts. L'affaiblissement entre des impulsions de 5 et 100 ns de largeur, est inférieur à 1 dB (figure 2).

Temps de recouvrement: le temps de recouvrement de l'élargisseur est de 0.5 $\mu$s.

**Remerciements**

Les auteurs souhaitent exprimer leurs remerciements à M. le Professeur A. Blanc-Lapierre, Directeur de l'Institut d'Etudes Nucléaires d'Alger pour les conseils et l'aide qu'il leur a apportés.

NUCLEAR INSTRUMENTS AND METHODS 8 (1960) 73–75; NORTH-HOLLAND PUBLISHING CO.

# THE EFFECT OF GAMMA-BACKGROUND ON THE $BF_3$ PROPORTIONAL COUNTER

J. CSIKAI and M. BUCZKÓ

ATOMKI *Debrecen, Hungary*

Received 1 March 1960

The integral amplitude distribution of the $BF_3$ proportional counter was found to be changing by the effect of a strong gamma background. In the function of electronic amplification, the distortion of amplitude distribution was investigated with counters of different cathodes. The distortion of amplitude distribution due to the effect of gamma radiation may be explained by the positive space charge developing around the anode.

For the detection of slow neutrons, the $BF_3$ proportional counter is very widely used on account of the favourable cross-section of $B^{10}(n,\alpha)Li^7$ reaction. The neutrons often have to be detected in the presence of intensive gamma radiation, wherefore the effect of gamma background on the operation of $BF_3$ proportional counter was investigated. The investigation is very important from the point of view of determining the absolute neutron intensity as well as of such relative measurements where the intensity of gamma background varies (e.g. the measurement for the slowing down and diffusion lengths of neutrons with Ra–Be or $(\gamma,n)$ sources).

The investigations were carried out by two types of counters ("a", "b"). The walls of the counters were made from soda glass of 0.5 mm thickness. The sensitive volume of the "a" type counter was a 160 mm long cylinder 17 mm in diameter; the anode was tungsten 0.1 mm in diameter; a thin layer of graphite upon the inside surface of the glass wall served the purpose of cathode; the pressure of $BF_3$ gas was 260 mm Hg. The sensitive volume of "b" type counter was a 30 mm long cylinder 9 mm in diameter; the anode was tungsten of 0.1 mm in diameter; a layer of graphite upon the outer surface of the glass wall served as cathode; the pressure of $BF_3$ gas was 200 mm Hg. The $BF_3$ gas was produced by the thermal decomposition of $CaF_2(BF_3)_2$[1]. The electronegative

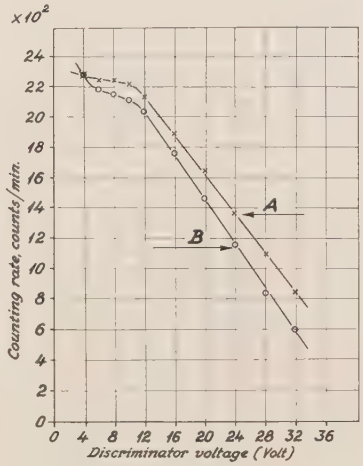


Fig. 1. Integral amplitude distribution of impulses derived from the neutrons: (A) without gamma background, (B) with gamma background.

contamination of the gas—estimated by the length and slope of the plateaux[2])—was not more than that of gas obtained from commercial $BF_3$ gas by two fractional distillations and thermodiffusion. During the investigations, the $BF_3$ counter was placed on the surface of a paraffin cylinder of 30 cm height and 25 cm in diameter, inside of which at 3 cm from the surface, there was a 3 curie Po–Be neutron

[1]) A. C. Graves and D. K. Froman, National Nuclear Energy Series, div. V. 3, 47 (McGraw-Hill Book Company, Inc. New-York, 1952).

[2]) A. Milojević, M. Kurepa and S. Ribnikar, Proceedings of the Second International Conference Geneva, 1958. Vol. 14, p. 325. P/493.

source. $Co^{60}$ isotope was made available for gamma source.

When placing a $Co^{60}$ isotope of 4 mc close by an "a" type counter, the integral amplitude

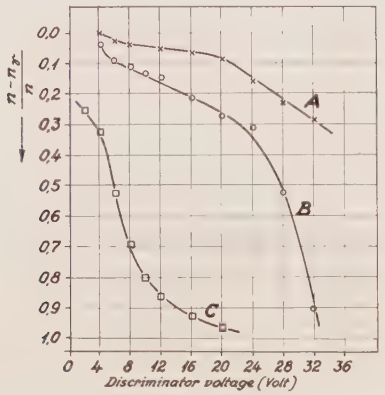


Fig. 2. The effect of gamma background on the operation of counters with different cathodes: (A) internal graphite, (B) internal brass and (C) external graphite.

distribution was found to become distorted by the effect of the strong gamma background. Fig. 1 shows the integral amplitude distribution of the impulses deriving from the neutrons without gamma background (A), and with gamma background (B). The voltage of the counter was 50 V lower than the voltage corresponding to the electron-threshold ($V_e$) and so the impulses produced by the electrons could not be detected. In case of high gamma intensity, the plateau of integral amplitude distribution disappears completely, in consequence of which the impulses produced by the neutrons and gamma rays cannot be seperated.

Under the same conditions, the distortion of amplitude distribution was examined by using counters of different cathodes. Fig. 2 shows the $(n - n_\gamma)/n$ quantity in the function of the discriminator voltage (where n and $n_\gamma$ represent the number of impulses from the neutrons without or with gamma background) when internal graphite (A), internal brass (B) and external graphite (C) cathodes were used. As it can be seen in fig. 2, the effect of gamma background is the smallest in the case of an internal graphite cathode.

The distortion of amplitude distribution was investigated also in the function of electronic amplification. At $V_e - 50$ V counter voltage in each single electronic amplification, the n and $n_\gamma$ values were measured at 10 and 20 V discriminator voltage. In fig. 3, the dependence from electronic amplification of $(n - n_\gamma)/n$ quantities obtained by a "b" type counter is shown when using two gamma sources of different intensities. At 10 (A, C) and 20 (B, D) V discriminator voltage, the A and B curves, were obtained by placing the $Co^{60}$ isotope of 3 mc close by the counter, while C and D curves were produced by placing the $Co^{60}$ isotope of 45 mc at a distance of 1 cm from the counter. As fig. 3 shows, at low electronic amplification, that is, at high gas amplification, the effect of gamma background is quite

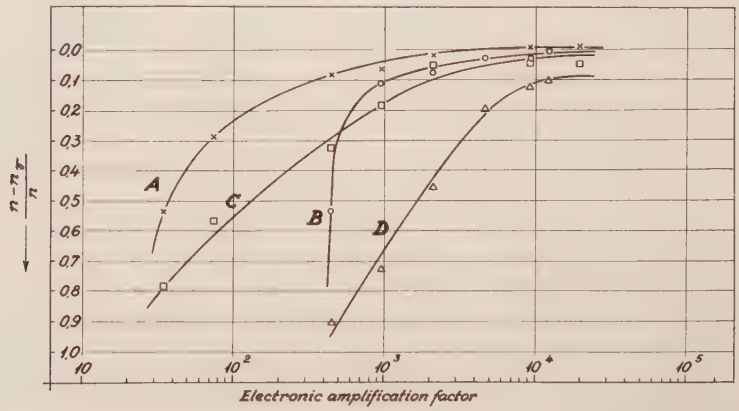


Fig. 3. The effect of gamma background on the amplitude distribution of a "b" type counter, in the case of different electronic amplifications.

significant and decreases to a considerable degree when electronic amplification is increased. For the sake of comparison, in the case of an "a" type counter, too, the $(n - n_\gamma)/n$ quantities were determined as the function of electronic amplification at 10 (C) and 20 (D) V discriminator voltage so that the $Co^{60}$ preparation of 45 mc was placed at a distance of 1 cm from the counter (fig. 4). As it can be seen in figs. 3 and 4, the investigation was made possible by the resolving time of the electronic apparatus.

Around the anode, a positive space charge develops because of electron multiplication. In the case of a given gamma intensity, the greater the value of the gas amplification factor, the greater are the positive space charges. An account of the positive space charges the multiplication of the electrons produced by the alpha particle and recoil nucleus deriving from $B^{10}(n,\alpha)Li^7$ reaction develops in a weaker electric field and thus gas amplification and through it the height of impulses will be

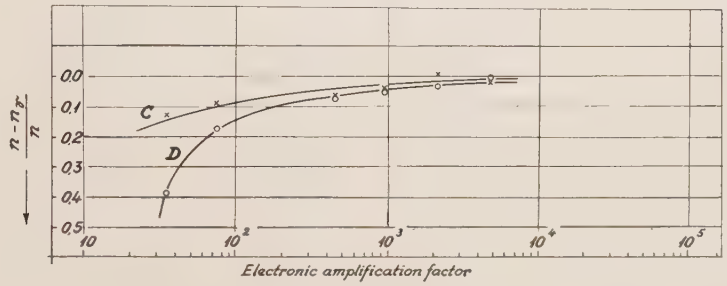


Fig. 4. The effect of gamma background on the amplitude distribution of an "a" type counter, in the case of different electronic amplifications.

The investigation reveals that the effect of gamma background upon the $BF_3$ counter is not negligible and depends on the cathode, the value of the gas amplification factor, the initial order of magnitude of ionization as well as on the intensity of gamma background. Presumably, these are responsible for the discrepancy of the results of measurements obtained[3,4,5]) in a strong gamma background by a $BF_3$ proportional counter and by a method insensitive to the gamma background.

The effect of gamma background upon the $BF_3$ proportional counter may be explained as follows: the great number of electrons produced by intensive gamma radiation multiplies because of gas amplification near the anode. smaller (fig. 1). In this manner, the effect of gamma background also has to decrease together with the decrease in the value of the gas amplification factor. This is actually proved by the data shown in figs. 3 and 4.

The dependence of the gamma background effect on the substance of the cathode can be explained by the fact that the number of electrons ejected from the cathode by the external radiation and by the photons produced during gas amplification—and through this the magnitude of space charges—change with the substance of the cathode. The greater effect on the counter with external cathode can be explained by its greater resolving time.

We are indebted to Prof. A. Szalay, director of this Institute for making these investigations possible. Thanks are due to Mr. B. Schlenk for having planned and constructed the necessary electronic apparatuses.

[3]) L. Nagy and O. Orient, KFKI Közlemények (Comm. Centr. Res. Inst. Phys., Budapest) 2 (1957) 253.

[4]) K. E. Larsson, Ark. f. Fys. 9 (1955) 293.

[5]) R. Montalbetti, L. Katz and J. Goldemberg, Phys. Rev. 91 (1953) 659.

NUCLEAR INSTRUMENTS AND METHODS 8 (1960) 76–78; NORTH-HOLLAND PUBLISHING CO.

# ÜBER DIE BESTIMMUNG DER ZUFÄLLIGEN KOINZIDENZEN IN SCHNELL-LANGSAM-KOINZIDENZ-ANORDNUNGEN

T. MAYER-KUCKUK

*Max Planck Institut für Kernphysik, Heidelberg*

und

R. NIERHAUS

*Kernreaktor Bau- und Betriebs-G.m.b.H., Karlsruhe*

Eingegangen am 28. März 1960

In some applications of fast slow coincidence circuits the random coincidence rate is not small compared with the true coincidence rate. In such cases it is usually necessery to correct for random coincidences. The random coincidence rate is considered as consisting of four parts, the first part corresponding to three randomly coincident pulses at the inputs of the slow triple coincidence circuit, the other parts corresponding to the three possibilities of true coincidences between two pulses at two inputs randomly coincident with a pulse on the third input of the slow circuit. The four parts can be determined separately either by calculation using measured coincidence resolving times,or by counting with delay lines before the inputs of the slow coincidence circuit. The determination of random coincidences only by using a delaying cable before one input of the fast coincidence circuit does not appear appropriate.

Um bei einer Zweifach-Koinzidenzstufe die Zählrate der zufälligen Koinzidenzen zu bestimmen, kann man entweder die Impulse des einen Koinzidenz-Eingangs verzögern, sodass alle systematischen Koinzidenzen ausgeschlossen sind, oder man bestimmt die Zählraten in beiden Koinzidenz-Eingängen und berechnet die Zahl der zufälligen Koinzidenzen hieraus und aus der gemessenen Koinzidenz-Auflösezeit $\tau$. Wenn $N_1$ und $N_2$ die Zählraten an den Koinzidenz-Eingängen bezeichnen, und wenn die Zählrate der systematischen Koinzidenzen $N_s$ genannt wird, dann ist die Zählrate der zufälligen Koinzidenzen $N_z = 2\tau\ (N_1 - N_s)\ (N_2 - N_s)$. Solange $N_1$ und $N_2$ gross gegen $N_s$ sind, ist näherungsweise $N_z = 2\tau N_1 N_2$.

Beide Methoden lassen sich auf Schnell-Langsam-Koinzidenz-Anordnungen übertragen. Abb. 1 zeigt das Blockschaltbild einer solchen Anordnung. Die Eingänge der "langsamen" Koinzidenzstufe sind mit $E_1$, $E_2$, $E_3$ bezeichnet. Auf $E_3$ kommen die Impulse aus der "schnellen" Koinzidenzstufe. Die Zählraten an den Eingängen $E_1$, $E_2$, $E_3$ seien $N_1$, $N_2$, $N_3$. Die Zählrate der zufälligen Koinzidenzen setzt sich aus vier Anteilen zusammen:

(1) zufällige Koinzidenzen zwischen $E_1$, $E_2$ und $E_3$, Zählrate $N_z^{123}$;

(2) zufällige Koinzidenzen zwischen $E_1$ und systematischen Koinzidenzen zwischen $E_2$ und $E_3$, Zählrate $N_z^{1(23)}$;

(3) zufällige Koinzidenzen zwischen $E_2$ und systematischen Koinzidenzen zwischen $E_1$ und $E_3$, Zählrate $N_z^{2(13)}$;

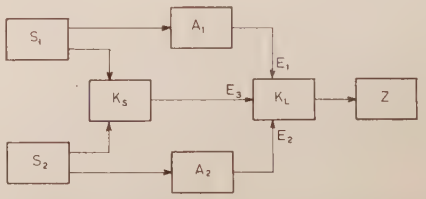


Abb. 1. Prinzipschaltbild einer Schnell-Langsam-Koinzidenz-Anordnung. $S_1$ und $S_2$ sind zwei Szintillationszähler. Rasch ansteigende Impulse daraus werden der schnellen Koinzidenzstufe $K_S$ zugeführt. Energieproportionale Impulse gehen auf die Analysatoren $A_1$ und $A_2$. $A_1$ und $A_2$ bestehen im allgemeinen aus Linearverstärkern mit Einkanal- oder Integral-Diskriminatoren. Auf die langsame Dreifach-Koinzidenzstufe $K_L$ kommen Impulse aus den Analysatoren und aus der schnellen Koinzidenzstufe. Z ist ein Zählgerät.

(4) zufällige Koinzidenzen zwischen $E_3$ und systematischen Koinzidenzen zwischen $E_1$ und $E_2$, Zählrate $N_z^{3(12)}$.

Wenn der Koinzidenzwirkungsgrad der Schnell-Langsam-Koinzidenz-Anordnung 1 ist, dann kann es nicht vorkommen, dass eine systematische Koinzidenz zwischen $E_1$ und $E_2$ vorliegt, die nicht auch systematisch mit $E_3$ koinzidiert. Es verschwindet dann der vierte Anteil.

Die vier Anteile lassen sich mit Verzögerungskabeln einzeln bestimmen. Zur Bestimmung des ersten Anteils braucht man zwei Verzögerungskabel, die man vor irgend zwei der drei Eingänge der langsamen Stufe schaltet, und deren verschiedene Längen so bemessen sind, dass nicht nur systematische Dreifach-Koinzidenzen, sondern auch alle systematischen Zweifach-Koinzidenzen ausgeschlossen sind. Bei der Bestimmung des zweiten Anteils wird man nur die Impulse des Eingangs $E_1$ verzögern. Von der gemessenen Zählrate muss man noch die Zählrate des ersten Anteils abziehen, um die Zählrate des zweiten Anteils zu erhalten. Das liegt daran, dass beim zweiten Anteil die systematischen Koinzidenzen zwischen $E_2$ und $E_3$ Koinzidenzpartner von $E_1$ sind, dass aber bei der Messung alle Koinzidenzen zwischen $E_2$ und $E_3$, d.h. auch die zufälligen Koinzidenzen, als Koinzidenzpartner von $E_1$ auftreten. Zur Bestimmung des dritten Anteils wird man die Impulse des Eingangs $E_2$ verzögern, zur Bestimmung des vierten Anteils die Impulse des Eingangs $E_3$. Die Zählrate des ersten Anteils muss immer subtrahiert werden. In praktischen Fällen werden häufig nur der zweite oder der dritte Anteil oder der zweite und der dritte Anteil eine Rolle spielen.

Es ist nicht möglich, die Zählrate der zufälligen Koinzidenzen dadurch zu bestimmen, dass man vor den einen Eingang der schnellen Koinzidenzstufe ein Verzögerungskabel schaltet. Durch ein solches Kabel würden alle systematischen Koinzidenzen in der schnellen Koinzidenzstufe ausgeschlossen. Ein grosser Beitrag von zufälligen Koinzidenzen rührt aber von Ereignissen her, die zu einer systematischen Koinzidenz in der schnellen Stufe führen.

Die Übertragung der zweiten Methode erfordert die Messung der Zählraten von Zweifach-Koinzidenzen in der langsamen Dreifach-Koinzidenzstufe und die Bestimmung der Koinzidenzauflösezeiten für zufällige Koinzidenzen. Wenn man die Eingangsimpulse an den Eingängen $E_1$, $E_2$, $E_3$ in ausreichender Näherung als Rechteckimpulse der Längen $t_1$, $t_2$, $t_3$ betrachten kann, die im Falle einer Überlappung eine Koinzidenz ergeben, dann ist der erste Anteil der zufälligen Koinzidenzen

$$N_z^{123} = 3\tau^2 N_1 N_2 N_3 \quad \text{mit} \quad 3\tau^2 = t_1 t_2 + t_1 t_3 + t_2 t_3 \dagger .$$

Bei der Bestimmung des zweiten Anteils kann man wieder so vorgehen, dass man die Zählrate der zufälligen Koinzidenzen zwischen $E_1$ und allen Koinzidenzen zwischen $E_2$ und $E_3$ ermittelt und dann den ersten Anteil subtrahiert. Um die Zählrate $N_k^{23}$ der Koinzidenzen zwischen $E_2$ und $E_3$ zu messen, wird der Eingang $E_1$ unwirksam gemacht. Die Zählrate der zufälligen Koinzidenzen zwischen $E_1$ und den Koinzidenzen zwischen $E_2$ und $E_3$ ist

$$N_z^{1(23)} + N_z^{123} = 2\tau_{1(23)}(N_k^{23} - N_s)\, N_1 .$$

$N_s$ bezeichnet die Zählrate der systematischen langsamen Dreifach-Koinzidenzen. Gegen $N_1$ ist $N_s$ vernachlässigt. Um die Koinzidenzauflösezeit $\tau_{1(23)}$ für zufällige Koinzidenzen zwischen $E_1$ und Koinzidenzen zwischen $E_2$ und $E_3$ zu messen, gibt man auf den Eingang $E_1$ Impulse aus einem Impulsgeber oder aus einem Szintillationszähler mit einem unabhängigen Präparat. Wenn dann $N_g^1$ die Zählrate an $E_1$ ist und $N_g^k$ die Koinzidenzzählrate, dann ist

$$\tau_{1(23)} = N_g^k/(2N_g^1 N_k^{23}) .$$

Da im allgemeinen die Impulslängen der Eingangsimpulse bekannt sind, läuft die Messung

† Die Zählrate der zufälligen Koinzidenzen zwischen $E_1$ und $E_2$ ist $N_z^{12} = (t_1 + t_2)\, N_1 N_2$. Wenn z.B. $t_1 < t_2$ ist, hat die Gesamtheit der Koinzidenzimpulse der Länge $< t_1$ die relative Wahrscheinlichkeit $2t_1$, alle Impulslängen $< t_1$ sind gleich wahrscheinlich; Koinzidenzimpulse der Länge $t_1$ haben die relative Wahrscheinlichkeit $t_2 - t_1$. Die mittlere Länge des Koinzidenzimpulses ist daher $t_1 t_2/(t_1 + t_2)$. Die Zählrate des ersten Anteils der zufälligen Koinzidenzen wird

$$N_z^{123} = (t_1 t_2/(t_1 + t_2) + t_3)\, N_z^{12} N_3 = 3\tau^2 N_1 N_2 N_3 .$$

darauf hinaus, dass man den mittleren Überlappungsgrad der koinzidierenden Impulse zwischen $E_2$ und $E_3$ bestimmt. Entsprechendes gilt für den dritten Anteil: Mit einem Impulsgeber oder einem unabhängigen Präparat wird die Koinzidenzauflösezeit $\tau_{2(13)}$ für zufällige Koinzidenzen zwischen $E_2$ und allen Koinzidenzen zwischen $E_1$ und $E_3$ ermittelt. Zur Bestimmung der Zählrate $N_k^{13}$ der Koinzidenzen zwischen $E_1$ und $E_3$ wird $E_2$ unwirksam gemacht. Es wird

$$N_z^{2(13)} = 2\tau_{2(13)} (N_k^{13} - N_s) N_2 - N_z^{123} .$$

Genauso findet man für den vierten Anteil

$$N_z^{3(12)} = 2\tau_{3(12)} (N_k^{12} - N_s) (N_3 - N_s) - N_z^{123} .$$

Die Zählrate aller zufälligen Koinzidenzen ist

$$\begin{aligned} N_z &= N_z^{123} + N_z^{1(23)} + N_z^{2(13)} + N_z^{3(12)} \\ &= 2\tau_{1(23)} (N_k^{23} - N_s) N_1 + 2\tau_{2(13)} (N_k^{13} - N_s) N_2 \\ &\quad + 2\tau_{3(12)} (N_k^{12} - N_s) (N_3 - N_s) - 6\tau^2 N_1 N_2 N_3 . \end{aligned}$$

In vielen Fällen werden $N_k^{23}$, $N_k^{13}$, $N_k^{12}$ und $N_3$ soviel grösser als $N_s$ sein, dass man auf die Subtraktion von $N_s$ verzichten kann. In anderen Fällen kann man für $N_s$ die Zählrate der gemessenen Dreifach-Koinzidenzen $N_k$ einsetzen, insbesondere wenn der Anteil der zufälligen Koinzidenzen nicht sehr gross ist. Der Aufwand einer Iterationsrechnung dürfte im allgemeinen nicht gerechtfertigt sein. Meistens werden nur höchstens zwei der vier Summanden Berücksichtigung verdienen.

NUCLEAR INSTRUMENTS AND METHODS 8 (1960) 79–91; NORTH-HOLLAND PUBLISHING CO.

# NONLINEAR OPERATIONS ON PULSES BY MEANS OF p–n JUNCTIONS

G. GIANNELLI and L. STANCHI

*Centro Studi Nucleari, Ispra, Italy*

Received 15 February 1960

Some researches on the voltage-current characteristics of *p–n* junctions are described. It has been found that by means of a suitable method of using a transistor, its emitter-base junction shows a characteristic that approximates the theoretical one much better than diodes do. In particular some types of transistors have been found whose $i_E$, $v_{EB}$ characteristic is strictly logarithmic over more than five decades of current while selected samples attain six decades. The use of such junctions for multiplying or dividing between them two or more pulses is described and the various problems arising in such application and in more general ones, like exponentials are analyzed.

## 1. Introduction

The method of mass identification of particles, described by Stokes *et al.*[1]) requires to carry out the product of two simultaneous pulses, coming from two detectors traversed by the same particle. The electronic apparatus used to obtain the product, developed by Briscoe[2]), is based on the formula:

$$AB = \tfrac{1}{4}[(A + B)^2 - (A - B)^2] \qquad (1.1)$$

and the squares have been obtained by means of special electronic tubes.

A similar method has been employed by L. Colli *et al.*[3]), see fig. 1. A beam composed of protons, deutons and tritons passes through a proportional counter in which the particles lose a very small part of their energy and then impinge a scintillation counter. The pulse $A$ of the proportional counter is approximately:

$$A \propto \frac{dE}{dx} \propto \frac{m}{E} \qquad (1.2)$$

the pulse $B$ of the scintillation counter is:

$$B \propto E \qquad (1.3)$$

where $E$ is the energy of the particle, $m$ is its mass and $dE/dx$ is the specific energy loss.

The computer executes the product $A \times B$, which is approximately independent of the mass. In this way the single-channel discriminator allows to obtain on the 100-channel

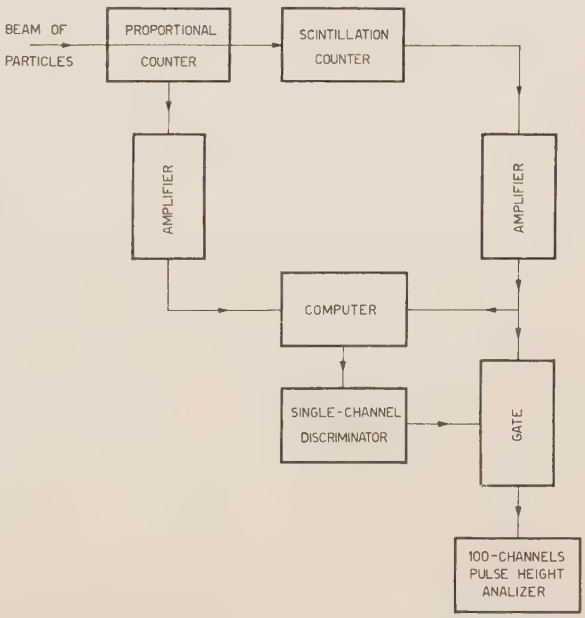


Fig. 1. Block diagram of the electronic set-up for the experiments of L. Colli *et al.*

[1]) R. H. Stokes, J. A. Northrop and K. Boyer, Apparatus for Measuring Energy Spectra of Mass-selected Particles in Coincidence with Fission, Rev. of Sc. Instr. **29** (1958).

[2]) William L. Briscoe, Electronic Computer for Mass Identification of Particles, Rev. of Sc. Instr. **29** (1958).

[3]) L. Colli, F. Cvelbar, S. Micheletti and M. Pignanelli, (n,d) Reactions with 14 MeV Neutron Energy, Il Nuovo Cimento Serie X, Vol. **13** (1959);

L. Colli, F. Cvelbar, S. Micheletti and M. Pignanelli, Structures in the Proton Spectra from (n,p) Reactions, Il Nuovo Cimento Serie X, Vol. **14** (1959);

L. Colli, F. Cvelbar, S. Micheletti and M. Pignanelli, (n,d) Reactions with 14 MeV Neutrons on $^{27}$Al, $^{40}$Ca, $^{55}$Mn, $^{63}$Cu, $^{103}$Rh., Il Nuovo Cimento Serie X, Vol. **14** (1960).

analyzer energy spectra of particles of a single type. A better discrimination in regard to the mass may be obtained with more elaborated operations. The problem is widely discussed by Stokes *et al.*[1]).

In this paper we describe a method for obtaining the product of pulses that we have developed for the experiments of L. Colli *et al.* The method is based on the formula:

$$\ln AB = \ln A + \ln B\,. \tag{1.4}$$

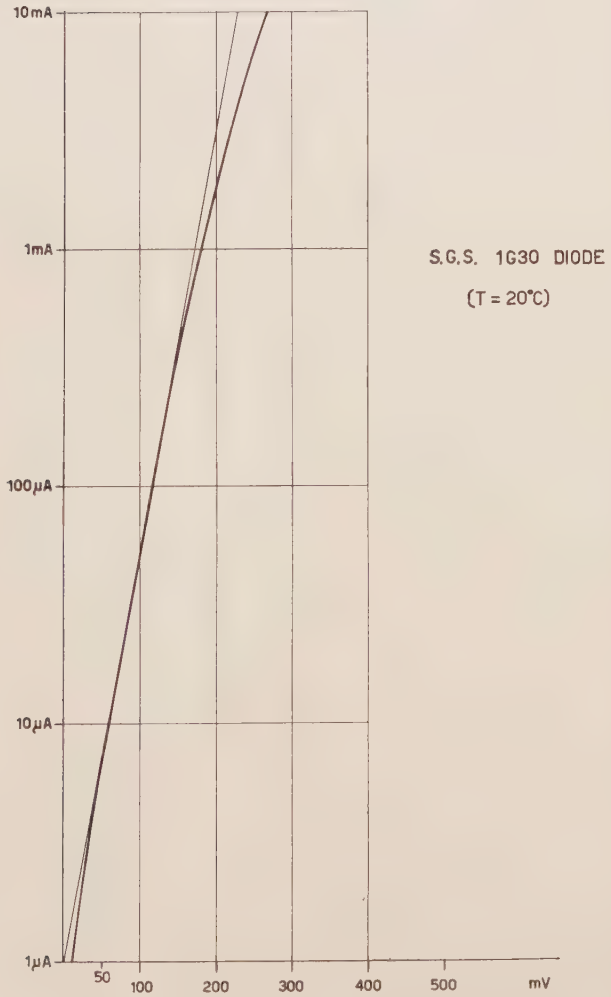


Fig. 2. Characteristic of a Ge junction diode.

This has been possible because we have found a new method to use semiconductor junctions in order to obtain logarithms with precision over a wide range. The method is versatile, it is possible to do in a simple way various mathematical operations and it can possibly find other applications in nuclear physics.

## 2. Method Used to Obtain the Logarithm

As well known the range of validity of the equation of the junction diode deduced by the linear theory[4]):

$$i = I_0 e^{\vartheta v} - I_0 \tag{2.1}$$

with $\vartheta = q/kT$ and $I_0$ constant at a given temperature, is limited. In the germanium it does not extend to the high injection levels, while in the silicon it does not nearly exist at room temperature. The studies on the divergences of the actual characteristics from (2.1) have been reviewed by J. L. Moll[5]). In the silicon, at low currents, the current produced by generation of charges in the depletion layer becomes appreciable in respect to the values given by (2.1). This phenomenon would appear also in the germanium at low temperature. At high currents, both in germanium and in silicon, the actual characteristics may be interpreted by a law of the type (2.1) but with a value $\vartheta = q/2kT$, and is explained by the phenomenon of the conductivity modulation in the less doped material. In addition, the effect of the ohmic resistance of the junction materials becomes appreciable at high currents. Finally for a logarithmic conversion it is necessary to restrict the range to values of current sufficiently greater than $I_0$.

In fig. 2 we give the measured characteristic of a germanium junction diode that is typical of a class of examined diodes. This characteristic in the semilogarithmic diagram is never truly rectilinear.

We thought that we would obtain better results with the use of the emitter-base junction of a germanium transistor, with the collector

[4]) W. Shockley, The Theory of p—n Junctions in Semiconductors and p—n Junction Transistors, The Bell Syst. Techn. J. **28** (1949).

[5]) J. L. Moll, The Evolution of the Theory for the Voltage-Current Characteristic of p–n Junctions, Proc. I.R.E. **46** (1958);

See also E. Baldinger, W. Czaja and M. Nicolet, Der Einfluss nichtidealer Emitterübergänge auf das Verhalten von Flächentransistoren, Helvetica Physica Acta **29** (1956) 428.

nversely biased at constant voltage (fig. 3). The chief reasons were: (a) in the low current region we should have a decrease of importance of the second term of the right-hand side of the (2.1).

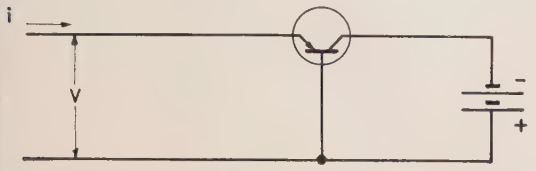


Fig. 3. Connection of transistors which for the emitter-base unction gives a characteristic that is logarithmic over a wide range.

The equation for such a junction, that is calculated in the Appendix A, is:

$$i_E = I_{ES}\, e^{qv_{EB}/kT} - \rho I_{ES} \qquad (2.2)$$

where $\rho = 1 - \alpha = \alpha/\beta$ and $\alpha$ and $\beta$ are respectively the common-base and common-emitter current gains of the transistor.

(b) at high currents should be less the influence of the series resistance which in this case is the base spreading resistance divided per $\beta$. Besides in the base of transistors the conductivity modulation, which strongly influences the current gain[6]), should not appreciably affect the relation between the concentration at the emitter junction and the current. This relation is determined by the width of the base while in diodes is function of the diffusion length which is affected by conductivity modulation.

We have measured the characteristics $i_E$, $v_{EB}$ of six types of $p$–$n$–$p$ and $n$–$p$–$n$ alloy-junction transistors. The best results have been obtained with transistors 2N404, whose characteristics have been measured on 14 samples. The characteristics of the best sample, of the worst and of a typical one are shown in fig. 4. The characteristics are accurately logarithmic in a range that in the worst sample is of two decades and in the best one is of four. Moreover we have noted that in all the samples the logarithmic range includes the two decades from 10 $\mu$A to 1 mA. The semilogarithmic slope of the characteristics is exactly equal to the theoretical value.

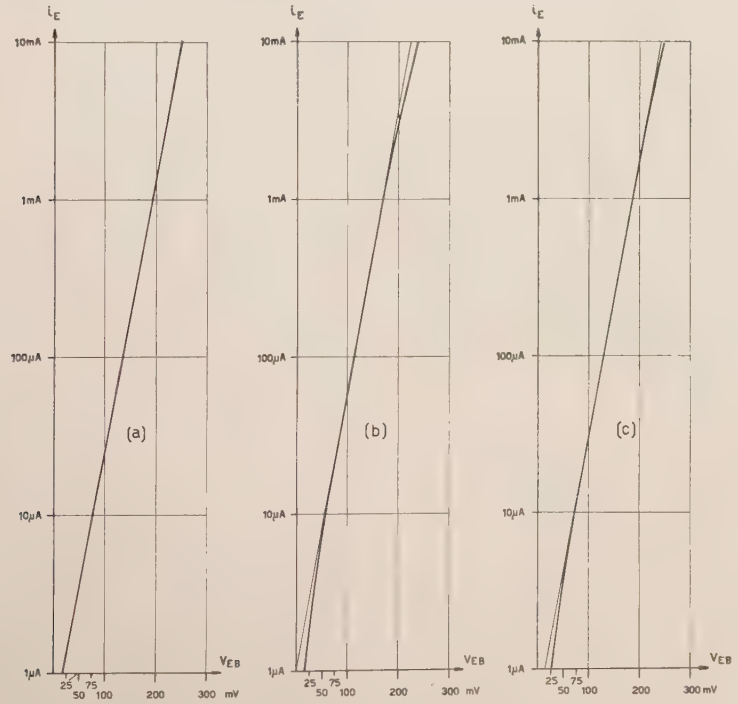


Fig. 4. Voltage-current characteristics of R.C.A. alloy-junction transistors type 2N404 at $V_{CB} = -2$ V and $T = 20$ °C. (a) best sample which shows a logarithmic range of four decades, (b) worst sample: two decades, (c) typical sample.

The characteristic at high currents has been studied on a sample. The voltage difference between the characteristic and the extrapolated logarithmic line is shown in fig. 5 as a function of the base current and it is seen that the difference from the characteristic as given by eq. (2.2) is fully explained by a simple

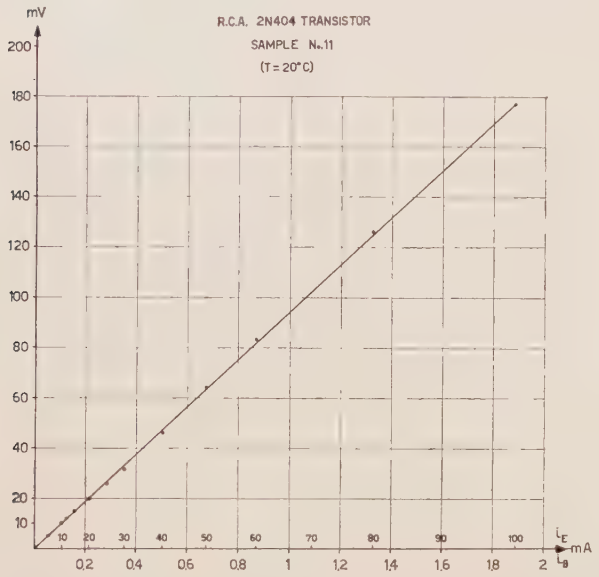


Fig. 5. Difference between the measured emitter-base voltage and the junction voltage calculated extrapolating the low-current characteristic, plotted against base current. This diagram shows that difference between the external characteristic and the theoretical characteristic of the junction is fully explained by an ohmic resistance in series to the junction.

ohmic resistance of the value of 94 ohms that we interpret as the base spreading resistance $r_{BB'}$ through which the base current flows.

In the samples we have examined the term $I_{ES}$ varies between 0.5 and 1.1 $\mu$A at 20° C. The low limit of the logarithmic range is somewhat greater than the value of $I_{ES}$. We think that this limited advantage in respect to the diodes is due to the fact that at low current $\beta$ decreases[6]) so that the advantage due to the coefficient $\rho$ in eq. (2.2) is reduced.

The drift transistors give markedly superior results. The logarithmic range at the low current side extends down to values practically equal to $I_{ES}$ and at the high current side up to values somewhat higher to those found on alloy-junction transistors; in addition they have much smaller values of $I_{ES}$. Measurements on five samples of drift transistors type 2N274 have shown a logarithmic range of four decades: from $10^{-6}$ to $10^{-2}$ A (at 20° C). Measurements on five samples of drift transistors type 2N384 have shown a logarithmic range greater than five decades, common to all the samples examined, and values of $I_{ES}$ between 0.015 and 0.05 $\mu$A (at 20° C). A typical characteristic is shown in fig. 6. All the measurements have been made with transistors immersed in oil and thermostated with the precision of $\pm$ 0.1° C. Moreover at high currents the measurements have been carried out in such a way that errors due to self-heating of the junction did not affect the precision of the measures.

The logarithmic range is influenced by the temperature and by the collector voltage. The temperature affects only the lower limit, which varies with $I_{ES}$. The collector voltage affects only the higher limit, which increases with it. For the 2N384 with $V_{CB} = -2$V, the higher limit of the logarithmic range common to all samples is $10^{-2}$ A.

We call conversion junction the emitter-base junction of a transistor employed as in the diagram of fig. 3 in order to obtain the logarithmic conversion of pulses. We represent its characteristic in the logarithmic region by the equation:

$$v_{EB} = A \ln \frac{i}{I_0} \tag{2.3}$$

where $v_{EB}$ is the emitter-base voltage

$i$ is the total emitter input current

$A$ and $I_0$ are parameters which depend on the temperature. A results equal to the theoretical value (25 mV at 20° C); $I_0$ which substitutes $I_{ES}$ of the formula (2.2), varies from a sample to another.

### 3. Polarization of the Conversion Junctions

The term $I_0$ of eq. (2.3) varies strongly with temperature and is different from a sample to

[6]) W. M. Webster, On the Variation of Junction-Transistor Current-Amplification Factor with Emitter Current, Proc. I.R.E. **42** (1954).

another. It is possible to obtain a logarithmic characteristic with a fixed value of $I_0$ by the use of a particular method of polarization. This method consists in polarizing the conversion junction with a constant current $I_P$ that is set to zero each time a pulse arrives and for the whole duration of the pulse. In this way the amplitude $v_S$ of the output voltage pulse is the difference between the voltage $v_{tot}$ produced by the input pulse of current $i_S$ and the voltage $V_P$ existing across the junction before and after the pulse that is the voltage due to the current $I_P$:

$$v_S = v_{tot} - V_P \tag{3.1}$$

$$i_S = I_0 \left(e^{v_{tot}/A} - \rho\right) = I_0 \left[e^{(v_S + V_P)/A} - \rho\right] \tag{3.2}$$

$$I_P = I_0 \left(e^{V_P/A} - \rho\right) . \tag{3.3}$$

From these we obtain:

$$i_S = I_0 \left[\frac{I_P + \rho I_0}{I_0} e^{v_S/A} - \rho\right] =$$

$$= (I_P + \rho I_0) \left[e^{v_S/A} - \frac{\rho I_0}{I_P + \rho I_0}\right] . \tag{3.4}$$

With the normal values for drift transistors the order of magnitude of

$$10^{-9} \text{ A} \quad \text{and} \quad \rho I_0/(I_P + \rho I_0)$$

for $I_P \geqslant 1\ \mu$A is absolutely negligible, so that the relation $v_S$, $i_S$ is practically independent from $I_0$. This simplifies the problems of temperature compensation, because the temperature effect appears only in the $A$ term. In addition the substitution of the constant $I_0$ proper of the junction with an arbitrary constant $I_P$ gives more freedom for satisfying the various requirements and in particular allows to choose the most suitable dynamic range of the output signal $v_S$.

## 4. Problems of the Application of the Method

In the case of pulses applied to a conversion junction, eq. (2.3) is valid for the istantaneous values only if the rise time of the pulses is sufficiently larger than the rise time of the conversion junction that is determined by the $\alpha$ cut-off frequency of the transistor. The parameter of the pulse which is of interest is always the amplitude and therefore all the operations must result as operations on the amplitudes.

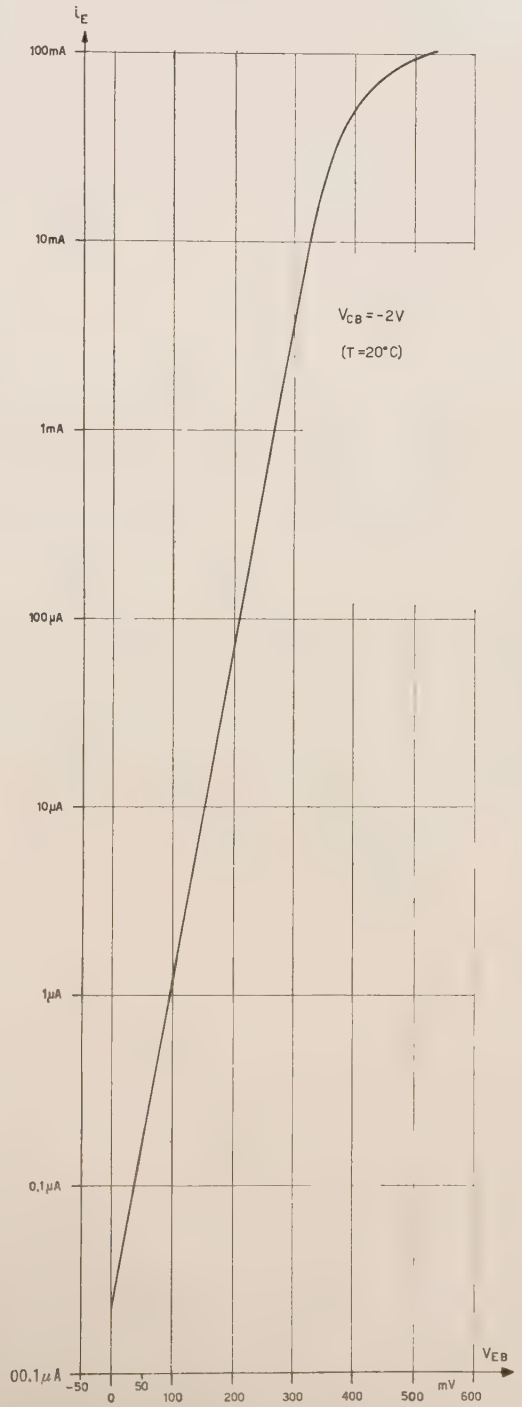


Fig. 6. Typical voltage-current characteristic of R.C.A. drift transistor 2N384.

To do so the maxima of the pulses must be simultaneous. The best way (but not the only one) to satisfy these two requirements is to work with rectangular pulses having a duration larger than both the conversion junction rise time and

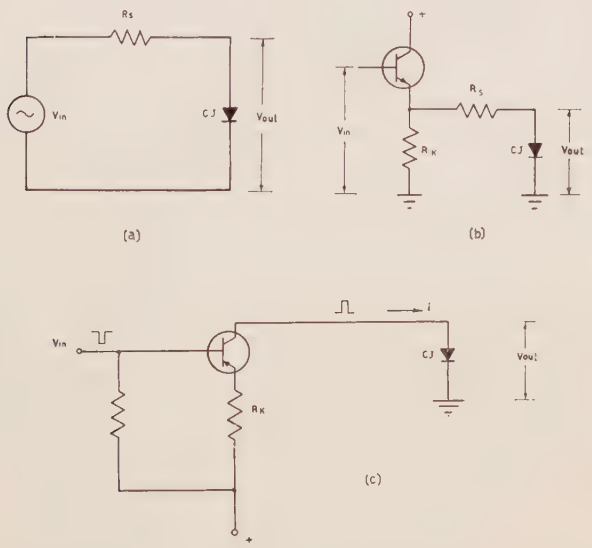


Fig. 7.
Methods for current driving the conversion junctions CJ.

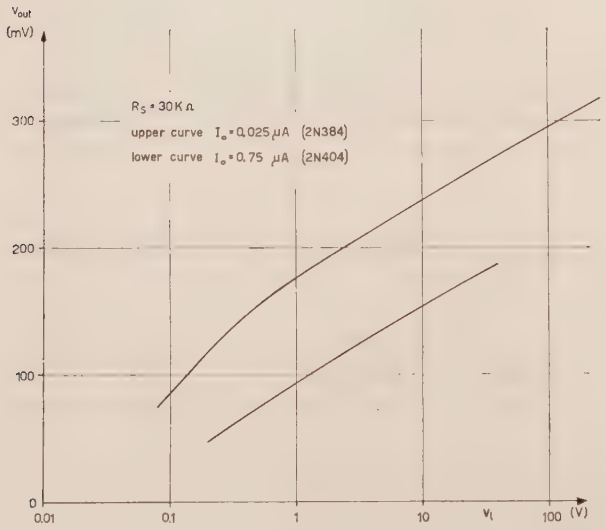


Fig. 8. Characteristic of the circuit of fig. 7(a) calculated from eqs. (4.1) for a typical 2N404 and a typical 2N384 transistors.

the difference in the rise times of the detectors, or generally than the coincidence time of the pulses as defined for each experiment.

For obtaining the logarithm the conversion junction must be driven by a current generator that must have particular requirements. Essentially it must: (a) supply pulses of a single sign because the negative signals produce high negative voltages (theoretically infinite) across the junction; (b) have an internal resistance much higher than the maximum junction resistance in the working range; (c) have an output current equal to zero when signals are not present. We examined many solutions. The simplest (fig. 7a) is a voltage generator $v_{in}$ transformed in a current generator by means of a high series resistance $R_s$. There is an error due to the voltage drop on the conversion junction, which is subtracted from $v_{in}$. The relation between the input voltage $v_{in}$ and the output voltage $v_{out}$ is given by the system:

$$\begin{cases} v_{out} = A \ln \dfrac{i}{I_0} \\ v_{in} = R_s i + v_{out} . \end{cases} \tag{4.1}$$

The resulting characteristics, similar to the type shown in fig. 8, are analyzed in the Appendix B.

In order to minimize the error, $v_{in}$ must be much greater than $v_{out}$, thus this method can be used only with limited dynamic ranges. In this case it appears more convenient to use the 2N404 transistors than the 2N384 ones, because the 2N404 may be used at higher currents with lower impedance levels.

The voltage generator may be an emitter follower (fig. 7b) with base-emitter voltage equal to zero in the quiescent state. In this case there is another error due to the base-emitter voltage drop in the emitter-follower. It is not possible to use an electronic tube cathode follower.

High precisions may be obtained by more elaborated systems. One could think of amplifiers with current feed-back, or of amplifiers with voltage feed-back where in the latter the voltage across the conversion junction is added to the input as in the diagram of fig. 9, but it is easy to see that these two methods are actually simply different ways of viewing the same

diagram. We point out that the more simple current feed-back amplifier, that is a transistor with emitter feed-back resistance and output taken from the collector, see fig. 7c, drives to errors of the same type of those of the circuit of fig. 7a because of the drop in the base-emitter junction of the transistor itself. Here $R_s$ is substituted by the emitter feed-back resistance $R_k$.

Finally another cause of error to take into account is the load applied to the conversion junction by the utilizer circuit.

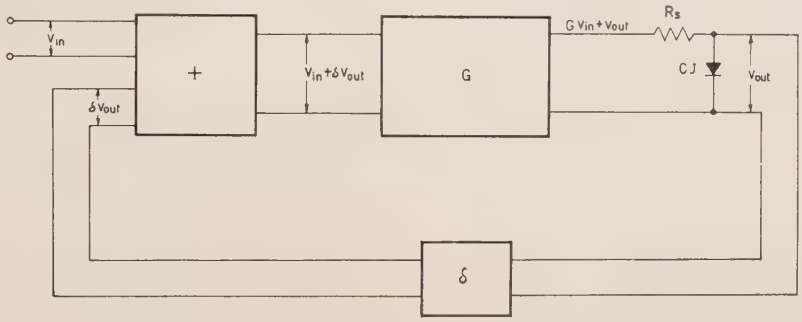


Fig. 9. System for compensating the voltage drop on the conversion junction CJ driven by a low output impedance amplifier through the resistance $R_s$. It is required that $\delta = 1/G$, then the voltage across $R_s$ will be:
$G\,(v_{in} + \delta v_{out}) - v_{out} = Gv_{in}$ .

## 5. Arithmetical Operations with the Conversion Junctions

On the logarithm pulses (that is the pulses proportional to the logarithm of the amplitude of the input pulses) all linear operations can be performed in a quite conventional way. In a general way, by means of an adder, a pulse will be obtained whose amplitude $v_u$ is proportional to $\ln u$, and $u$ is given by the formula:

$$u = k_0 \prod_1^n{}_i\, (a_i + k_i)^{h_i} \qquad (5.1)$$

here the $a_i$ are numbers proportional to the amplitudes $i_i$ of the input pulses and $k_0$, $k_i$, $h_i$ are constants. The constants $k_i$ are obtained by adding to the pulses $a_i$ pulses of constant amplitude and simultaneous to them.

In the quite general case when at least one of the $k_i$ is equal to zero it is necessary to provide a system that maintains the output at the zero value whenever one of the pulses $a_j$ whose corresponding $k_j$ is zero, is absent. That because the physical system cannot represent logarithms of zeroes. This requirement is satisfied by a coincidence among the input pulses that controls a gate on the output pulse. Since the logarithmic characteristic holds only in a finite range the system must in addition supply the output pulse only when the input pulses $(a_i + k_i)$ are within the logarithmic range.

In the particular case of the simple division of two pulses, if the input pulses have the same shape, that is they are defined by the same time function and are simultaneous, in the time interval in which the instantaneous values of both pulses fall in the logarithmic characteristic the output pulse is horizontal. If the above-mentioned conditions are not satisfied and even if the maxima are simultaneous, spikes higher than the horizontal portion can be produced in

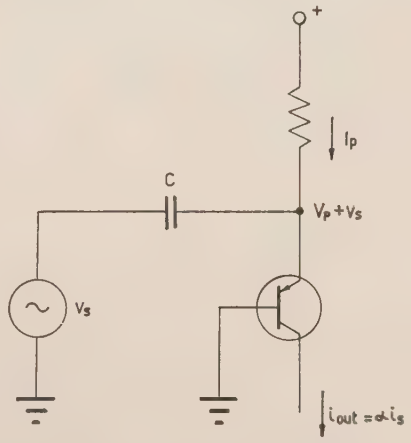


Fig. 10. Principle of voltage driving a conversion junction polarized with constant current with the method of section 3.

correspondence to the rise and decay of the pulses and it is necessary to operate with rectangular pulses and to isolate the horizontal portion by suitable linear gate systems[7]). Similar phenomena can occur in correspondence of the interval of time where one or both the pulses are out of the logarithmic region. Also operations of type (5.1) can give the same type of phenomena when some $h_i$ are smaller than zero.

The product of the pulses $(a_i + k_i)^{h_i}$ may be greater or smaller than unity and the corresponding logarithm pulse will be positive or negative. If this pulse is to be sent to a conversion junction in order to obtain the quantity $u$ no change of sign is allowed. The constant $k_0$ of eq. (5.1) has been inserted to take care of that. This may be necessary even when the logarithm pulse is directly utilized.

### 6. Operations on Pulses ln *u*

In many cases the pulse $\ln u$ given by (5.1) may be directly used; it can be analyzed by a pulse-height analyzer in order to obtain a spectrum having constant resolution in $u$. If it is necessary to obtain the pulse $u$ a conversion junction voltage driven by the pulse $\ln u$ can be used and the pulse of current proportional to $u$ is taken from the collector. Problems about the extension of the dynamic range can arise because if the dynamic range of the input pulses $a_i$ is of $p$ decades, the dynamic range of the pulse $u$ will be of:

$$p \sum_1^n{}_i |\, h_i \,|$$

decades but for corrections due to the $k_i$. Generally the dynamic range that may be used with a conversion junction shall be smaller, i.e. of the order of the one of the pulses $a_i$, and it may be chosen on the $p \sum h_i$ decades by subtracting from the pulse $v_u$ proportional to $\ln u$ a pulse of suitable amplitude.

Between the conversion junction which supplies the output pulse of amplitude $u$ and those which operate on the input pulses there is some temperature compensation and precisely are eliminated only the variations due to the parameter $A$ of eqs. (4.1) not those due to $I_0$. If all the conversion junctions are polarized following the method described in section 3 a complete temperature compensation is obtained.

In order to apply this type of polarization to junctions used for conversion from logarithms to numbers it is necessary to use the circuit of fig. 10. The polarization current $I_P$ is supplied continuously, that is also during the pulses. Then if the capacitance $C$ is sufficiently large, the voltage across the junction during the pulse is:

$$V_P + v_S$$

where $V_P$ is the voltage produced by the current $I_P$ alone, i.e. in the absence of the pulse and is given by (3.3) and the total current in the junction is $i_S$ given by (3.4).

An interesting operation because by it a complete temperature compensation is attained is that of calculating the root of order $\sum h_i$ of the pulse $u$†. The demonstration is given in Appendix C. If the root of order $\sum h_i$ is calculated the dynamic range of the output pulse

$$(u)^{\frac{1}{\sum_1^n{}_i h_i}}$$

is equal to the dynamic range of the input pulses. If all the $h_i$ are positive, both the reduction of the dynamic range and the temperature compensation is attained.

### 7. Apparatus Constructed

For L. Colli *et al.*'s experiments, see fig. 1, we have constructed a computer which makes the operation $a \times (b + b_0)^h$, where $a$ is the pulse from the proportional counter, $b$ is the pulse from the scintillation counter and $b_0$ is a constant. $b_0$ and the exponent $h$ have been added in order to investigate the possibility of obtaining a better discrimination in respect to the mass.

The schematic of the computer is given in fig. 11.

[7]) G. Giannelli, Transistorized Linear Gate, To be published.

† It is impossible to effect this operation in the case of the simple division and generally when $\sum h_i = 0$.

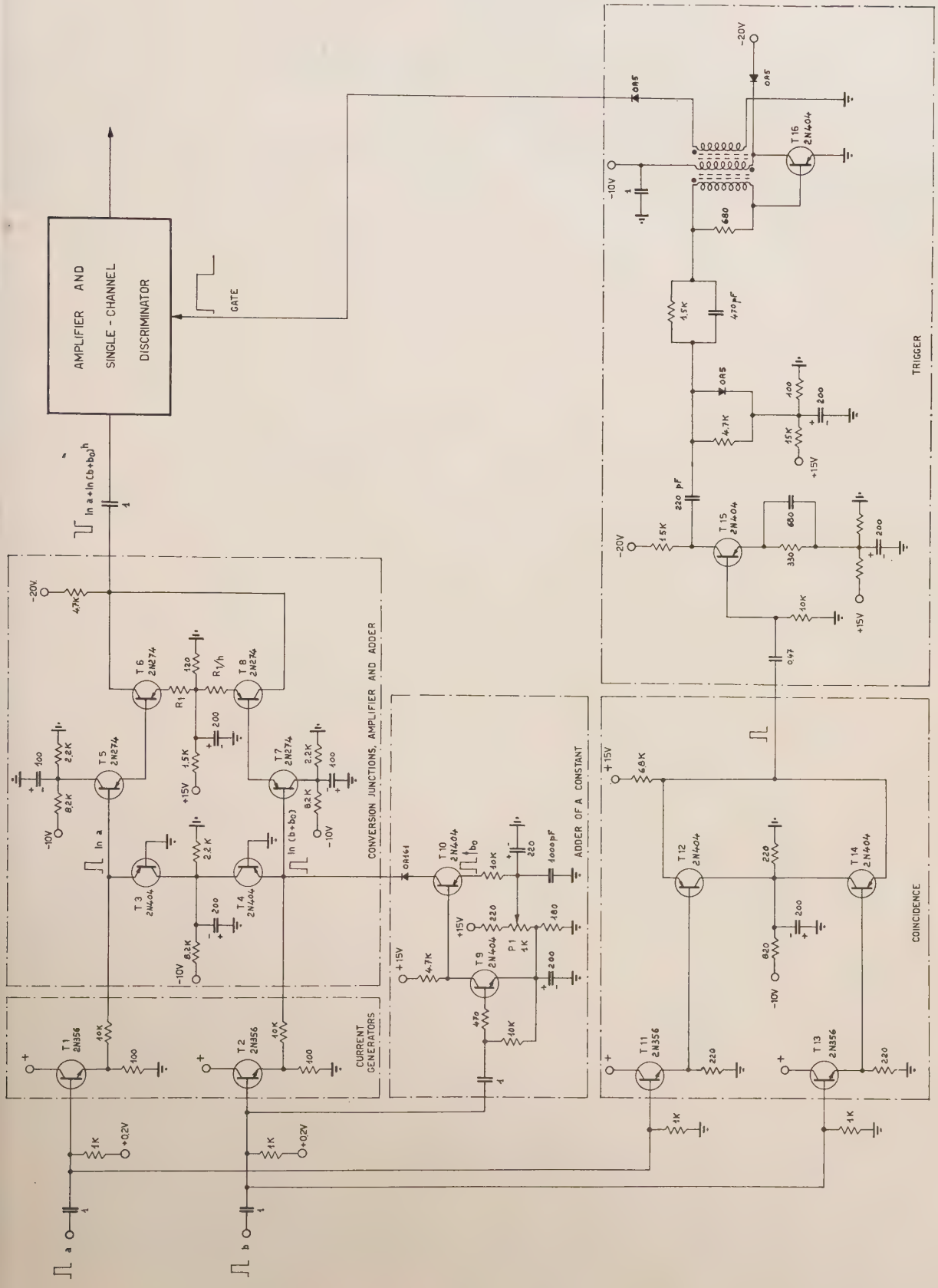


Fig. 11. Schematic of the computer.

The rise-time of the pulse $\ln a + \ln (b + b_0)^h$ is of $2 \times 10^{-7}$ s. The pulses $a$ and $b$ are rectangular. The computer has been built for a dynamic range of the input pulses of 20 to 1, widely sufficient in this particular application; this dynamic range corresponds to input currents to the conversion junctions ranging from 50 $\mu$A to 1 mA. To improve the performance of the current generators at low currents we found useful to keep them in a state of slight conduction.

The high input impedance of the amplifiers which follow the conversion junctions is obtained through the use of the double emitter followers.

The exponent $h$ is given by the ratio of the emitter resistors of the transistors T6 and T8.

The coincidence, whose necessity has been already put in evidence in section 5, is identical to a conventional diode coincidence where diodes are substituted by transistors which act as emitter followers. In this way a higher input

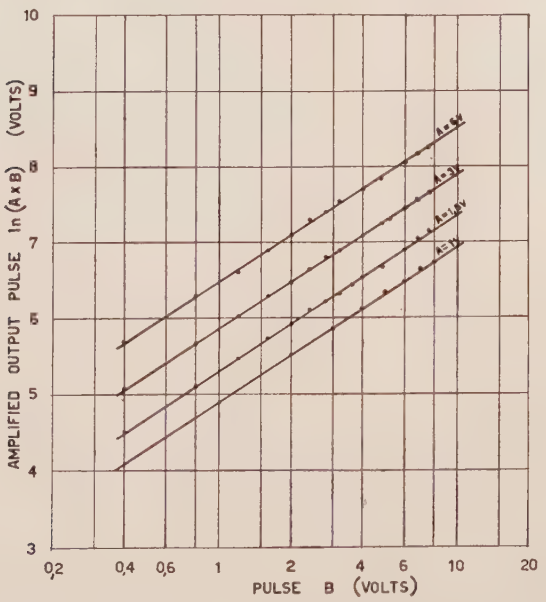


Fig. 12. Measured characteristics of the computer of fig. 11.

impedance is obtained for the same response time. The trigger circuit is driven by the output of the coincidence, that is by the smallest between the two input pulses $a$ and $b$.

In the adder-of-a-constant circuit transistor T9 saturates if pulse $b$ exceeds 50 mV; then T10 supplies a current pulse that is adjustable from 0 to 1 mA by means of the potentiometer P1.

The single-channel analyzer is set so as to encompass the whole line of pulses produced by particles having the selected mass. This analyzer, that is transistorized and of a type previously developed in this laboratory[8]), controls the gate of the 100-channels pulse height analyzer.

The whole computer is thermostated with tap water.

In fig. 12 the measured characteristics are plotted.

## Appendix A

Derivation of formula (2.2).

From the general transistor equations:

$$i_E = I_{ES}\,(e^{qv_E/kT} - 1) - \alpha_I I_{CS}\,(e^{qv_C/kT} - 1)$$

$$i_C = -\alpha_N I_{ES}\,(e^{qv_E/kT} - 1) + I_{CS}\,(e^{qv_C/kT} - 1) \qquad (A.1)$$

when $-v_C \gg kT/q$ one obtains:

$$i_E = I_{ES}\,e^{qv_E/kT} - I_{ES} + \alpha_I I_{CS} =$$

$$= I_{ES}\,e^{qv_E/kT} - I_{ES}\,(1 - \alpha_N) =$$

$$= I_{ES}\,e^{qv_E/kT} - \frac{\alpha_N}{\beta_N} I_{ES} \qquad (A.2)$$

that with the substitution:

$$\rho = 1 - \alpha_N = \frac{\alpha_N}{\beta_N}, \qquad (A.3)$$

can be written:

$$i_E = I_{ES}\,(e^{qv_E/kT} - \rho) \qquad (A.4)$$

or:

$$v_E = \frac{kT}{q} \ln \frac{i_E + \rho I_{ES}}{I_{ES}}. \qquad (A.5)$$

Equations (A.1) are written according to the I.R.E. Standards[9]) and for the sake of clarity taking the currents $I_{ES}$ and $I_{CS}$ always positive. In this way the equations are in a form consistent with that for the diodes, see (2.1). The equations written in this way hold both for transistor $p$–$n$–$p$ and for transistor $n$–$p$–$n$ if

[8]) L. Stanchi, Discriminatore d'ampiezza d'impulso a transistor, Strumentazione e Automazione (June 1959).

[9]) I.R.E. Standards on Letter Symbols for Semiconductor Devices, 1956, Proc. I.R.E. **44** (1956).

currents $i_E$, $i_C$ and voltages $v_E$, $v_C$ are taken as the direct currents and voltages of the emitter and collector junctions, that is $i_E$ ($i_C$) is positive when entering in the emitter (collector) for transistors *p–n–p* and when coming out for transistors *n–p–n*.

$$y = x + \ln (1 - ay\, e^{-x}) . \qquad (B.2)$$

Eq. (B.2) has been calculated for different values of the parameter $a$ and is plotted in the diagram of fig. 13.

For the utilization of the circuit of fig. 7a for

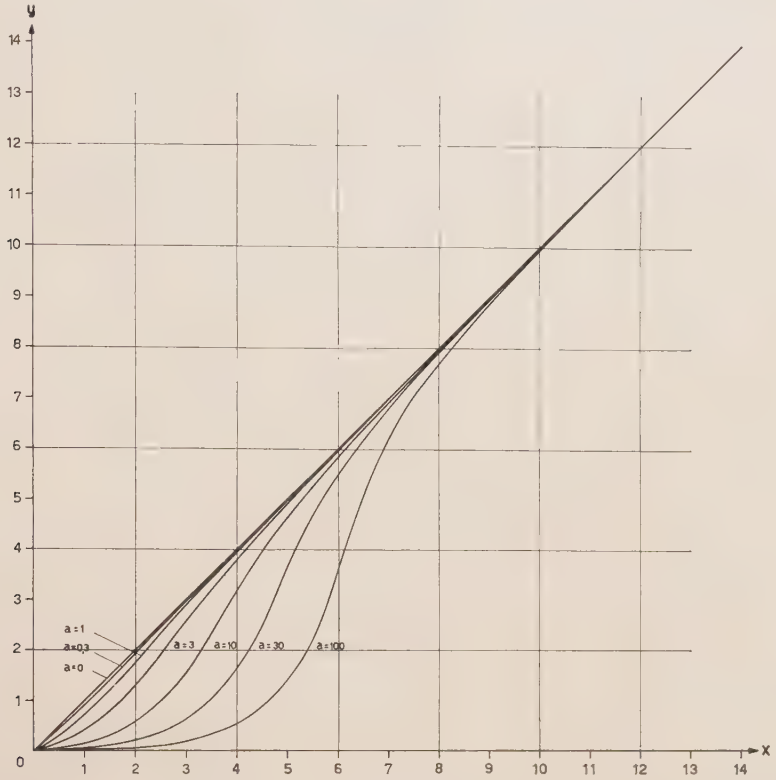


Fig. 13. Plot of the eqs. (4.1) calculated with the adimensional quantities $x$, $y$ and $a$ defined in (B.1).

## Appendix B

From eqs. (4.1) it is possible to eliminate the current and obtain a direct relation between $v_{in}$ and $v_{out}$. Making the substitutions:

$$x = \ln \frac{v_{in}}{R_S I_0}$$

$$y = \frac{v_{out}}{A}$$

$$a = \frac{A}{R_S I_0}, \qquad (B.1)$$

this relation is written in adimensional form:

logarithmic conversion it is important to find the characteristic of the type:

$$v_{out} = B \ln \frac{v_{in}}{V_0} \qquad (B.3)$$

which approximates the actual characteristic with a minimum given error $\varepsilon$. For an easy determination of the parameters $B$, $V_0$ and of the error $\varepsilon$, the diagram of fig. 14 derived from fig. 13 has been plotted; its ordinates are the differences $(y - x)$. The characteristics of the type of eq. (B.3) are straight lines in this diagram. It will be noted when the error $\varepsilon$ is taken as an horizontal segment of constant length, it represents a constant percentile error in $v_{in}$.

## Appendix C

In the text it has been stated that if one derives the root of order $\sum_1^n {}_i h_i$ of the quantity $u$, a complete compensation of temperature variation is achieved. This requires that for all the conversion junctions the parameter $A$ be the same and the parameters $I_0$ vary with temperature in the same ratio. The compensation of the variations of these parameters takes place between the junctions that calculate the logarithm from one side and the junction that calculate the inverse from the other side.

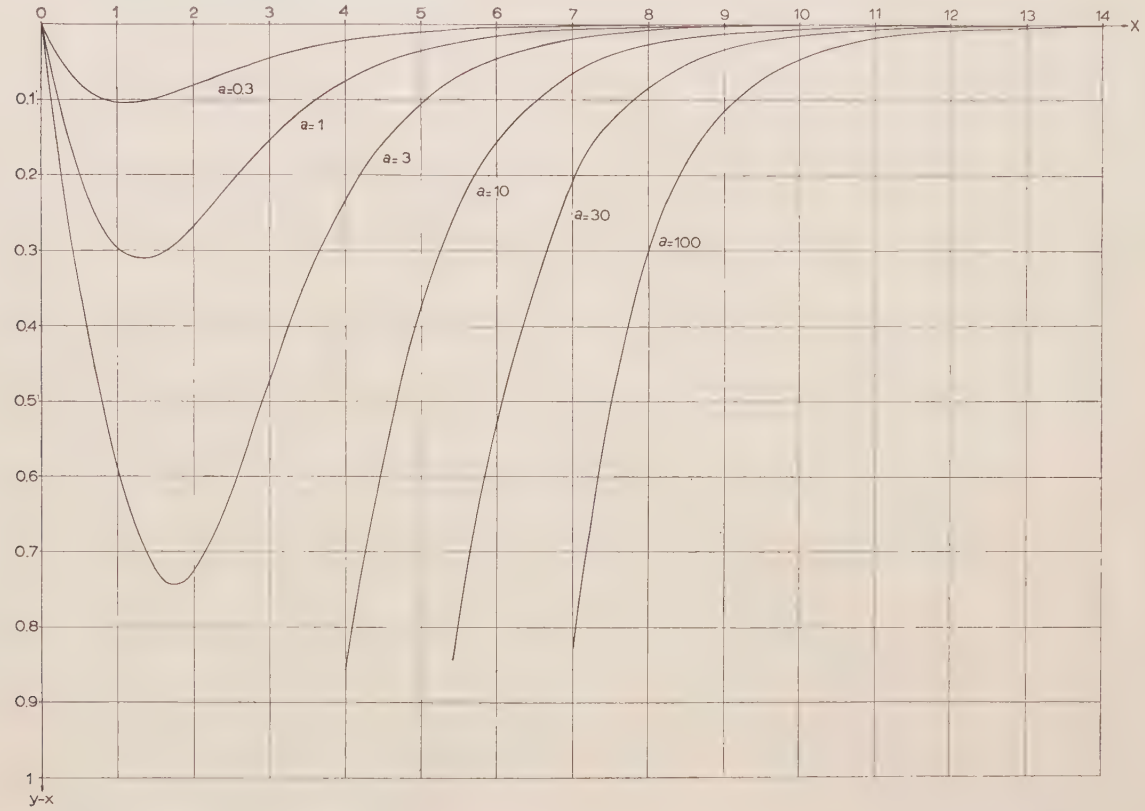


Fig. 14. Diagram obtained from fig. 13 plotting $(y—x)$ on the axis of ordinates with an expanded scale.

Let $i_i$ and $l_i$ $(i = 1,2\cdots n)$ be the currents injected to those conversion junctions which calculate the logarithm, related to the quantities $a_i$ and $k_i$ of eq. (5.1) by a proportionality factor having the dimensions of a current:

$$i_i = I_c a_i$$
$$l_i = I_c k_i \ . \qquad \text{(C.1)}$$

From (C.1), (2.3), (5.1) the pulse $v_u$ (proportional to $\ln u$) is:

$$v_u = \sum_1^n {}_i h_i A \ln \frac{i_i + l_i}{I_i f(T)} + A \ln k_0 \qquad \text{(C.2)}$$

where $I_0$ of the (2.3) is given by:

$$I_{0i} = I_i f(T) \qquad \text{(C.3)}$$

where $I_i$ is a constant and is different for each junction and $f(T)$ is a function of temperature and is the same for all the junctions. We divide (C.2) by $\sum_1^n {}_j h_j$:

$$\frac{v_u}{\sum_1^n {}_j h_j} = \frac{A}{\sum_1^n {}_j h_j} \ln \left\{ k_0 \left[ \prod_1^n {}_i \left( \frac{i_i + l_i}{I_i} \right)^{h_i} \right] \left[ \frac{1}{f(T)} \right]^{\sum_1^n {}_i h_i} \right\} =$$

$$= A \ln \left\{ \frac{1}{f(T)} \left[ k_0 \prod_1^n {}_i \left( \frac{i_i + l_i}{I_i} \right)^{h_i} \right]^{\frac{1}{\sum_1^n {}_j h_j}} \right\} . \qquad \text{(C.4)}$$

If we apply this voltage pulse to the terminals of a conversion junction having the characteristic:

$$i = I_{n+1} f(T)\, e^{v/A}, \qquad \text{(C.5)}$$

the current pulse in the junction will have an amplitude $i_u$ given by:

$$i_u = I_{n+1} f(T)\, e^{v_u/(A \sum_1^n j^{h_j})} = I_{n+1} \left[ k_0 \prod_1^n {}_i \left( \frac{i_i + I_i}{I_i} \right)^{h_i} \right]^{\frac{1}{\sum_1^n j^{h_j}}} = \frac{I_{n+1} I_c}{\left[ \prod_1^n {}_i (I_i)^{h_i} \right]^{\frac{1}{\sum_1^n j^{h_j}}}} (u)^{\frac{1}{\sum_1^n j^{h_j}}} \qquad \text{(C.6)}$$

where all temperature dependent terms are absent.

It is to be noted that if all $I_0$ are equal between themselves, that is:

$$I_1 = I_2 = \cdots = I_n = I_{n+1} \qquad \text{(C.7)}$$

one simply has:

$$i_u = I_c (u)^{\frac{1}{\sum_1^n i^{h_i}}} . \qquad \text{(C.8)}$$

NUCLEAR INSTRUMENTS AND METHODS 8 (1960) 92–105; NORTH-HOLLAND PUBLISHING CO.

# DETECTEUR DE PARTICULES LOURDES A JONCTION n–p AU SILICIUM

G. AMSEL, P. BARUCH et O. SMULKOWSKI

*Laboratoire de Physique Nucléaire de l'Ecole Normale Supérieure, Paris*

Reçu le 28 mars 1960

Silicon n–p junctions were used to detect heavy charged particles produced by nuclear reactions inside the accelerator vacuum chamber, at room temperature, The response to particle energy dissipated in the barrier, is linear. The width of resolved peaks at half maximum is independent of incident particle energy and is equivalent to 40 keV for $\alpha$ particles and 30 keV for protons and deuterons. The rise time of the signal due to particles stopped in the barrier is of the order of 1 millimicrosecond while that due to particles traversing it has a slow component; this allows their distinction electronically. The detectors are insensitive to $\gamma$ rays and neutrons.

## 1. Introduction

Les réactions nucléaires provoquées par des ions lourds ont fait l'objet d'un grand nombre de travaux au cours des dernières années. Ces réactions s'accompagnent de l'émission de particules chargées de diverses natures dont l'identification pose un problème délicat. De plus, la détection doit s'opérer souvent en présence d'un flux intense de neutrons et de rayons $\gamma$, qui produisent un important bruit de fond.

L'analyse de spectres aussi complexes pose des problèmes difficiles, qui n'ont été que partiellement résolus par les détecteurs de particules lourdes utilisés jusqu'à présent. Il semble qu'un pas en avant peut être accompli par les détecteurs à jonction, dont l'étude date d'une époque récente. McKenzie et Bromley[1]) ont réalisé parmi les premiers un détecteur de ce type à l'aide de jonctions or-germanium. Cependant, le bruit élevé dû au germanium ne permet l'emploi de ce type de détecteur qu'à la température de l'azote liquide.

Pour éviter cet inconvénient, nous avons entrepris l'étude d'un détecteur à jonction au silicium, qui peut fonctionner à la température ambiante[2]).

Nous exposons ici les résultats obtenus ainsi qu'un essai d'interprétation des phénomènes observés.

## 2. Principe du Détecteur à Jonction

Une particule chargée crée dans un semiconducteur des paires d'électron-trou de la même façon qu'elle crée des paires d'ions dans un gaz. McKay[3]) a mesuré l'énergie nécessaire

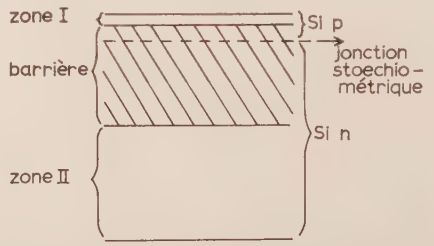


Fig. 1. Représentation schématique d'une jonction réalisée par diffusion de gallium dans du silicium de type n.

pour la création d'une paire de porteurs libres: elle est de 2.9 eV dans le germanium, soit environ 10 fois plus faible que dans un gaz. Dans le silicium elle est de 3.25 eV. Les paires électron-trou ont une durée de vie finie dont la valeur dépend de la concentration des impuretés. La collection des charges est totale lorsque le temps de collection est négligeable devant la durée de vie. Pour recueillir les charges, il faut que les porteurs se déplacent avec une grande

[1]) J. M. McKenzie and D. A. Bromley, Phys. Rev. Letters (April 1, 1959) 303.

[2]) G. Amsel, P. Baruch et O. Smulkowski, Comptes rendus des Séances de l'Académie des Sciences (22 Février 1960) p. 1468.

[3]) K. G. Mc Kay, Phys. Rev. **84** (1951) 829.

vitesse: pour cela un champ électrique intense est nécessaire.

Lorsqu'on polarise une jonction (fig. 1) en non conduction, il s'établit de part et d'autre de la jonction stoéchiométrique une zone B où le champ électrique est très intense. Cette zone où le champ est de l'ordre de $10^4$ V/cm, est appelée zone de charge d'espace ou "barrière". Les porteurs s'y déplacent à des vitesses de l'ordre de $10^7$ cm/s, donc le temps nécessaire pour parcourir une distance de 100 $\mu$ est de $10^{-9}$ s. Ce temps est négligeable devant la durée de vie, bien supérieure à la $\mu$s dans la région non dopée. Une collection totale de la charge créée dans la barrière est donc réalisée. Cette charge produit une impulsion de tension inversement proportionnelle à la capacité du détecteur.

En dehors de la barrière, il existe deux zones dans lesquelles le champ électrique est nul ou très faible et où les porteurs se déplacent par diffusion.

Dans la zone I fortement dopée comprise entre la barrière et la surface d'entrée, la durée de vie est très faible; la collection y est nulle. Cette zone se comporte comme la fenêtre d'un compteur proportionnel. Dans la zone II, où la durée de vie est élevée, une fraction des porteurs créés peut atteindre la barrière et contribuer au signal.

L'épaisseur ($\varepsilon$) de la barrière varie sensiblement comme $V^{\frac{1}{2}}\rho^{\frac{1}{2}}$, où $V$ est la tension de polarisation et $\rho$ la résistivité du matériau de base. Pour une jonction donnée, l'épaisseur maximum n'est limitée que par la tension de claquage. La capacité varie approximativement comme $\varepsilon^{-1}$.

### 3. Réalisation

Les jonctions sont obtenues par diffusion d'éléments III ou $V$ dans du silicium. Par exemple par diffusion de gallium dans du silicium de type n ou de phosphore dans du silicium de type p.

Des jonctions du premier type utilisant du silicium du type n de résistivité voisine de 35 $\Omega$cm, ont été réalisées sur notre proposition[4]). La concentration en surface du gallium est de l'ordre de $3 \times 10^{17}$ par cm$^3$. La jonction stoéchiométrique se situe à 5 $\mu$ de la surface. La tension de claquage varie légèrement d'une jonction à l'autre; elle est généralement comprise entre 60 et 80 V. La surface des jonctions est de l'ordre de 4 mm$^2$. Nous donnons en exemple la variation du courant inverse en fonction de la polarisation (fig. 2) pour une des jonctions utilisées.

Ce type de détecteur a été l'objet d'une étude approfondie pendant que d'autres jonctions ayant des caractéristiques différentes étaient en cours de réalisation. Nous avons cherché à améliorer plus particulièrement deux caractéristiques du détecteur, en réalisant:

(1) une zone insensible à l'entrée plus mince par une diffusion moins profonde et un dopage en surface moins élevé;

(2) une zone de collection totale plus étendue,

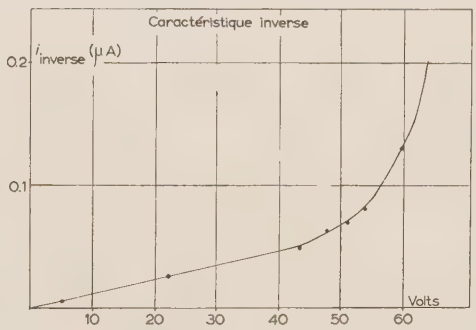


Fig. 2. Caractéristique inverse d'une jonction, placée dans son vide et dans la pénombre. La tension de claquage est définie par le coude de la caractéristique.

en repoussant la limite de la tension de claquage et en utilisant du silicium plus pur. Ceci nous a conduit à choisir du silicium de type p, la jonction s'obtenant alors par diffusion de phosphore.

Cette variété de silicium peut atteindre des résistivités allant jusqu'à plusieurs milliers d'ohms·cm. La résistivité d'un monocristal ne détermine la concentration des impuretés que dans le seul cas où ces impuretés sont constituées par des éléments d'un même groupe, autrement dit que le cristal n'est pas compensé. Généralement le silicium de type n de haute résistivité

[4]) Les jonctions ont été réalisées par la Cie LTT, Conflans Ste Honorine, France.

est compensé. Ceci est dû au fait qu'il est pratiquement impossible d'éliminer totalement le bore dont la présence dans le silicium lui confère le caractère p.

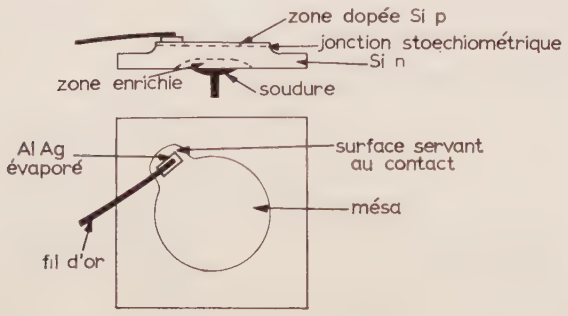


Fig. 3. Forme schématique de la jonction. Le contact sur la face diffusée ne doit pas empiéter sur la surface utile circulaire.

Pour obtenir du silicium n de haute résistivité, on est obligé de le doper par un élément du groupe V, généralement le Phosphore.

Le silicium p atteint donc des puretés beaucoup plus grandes que le silicium n. Des jonctions réalisées avec du silicium de type p, ont été étudiées récemment par Friedland *et al.*[5]).

### 3.1. STRUCTURE DU DETECTEUR

La jonction est réalisée, dans une plaquette de silicum poli optiquement, par diffusion sur

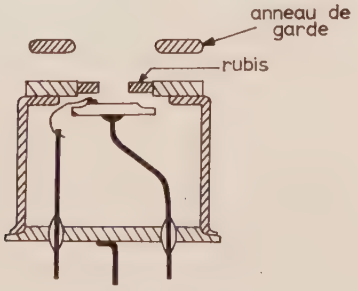


Fig. 4
Aspect d'un détecteur avec diaphragme et anneau de garde.

l'une des faces. La surface utile appelée "mésa", de forme circulaire, à laquelle est attenante une petite plage servant à la connexion électrique, est dégagée par attaque à l'acide. On obtient la forme indiquée figure 3. Le contact sur la face dopée est réalisé au moyen d'un fil d'or soudé par thermocompression sur une plage de métal évaporé et allié. Le contact avec la plaquette s'obtient par soudure après enrichissement local du silicium.

La jonction est montée sur une embase de transistor de façon que la surface dopée puisse être exposée au faisceau des particules (fig. 4). La surface de la "mésa" est légèrement en retrait du plan supérieur du capuchon sur lequel est fixé un diaphragme. Ce diaphragme sert à délimiter la partie utile de la surface de la jonction; il est réalisé par un rubis de montre enchassé dans un disque métallique. Le rubis a été choisi pour des raisons qui sont exposées dans le chapître traitant des résolutions. Un anneau de garde isolé et polarisé négativement par rapport à la masse est placé devant le diaphragme. Son rôle est de repousser les électrons secondaires émis par la cible, cf. section 8.

### 3.2. MONTAGE ET UTILISATION

Le détecteur peut être monté dans la chambre à diffusion de l'accélérateur. Son faible encombrement permet d'observer les produits de réactions à des angles très faibles par rapport au faisceau des particules incidentes. Le montage dans le vide évite toute fenêtre entre la cible et la face d'entrée du détecteur.

Pour réduire au minimum les capacités de connexions, une cathodyne est montée sous vide

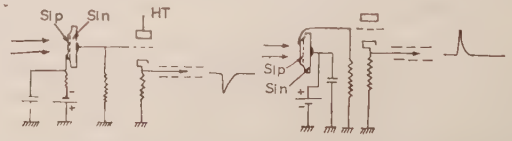


Fig. 5. Schémas de montages électriques permettant d'obtenir des impulsions de signe voulu. On remarque que la face d'entrée n'est jamais portée à un potentiel positif.

près du détecteur. Ce tube peut être remplacé par un transistor connecté "base à la masse". Dans notre expérience, nous avons utilisé un tube subminiature 6AK5.

Pour ne pas annihiler l'effet de l'anneau de garde, il faut choisir un montage électronique tel que la face d'entrée du détecteur ne soit pas

[5]) Stephen S. Friedland, James W. Mayer and John S. Wiggins, Nucleonics (February 1960).

portée au potentiel positif. La figure 5 montre deux schémas possibles, fournissant des impulsions, soit négatives, soit positives.

## 4. Méthode d'Etude du Détecteur

La réponse du détecteur a été étudiée sous trois aspects:

L'évolution de l'amplitude et du temps de montée des impulsions en fonction de l'énergie pour diverses particules et pour diverses tensions de polarisation;

La valeur absolue de ces amplitudes;

La dispersion en amplitude des impulsions dues à des particules mono-cinétiques.

Trois types de particules ont été utilisées: protons, deutons et rayons $\alpha$. Ces particules étaient produites par des réactions nucléaires: des cibles minces sans support ont été soumises au bombardement du faisceau de protons ou de deutons de l'accélérateur Van de Graaff de 2 millions de volts de l'Ecole Normale Supérieure.

Les réactions utilisées pour obtenir les diverses particules étaient les suivantes:

deutons: diffusion élastique par

$$Ag,\ Al^{27},\ O^{16},\ C^{12}\ .$$

Domaine d'énergie: 0.2 à 2 MeV.

protons: diffusion élastique par $Al^{27}$, ainsi que les réactions

$$O^{16}\,(d,p)\,O^{17};\qquad Q = 1.92\ \text{MeV}\ .$$

$$C^{12}\,(d,p)\,C^{13};\qquad Q = 2.72\ \text{MeV}\ .$$

Domaine d'énergie: 0.3 à 4.5 MeV.

particules $\alpha$:

$$O^{16}\ (d,\alpha)\ N^{14}\ ;\qquad Q = 3.12\ \text{MeV}\ .$$

$$Al^{27}\,(d,\alpha)\,Mg^{25}\ ;\qquad Q = 6.70\ \text{MeV}\ .$$

Une source de polonium fournissait des particules $\alpha$ de 5.3 MeV.

Domaine d'énergie: 2.7 à 7 MeV.

Les cibles utilisées étaient des films minces de:

$Al_2O_3$ de 40 et 20 $\mu g/cm^2$

Al de 20 et 7 $\mu g/cm^2$

Ag de 50 $\mu g/cm^2$ .

Le carbone était présent sur toutes ces cibles, à l'état de contamination.

Les impulsions du détecteur étaient amplifiées par un amplificateur Ecko et envoyées, après passage à travers un amplificateur loupe, dans un analyseur d'impulsions à 100 canaux, du type RIDL.

## 5. Evolution de l'Amplitude et du Temps de Montée des Signaux

5.1.

1. Pour déterminer les conditions d'utilisation du détecteur, il est nécessaire de relever les courbes amplitude-énergie. Le réseau de ces courbes tracées pour diverses tensions de polarisation et pour diverses particules décrit le comportement du détecteur. De même il est important de connaître l'évolution du temps de montée des impulsions; en effet l'amplitude elle-même, après amplification, dépend du temps de montée, selon le choix du temps d'intégration et de différentiation de l'amplificateur. L'étude de toutes ces courbes montrera qu'il est possible d'effectuer une discrimination entre particules de diverses natures et de faire l'étude sélective de spectres de particules $\alpha$, protons, deutons, etc.

2. L'analyse mathématique des courbes obtenues permet d'interpréter les phénomènes observés. Elle explique le mécanisme de la collection des charges et permet l'investigation des propriétés du semiconducteur dans la masse en fonction de la profondeur. Ces calculs, ainsi que les propriétés de la jonction qu'on en déduit, sont présentés en appendice.

5.2. DESCRIPTION DU MECANISME DE COLLECTION

1. *Dans la barrière*

La collection est totale; la relation amplitude-énergie dissipée est linéaire. Le temps de montée des impulsions est de l'ordre de $10^{-9}$ s.

2. *Au dela de la barrière*

Dans cette zone les porteurs se déplacent par diffusion. Les particules qui pénètrent dans cette zone donnent naissance à une impulsion qui a deux composantes. Une composante rapide correspondant à l'énergie dissipée dans la barrière. Une composante lente correspondant

à la collection par diffusion; cette collection est incomplète, car les porteurs ont une durée de vie finie dans le silicium, de l'ordre de quelques $\mu$s.

5.3.

Ainsi la courbe amplitude-énergie s'écarte de la linéarité lorsque la particule pénètre dans la zone de diffusion. Sa forme dépend des constantes de temps de l'amplificateur utilisé, qui peut transmettre plus ou moins fidèlement la composante lente de l'impulsion. La courbe passe par un maximum d'autant plus aigu que la constante de temps de différentiation est plus faible.

pour des tensions de polarisation comprises entre 9 et 45 V. L'épaisseur de la zone insensible est de 1.5 $\mu$ à 10% près. On voit que la barrière s'avance largement dans la zone dopée, puisque la jonction stoechiométrique est à 5$\mu$ de la surface. En réalité, l'épaisseur de la zone insensible varie avec la tension, mais si lentement qu'il n'est pas possible de le mettre en évidence.

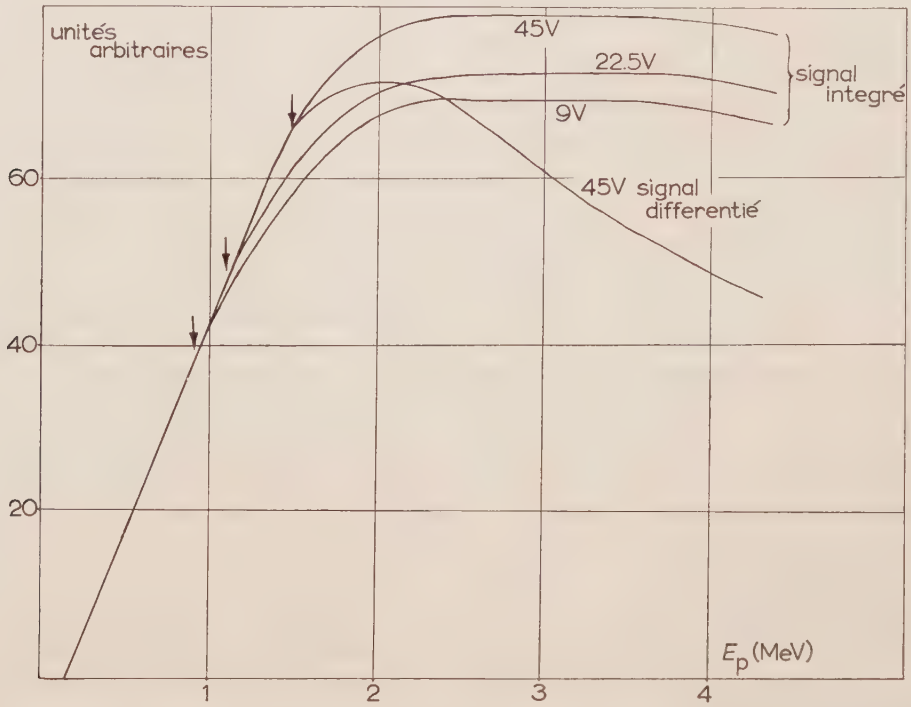


Fig. 6. Courbes d'amplitude du signal en fonction de l'énergie des protons incidents pour diverses tensions de polarisation. Les flèches indiquent les énergies pour lesquelles la réponse s'écarte de la linéarité.

L'épaisseur de la barrière est à 2$\mu$ près:

à 9 V: 17 $\mu$

à 22 V: 21 $\mu$

à 45 V: 27 $\mu$ .

5.4. RESULTATS

Pour illustrer les considérations qui précèdent, nous présentons les résultats de l'étude de l'un des détecteurs que nous avons utilisés.

La figure 6 montre les courbes d'amplitude mesurées avec des protons pour diverses tensions de polarisation. Les courbes ont été normalisées au même gain. Toutes ces courbes coupent l'axe des énergies au point d'abscisse 140 keV

La variation semble suivre une loi en $V^{0.4}$ plutôt que $V^{\frac{1}{2}}$.

La figure 7 montre les 2 familles d'impulsions dues à des particules arrêtées dans la barrière et à des particules plus pénétrantes.

La partie rapide des impulsions a été obervée avec un oscilloscope Tektronix et des amplificateurs Hewlett Packard d'une bande passante de 200 Mc/s. Le temps de montée des impulsions

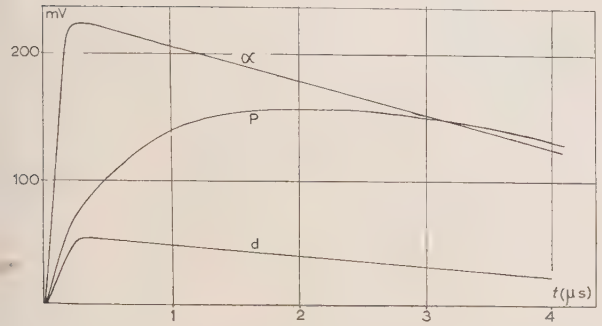


Fig. 7. Formes des impulsions suivant le parcours de la particule, les particules $\alpha$ et les deutons sont arrêtés dans la barrière, les protons ont par contre une notable partie de leur parcours dans la zone de diffusion.

était le temps de montée propre de l'électronique, soit $10^{-8}$ s. Notons que Friedland *et al.*[5]) ont également observé un temps de montée égal à celui de leur électronique, soit $3 \times 10^{-9}$ s. Ceci est en accord avec le temps de montée théorique de $10^{-9}$ s.

La composante lente des impulsions a été observée avec un préamplificateur Ecko de gain 40 et de bande passante 4 Mc/s, dont la constante de temps de différentiation était supérieure à 10 $\mu$s. La constante de temps d'intégration était de 12 $\mu$s.

La figure 8 montre l'évolution du temps de montée de la composante lente en fonction du parcours. On voit que la variation est d'abord sensiblement linéaire, avec une pente de l'ordre de 0.3 $\mu$s/10$\mu$. La pente est légèrement plus faible avec des tensions plus fortes ce qui prouve qu'un faible champ électrique résiduel subsiste dans la zone de diffusion et contribue au mouvement des porteurs. De plus, la relation cesse d'être linéaire pour les temps supérieurs à 3 $\mu$s environ, c'est-à-dire comparables à la durée de vie.

Cette évolution du temps de montée peut s'expliquer par la théorie de la diffusion.

### 5.5. DISCRIMINATION ENTRE PARTICULES

Constatons que les résultats ci-dessus s'expriment tous en fonction du parcours. Les courbes d'amplitude pour diverses particules se déduisent les unes des autres par affinité, si on prend le parcours comme variable. C'est ce qui a été vérifié pour les deutons. Ainsi la barrière maximum que nous avons obtenue avec cette jonction étant de 27$\mu$, la limite de linéarité est de 1.5 MeV pour les protons, 2 MeV pour les deutons, 5.5 MeV pour les particules $\alpha$.

Deux méthodes permettent de distinguer des particules de diverses natures:

(a) La zone de diffusion peut jouer le rôle de détecteur d'anticoïncidence. Un dispositif électronique simple permet d'éliminer la famille d'impulsions ayant une composante lente. Ainsi les particules pénétrantes sont identifiées. Cette méthode est d'autant plus souple qu'on peut contrôler électriquement l'épaisseur de la barrière, donc le domaine d'énergie exploré, pour diverses particules. Signalons qu'on peut opérer sans polarisation, le potentiel de contact, qui est de 1.1 V, étant suffisant pour créer une mince barrière.

(b) Si on ne dispose pas d'un montage d'anticoïncidences pour éliminer complètement les impulsions gênantes dues à des particules pénétrantes, on peut néanmoins "déplacer" un pic dû à un groupe de particules pénétrantes par rapport aux autres pics, en modifiant les constantes de temps d'intégration et de différentiation de l'amplificateur. Ainsi les réactions $O^{16}$ (d,d) $O^{16}$ et $O^{16}$ (d,$\alpha$) $N^{14}$ ont été étudiées simultanément en présence des réactions

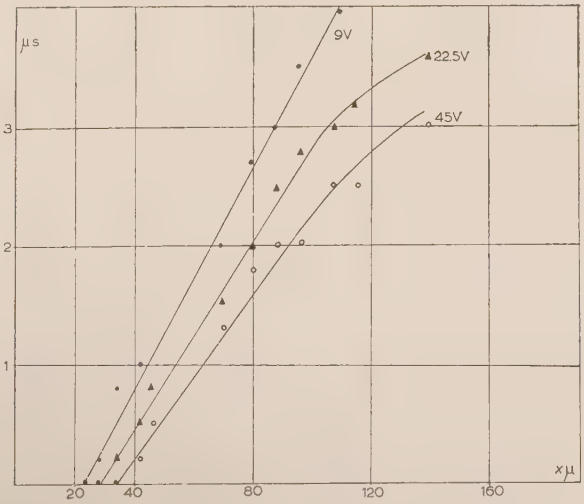


Fig. 8. Courbes représentant le temps de montée de la composante lente des impulsions dues à des particules très pénétrantes, pour diverses tensions de polarisation.

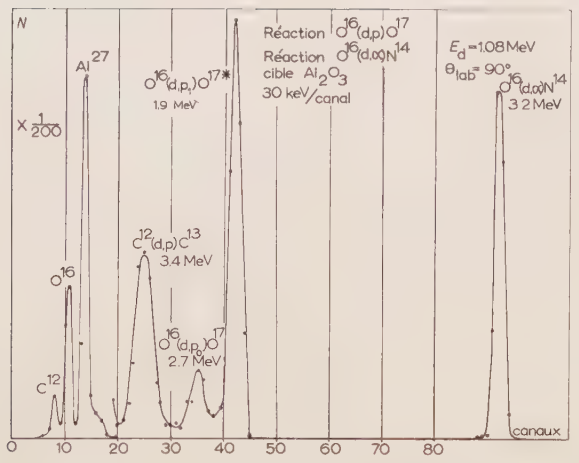


Fig. 9. Spectre complet obtenu par bombardement d'une cible de $Al_2O_3$ par des deutons.

$O^{16}$ (d,p) $O^{17}$ et $C^{12}$ (d,p) $C^{13}$. Les pics dus aux protons pouvaient être groupés de manière à ne pas gêner la lecture des spectres dans leur partie utile, en mettant à profit la forme de la courbe amplitude-énergie (figure 6).

Le spectre représenté fig. 9 illustre cette méthode. On constate l'ordre inversé et la place des trois pics de protons qui sont groupés de manière à ne pas empiéter sur les spectres des deutons et des particules $\alpha$.

REMARQUES

(1) Les mêmes principes s'appliquent aux électrons. Lorsque la barrière est suffisamment épaisse pour que les électrons y donnent des signaux gênants, on peut les éliminer, car les électrons traversent également la zone de diffusion et fournissent donc une composante lente.

(2) Observons que le parcours des particules lourdes dans le silicium, exprimé en mg/cm² est sensiblement égal à la moitié du parcours dans NaI (et CsI). Ainsi l'énergie perdue par les électrons dans la barrière d'un détecteur à jonction n'est que la moitié de celle perdue dans un cristal de NaI(Tl) d'épaisseur équivalente à celle de la barrière. En effet, l'énergie perdue par un électron relativiste est proportionnelle à la masse traversée. L'amplitude relative des impulsions dues aux électrons est donc deux fois plus faible pour le détecteur à jonction. Ceci explique qu'en général les impulsions dues aux électrons sont négligeables.

(3) Les rayons $\gamma$ peuvent produire des électrons soit dans la masse du détecteur, soit dans son voisinage. Ces électrons peuvent produire des impulsions, comme décrit ci-dessus.

(4) Les neutrons peuvent produire soit des rayons $\gamma$ soit des particules lourdes par des réactions (n,p), (n,$\alpha$) etc. Le détecteur est inévitablement très sensible à ces dernières, en général fort peu nombreuses.

(5) Dans certaines applications où le flux de particules pénétrantes (électrons haute énergie par exemple) est très important, il est utile de réduire la durée de vie dans la zone de diffusion pour éviter l'empilement des impulsions. Ceci est possible sans réduction de la profondeur de la barrière.

## 6. Valeurs Absolues des Amplitudes et Rapport Signal-Bruit

(a) L'amplitude de l'impulsion de tension produite par une particule d'énergie $E_{\mathrm{MeV}}$, $C$ étant la capacité totale, est:

$$V = \frac{q}{C} = \frac{E \times 10^6}{3.25} \frac{e}{C}$$

$$V_{\mathrm{mV}} = 50 \frac{E_{\mathrm{MeV}}}{C_{\mathrm{pF}}}$$

quel que soit le détecteur utilisé. Le gain varie donc comme $C^{-1}$. La mesure de $C^{-1}$ peut se faire en observant l'amplitude due à un groupe de particules d'énergie fixe, pour diverses tensions de polarisation. La courbe obtenue est normalisée par évaluation de la constante de temps de décharge de la capacité dans une résistance connue. L'avantage de cette méthode est qu'elle permet de faire la mesure dans les conditions mêmes de l'expérience, le détecteur étant en place dans la chambre à diffusion. Pour éviter la distorsion de la courbe due à la variation de l'épaisseur de la barrière, il faut opérer avec des particules de faible parcours. Il est facile de contrôler si une telle distorsion est apparue: deux groupes de deutons d'énergie voisine

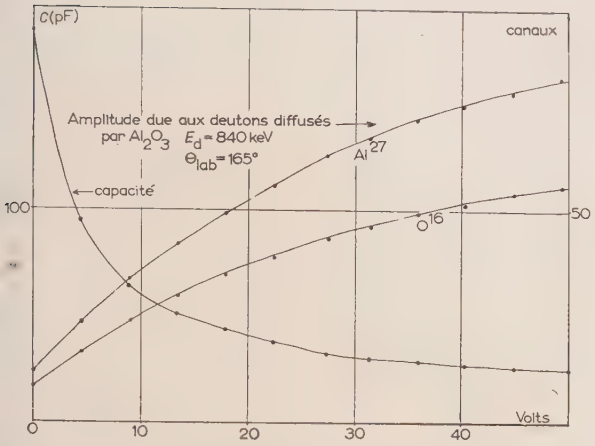


Fig. 10. Variation de la capacité du détecteur en fonction de la tension de polarisation.

(diffusés par $O^{16}$ et $Al^{27}$) sont utilisés; tant que le quotient de deux amplitudes reste constant, les courbes reproduisent fidèlement les variations de $C^{-1}$. La figure 10 montre la courbe des amplitudes et la fonction $C(V)$ corrigée pour les capacités parasites; cette courbe peut se mettre sous la forme:

$$C_{pF} = 25 \left( \frac{V}{45} \right)^{-0.6} .$$

Remarquons que $C$ ne varie pas tout à fait comme l'inverse de l'épaisseur de la barrière. L'amplitude absolue est de 1.5 mV/MeV pour une polarisation de 45 V. La stabilité en amplitude à long terme n'est limitée que par l'amplificateur.

(b) Le rapport signal/bruit est élevé pour deux raisons:

le temps de montée est très court; le nombre moyen d'impulsions fortuites dues au bruit pendant la durée de l'impulsion est d'autant plus faible que celle-ci est plus courte.

La valeur de l'énergie de création des paires d'électron-trou est faible (10 fois plus petite que dans un compteur à gaz). L'erreur absolue sur la mesure de la charge recueillie étant limitée dans tous les cas à quelques centaines de charges électroniques, le rapport signal/bruit est 10 fois meilleur que pour un compteur à gaz.

Le bruit dû à la jonction elle-même n'intervient pas à condition que le courant inverse soit de l'ordre de quelques dixièmes de microampère (voir section 8). L'énergie minimum détectable était limitée dans notre cas par le bruit d'entrée du préamplificateur Ecko. Aucune précaution spéciale n'avait été prise pour rendre le bruit minimum, la détection de signaux équivalent à une énergie dissipée de 100 keV était cependant possible.

La dispersion en amplitude à mi-hauteur du pic, due au bruit de l'amplificateur équivaut à moins de 10 keV si on opère avec une polarisation suffisante, pour rendre la capacité du détecteur assez faible. Le bruit ne limite donc pas la surface utile du détecteur à 4 mm². L'augmentation de cette surface est un problème de technologie de semi-conducteurs.

(c) Si l'on connecte plusieurs détecteurs en parallèle, une particule d'énergie $E$ pénétrant dans un quelconque des détecteurs, et arrêtée dans la barrière, provoque une impulsion d'amplitude proportionnelle à:

$$\frac{E}{\sum C_i} .$$

On peut ainsi utiliser plusieurs détecteurs avec une seule chaîne d'amplification et une polarisation commune. Ce montage peut être très utile pour l'étude de réactions fournissant un spectre simple.

Par exemple, la réaction $O^{16}$ (d,$\alpha$) $N^{14}$, fournit un seul groupe de particules $\alpha$, dont l'énergie varie très rapidement avec l'angle d'observation. Des détecteurs décalés d'une trentaine de degrés, permettraient l'enregistrement simultané, par un analyseur d'impulsions, de spectres relatifs à plusieurs angles.

## 7. Résolution

(1) La dispersion statistique de l'amplitude des impulsions dues à une particule monocinétique arrêtée dans la barrière, est indépendante de l'énergie de la particule. C'est là une des propriétés fondamentales du détecteur à jonction. La largeur à mi-hauteur du pic exprimée en unités d'énergie est en moyenne de 30 keV pour les protons et les deutons, 40 keV pour les particules $\alpha$.

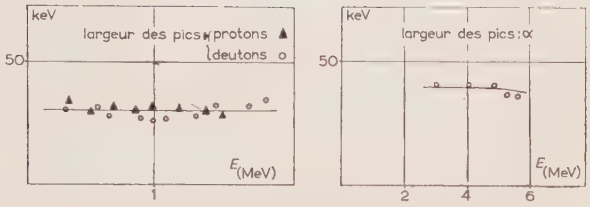


Fig. 11. Dispersion, évaluée en énergie, des impulsions dues à différentes particules.

La figure 11 montre les résultats pour les trois types de particules.

(2) Examinons les facteurs qui influent sur la dispersion en amplitude.

(a) La dispersion statistique sur le nombre de paires électron-trou créées est négligeable étant donné leur très grand nombre.

(b) Des irrégularités d'épaisseur de la zone insensible ne conduiraient pas à une largeur constante en fonction de l'énergie. Le phénomène observé, prouve au contraire que cette zone a une épaisseur bien constante.

(c) Le phénomène de dispersion statistique de l'énergie perdue dans la zone insensible ne conduit qu'à une dispersion de 9 keV pour les protons, faible devant les 30 keV observés.

(d) Le bruit électronique est inférieur à 10 keV, comme on l'a vu au chapître précédent.

(3) Nous avons ainsi conclu que les largeurs observées représentent une propriété intrinsèque du cristal. Ceci est confirmé par une mesure de Friedland *et al.*[5]) qui ont trouvé la même largeur que nous pour les particules $\alpha$ du polonium, avec des jonctions de type différent dont la zone insensible était bien plus faible.

Il est difficile d'expliquer pourquoi la dispersion est indépendante de l'énergie pour une particule de type donné. On peut néanmoins admettre que le phénomène qui provoque cette dispersion ne se manifeste que vers la fin du parcours de la particule. Il semblerait qu'au dessous d'une certaine vitesse, la particule peut céder de l'énergie au cristal par un processus autre que la création de paires d'électron-trou (ou créer des paires avec une énergie qui diffère localement de 3.25 eV). Quel que soit ce processus, il ne peut pas se répéter de nombreuses fois, sinon une forte dispersion ne pourrait pas prendre naissance. Ce processus pourrait être par exemple un phénomène de déplacement collectif d'atomes dans le réseau cristallin.

(4) Les précautions suivantes ont été prises pour la mesure précise des résolutions:

(a) les pics étaient toujours étalés de sorte que la largeur à mi-hauteur couvre au moins trois canaux de l'analyseur RIDL.

(b) les cibles étaient choisies de manière à rendre la dispersion en énergie des particules diffusées faible devant la dispersion à observer. Pour le vérifier, nous avons dans chaque cas, utilisé deux cibles, l'une ayant une épaisseur double de celle de l'autre. On constatait que les résultats fournis par les deux cibles étaient identiques.

Les diffusions élastiques ont été étudiées sur des cibles de $Al^{27}$ de 7 $\mu g/cm^2$. Pour cette cible, la dispersion en énergie des deutons et des protons diffusés à l'arrière était inférieure à 6 keV.

Pour les réactions nucléaires, nous avons utilisé des cibles de $Al_2O_3$ de 17 $\mu g/cm^2$: la dispersion de l'énergie des particules $\alpha$ était également inférieure à 6 keV.

Notons que des cibles de Al de 30 $\mu g$ déforment déjà notablement les spectres dus aux protons et deutons diffusés. En effet, le spectre d'énergie des particules diffusées est rectangulaire; sa largeur s'ajoute directement à la largeur observée, la loi de composition par le carré des largeurs n'étant pas appliquable dans ce cas.

(c) Toutes les réactions utilisées fournissent des particules dont l'énergie varie très rapidement en fonction de l'angle d'observation. L'ouverture angulaire du détecteur a été maintenue inférieure à 1.5°.

(d) Nous avons enfin constaté que la résolution baisse si les constantes d'intégration et de différentiation de l'amplificateur Ecko sont trop grandes. Nous avons choisi les deux constantes égales à 0.32 $\mu s$.

Ces précautions sont indispensables dans tout travail où l'on veut profiter au maximum des possibilités offertes par le détecteur.

Signalons que le taux de comptage peut

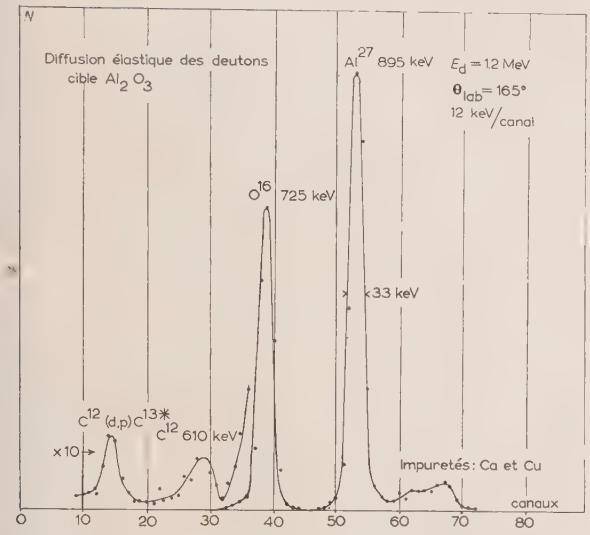


Fig. 12. Spectre des deutons diffusés élastiquement par une cible de $Al_2O_3$. Il faut remarquer que le carbone est inévitablement présent sur la cible, à l'état de contamination.

atteindre $10^4$ c/s sans que la résolution soit diminuée.

(5) La forme des pics est sensiblement gaussienne. Pour réduire le nombre de coups en dehors des pics, nous avons utilisé un diaphragme en rubis d'horlogerie. Celui-ci présente plusieurs avantages:

les bords du trou sont parfaitement polis;

le diamètre du trou est connu au micron près ce qui facilite les mesures de section efficace absolue;

la diffusion coulombienne par les bords est faible, le rubis étant formé des noyaux légers $Al^{27}$ et $O^{16}$.

Avec ce dispositif, le nombre de coups en dehors du pic était inférieur à 1% du total pour les particules $\alpha$ du polonium.

(6) Les figures 9, 12, 13, 14, 15 présentent quelques spectres caractéristiques. Tous ces spectres ont été enregistrés avec une cible de $Al_2O_3$ d'une épaisseur de 35 $\mu g/cm^2$.

La figure 12 montre un spectre de deutons diffusés élastiquement. Le petit pic double, au dessus du pic de Al, est attribué à des impuretés de masse voisine de celle de Ca et de Cu, présentes dans l'aluminium à raison de quelques $^0/_{00}$. Les protons de la réaction $C^{12}$ (d,$p_1$) $C^{13}$*, d'une énergie de 440 keV sont également détectés.

La largeur des pics est un peu supérieure à 30 keV à cause de l'épaisseur de la cible.

La figure 13 montre un spectre de protons diffusés; l'écartement des groupes est ici bien plus faible. En pratique, on peut distinguer facilement deux groupes de protons séparés par 50 à 60 keV.

Le spectre complet dû à l'effet des deutons sur $Al_2O_3$ a été présenté figure 9. Pour enregistrer correctement un tel spectre en entier, il faudrait disposer de 300 ou 400 canaux. On voit que la résolution sur les protons est mauvaise: les particules qui pénètrent dans la zone de diffusion fournissent en effet un spectre mal résolu.

La figure 14 représente les nombreux pics dus à la réaction $Al^{27}$ (d,$\alpha$) $Mg^{25}$. On distingue les pics correspondant à 9 niveaux de $Mg^{25}$. Les pics apparaissaient plus larges qu'ils ne sont en réalité, le nombre des canaux étant insuffisant pour étudier en détail un spectre aussi étendu. Ainsi le doublet correspondant au niveaux excités 6 et 7 de $Mg^{25}$ et les pics dus à la réaction $O^{18}$ (d,$\alpha$) $N^{16}$ ne sont pas séparés (la section efficace de cette dernière réaction est si élevée qu'elle s'observe en dépit de la faible proportion de $O^{18}$, 0.2%, présent dans l'oxygène naturel). Observons que le pic dû à l'état fondamental de $Mg^{25}$ est élargi à la base, en effet la particule $\alpha$ de 6.4 MeV, pénétrait légèrement dans la zone de diffusion.

La figure 15 illustre la limite des possibilités de séparation de groupes de particules $\alpha$. Le détecteur a été placé à divers angles et les

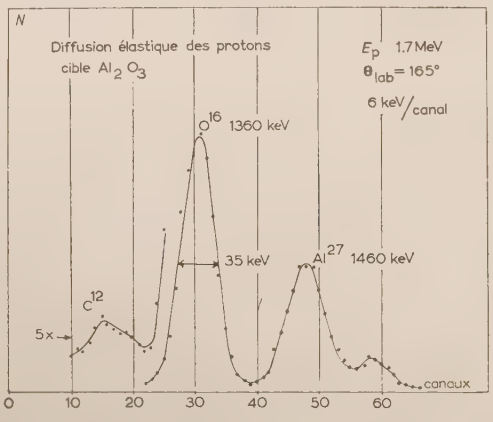


Fig. 13. Spectre des protons diffusés par une cible de $Al_2O_3$.

spectres enregistrés successivement, l'énergie de bombardement restant fixe. La séparation en énergie due au déplacement angulaire est portée

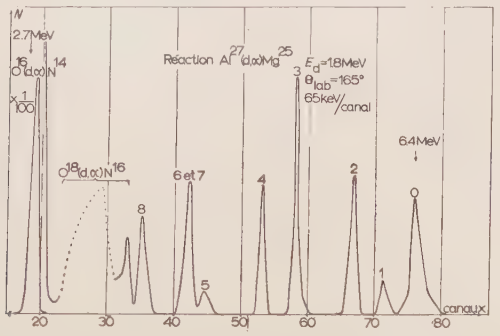


Fig. 14. Spectre complet de la réaction $Al^{27}$ (d,α) $Mg^{25}$. Le pic dû à $O^{16}$ est à une échelle 100 fois plus petite.

sur la figure. On voit que deux groupes dont les énergies diffèrent de 90 keV peuvent être complètement séparés. Deux groupes distants de 60 keV donnent deux pics qui sont encore aisément décomposables. Le spectre montre que l'ouverture angulaire doit être maintenue très faible pour cette réaction, si on veut éviter l'élargissement des raies.

### 8. Stabilité des Caractéristiques

Le détecteur est essentiellement constitué par une diode, polarisée en non conduction, dont deux caractéristiques électriques sont particulièrement importantes:

tension de claquage,
courant de saturation, ou courant inverse.

(a) La tension de claquage limite la tension de polarisation par conséquent l'épaisseur maximum de la barrière. Il est important que cette barrière soit aussi profonde que possible pour étendre le domaine de linéarité et rendre la capacité petite. Il faut remarquer que le détecteur ne fonctionne pas d'une manière satisfaisante si la tension de polarisation est trop voisine de la tension de claquage. Il peut se produire des impulsions de courant ou "microplasmas" même si la tension de polarisation est nettement inférieure à la tension de claquage. Ces microplasmas se manifestent par des impulsions qui augmentent en nombre et en ampli-

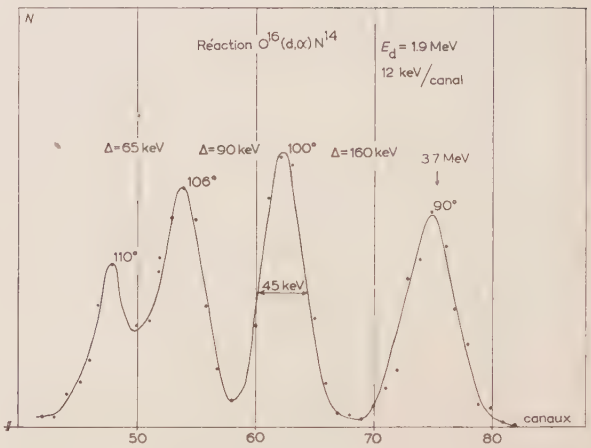


Fig. 15. Spectre illustrant les limites des possibilités de séparation de groupes de particules α. Il a été obtenu artificiellement à partir du groupe des particules α dues à la réaction $O^{16}$(d,α)$N^{14}$, en déplaçant angulairement le détecteur: les pics ont été enregistrés successivement sans effacer la mémoire de l'analyseur RIDL.

tude lorsque la tension de polarisation croit. Un de nos détecteurs présentait ce phénomène pour une tension de l'ordre de 45 V alors que le coude de la caractéristique inverse se situait vers 70 V. Les microplasmas sont la conséquence de défauts accidentels dans la jonction: dislocations dans le cristal, non uniformité de la diffusion, etc. pouvant créer des petites zones où le champ électrique est plus élevé. Le phénomène des microplasmas a été étudié par D. G. Rose[6]). La tension de claquage varie selon les échantillons d'un même lot de fabrication. Par contre, pour une même jonction, elle apparaît stable au cours du bombardement.

(b) Le courant inverse détermine le bruit de la jonction. Ce bruit peut avoir différentes sources:

bruit thermique: faible dans le silicium;
bruit de surface: la jonction étant dans le vide, ce bruit est supprimé;
bruit de recombinaison-génération, analogue au bruit de grenaille, il croît très rapidement avec le courant inverse. Celui-ci doit être inférieur au microampère pour que le bruit de la jonction soit négligeable devant celui de l'amplificateur.

[6]) D. J. Rose, Phys. Rev. **105** (1957) 413.

Nous avons constaté que le courant inverse peut augmenter rapidement au cours de l'utilisation si les précautions suivantes ne sont pas prises; et pour lesquelles il faut:

maintenir la jonction dans la pénombre;

empêcher les électrons secondaires, émis par la cible, d'atteindre la surface du détecteur. Ceci peut être fait, par exemple au moyen d'un anneau de garde fortement polarisé.

Si toutefois le courant atteint une valeur excessive par suite d'un bombardement électronique de la surface, une "guérison" de la jonction s'obtient par exposition pendant quelques minutes à l'air. Nous avons attribué ce phénomène à la chimi-désorbtion de l'oxygène, accélérée sous vide par la lumière et le bombardement électronique.

Le bombardement par des particules lourdes pénétrantes provoque une lente augmentation du courant inverse; cependant la jonction est régénérée en quelques heures de repos. Cet effet est dû à l'introduction de défauts dans la masse. Néanmoins, un flux intégré de l'ordre de $10^{11}$ particules par $cm^3$ en 10 heures, ne provoque pas une augmentation gênante du courant inverse. Ceci permet de travailler avec des taux de comptage usuels en spectroscopie. Un de nos détecteurs a été soumis au bombardement pendant plus de 200 heures au cours de nos expériences, sans subir de dommages.

## 9. Applications

(1) Nous avons étudié la diffusion élastique des deutons par $O^{16}$ et $Al^{27}$ dans le domaine d'énergie de bombardement de 0.6 à 2 MeV. Cette expérience avait été primitivement abandonnée; aucun instrument pour la détection des deutons de faible énergie ne convenait pour la réaliser.

La figure 16 montre la courbe d'excitation de la diffusion élastique des deutons par $O^{16}$ et de la réaction $O^{16}$ (d,$\alpha$) $N^{14}$ tracées simultanément au cours d'une même expérience. Une telle courbe comporte 120 points et a pu être réalisée en une seule journée.

Une étude de distribution angulaire sur la réaction $O^{16}$ (d,$\alpha$) $N^{14}$ est en cours avec un

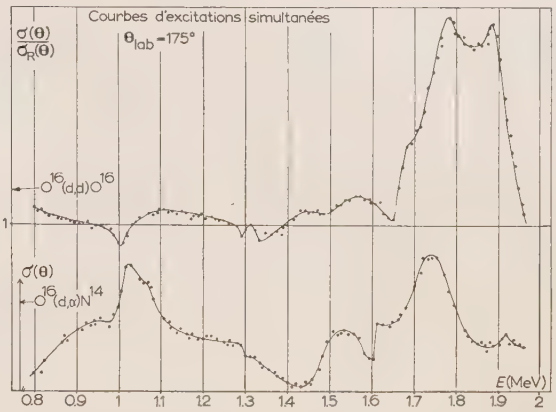


Fig. 16. Courbes d'excitations des deux réactions $O^{16}$(d,$\alpha$)$N^{14}$ et $O^{16}$(d,d)$O^{16}$ tracées simultanément, au cours d'une seule journée de travail (chaque courbe comporte 120 points).

système de trois détecteurs utilisés en parallèle. Cette expérience continue un travail commencé avec des compteurs proportionnels, utilisés aux prix de grandes difficultés, vu la faible énergie des particules $\alpha$ (2.7 à 3.5 MeV).

L'étude de la réaction $O^{18}$ (d,$\alpha$) $N^{16}$ est en préparation. Cette réaction produit 4 groupes de particules $\alpha$ séparés en moyenne de 90 keV. L'expérience apparaît possible à réaliser avec le nouveau détecteur.

(2) Envisageons quelques possibilités nouvelles du détecteur en physique nucléaire classique.

La diffusion élastique des deutons et des protons par les noyaux légers devient aisée à étudier. Des spectres de protons de faible énergie, provenant par exemple de réactions (d,p) de $Q$ faible ou même négatif, peuvent être explorés en présence de protons énergiques, sans que le bruit de fond dû aux neutrons ou aux rayons $\gamma$ ne masque le spectre. Des niveaux très serrés peuvent être explorés.

Des corrélations angulaires peuvent être étudiées avec des coïncidences très rapides, des durées de vie très brèves peuvent être mesurées.

Enfin, des ions plus lourds peuvent être détectés avec des jonctions dont la zone insensible est assez faible.

(3) Le faible encombrement du détecteur et son prix bas (pas de haute tension stabilisée, pas de photo-multiplicateur) permettent l'utilisation simultanée d'un très grand nombre

d'unités. Par exemple l'exploration du plan focal d'un aimant peut être prévu avec une "mosaïque" de détecteurs montés sur une même embase.

(4) En physique des hautes énergies, le détecteur utilisé directement dans un montage coaxial devrait permettre la mesure de temps de l'ordre de $10^{-10}$ s. On pourrait réaliser ainsi des mesures de temps de vol sur de très faibles distances.

## Appendice

CALCUL DE L'EFFICACITE DE COLLECTION; LONGUEUR DE DIFFUSION

(1) Rappelons que la diffusion des porteurs libres dans une zone où le champ électrique est nul obéit à l'équation

$$D\Delta q = \frac{q}{\tau} + \frac{\partial q}{\partial t} \qquad (1)$$

où $q$ est la densité de charge, $D$ la constante de diffusion qui vaut 10 cm²/s pour le silicium et $\tau$ la durée de vie des porteurs. L'équation (1) n'est valable que si $\tau$ est constante dans la masse. Il résulte de (1) qu'en régime permanent, la densité de charge varie comme $e^{-x/L}$, $x$ étant la distance à une source de charge ponctuelle. $L$ est appelé longueur de diffusion et vaut: $L = \sqrt{D\tau}$.

(2) L'analyse de la courbe représentative de la charge totale recueillie, en fonction du parcours de la particule, permet le calcul de la longueur de diffusion. Le tracé de ces courbes a été effectué à l'aide d'un oscilloscope Tektronix 545 A; la jonction débitant sur une résistance de 400 k$\Omega$, ce qui conduisait à une constante de temps de 12 $\mu$s. On était ainsi assuré de ne pas déformer les impulsions en amplitude, de sorte que celles-ci étaient proportionnelles à la charge totale recueillie.

(3) *Calcul de l'efficacité de collection*

(a) Pour établir une correspondance entre l'énergie et la profondeur de pénétration des particules dans la jonction, il faut connaître la relation parcours-énergie dans le silicium. Ces données ont été extraites de l'ouvrage de Wahling[7]) par interpolation entre les valeurs données pour Al et A. Indiquons qu'une expression analytique simple exprime le pouvoir d'arrêt du silicium pour des protons d'énergie comprise entre 0.25 et 5 MeV.

$$-\frac{dE}{dx}\, 10^{-15}\ \mathrm{eV/cm^2\ atome} = 8\, E_{\mathrm{MeV}}^{-0.63} = 23\, R^{-0.39}\,\mu .$$

Cette expression a servi aux calculs qui vont suivre.

(b) La fraction $f(x)$ de la charge $q(x)$ créée entre les profondeurs $x$ et $x + dx$, qui est effectivement recueillie aux bornes de la jonction est appelée efficacité de collection. On suppose que $f(x)$ est indépendante de la densité de charges. Le but des mesures est la détermination de $f(x)$. Exprimons les amplitudes en unités de charge électrique et prenons comme variable non pas l'énergie $E$ mais le parcours $R$ de la particule incidente. Alors la charge totale recueillie $A(R)$ pour une particule de parcours $R$ est:

$$A(R) = \int_0^R f(x)\cdot q(x,R)\, dx ,$$

$q(x,R)$ étant la charge produite par une particule de parcours $R$ à la profondeur $x$. Or, $q(x,R)$ est de la forme $q\,(R - x)$, $R - x$ étant le parcours résiduel de la particule au point $x$. $q(x)$ est proportionnel à $dE/dx$. Donc

$$A(R) = \int_0^R f(x)\cdot q\,(R - x)\, dx = f * q . \qquad (2)$$

Ainsi A(R) est le produit de convolution de $f$ et de $q$ et se calcule aisément par transformation de Laplace. $A(R)$ étant obtenu par l'expérience et $q(x)$ étant une fonction connue, le calcul de $f(x)$ s'opère par inversion de l'équation intégrale (2). Dans notre cas $(x)$ est de la forme $x^{-p}$ et

$$A(R) \sim \int_0^R \frac{f(x)\, dx}{(R - x)^p} .$$

Cette équation est du "type d'Abel" et sa solution fournie par sa transformée de Laplace est

$$f(x) = \frac{\sin p\pi}{\pi} \int_0^x \frac{A'(t)\, dt}{(x - t)^{1-p}} . \qquad (3)$$

Cette expression simple a servi aux calculs numériques.

[7]) Ward Wahling, Handbuch der Physik, Vol. 34, p. 202.

(c) Le calcul numérique de l'efficacité de collection a été effectué uniquement dans la zone de diffusion. On a admis que l'efficacité vaut 1 dans la barrière, dont les limites ont été déterminées comme indiqué section 5. Pour une tension de 45 V. nous avons trouvé que l'efficacité de collection peut se mettre sous la forme

$$f(r) = e^{-r/L} \quad \text{avec} \quad L = 60 \pm 5\mu\,,$$

$r$ étant l'abscisse dans la zone de diffusion.

Ceci prouve que le silicium est bien homogène dans sa masse. En admettant que la constante de diffusion est 10 cm²/s, on trouve pour la durée de vie

$$\tau = \frac{L^2}{D} = 3.6 \pm 0.6\,\mu\text{s}\,.$$

La longueur de diffusion $L$ calculée pour d'autres tensions de polarisation est sensiblement la même, comme il fallait s'y attendre.

La figure 17 représente l'efficacité de collection pour une polarisation de 45 V:

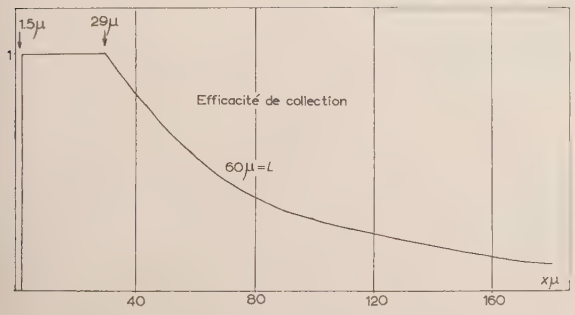


Fig. 17. Courbe représentative de l'efficacité de collection en fonction de la distance de la face d'entrée.

La figure 18 montre la courbe d'amplitude mesurée à 45 V et la courbe calculée avec l'efficacité de collection déterminée ci-dessus.

(d) Cette méthode est générale: elle permet l'étude directe des semiconducteurs, même non homogènes, en profondeur. L'équation (3) permet le calcul de la longueur de diffusion même quand elle varie dans la masse.

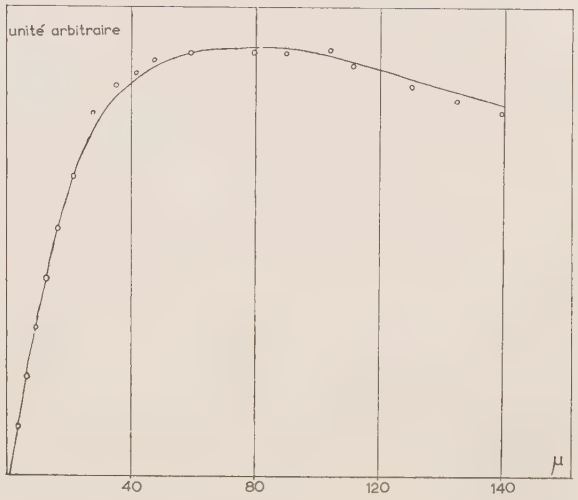


Fig. 18. Courbe théorique de l'amplitude calculée à partir de l'efficacité de collection représentée figure 17, et points expérimentaux. Nous avons porté en abscisse le parcours des particules, c'est la raison pour laquelle cette courbe ne présente pas de partie linéaire.

**Remerciements**

Nous remercions Monsieur le Professeur Y. Rocard qui a mis à notre disposition les facilités du Laboratoire de Physique de l'Ecole Normale Supérieure et Monsieur le Professeur H. Halban pour ses encouragements et ses conseils.

Nous remercions Monsieur G. Bishop pour ses conseils dans le domaine de la Physique Nucléaire.

Nous remercions Monsieur le Professeur P. Aigrain dont les conseils en matière de Physique du Solide nous ont apporté une aide importante pour la réussite de nos expériences.

Nous remercions la Compagnie LTT pour la réalisation des détecteurs ainsi que le Commissariat à l'Energie Atomique pour l'aide matérielle qu'il a bien voulu nous accorder.

NUCLEAR INSTRUMENTS AND METHODS 8 (1960) 106–116; NORTH-HOLLAND PUBLISHING CO.

# RESPONSE OF SEMICONDUCTOR SURFACE-BARRIER COUNTERS TO NITROGEN IONS AND ALPHA PARTICLES

M. L. HALBERT and J. L. BLANKENSHIP

*Oak Ridge National Laboratory†, Oak Ridge, Tennessee*

Received 8 April 1960

Silicon and germanium surface-barrier counters for detection of short range ionizing particles were constructed and tested. Measurements with artificial pulses showed that the barrier height $V_0$ is about 0.6 volt in Si, and that with variation of the applied bias $V$, the barrier capacity is linear with $(V_0 + V)^{-\frac{1}{2}}$ as expected from the Schottky exhaustion-layer theory. Measurements with natural alpha particles showed that the charge-collection efficiency is probably 100%, the energy loss per electron-hole pair is $3.50 \pm 0.05$ eV in Si and $2.83 \pm 0.03$ eV in Ge, and the pulse-height resolution is outstandingly good. Two independent measurements with cyclotron-produced $N^{14}$ ions up to 25 MeV showed that the pulse-height response is linear with energy. The ratio of $N^{14}$ to alpha pulse height is equal to the energy ratio within 1%. The response to a continuous energy distribution of alpha particles indicates that the sensitive depth is on the order of 20 $\mu$ greater than the barrier depth calculated from the Schottky theory. The excess sensitive depth probably represents diffusion into the exhaustion layer of holes produced below it.

## 1. Introduction

In heavy-ion nuclear physics there has long existed a need for a detector with linear pulse-height response and good resolution. The development of surface-barrier counters by Mayer and Gossick[1]) and the extensive measurements on them by Walter *et al.*[2,3]) showed that these devices would probably be ideal detectors for short-range particles. These counters in many respects behave as thin solid-state ionization chambers. Aside from linearity and good resolution, the absence of windows, their compact size and short rise time, and their insensitivity to gamma rays, neutrons, and fast charged particles indicated that a program to make such counters for heavy-ion detectors would be well worthwhile. Additional advantages anticipated for these counters were their relative insensitivity to magnetic fields and the possibility of changing the depth of the sensitive region simply by varying an external bias.

The existence of an asymmetric potential barrier at the surface of a semiconductor is a well known phenomenon in semiconductor physics[4]). The barrier on the surface of an n-type crystal is thought to be due to surface states which trap the mobile electrons from the interior, leaving behind a region of fixed positive charge. Typically, for high-resistivity germanium and silicon the depth of the barrier region may be on the order of 10 $\mu$ and the barrier height about 0.6 volt. The electric field is strong enough to sweep out electrons and holes liberated within the barrier region.

The successful surface-barrier alpha spectrometer of Mayer and Gossick[1]) consisted of a

† Operated for the USAEC by Union Carbide Nuclear Company.

[1]) J. Mayer and B. Gossick, Rev. Sci. Instr. **27** (1956) 407; James W. Mayer, J. Appl. Phys. **30** (1959) 1937.

[2]) Walter, Dabbs, Roberts and Wright, Oak Ridge National Laboratory Report CF 58-11-99 (1958);
Walter, Dabbs and Roberts, Oak Ridge National Laboratory Report ORNL-2877 (1960).

[3]) Walter, Dabbs and Roberts, Bull. Am. Phys. Soc., Series II, **3** (1958) 181;
Walter, Roberts and Dabbs, Bull. Am. Phys. Soc., Series II, **3** (1958) 304;
Walter, Dabbs and Roberts, Bull Am. Phys. Soc., Series II, **5** (1960) 38.

[4]) J. Bardeen, Flow of Electrons and Holes in Semiconductors, Part 8, Chapter 4 of Handbook of Physics, edited by E. U. Condon and Hugh Odishaw (McGraw-Hill Book Company, Inc., New York, 1958), especially the section beginning on p. 8–60.

thin gold film deposited on n-type Ge. Large-area (up to one square inch) Au-Ge surface-barrier counters have been used by Walter *et al.* for detection of alpha particles and fission fragments[2,5]). Similar counters of smaller area were made by McKenzie and Bromley[6]) and used successfully for detection of protons and alphas.

Silicon counters have a great advantage over germanium in that they perform well at room temperature. For good resolution, Ge counters must be chilled to dry ice or liquid nitrogen temperatures. Considerable work on Si surface-barrier counters has been reported recently[7–10a]).

Successful high-resolution counters have also been made of p-type silicon[11–13]). These are analogous to the surface-barrier counters described here, except that hole-trapping sites are established at the surface by applying a hole-trapping material, usually phosphorus.

Other semiconductor devices have been used for detection of ionizing particles: point-contact germanium diodes[14]), p–n junctions in germanium[15,16]) and silicon[17]), and p–n–p transistors[18]). All of these devices have, however, very small sensitive area and are not well suited for energy measurements.

## 2. Calculation of Barrier Characteristics

In this section several approximate formulas are given for estimating barrier characteristics which are important in the design of particle detectors. They are based on the exhaustion-layer theory of Schottky[4]).

The origin of the trapping sites normally present on the semi-conductor surface and the factors controlling their density are not fully understood[19]). Fortunately, the barrier characteristics which are of interest for particle detection may be calculated without knowing the detailed properties of the surface states. The basic assumption of the simple exhaustion-layer theory is that all the mobile electrons within a certain depth $D$ are trapped at the surface, leaving behind a uniform density of positive charge. By solving Poisson's equation with appropriate boundary conditions, it is easily shown that $D = (KV_0/2\pi eN)^{\frac{1}{2}}$, where $K$ is the dielectric constant, $V_0$ is the magnitude of the barrier height, $e$ is the electronic charge, and $N$ is the excess density of donors over acceptors. The depth may be increased by applying a negative bias to the surface. If the magnitude of the bias is $V$, the depth $D$ is then given by $[K(V_0 + V)/2\pi eN]^{\frac{1}{2}}$ or

$$D = 1051 \sqrt{\frac{K(V_0 + V)}{N}} \text{ cm} \qquad (1)$$

if potentials are in volts and $N$ is in cm$^{-3}$.

For Ge and Si, $K = 16$ and 11.8, respectively[20]). The net impurity concentration $N$ for n-type material may be estimated from the room temperature resistivity $\rho$ and the relation $N = 1/\rho\mu_n e$; the electron mobility $\mu_n$ is 3900 cm$^2$/sec-volt for Ge and 1200 for Si[21]). In the counters that were made at this laboratory, $N$ was in the range of $10^{12}$ to $10^{14}$ cm$^{-3}$.

[5]) Dabbs, Walter, Roberts and Parker, Bull. Am Phys. Soc., Series II, **5** (1960) 22.

[6]) J. M. McKenzie and D. A. Bromley, Phys. Rev. Letters **2** (1959) 303.

[7]) J. M. McKenzie and D. A. Bromley, Bull. Am. Phys. Soc., Series II, **4** (1959) 457.

[8]) E. Nordberg, Bull.Am. Phys. Soc., Series II, **4**(1959) 457.

[9]) Halbert, Blankenship and Goldman, Bull. Am. Phys. Soc., Series II, **5** (1960) 38.

[10]) J. L. Blankenship and C. J. Borkowski, Bull. Am. Phys. Soc., Series II, **5** (1960) 38; Proceedings of the Seventh Scintillation Counter Symposium, I. R. E. Transactions on Nuclear Science (to be published).

[10a]) G. Dearnaley and A. B. Whitehead, Harwell Report AERE-R-3278.

[11]) Friedland, Mayer and Wiggins, Nucleonics **18**, No. 2 (Feb. 1960) 54.

[12]) Miller, Brown, Donovan and Mackintosh, Proc. Seventh Scintillation Counter Symposium, I.R.E. Transactions on Nuclear Science (to be published).

[13]) R. W. Jackson, RCA Victor Research Laboratories, Montreal (private communication).

[14]) K. G. McKay, Phys. Rev. **76** (1949) 1537.

[15]) Orman, Fan, Goldsmith and Lark-Horowitz, Phys. Rev. **78** (1950) 646.

[16]) K. G. McKay, Phys. Rev. **84** (1951) 829.

[17]) K. G. McKay and K. B. McAfee, Phys. Rev. **91** (1953) 1079.

[18]) D. C. Brown and B. P. Faraday, Nuclear Instruments **1** (1957) 133.

[19]) Semiconductor Surface Physics, edited by R. H. Kingston (University of Pennsylvania Press, Philadelphia, 1957).

[20]) American Institute of Physics Handbook (McGraw Hill Book Company, Inc., New York, 1957), p. 5–132.

[21]) Reference 20, page 5–159.

The value of $V_0$ depends on the properties of the material and the temperature. For a Ge counter at 77° K, $V_0 \approx 0.6$ volt[2]). Measurements described below on a Si counter at room temperature gave $V_0 \approx 0.5$ volt. Other Si counters have shown $V_0 \approx 0.7$ to 0.8 volt.

The external bias $V$ that may be applied varies considerably from one counter to another. An objectionable amount of noise is generated by some counters without any bias. However, the counters used in these measurements will tolerate an external bias of about 5 volts for Ge and 70 volts for Si without becoming excessively noisy.

The Si counter to be described has been operated with a barrier depth of about 30 $\mu$ (7.2 mg/cm$^2$) with no difficulty. It is possible to achieve much deeper barriers in higher-purity material.

The signal voltage appearing across the counter for a charge $q$ collected by the barrier is $q/(C_b + C_s)$, where $C_b$ is the capacity of the barrier and $C_s$ is the stray capacity. For a surface barrier of area $A$, $C_b = KA/4\pi D$, or

$$C_b = 8.41 \times 10^{-5} A \sqrt{\frac{KN}{V_0 + V}} \text{ pF} \qquad (2)$$

if potentials are in volts, $N$ in cm$^{-3}$, and $A$ in cm$^2$. In this work $C_b/A$ was typically on the order of several hundred picofarads/cm$^2$. The charge $q$ collected for energy $E$ dissipated in the sensitive region is given by

$$q = e \frac{E}{\varepsilon} \eta \qquad (3)$$

where $\varepsilon$ is the average energy per electron-hole pair and $\eta$ is the charge collection efficiency.

The published values of $\varepsilon$ are about 3.0 eV in Ge[16]), and 3.6 eV in Si[17]). If we compare these figures with the typical value of $\varepsilon = 30$ eV for gases, it is clear that for the same capacity the surface barrier counter is capable of better resolution than a gas counter. In practice, because of the larger capacity of barriers of reasonable area, it has been difficult to surpass the best resolution that can be achieved with a carefully designed Frisch grid ionization chamber. Recently, however, this has been accomplished. Spectra of natural alpha particles have been obtained which show less than 0.3% full width at half maximum[10]).

### 3. Manufacture of Counters

Making surface-barrier counters is basically simple. Our procedure may be outlined as follows. Single-crystal material is cut into 1 mm-thick wafers of the desired area. The wafers are carefully lapped and a copper wire or foil is soldered to one face to make an ohmic contact with the body of the crystal. One can solder directly to Ge; for Si the surface is first nickel plated. The crystal is then cast in epoxy resin so that the other face is exposed. After further preparation of the surface, including etching in modified CP-4 (5 parts nitric acid, 3 parts hydrofluoric, and 3 parts glacial acetic acid), a semi-transparent layer of gold is evaporated onto the crystal and the surrounding resin to form an electrical connection with the surface barrier. A photograph of the various steps in the manufacture of a counter is shown in fig. 1. More detailed instructions on the manufacture of these counters are given by Blankenship and Borkowski[10]).

Extreme care must be taken in all steps to

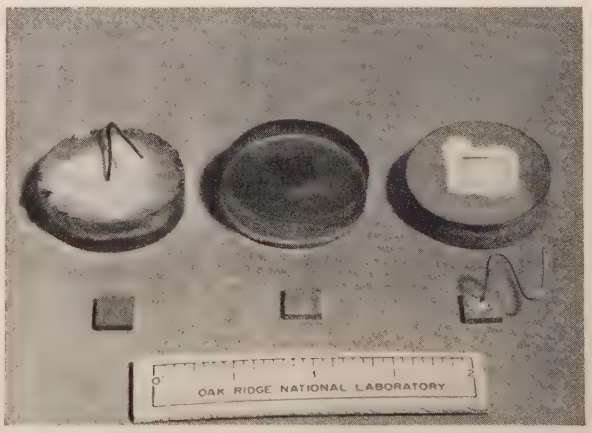


Fig. 1. Manufacture of silicon counters. From left to right in the foreground are 5 × 5 mm silicon wafers, first after being cut to shape and lapped; next, after nickel plating; and then after soldering a wire to the rear. In the background are shown the rear of a counter after casting in epoxy resin; the front of a counter after the final lapping; and a completed counter after etching, masking with polystyrene, and evaporation of the gold film.

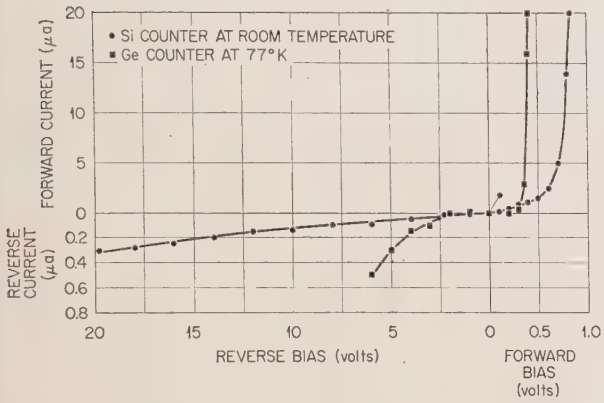


Fig. 2. Current-voltage characteristics of the counters used in this work.

achieve a high proportion of successful counters. Assuming that the surface has been carefully prepared so that it is free of irregularities which would degrade the resolution, the major problem is to keep the noise level as low as possible. It appears that selection of highly perfect crystals, meticulous cleanliness, and thorough, rinsing after etching are important.

The measurements to be described here were made with two of the first successful counters. The Ge counter was made of 40 ohm-cm material and the Si counter of 50 ohm-cm material. The exposed surface of each was a 5 × 5 mm square. The effective area was actually smaller, probably $\frac{1}{6}$ cm², because a layer of polystyrene, intended to minimize leakage, was applied around the edge of the embedded wafer before evaporation of the gold. The polystyrene is evident in the photograph. The thickness of gold on the Si counter was sufficient to cut transmission of white light approximately 50%. By neutron activation analysis, the gold film was found to be about 150 $\mu$g/cm². The gold on the Ge was of similar thickness but its thickness was not measured.

## 4. Testing of Barriers

A rapid qualitative test of a counter may be made by measuring its current-voltage characteristic. Fig. 2 shows a portion of the characteristic for the two counters used in this work. It was generally found that the counters with the smallest reverse current have the lowest noise levels. However, no quantitative relationship between reverse current and noise level could be established. For example, the Si counter at 0.6 $\mu$A reverse current showed no increase in noise above that generated by the electronics, but for the same current the Ge counter was so noisy that the pulse-height resolution was markedly degraded.

A low-noise preamplifier with gain 1000 was designed especially for this type of counter. It has a cascode input with a 5842/417 A high-performance triode and uses the large capacity at the input to keep the grid-current noise low. The equivalent noise at the input is about 5 $\mu$V rms.

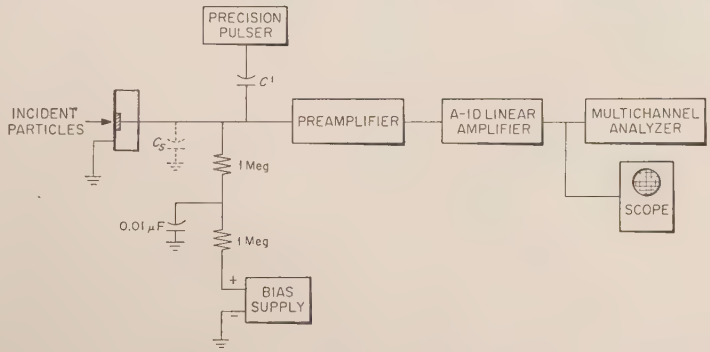


Fig. 3. Schematic diagram of electronics, showing connections to the preamplifier, bias supply, and test pulser. The capacitor $C'$ was approximately one picofarad.

(In normal operation the signal from the Si counter is about 400 $\mu$V/MeV.) The preamplifier was connected by about 200 feet of coaxial cable to an A-1D linear amplifier with delay-line clipping. The clipping time was normally 1.0 $\mu$sec, ample to collect all the charge carriers

liberated within the barrier region. Since the preamplifier gain was so high the amplifier was modified to provide increased inverse feedback in both loops. The amplifier output went to a 256-channel pulse height analyzer.

Fig. 3 shows how the counters were connected. The gold surface was grounded and positive bias applied to the back. This gave negative signal pulses. One can equally well ground the back and put a negative bias on the front, giving positive pulses. There may be a slight disadvantage in the latter arrangement since dust might be attracted to the front surface.

The bias voltage was supplied by a battery through an $RC$ filter network. The upper one-megohm resistor served also to determine the decay time of the pulses since the back resistance of the barrier is usually much greater.

Test pulses were put on the counter through the capacitor $C'$ ($\approx 1$ pF in the present work). The linearity of the entire system was checked by using a highly stable mercury-relay pulse generator having an output attenuator linear to 0.1%. The pulser was very useful for measuring barrier characteristics as well. If the pulse amplitude is $V_p$ and $C$ is the total capacity to ground, the signal $V_s$ at the preamplifier input is given by

$$V_s = V_p \frac{C'}{C + C'} \tag{4}$$

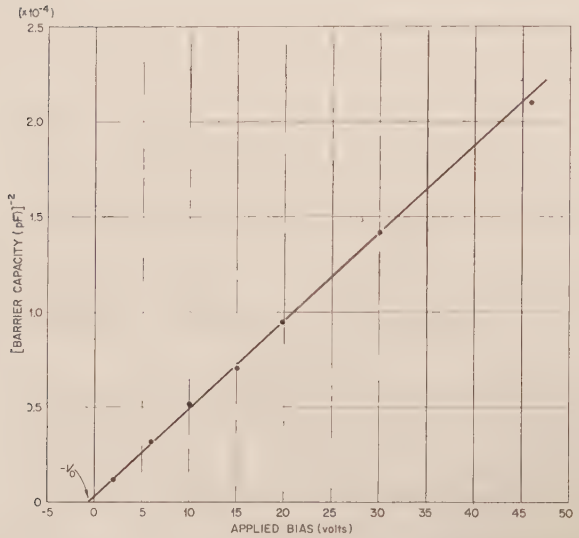


Fig. 4. Experimental check of eq. (2) for the Si counter.

or $V_p C'/C$ if $C' \ll C$. To determine the stray capacity $C_s$, the output pulse height $V_{out}$ was measured for a fixed $V_p$ with the barrier counter replaced by capacitors of known size. The intercept on a plot of $1/V_{out}$ against the added capacity wa equal to $C_s$. The barrier capacity $C_b$ could then be determined easily by re-installing the counter and measuring $V_{out}$ for the same $V_p$.

For the Si counter $C_b$ was measured in this way as a function of bias voltage. Fig. 4 shows that $1/C_b^2$ varies linearly with $V$, verifying the prediction of the Schottky theory (eq. (2)). The intercept gives $V_0 = 0.5 \pm 0.1$ volt. The slope of the line, assuming $K = 11.8$ and $A = \frac{1}{8}$ cm$^2$, gives $N = 0.90 \times 10^{14}$ cm$^{-3}$. This agrees, within the expected errors, with $N = 1.04 \times 10^{14}$ cm$^{-3}$, as calculated from the manufacturer's specification of the resistivity. The capacity of the Ge counter was measured at one bias voltage, giving $N = 0.36 \times 10^{14}$ cm$^{-3}$. This is also in satisfactory agreement with the value $0.41 \times 10^{14}$ from the nominal value of the resistivity.

## 5. Measurements with $N^{14}$ Ions and Alpha Particles

### 5.1. EXPERIMENTAL DETAILS

The Oak Ridge 63-Inch Cyclotron accelerates triply-charged $N^{14}$ to 27.7 MeV. A portion of the beam is deflected and passes through a scattering chamber. Some of the measurements on the Si counter were made by detecting the $N^{14}$ scattered at various angles by a thin ($\approx 0.2$ mg/cm$^2$) aluminum target. The counter was mounted on a movable arm inside the chamber and the angle with the incident beam was varied between 13° and 58°. The energy variation with angle is appreciable; in this way the relative pulse height for $N^{14}$ from about 15 to 25 MeV was determined quite accurately.

Data were also obtained for both the Ge and Si counters over a wider range of energies by degrading the beam energy with nickel absorbers of known thickness. For these measurements the Al target was removed so that the beam passed undisturbed through the scattering chamber. A foil changer was placed at the exit port and

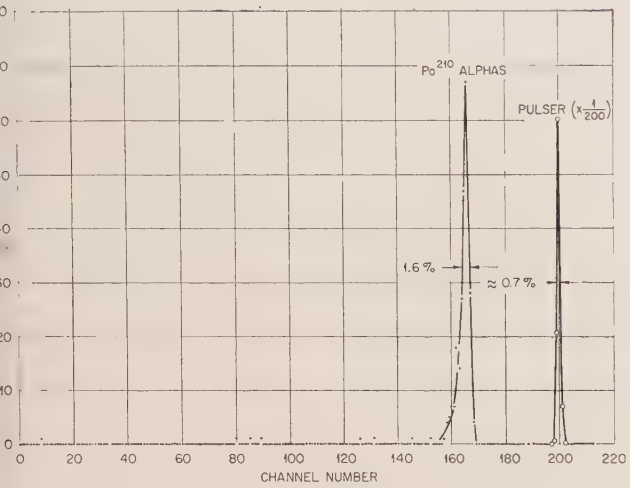


Fig. 5. Pulse-height spectrum of $Po^{210}$ alphas. Si counter, 19 volts bias.

beyond it a 0.2 mg/cm² target of gold leaf oriented at 45° to the beam direction. Nitrogen ions from the cyclotron traversed the Ni absorber, were scattered through 90°, and passed through the target to the counter under test. The counter was mounted on re-entrant cylinder which was filled with liquid nitrogen when the Ge counter was being tested. Near the counter was a weak polonium-210 source. The angular spread of the incident particles was limited by a $\frac{3}{32}$-inch diameter collimator placed on the counter.

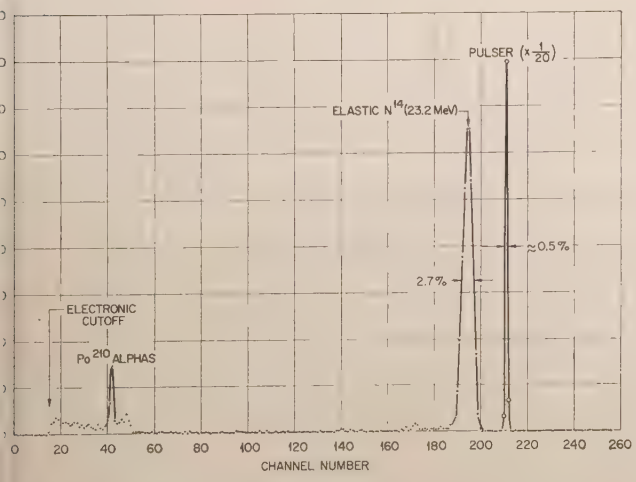


Fig. 6. Pulse-height spectrum of $N^{14}$ ions scattered from gold. Si counter, 19 volts bias.

22) Reynolds, Scott and Zucker, Phys. Rev 95 (1954) 671.

Fig. 5 shows a spectrum of alpha particles from the $Po^{210}$ source taken with the Si counter at 19 volts bias. The pulser was operating simultaneously; the cyclotron was off. The full width at half maximum, 1.6%, is actually quite poor compared with what has been obtained (0.3%) with more recently manufactured counters and a lower-noise preamplifier[10]). Nevertheless, it is interesting that even for this counter the resolution approaches the limit set by the signal-to-noise ratio, as indicated by the width of the pulser peak. The noise generated by the counter itself was always negligible compared with the electronic noise.

Unlike the Si counter, the Ge counter often exhibited changes in pulse height and noise level from day to day, though for any one set of data the results were consistent. This may have been due to disturbances caused by the frequent cycling between room temperature and liquid nitrogen temperature. Operated at 77° K and 5 volts bias, the Ge counter gave 2.0% resolution on several occasions. This counter did generate appreciable noise; at best, the noise level at 5 volts was about 20% higher than at 0 volts.

A typical beam-on spectrum for the Si counter at 19 volts bias with no absorber in the beam is shown in fig. 6. The peaks for the elastic $N^{14}$, $Po^{210}$ alphas, and the test pulser are evident. The $N^{14}$ peak is considerably broader than the alpha-particle peak of fig. 5. From signal-to-noise considerations the opposite would be expected. It may be concluded that most of the width is due to spread in the beam energy, non-uniformity in the gold target, straggling, etc. When absorbers were placed in the beam, the width was greater.

The initial beam energy was determined by replacing the gold scattering apparatus with a hydrogen gas target. Protons recoiling in the forward direction were stopped in nuclear emulsions and their track length was measured. This method has been used previously[22]). The energy after the beam passed through the various Ni absorbers could be determined to an accuracy of about $\pm$ 1 MeV from the experimental range curve by Reynolds, Scott and Zucker[22]).

The fringing field of the cyclotron was about 80 gauss where the counters were located. No magnetic shielding was provided for them. The preamplifier, placed in a region of much stronger field, was shielded. The pulse height dropped about 2.5% when the magnetic field was turned on. Since the same shift was observed for both alphas and test pulses, it is probable that imperfect shielding of the preamplifier was responsible, and the counter itself is insensitive to a magnetic field of this strength.

at 1.6 volts bias, is also linear. No aluminum scattering was measured, however, because of the difficult mechanical problem of maintaining the counter at 77° K while permitting it to be moved inside the scattering chamber.

### 5.3. RELATIVE RESPONSE TO ALPHAS

A careful investigation was made to determine if the counter response depends on the type of particle traversing the sensitive region, as it does with scintillation counters. From spectra

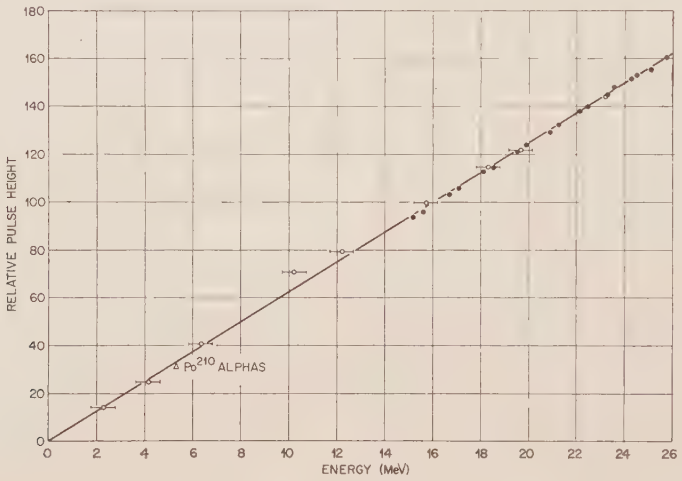


Fig. 7. Relative pulse-height response of the Si counter to $N^{14}$ ions and to $Po^{210}$ alpha particles. For the solid dots, the $N^{14}$ was scattered by a thin Al foil; the energy variation was accomplished by changing the angle of scattering, and the bias was 45 volts. For the open circles, the $N^{14}$ was scattered at 90° by a gold foil; the energy was varied by degrading the incident beam energy with nickel absorbers, and the bias was 19 volts. The error bars are estimates of the uncertainty in the range-energy relation used to convert absorber thickness to energy loss.

### 5.2. RESPONSE TO $N^{14}$ IONS

Fig. 7 shows all the data on the response of the Si counter for $N^{14}$. For the open circles the energy variation was accomplished by degradation in Ni absorbers; the bias was 19 volts. The solid dots are based on the scattering of $N^{14}$ by Al at various angles; for these points the counter was operated at 45 volts. The response to $N^{14}$ appears to be linear. As a check of the linearity, the ratio of pulse height to energy was calculated for all the solid dots; the rms deviation from the mean ratio is only 0.5%, which is comparable with the errors in locating the peak positions and the uncertainty in energy loss as the $N^{14}$ passes through the target.

A similar curve, obtained for the Ge counter such as that of fig. 6, the pulse-height ratio for the $N^{14}$ ions and the alpha particles was found to be equal to their energy ratio within a few percent.

To check this point further, more accurate measurements were made with the Si counter in which the analyzer was used essentially as a null instrument. The 0.1% helical potentiometer on the test pulser output was adjusted to give exactly the same pulse height as the $N^{14}$ particles. Then the amplifier gain was increased until the alpha pulses were being counted in the same channel. Again the pulser was adjusted for artificial pulses of the same size. The $N^{14}/\alpha$ pulse-height ratio was thus equal to the attenuation ratio. The results with this method are probably accurate to about $\frac{1}{2}$%.

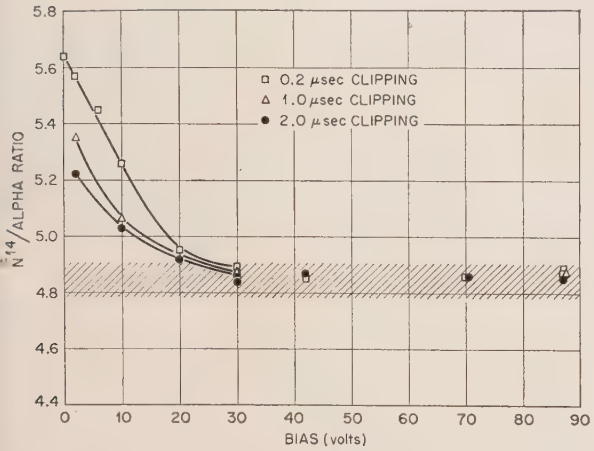


Fig. 8. Ratio of pulse height for $N^{14}$ ions and $Po^{210}$ alpha particles as a function of bias voltage and amplifier clipping time. The diagonal lines represent the measured energy ratio and its limits of error.

Two independent sets of measurements were carried out, one with $N^{14}$ scattered through 90° by Au and the other with $N^{14}$ scattered through 20° by an Al foil. The length of the delay line used for clipping was also varied in the latter runs to see how the ion collection time affected the $N^{14}/\alpha$ ratio. The Al data are shown in fig. 8. For comparison, the energy ratio with its estimated uncertainty ($4.83 \pm 0.06$) is given as a row of diagonal lines. This energy ratio includes a correction for energy loss of the $N^{14}$ in the scattering foil and for both particles in the 150 $\mu g/cm^2$ evaporated gold film on the counter.

It is evident from fig. 8 that above 40 volts the pulse-height ratio equals the energy ratio within the accuracy to which the latter is known. The same result was found for the data obtained by scattering from the Au target. The behavior of the pulse-height ratio at low bias may be explained qualitatively. The alphas have a longer range than the $N^{14}$ ions. As the barrier depth is reduced the $N^{14}/\alpha$ pulse-height ratio should therefore increase. The curves for different clipping times indicate that with longer collection time more of the holes produced below the exhaustion region can contribute to the pulse height.

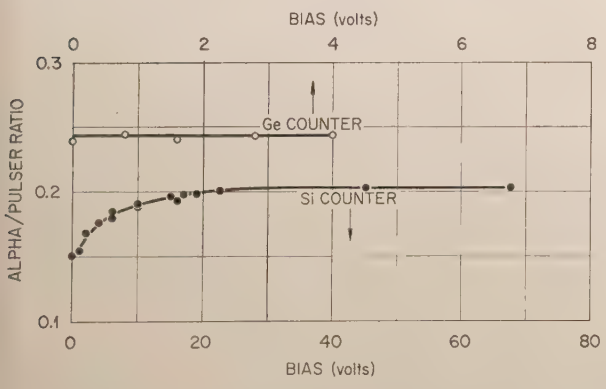


Fig. 9. Ratio of pulse height for $Po^{210}$ alpha particles and fixed test pulser input as a function of bias voltage.

### 5.4. DETERMINATION OF $\varepsilon$

The pulse height for particles of a given energy increases as the bias is raised. Several effects are reasponsible. First of all, $C_b$ decreases according to eq. (2). Second, if $\eta < 1$, then raising the bias would tend to increase $\eta$ and also the pulse height. Third, there will be an increase in the pulse height if the depth of the sensitive region at the initial bias is not great enough to stop the particles.

It is of interest to study the latter two effects because of their importance for precise energy measurements. This necessitates eliminating the effect of the variation in $C_b$, which may be easily done by taking the ratio of pulse height for the particles and for a fixed pulser signal. The ratio for the alpha particle data (from spectra such as that in fig. 5), is given for both counters in fig. 9 as a function of bias voltage. The ratio does not increase in the Ge counter as the bias is raised. This indicates that $\eta = 1$. The same behavior is seen at high bias with the Si counter. The variation at low bias is understandable if the range of the alphas exceeds the sensitive depth at low bias.

Taking $\eta = 1$ in the level portion of each curve, it is possible from eqs. (3) and (4) to calculate the magnitude of $\varepsilon$ for each counter. The numbers obtained from these curves are $\varepsilon_{Si} = 3.3 \pm 0.3$ eV and $\varepsilon_{Ge} = 2.8 \pm 0.3$ eV, in agreement with McKay's values of $3.6 \pm 0.3$ and $3.0 \pm 0.3$, respectively. The error is due principally to uncertainty in the capacity $C'$. The ratio $\varepsilon_{Si}/\varepsilon_{Ge}$ from these data is more accurate since it does not depend on $C'$. It

equals 1.20 ± 0.05, in excellent agreement with the ratio of McKay's values. From more precise work with other counters, the values of $\varepsilon$ obtained were 3.50 ± 0.05 eV for Si and 2.83 ± 0.03 eV for Ge.

Fig. 10 shows the ratio of pulse height for the $N^{14}$ ions (23.2 MeV in counter) to the pulse height for the same pulser input as in fig. 9. The Si counter shows a long plateau beginning at 19 volts. It appears, however, that collection is incomplete for the Ge counter, at least below 4 volts bias. The higher ionization density and lower electric field in the Ge barrier may account for the difference in behavior between the Ge and Si. The data above 19 volts for the Si counter and at 4 volts for the Ge counter give $\varepsilon_{Si}/\varepsilon_{Ge} = 1.23$. This is in agreement with the ratio obtained with the $Po^{210}$ alphas, indicating that $\eta \approx 1$ for the Ge counter at 4 volts.

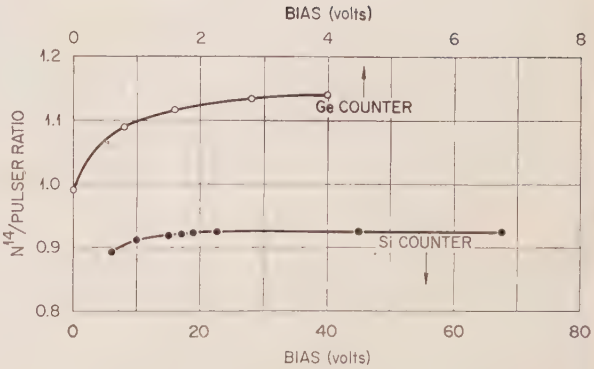


Fig. 10. Ratio of pulse height for $N^{14}$ ions and fixed test pulser input as a function of bias voltage.

for the Si and ≈ 7 volts for the Ge. The ratio plotted in fig. 9 should be expected to increase at first and then become level. This behavior was observed for the Si counter, but the plateau begins at a considerably lower bias than the predicted 70 volts. The Ge points form a plateau

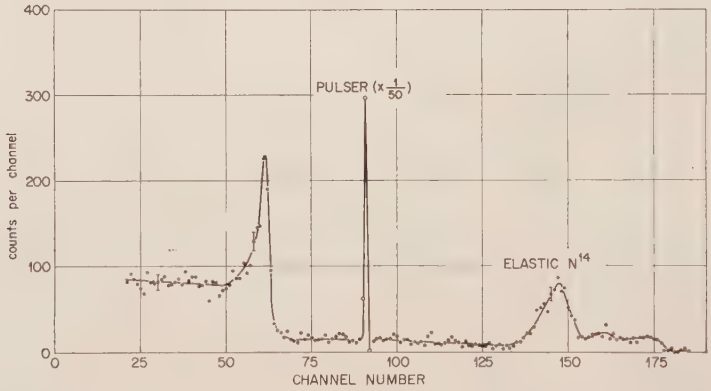


Fig. 11. Pulse-height spectrum of particles from $N^{14}$ bombardment of carbon. Si counter, 45 volts bias.

5.5. SENSITIVE DEPTH

The data of figs 9 and 10 may also be used to estimate the sensitive depth of the counters. The range of 5.3-MeV alphas is about 31 $\mu$ in Si and 19 $\mu$ in Ge. These numbers were obtained as follows. For silicon, the ratio of alpha range in Si to that in Al was calculated from the data of Gobeli[23]) and multiplied by the range in Al interpolated from Whaling's tabulation[24]). For germanium, Gobeli's ratio of Ge to Cu range was multiplied by Whaling's value for the Cu range.

The barrier depth $D$ according to eq. (1) is equal to the alpha range if $V_0 + V \approx 70$ volts beginning practically at zero bias. These data indicate that the depth of the sensitive region is greater than the barrier depth.

The range of 23.2-MeV $N^{14}$ ions is about 19 $\mu$ in Si and about 12 $\mu$ in Ge. These estimates are based on experimental range-energy data for $Al^{25}$) and $Ni^{22}$), respectively. The bias voltage needed to achieve these barrier depths, according to eq. (1), is about 30 volts for the Si and 2 volts

[23]) G. Gobeli, Phys. Rev. **103** (1956) 275.

[24]) W. Whaling, The Energy Loss of Charged Particles in Matter, in Handbuch der Physik, edited by S. Flügge Vol. **34** (Springer-Verlag, Berlin, 1958) p. 193.

[25]) Webb, Reynolds and Zucker, Phys. Rev. **102** (1956) 749.

for the Ge. Referring to fig. 10, the Si curve levels off well before the predicted bias is reached, again suggesting that the sensitive depth is greater than $D$.

A somewhat more direct measurement of the sensitive depth in the Si counter was made as a byproduct of another experiment intended to study the scattering of $N^{14}$ by $C^{12}$. Fig. 11 shows a typical spectrum at 45 volts bias. The peak in channel 147 is due to $N^{14}$ elastically scattered from $C^{12}$ (energy in counter = 15.7 MeV). The resolution is poorer than with the Au target, probably because the carbon target is thicker and less uniform, and the energy in the counter is smaller. In the low channels a continuum may be seen which rises and then drops sharply. This continuum is probably due to the continuous distribution of alpha particles produced by nuclear reactions in the target. The peak corresponds to the maximum alpha particle energy that can be lost in the counter, and is due to alphas of range equal to the depth of the sensitive region. A series of similar spectra was obtained as a function of bias voltage for three choices of amplifier clipping time. Alphas from the $Po^{210}$ source established the energy scale. The cutoff energies were calculated and then the corresponding alpha ranges estimated from the range in Al as previously described.

As shown in fig. 12, the sensitive depth determined in this way is greater than the calculated depth and increases with increasing clipping time. This result may be a consequence of the diffusion of holes produced below the exhaustion layer. If a pulse of charge carriers is introduced into a field-free region, the pulse quickly assumes a Gaussian shape which spreads with the passage of time[26]). The characteristic width is given by $\sqrt{D_p t}$. Here $t$ is the time after injection and $D_p$ is the diffusion constant. The latter may be calculated from the relation $D_p = \mu_p kT/e$ where $\mu_p$ is the hole mobility,

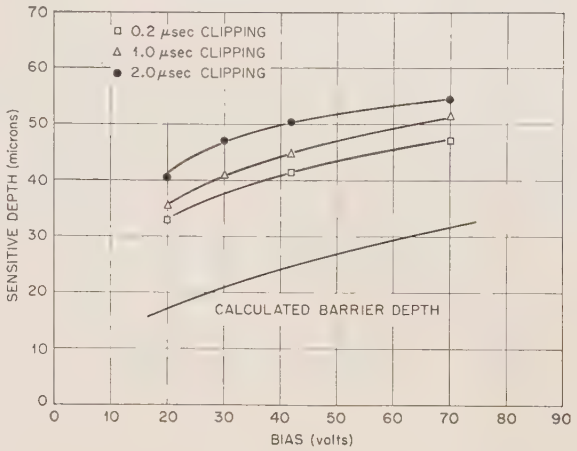


Fig. 12. Sensitive depth as a function of bias and amplifier clipping time.

$k$ = Boltzmann's constant, and $T$ = absolute temperature[27]). In the present problem, concerning holes diffusing through silicon at room temperature, $D_p \approx 10$ cm²/sec. For the clipping times used in these measurements, $\sqrt{D_p t}$ varies between 15 and 45 $\mu$. Although no quantitative estimate of the excess sensitive depth has been made, it ought to be of the same order of magnitude. The measured values of the excess depth are approximately 15, 20, and 25 $\mu$ for amplifier clipping times of 0.2, 1.0 and 2.0 $\mu$sec, respectively. It is therefore concluded that the data show qualitatively the effect of diffusion into the exhaustion region of holes produced below it.

## 6. Further Remarks

Surface-barrier counters probably will be of great value in detection of high energy heavy ions. For example, 160-MeV $O^{16}$ ions have a range of approximately 46 mg/cm² Al[28]), corresponding to about 200 $\mu$ of silicon. A counter with this great a barrier depth was recently made of 3600 ohm-cm n-type silicon. The pulse-height resolution with such energetic particles should of course be extremely good.

A solid-state particle-selective spectrometer would be a very useful device. Several schemes are possible using the well-known $dE/dx$, $E$ method. For short-range particles, it may be possible to deposit a thin dielectric layer and

[26]) W. Shockley, Electrons and Holes in Semiconductors (D. Van Nostrand Company, Inc., New York, 1950) p. 350.

[27]) Transistor Teachers Summer School, Phys. Rev. 88 (1952) 1368.

[28]) L. C. Northcliffe (private communication).

then another metallic film on top of a surface-barrier counter. The dielectric would be operated as a conduction counter to furnish $dE/dx$ pulses. Alternately, if a successful solid-state detector for long-range charged particles is developed[29,30]), then either a thin surface barrier or a dielectric layer might be used as the $dE/dx$ section. A surface barrier for this purpose would have a great advantage: its thickness could be easily adjusted to suit experimental requirements.

[29]) J. L. Blankenship, Proc. Sixth Tripartite Instrumentation Conference, Part 5, Atomic Energy of Canada Ltd.,, Chalk River Report AECL-805, p. 75 (1959).

[30]) J. D. Van Putten, Jr., and J. C. Vander Velde, Bull. Am. Phys. Soc., Series II, 5 (1960) 197.

**Acknowledgements**

We wish to thank C. E. Ryan and M. V. Goldman for the manufacture of the counters, E. E. Fairstein for the design of the special preamplifier, G. W. Leddicotte for the activation analysis of the evaporated gold film, G. A. Palmer for assistance in taking data, and W. L. Brown, F. J. Walter, and A. Zucker for helpful discussions.

NUCLEAR INSTRUMENTS AND METHODS 8 (1960) 117–120; NORTH-HOLLAND PUBLISHING CO.

# A STABILIZING SYSTEM FOR A 700 kV CASCADE GENERATOR

J. C. TIEMEYER

*Scientific Equipment Division of N.V. Philips' Gloeilampenfabrieken Eindhoven, The Netherlands*

Received 22 April 1960

A 700 kV 4-stage cascade generator in open air driving an ion accelerating tube with a beam current of 1.2 mA, was stabilized by a double-loop feedback system. A stability of the high voltage of 0.03% per hour with a maximum deviation of 0.1% was noted on the measuring potentiometer. The energy resolution was found to be approx. 100 eV by measuring (p,$\gamma$) resonances in $Al^{27}$.

## 1. Introduction

In some forms of nuclear research and measurements, accelerated ions of accurately defined energy are frequently used. These ions are often produced in a H.T. accelerator in which the ions traverse a potential difference in an evacuated tube.

In the installation in question the potential difference is produced by a 4-stage cascade generator with selenium rectifiers. The generator is supplied with 500 c/s, by a 10 kVA converter via a H.T. transformer.

Without special precautions the output voltage of a cascade generator shows some minor variations. The slow components up to a frequency of approx. 0.1 c/s may run up to 5% of the output voltage and originate from:

(a) mains-voltage variations,

(b) warming-up of the generator,

(c) slow load variations.

The fast components amount to 1% of the output voltage and originate from:

(d) the load ripple, i.e. 500 c/s and 1500 c/s (3rd harmonic),

(e) fast load fluctuations, e.g. corona effects.

Owing to these H.T. variations the accelerated particles have a certain energy dispersion. Measurement of and research on nuclear reactions occurring at a critical energy level, (nuclear resonances) is greatly hampered or even prevented by this dispersion.

For this reason, limitation of the energy dispersion in the accelerated particles by means of the best possible stabilization is desirable and increases the useful scope of the accelerator.

## 2. Stabilization with a Double-Loop Feedback System

The H.T. can be stabilized by feedback of the H.T. variations via the exciting winding of the converter at the 500 c/s supply voltage of the cascade generator.

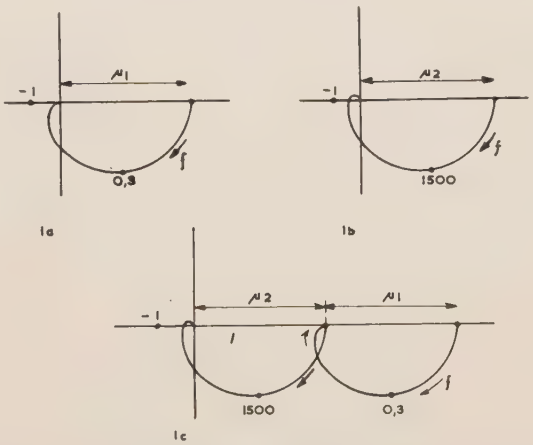


Fig. 1. Nyquist diagram of 1a: Slow feedback loop. 1b: Fast feedback loop. 1c: Fast and slow feedback loop parallel.

Owing to the time-constants of converter and cascade generator, the closed-loop gain already starts to decrease at frequencies as low as 0.3 c/s at a rate of 40 db/decade; consequently this loop is only suitable for correcting slow variations. The Nyquist diagram of this slow feedback loop is shown in fig. 1a.

Fast variations can only be stabilized in a circuit with time constants smaller than $10^{-4}$ sec, corresponding with a cut-off frequency of at least 1500 c/s, so that the 3rd harmonic of the load ripple is also stabilized.

For fast stabilization of the H.T. the following methods of affecting the H.T. are suited:

1. Control with a stabilizing tube between H.T. generator and load. This is used for stabilizing low-tension supply apparatus, but presents difficulties with positive H.T. in the control of the stabilizing tube which operates under full H.T.[1]).

2. Controlling the internal resistance of the H.T. generator with the aid of an additional adjustable load current.

This control current can be obtained:

a. by a stabilizing tube in parallel with the load, as used in shortcircuit protected L.T. supply apparatus and small H.T. supply apparatus.

b. by an adjustable corona discharge[2]).

This method increases the risk of breakdown of the H.T. generator, and furthermore it is acting too slowly owing to the transit time of the electrons.

c. in ion accelerators, by an electron beam emitted from ground potential into the accelerating tube, the intensity of which can be controlled[3]). This produces a dangerous gamma radiation in the H.T. electrode.

3. Control of the ground potential; i.e. the H.T. generator is connected to ground via an adjustable voltage source, which may be in the form of a triode amplifier.

In view of the drawbacks of the first two stabilizing methods, the installation in question employed ground-potential control. This method of stabilization is moreover entirely independent of the cascade generator and the accelerating tube, and can therefore be readily added to existing installations.

The Nyquist diagram of a fast feedback loop obtained with earth potential control is shown in fig. 1b.

To limit the necessary control range and accordingly the size of the fast stabilizer, the fast feedback loop was arranged in parallel with a slow feedback loop stabilizing the H.T. via the 500 c/s converter. The fast stabilizer is then kept in its operating point by the slow feedback loop and has to stabilize only the fast variations, which amount to 7 kV in this case.

The Nyquist diagram for the combined slow and fast stabilization is then formed by the vector sum of both diagrams (1a and 1b). Owing to the large difference in cut-off frequency (0.3 and 1500 c/s respectively) the locus of the slow feedback loop is affected in such a way that the origin is displaced to the beginning of the locus of the fast feedback loop. For the slow feedback loop locus the point $-1, +j0$, which determines the stability, is therefore moved to the left by a factor of $\mu_2$. The closed-loop gain in the slow loop can now be increased by a factor $\mu_2$ without risk of oscillating.

In this way a feedback factor of $10^4$ and more can be realized for slow variations. In practice this means that the long-term stability will be limited only by the quality of the error detection.

### 3. Error Detection

The H.T. is measured with an oil-cooled measuring resistor, made up of 4 sections, each for 175 kV. Each section consists of 600 wirewound 150 k$\Omega$ resistors, shunted with a 400 pF paper capacitor ($C_m$) for improving the frequency response. The temperature coefficient of the resistors used is below $25 \times 10^{-6}/°$ C; the permanent resistance deviation is within 0.1%. The reference voltage is variable between 0 and — 150 V with a 10-turn helical potentiometer, has a stability of better than 0.01% per hour, and is taken up from a high-quality stabilized supply unit.

### 4. The Control Circuit

A block diagram of the circuit is shown in fig. 2.

The error signal is primarily amplified by a Landsberg-type[4]) D.C. amplifier stabilized against drift, with a bandwidth of 100 kc/s and a gain of 20 000.

The amplifier output controls both the slow and the fast control systems. The fast feedback loop comprises a triode amplifier with 2 series-connected transmitting tubes TB 4/1250. The

[1]) G. Dome and H. D. Hoop, Electronics (June 20, 1958).

[2]) J. L. Mc. Kibben, D. H. Frisch and J. M. Hush, Phys. Rev. **70** (1946) 117.

[3]) S. J. Bame and L. M. Baggett, Rev. Sci. Instr. **20** (1949) 839.

[4]) S. Landsberg, Philips Res. Rep. 11.161–171 (1956).

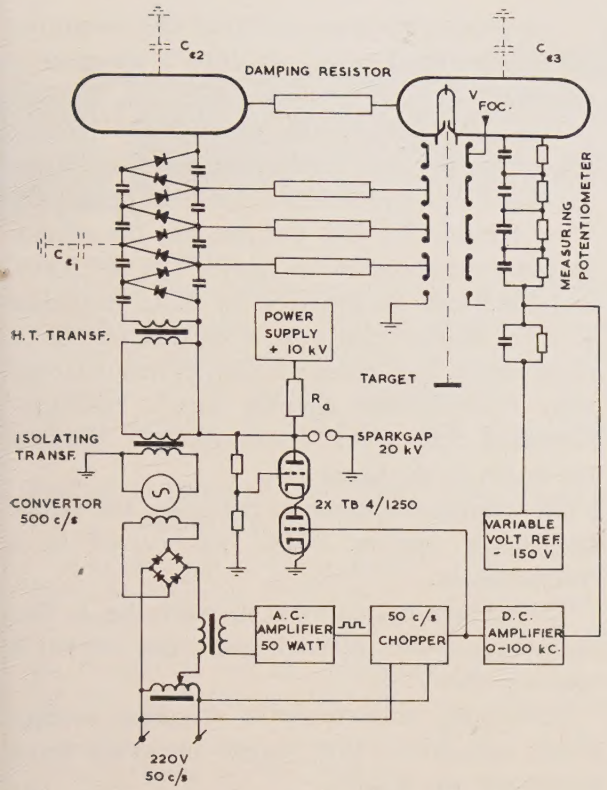


Fig. 2. Block diagram of stabilized 700 kV cascade generator.

effective control range is 7 kV at an anode supply voltage of 10 kV. The plate-current at the operating point is approx. 80 mA.

The design of this amplifier, aside from the desired control range is primarily determined by 500 c/s currents which flow from the a.c. side of the cascade generator, via stray capacitances such as $C_{e_1}$, to earth. Owing to the voltage feedback from the output of the fast stabilizer via the cascade generator and measuring resistor, to the input, the triode amplifier will be controlled in such a way that these earth currents are only passed via the triodes.

The plate-current at the operating point must therefore be greater than the amplitude of these earth currents and the internal resistance of the circuit must be low to prevent accessive modulation of the triodes. In the fast feedback loop a closed-loop gain of approx. 200 is possible. The following time constants determine the frequency response and stability:

1. upper damping resistance (800 k$\Omega$) with load capacitance $(C_{e_3} + C_m) = 10^{-4}$ sec; cut-off frequency approx. 1500 c/s.

2. internal resistance of the fast stabilizer with earth capacitances $C_{e_1}$ and $C_{e_2} = 16 \times 10^{-6}$ sec; cut-off frequency approx. 10 kc/s.

3. cut-off frequency D.C. amplifier = 100 kc/s.

In the slow feedback loop the amplified error signal is converted by a vibrator into an alternating-voltage signal of the mains frequency and then amplified up to about 50 W at full modulation.

This output is in series with the supply of the rectifier producing the exciting current of the converter. Depending upon the polarity of the error signal, the output voltage of the A.C. amplifier is either in phase or on anti-phase with the mains voltage and increases or reduces the generator output. The control range is $\pm 10\%$. A variable transformer with servomotor keeps the control automatically in the centre of the control range.

If only the slow feedback loop is used a closed-loop gain of approx. 100 $\times$ is permissible. The following time constants determine the frequency response and stability:

1. converter: 0.5 sec; cut-off frequency approx. 0.3 c/s.

2. cascade generator: dependent upon the load; was averaged at 0.5 sec.

The db-log $f$ diagram of the combined slow and fast stabilization is the sum of the separate diagrams and is shown in fig. 3. The curve directly indicates the feedback factor for each frequency.

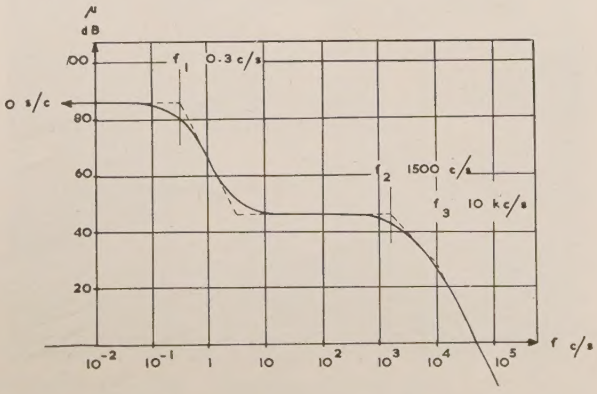


Fig. 3. Db–log $f$ curve of double loop feedback system.

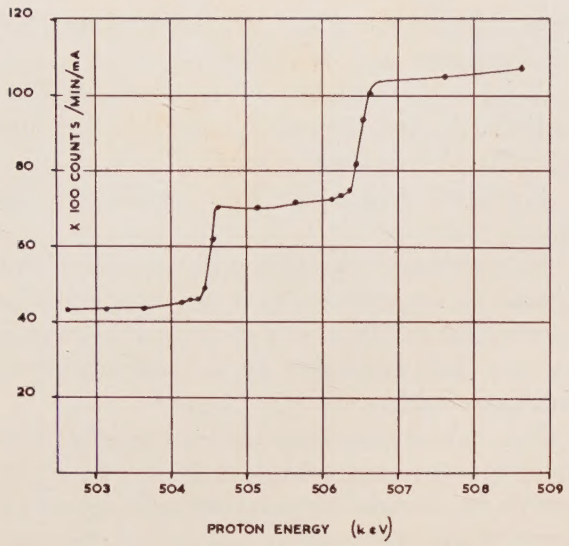


Fig. 4 Gamma ray curve of $Al^{27}(p,\gamma)$ $Si^{28}$.

## 5. Results

The long-term stability was examined by measuring the current in the measuring potentiometer with the aid of a compensation circuit. The stability of the measuring current was found to be better than 0.03% per hour with a maximum drift of 0.1% throughout the measuring periode (10 hours).

Considering the high quality of the measuring potentiometer, the H.T. stability is assumed to be equal.

The short-term stability and the energy resolution of the accelerated particles were examined by measuring a nuclear resonance. Very suitable for this purpose are the closely spaced resonances in $Al^{27}(p,\gamma)Si^{28}$ at 504.5 keV and 506.5 keV, as reported by S. L. Andersen *et al.*[5]). Measurements were carried out on a thick target. The gamma radiation was detected with a scintillation counter with a thallium-activated NaI-crystal fitted directly beneath the target in the beam axis.

To suppress background radiation, the radiation below approx. 2 MeV was cut-off in a discriminator.

The gamma-ray curve is shown in fig. 4. The half-width value derived from this curve is approx. 100 eV.

Resonance measurements at other energy levels and with other target materials have confirmed this result[6]).

[5]) S. L. Andersen, T. Holtebekk, C. Lönsjö and R. Tangen, Nucl. Phys. **4** (1957) 39–43.

[6]) S. Wagner and M. Heitzmann, Zeitschr. f. Naturfors. (1960) To be published.

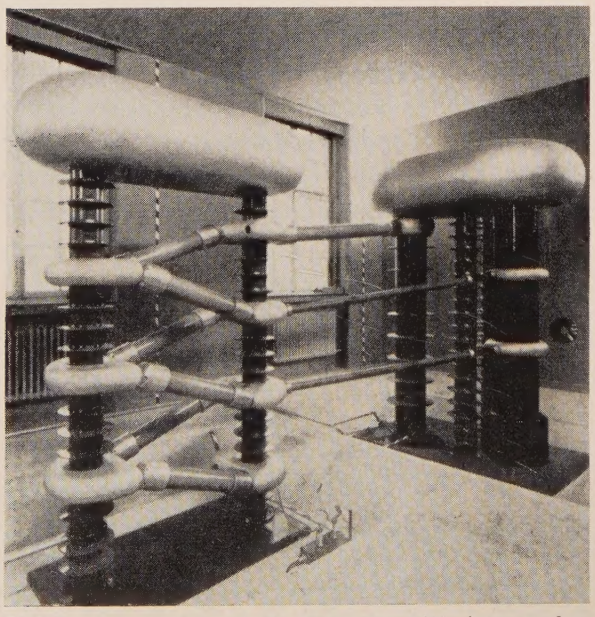

Stabilized 3 stage cascade generator with ion accelerator, installed at Staatliche Ingenieursschule, Essen, Germany.

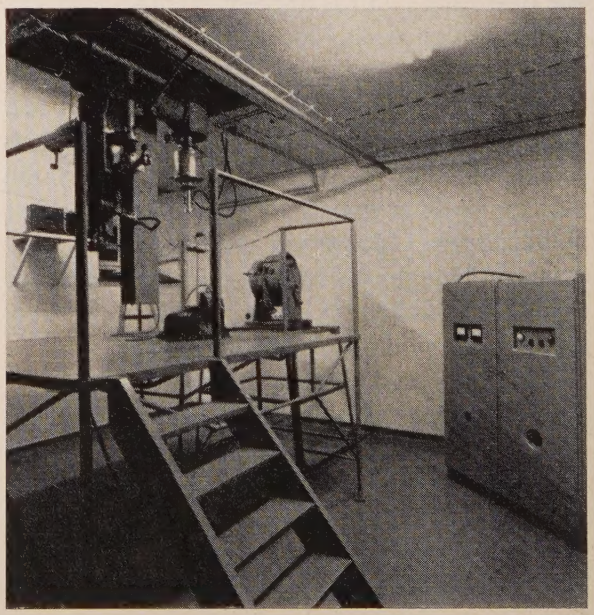

Target room of ion accelerator. Note the fast stabilizer in the right of the figure. The slow stabilizer is built in the control desk situated in the control room.

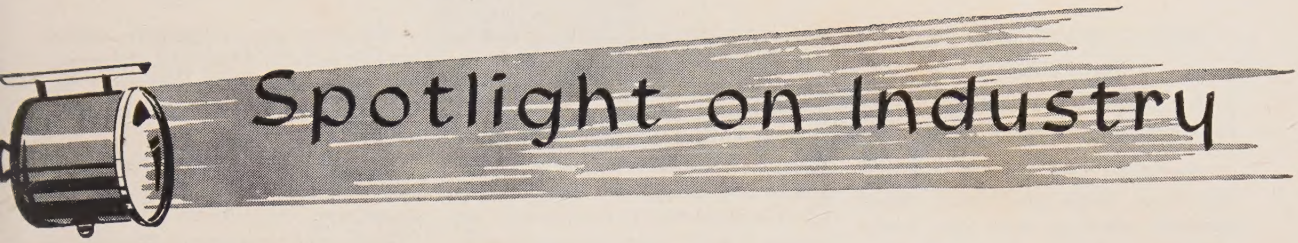


This section appears each month and features various happenings of interest in the nuclear industrial world and objective information on products of the nuclear manufacturers. It is offered entirely as a service and all nuclear manufacturers are cordially invited to submit clearly objective and descriptive material on their endeavours and product developments for consideration for use in this section.

### BRITISH ELECTRONIC COMPUTER EXHIBITION 1961

Great Britain is to hold a second Electronic Computer Exhibition in the National Hall, Olympia, London, from Wednesday, October 4 to Thursday, October 12, 1961, and a second Business Computer Symposium will be held concurrently.

This announcement is made by the Joint Committee of the Electronic Engineering Association (E.E.A.) and the Office Applicance and Business Equipment Trades Association (O.A. B.F.T.A.), which organised the very successful Exhibition in the same place at the end of 1958.

As on the last occasion the Exhibition and Symposium will be aimed to interest potential users of computers and data processing systems and to demonstrate to them the recent considerable progress made in Great Britain in design, manufacture and use of computers.

Secretary of the Joint Committee remains Mr. D. C. Scoones, Messrs. Peat, Marwick & Mitchell & Co., 94–98 Petty France, London, S.W. 1.

---

### 3 NEW 10 Mc/s TRANSISTOR COUNTER-TIMERS

*Ad. Auriema, Inc., Exporters, 85 Broad Street, New York 4, N.Y., U.S.A.*

Three new all solid-state dc to 10 Mc/s counting, timing, and frequency measuring instruments have been developed by Computer-Measurements Co.: the Model 727A Transistor Universal Counter-Timer, the Model 707A Transistor Frequency-Period Meter, and the Model 757A Transistor Time Interval Meter.

Not a single vacuum tube is used in the three 10 Mc/s instruments, providing increased reliability, reduced power consumption, size and weight. Power consumption is 35 W, about $\frac{1}{10}$ the requirement for present day vacuum tube models and weight is only 27 lbs. All components are derated. The instruments are light enough for airborne operation and small enough to fit standard explosion proof housings.

The Model 727A combines the functions of a counter, time interval meter, and frequency/period meter. It performs five basic functions selectable by a front panel switch. Input circuitry has been designed to exploit the desirability of remote operation and switching without special regard to cable lengths, type of cable, impedance matching, etc. All functions are brought to the rear. This flexibility makes the instrument extremely useful for automatic programming of the control functions.

The Universal Counter-Timer consists of three input channels, a special decade count-down time base, time eliminates the need for divider adjustment, and a series of plug-in, transistorized decade counting units. Output information from each DCU will operate digital printers, punches, inline readouts and other data processing equipment. Readout is available in either the standard vertical numeral panels as shown or in the inline Nixie version.

The Universal Counter-Timer's measurement ranges are dc to 10 Mc/s for frequency; 0.1 $\mu$sec to $10^7$ second for time interval; 0.1 $\mu$sec for period. Frequency converters are available for higher frequencies. Accuracy is $\pm$ 1 count $\pm$ oscillator stability. Sensitivity is 0.25 v rms; input impedance is 25 k $\Omega$ per volt.

---

### a-c — d-c ELECTRONIC VOLTMETER

*Metronix, Inc., Chesterland, Ohio*

Both a-c and d-c voltages as small as 10 millivolts f.s.d. may be measured accurately with a new multi-range electronic voltmeter, especially designed for built-in half relay-rack mounting in systems and consoles.

SPD-35 permits continuous monitoring of critical parameters and will handle virtually all needs for electronic voltmeters in systems.

The instrument is a standard $9\frac{1}{2}$ inches wide, 7 inches high and 9 inches deep. Its 6-inch meter has an arc length of $5\frac{1}{8}$ inches, for easy readout.

For a-c measurement, SPD-35 has a high input impedance of 5 M$\Omega$, shunted by less than 25 $\mu\mu$F. Its frequency range is 25 cps to 250 kc/s. Accuracy for a-c is $\pm$ 3 per cent f.s.d. up to 100 kc/s and $\pm$ 5 per cent up to 250 kc/s.

The d-c circuit of the instrument is stabilized by two feedback loops, one of them including a chopper which insures exceptionally low drift. Accuracy is $\pm$ 3 per cent on all ranges.

Ten standard voltage ranges in both a-c and d-c, up to 300 volts, are available in SPD-35.

---

## RISE, STORAGE AND FALL TIME METER

*E-H Research Laboratories, Inc., 1922 Park Boulevard, Oakland 6, California*

The Model 140 Rise, Storage and Fall Time Meter provides a direct read-out allowing very fast measurements to millimicrosecond accuracies. Time is displayed directly on pannel meters or presented as voltages in full scale ranges from 10 millimicroseconds to 10 microseconds, for each of three independently adjustable time difference channels. The instrument is particularly suitable to production line or routine inspection testing methods, as well as laboratory usage.

---

## THE INDIAN POINT ATOMIC POWER PLANT

Indian Point will have a total generating capacity of 275 000 kW when operation begins early in 1961. The reactor will be of the pressurized water type using a mixture of 93 per cent enriched uranium oxide ($UO_2$) and thorium oxide ($ThO_2$) as fuel.

The $UO_2$ and $ThO_2$ fuel will be homogeneously mixed, formed into pellets, and placed in rod type fuel elements clad with stainless steel.

Water under pressure flows through the core and is heated to 518° F.

The water then flows to one of four heat exchangers, where the heat is transferred to water that is not under pressure, thus changing it to steam having a temperature of 449° F. Total heat output of the reactor equals 585 MW, which will produce steam at the rate of 2 200 000 pounds per hour.

The steam at this temperature is capable of producing 163 000 kW of electricity. However, before going to the steam turbines, it flows through an oil fired super-heater, which raises the temperature to 1000° F, and increases its capacity to produce electricity to 275 000 kW.

Initially the atomic core will contain about 17 200 kg of thorium oxide and about 1100 kg of uranium-235 oxide. During the estimated useful core life of 600 days, approximately 350 kilograms of thorium oxide and 405 kg of uranium oxide will be used, leaving 16 950 kg of $ThO_2$ and 695 kg of $UO_2$, which can be processed for re-use. An additional 147 kg of fissionable U-233 will also be available for re-processing.

The active portion of the reactor core, which is the portion that actually contains active atomic fuel, resembles a right circular cylinder 8-ft high and 6.5-ft in diameter. It is housed in the reactor vessel that resembles a cylinder measuring 11 ft. in diameter by 40 ft high. Weighing approximately 255 tons, the reactor vessel is designed to operate at a pressure as high as 1800 pounds per square inch.

Outstanding feature of the Indian Point atomic power plant is the 180-ft diameter concrete external radiation shield with self-supporting dome which surrounds the 160-ft diameter steel sphere that will house the nuclear "hardware".

---

## 150 kV POSITIVE ION ACCELERATOR TYPE JH

*Detailed Specification*

*Electrostatic Generator:* 150 kV 2.5 milliamps, positive polarity.

*Working Conditions:* Ambient working temperature must not exceed 40° C. The generator is designed to function if necessary continuously for 24 hours per day on full load.

*Controls and Accessories:* The controls for the generator are mounted on the main control desk of the installation, together with all the necessary controls and measuring instruments. A kilovoltmeter gives a continuous indication of the actual working voltage.

Various safety devices protect the apparatus from accidents, or errors of adjustment made by the operator are nicorporated in the Generator.

*Ion Source: Description.* The radio frequency ion source consists of an H.F. oscillator, the ion source itself, a palladium leak, and the power supplies for the extraction and focus voltages.

The assembly, which is contained in the high voltage head of the tube, is supplied by five insulating transformers. A spare ion source tube is provided with the accelerator.

The ion source is capable of giving a maximum beam current between 0.75 and 1.00 milliamps. It can be used either with hydrogen or with deuterium.

The ion source is remotely controlled and one can adjust the HF power, the gas diffusion rate through the palladium leak and the extraction voltage.

A gas bottle of 300 cc capacity is provided for the hydrogen or deuterium.

Measuring instruments mounted in the H.T. electrode permit the oscillator current and the output current of the extraction potential power supply to be read.

*Pulsing Unit:* This unit enables the ion beam to be pulsed at repitition rates between 0.65—3 kc/s between 50 and 100 $\mu$s.

*Accelerator Tube and Pumps:* The tube is of the two-stage type. The focussing voltage is provided by a special power supply, incorporated in the high voltage electrode. This focussing voltage is adjusted from the control desk.

A device is incorporated which limits the flow of electrons to the high voltage electrode of the tube.

The accelerator tube is provided with a complete pumping installation with mechanical backing pump, oil diffusion pump together with the necessary valves and taps. An indicator lamp is mounted on the pumping system and a remote indication of the pressure can be obtained by a two channel device connected to two pressure gauges which are mounted in the high vacuum and backing pressure lines.

A safety device is provided on the diffusion pump in the event of failure of the cooling water supply.

*Target:* The target mounting is designed so that the target can be changed without letting down the vacuum. If requested, an extension tube about 1 metre long can be provided.

The target is essentially at earth potential.

The following supplies are necessary:

The power supply used for the installation is a 50 c/s three-phase alternating supply.

The power consumption is about 8 kVA.

A water supply-minimum flow rate, 20 litres per minute is necessary for cooling purposes.

---